



Meilijson, A., Hilgen, F., Sepúlveda, J., Steinberg, J., Fairbank, V., Flecker, R., Waldmann, N. D., Spaulding, S. A., Bialik, O. M., Boudinot, F. G., Illner, P., & Makovsky, Y. (2019). Chronology with a pinch of salt: Integrated stratigraphy of Messinian evaporites in the deep Eastern Mediterranean reveals long-lasting halite deposition during Atlantic connectivity. *Earth-Science Reviews*, 194, 374-398. <https://doi.org/10.1016/j.earscirev.2019.05.011>

Peer reviewed version

License (if available):
CC BY-NC-ND

Link to published version (if available):
[10.1016/j.earscirev.2019.05.011](https://doi.org/10.1016/j.earscirev.2019.05.011)

[Link to publication record in Explore Bristol Research](#)
PDF-document

This is the accepted author manuscript (AAM). The final published version (version of record) is available online via Elsevier at <https://doi.org/10.1016/j.earscirev.2019.05.011> . Please refer to any applicable terms of use of the publisher.

University of Bristol - Explore Bristol Research

General rights

This document is made available in accordance with publisher policies. Please cite only the published version using the reference above. Full terms of use are available: <http://www.bristol.ac.uk/red/research-policy/pure/user-guides/ebr-terms/>

1. Introduction

An international and multidisciplinary group of scientists have recently joined efforts to organize the challenging endeavor of drilling through the thick Messinian evaporites found in deep Mediterranean basins (IODP pre-Proposal P857B DREAM; Camerlenghi et al., 2014; Lofi and Camerlenghi, 2014). The targeted deep basin evaporites reach up to 3 km in thickness (Hsü, 1973) and are thought to have resulted from restricted connectivity of the Mediterranean Basin to the Atlantic Ocean that lead to the Messinian Salinity Crisis (MSC). It has been suggested that deposition of the MSC salt giant has greatly affected the global oceans by sequestering 5% (Ryan, 1973; 2008) to 10% (Garcia-Castellanos and Villaseñor, 2011) of their salt content into the Mediterranean. Also, by contributing warm, saline water to northern latitudes, the MSC influenced Atlantic Meridional Overturning Circulation and, consequently, global climatic shifts (Hernández-Molina et al., 2014). Among the major stratigraphically-driven findings of modern geoscience, the MSC stands alone as being supported by an 'outrageously under-sampled stratigraphic record' (CIESM, 2008). For several decades, focused investigation of the MSC within various interdisciplinary studies was aimed at understanding the mechanisms governing its timing, paleogeography, and the inter-relationship between external forcing and physical systems response. However, while the deep-basin halite was penetrated in its uppermost part (Fig. 1), the prohibitive risk and high drilling cost of ~~drilling-recovering~~ cores through the entire deep-basin MSC unit has resulted in a critical lack of data. Scientific drilling of the deep Mediterranean basins has been repeatedly called for in order to test and validate different hypotheses regarding the MSC in the deep Mediterranean basins (CIESM, 2008; Dela Pierre et al., 2014; Gvirtzman et al., 2017; Manzi et al., 2015, 2018; Meilijson et al., 2018), but has yet to be achieved.

57
58
59 24 The MSC came into awareness and was documented as early as the 1950's, when massive
60
61 25 evaporite outcrops in the peri-Mediterranean were identified as co-occurring around the end of
62
63 26 the Miocene (Selli, 1954; Ogniben, 1957). However, the MSC magnitude and extent became
64
65 27 clear only when seismic imaging penetrated the massive diapiric and stratified salt bodies of the
66
67 28 Mediterranean Sea, reaching more than 2 km in thickness and stretching across vast parts of the
68
69 29 basin (e.g., Bourcart et al., 1958; Alinat and Cousteau, 1962; Cornet, 1968; Ryan et al., 1971;
70
71 30 Bellaiche et al. 1974; Ryan, 1976). One of the oldest controversies related to the MSC concerns
72
73 31 the magnitude and timing of sea-level lowering and desiccation, where several models for
74
75 32 evaporite formation have been suggested. Some have proposed that salt was precipitated in deep
76
77 33 basins under a deep-water environment (Schmalz, 1969; Debenedetti, 1982; Sonnenfeld and
78
79 34 Finetti, 2011), while other scenarios promoted a desiccated shallow-water environment (Hsu,
80
81 35 1973). A hybrid model was proposed, with early brine formation in the deep Mediterranean,
82
83 36 preceding substantial drawdown, followed by massive salt precipitation during gateway closure
84
85 37 (Ryan, 2008; Garcia-Castellanos and Villaseñor, 2011; Lofi et al., 2011). Clauzon et al. (1996)
86
87 38 recognized the occurrence of shallow-water first cycle gypsum beds of the same age in many
88
89 39 localities in the western and eastern Mediterranean. Based on this observation they presented a 2-
90
91 40 step model, in which the surface of the Mediterranean Sea remained close to the global oceans
92
93 41 level during the early part of the crisis, and deep-basin evaporites formed following sea-level
94
95 42 drop of the subsequent step. Based on this model, Ryan (2011) described the geodynamic
96
97 43 response of the basin to each of these steps: 1) Significant deepening of the basins by isostatic
98
99 44 load due to an increase in weight of the brine layer. 2) As the basins dried out, the loss of weight
100
101 45 of the water led to regional isostatic uplift that permanently closed the prior inlets.
102
103
104
105
106
107
108
109
110
111
112

113
114
115 46 Van Couvering et al. (1976) were the first to propose a similar 2-step model, which also
116
117 47 portrays an early deposition of halite in the deep basins: (1) An initial deep-water phase marked
118
119 48 by refluxive concentration of brines and controlled by a tectonically elevated sill, during which
120
121 49 evaporites and associated sediments accumulated simultaneously near the surface in marginal
122
123 50 areas (gypsum) and within great saline water bodies in the depths of the basin (halite). (2) A
124
125 51 terminal phase of total isolation, caused by an eustatic sea-level drop, during which erosion and
126
127 52 desiccation features were developed that fit the "deep-basin, shallow-water" model. However,
128
129 53 this model was later abandoned in favor of what developed into the CIESM (2008) workshop
130
131 54 consensus stratigraphic model, which was elaborated in the extensive review of the MSC by
132
133 55 Roveri et al. (2014a) and widely cited.

136
137 56 The CIESM (2008) stratigraphic model of the MSC is based on correlation of Mediterranean
138
139 57 evaporite sequences deposited in marginal to intermediate basins, and their isotopic signatures
140
141 58 (Keogh and Butler, 1999; Müller and Mueller, 1991; Flecker and Ellam, 2006). While the
142
143 59 division of MSC units differs slightly in terminology between the CIESM (2008) model and the
144
145 60 widely used review of the MSC presented by Roveri et al. (2014a), they both stem from the same
146
147 61 stratigraphic concepts, and are jointly referred to here as the 'consensus model' for MSC
148
149 62 chronology. These studies demonstrate that partial connectivity with the Atlantic Ocean persisted
150
151 63 throughout the first phase of gypsum deposition, lasting for ~370 kyr and known as MSC phase
152
153 64 1: Primary Lower Gypsum [PLG], 5.97–5.6 Ma.

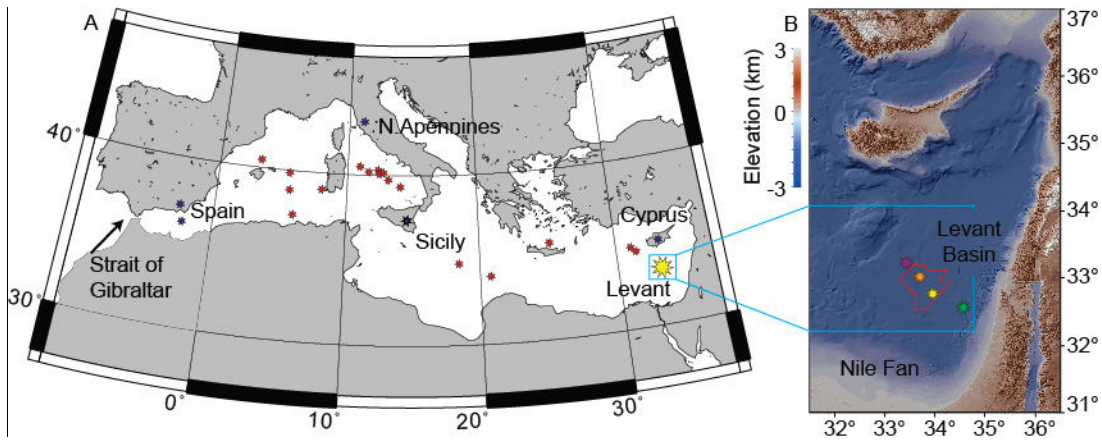


Figure 1. Map of the Mediterranean Sea marking the study area and referenced sections.

A. Map of Mediterranean Sea marking study area (yellow star); main referenced sections (blue stars); and Deep Sea Drilling Project and Ocean Drilling Program wells (red stars), which penetrated MSC halite deposits only at their uppermost part. B. Bathymetry A shaded relief map of the Levant Basin and surrounding area (Hall et al., 1994, 2015). Red polygon outlines the three-dimensional seismic cube referred to in this study. Well locations marked by stars: Aphrodite-1 (purple star), Leviathan-1 (orange), Dolphin (yellow), and Sara (Green).

During the PLG, euxinic shales and dolostones were thought to have been deposited in the deep basins in parallel to gypsum deposition in the proximal settings (Lange and Krijgsman, 2010). However, using sonic and resistivity logs and samples from cuttings of the 497-Muchamiel oil-industry well, Ochoa et al. (2015) found-observed all 14 of the known first-stage gypsum beds present in the Sorbas Basin, offshore southeast Spain, deep (875 -965 m) below the present-day sea level. This finding-observation was interpreted-to-contradict-regarded opposite to previous assumptions that only shales would be present in this interval of the deep basins (CIESM, 2008; Roveri et al., 2014a).

The thick salt unit was interpreted as being accumulated during the succeeding MSC acme, a short period of ~50 kyr known as MSC phase 2: Resedimented Lower Gypsum [RLG], 5.6–5.55 Ma (although its top is often marked at 5.53 Ma in different cyclostratigraphic schemes (e.g.,

225
226
227
228
229
230
231
232
233
234
235
236
237
238
239
240
241
242
243
244
245
246
247
248
249
250
251
252
253
254
255
256
257
258
259
260
261
262
263
264
265
266
267
268
269
270
271
272
273
274
275
276
277
278
279
280

85 Roveri et al., 2014a; Manzi et al., 2015) due to the ‘Messinian gap’, during which Messinian
86 erosion and/or deposition of resedimented gypsum and halite occurred). A model depicting the
87 desiccation of the Mediterranean during stage 2 was proposed to explain its formation over such
88 a short period of time. This model entails a massive sea-level drawdown and consequent
89 removal and re-deposition of the PLG gypsum, and a seasonal or long-term deposition of halite
90 in intermediate to deep-water basins. Lastly, the third phase of the MSC was defined within the
91 Upper Evaporites or Gypsum sequences (UG), which include clastic or brackish sediments
92 culminating in the Lago-Mare deposits (5.55-5.33 Ma). The latter consists of several units with
93 7-10 sedimentary cycles identified in the Upper Gypsum of Italy overlying erosional surfaces
94 and angular unconformities, and underlying Pliocene sediments (Hilgen et al., 2007; Krijgsman
95 et al., 2010; Roveri et al., 2014a). A recent review of different Lago-Mare deposits depicts that
96 three main pulses of seaward-transport occurred within the time-interval 5.7064-5.3033 Ma, and
97 suggests abandonment of previous concepts dealing with a unique chronostratigraphic unit,
98 favoring several episodes of flooding (Couto et al., 2014). Nonetheless, the first influx of
99 Paratethyan organisms, identified through the dinoflagellate cyst record near Malaga within a fan
100 delta, was found overlying the intra-Messinian truncation surface (IMTS) (Couto et al., 2014).

101 Recent industrial activities targeting hydrocarbon reservoirs in the Eastern Mediterranean
102 basin-Basin provide the scientific community with unparalleled seismic~~s~~, well logs, and cuttings
103 across the salt interval. The current work takes advantage of these industrial data to address two
104 critical issues regarding Messinian stratigraphy in the deep Eastern Mediterranean Basin, which
105 impact our basic understanding of this event: (1) To evaluate the composition, age and duration
106 of evaporite deposition in the Eastern Mediterranean. (2) To characterize, interpret, and
107 stratigraphically position the sediments overlying the IMTS (as in Gvirtzman et al., 2017),

281
282
283 108 termed here the Interbedded and Argillaceous Evaporites. Here, we report previously unknown
284
285 109 features and lithology of the deep basin MSC₇ and₂ by using a multi-disciplinary approach, we
286
287 110 provide further interpretation of their stratigraphic significance.

289 290 111 **2. MSC deposits in the Levant**

291
292 112 Feng et al. (2016) analyzed jointly well-log measurements and a pervasive seismic dataset,
293
294 113 and demonstrated that the seismically transparent layers composing the majority of the
295
296 114 Messinian evaporites sequence deposits across the deep Levant Basin is-are composed of pure
297
298 115 halite. The reflective layers appearing within the halite (Figs- 2, 3) were interpreted as bundles of
299
300 116 thin clay layers interbedded in the halite background, having a cumulative thickness of 25--40
301
302 117 m. Feng et al. (2016) also reported high--amplitude fan structures on the deepest internal
303
304 118 reflectors₂ which may suggest transport mechanisms. Later, Gvirtzman et al. (2017) argued
305
306 119 against a complete desiccation of the Eastern Mediterranean₂ following the seismic identification
307
308 120 of the IMTS at ~100 m below the Messinian-Zanclean boundary in the Levant Basin. Based
309
310 121 solely on interpretation of well logs and correlation to shallower-water wells, Gvirtzman et al.
311
312 122 (2017) suggested that the post-truncation Messinian unit is different from the underlying salt
313
314 123 deposits and mostly consists of shale, sand and anhydrite. Lastly, two separate studies (Manzi et
315
316 124 al., 2018; Meilijson et al., 2018) have investigated the sediments underlying the evaporites, based
317
318 125 on data from different wells within the Levant Basin. Both studies address the stratigraphy of the
319
320 126 Pre-Evaporites and are aimed at providing an indication for the age of the base of the halite in the
321
322 127 deep Eastern Mediterranean, represented on seismic data in the region as the 'N' reflection
323
324 128 (Ryan, 1978; Bertoni and Cartwright, 2007). Establishing the age and duration of the deep-basin
325
326 129 halite is perhaps the most enigmatic aspect of MSC research. Both recent studies test the CIESM
327
328 130 stratigraphic model of the MSC (CIESM, 2008; Dela Pierre et al., 2014; Roveri et al., 2014a).

337
338
339 131 Manzi et al. (2018) and Meilijson et al. (2018) report several similar findings, such as the
340
341 132 seismic interpretations regarding the conformity of the base of the evaporites, and thus refuting
342
343 133 the occurrence of a long hiatus at the base of the evaporites. In addition, both studies indicate
344
345 134 little deformation of the Levant ~~pre~~Pre-~~e~~Evaporite interval and a continuous record of the ~~upper~~
346
347 135 Tortonian to ~~Lower~~Messinian ~~intervals~~sediments. Still, different observations reported in these
348
349 136 studies have led to continued uncertainty concerning the age and duration of salt deposition.
350

351
352 137 Meilijson et al. (2018) considered two alternatives for the age of the base evaporites in the
353
354 138 deep basins: (1) during stage 1 (PLG) of the MSC at around 5.9 Ma, or (2) at around 5.6 Ma
355
356 139 during stage 2 (RLG) of the MSC, as is described in the CIESM stratigraphic model (CIESM,
357
358 140 2008; Roveri et al., 2014a). The latter would imply a major hiatus of ~370 kyr (missing the PLG
359
360 141 equivalent unit) at the base of the salt, or alternatively that the PLG is expressed as a very thin
361
362 142 interval in the uppermost Pre-Evaporites unit. A hiatus in the deep basin has not been identified,
363
364 143 but rather a visible lateral continuity of seismic reflectors below and at the boundary itself
365
366 144 (Meilijson et al., 2018). This finding is consistent with published regional seismic sections (Feng
367
368 145 et al., 2016; Manzi et al., 2018; Roberts and Peace, 2007) and elsewhere in the deep domain of
369
370 146 the Mediterranean (Lofi et al., 2011). Thus, Meilijson et al. (2018) concluded that the studied
371
372 147 section is in fact conformal and halite began to precipitate around the onset of the PLG in the
373
374 148 marginal basins, predating the CIESM consensus for halite deposition by ~300 kyr.
375
376

377
378 149 Manzi et al. (2018) reported that in the Aphrodite-2 well (Fig. 1), which is the deepest
379
380 150 location along their four-well cross-section, a complete absence of foraminifera occurs from
381
382 151 3959 m upwards, 28 m below the first occurrence of anhydrite, and 33 m from the base of halite
383
384 152 deposition. They interpret this foraminifera barren interval (FB~~I~~I) as corresponding to the Non-
385
386 153 Distinctive Zone (NDZ) marking the onset of the MSC (5.971 Ma) in marginal settings (Gennari et
387
388
389
390
391
392

393
394
395 154 al., 2013; Manzi et al., 2013). Manzi et al. (2018) proposed that this interval represents the deep basin
396
397 155 expression of the PLG, followed by halite deposition during stage 2 of the MSC at around 5.6 Ma.
398
399 156 This FBI is argued by them to be further substantiated by a prominent peak of *Sphenolitus abies* at
400
401 157 3961 m, closely followed by a decrease in the number of species of calcareous nannofossils. The
402
403 158 FBI was also identified by Manzi et al. (2018) in the Myra well, which is situated in a more proximal
404
405 159 position, 90 km SW to the Aphrodite well. ~~Further~~ Farther landward to the west, the FBI is no longer
406
407 160 recognized in the Sara well, where the Aphrodite well equivalence of about 60 m underlying the base
408
409 161 of the evaporites is missing. This observation indicates that the Dolphin well should also include an
410
411 162 equivalent FBI, as it is positioned between the Myra well, and closer to the latter (Fig. 1). However,
412
413 163 such an FBI is not present in the Dolphin well, in which the samples include a relatively open-
414
415 164 marine foraminiferal assemblage up to the uppermost sample available for analysis, representing the
416
417 165 interval 0-9 m below the base of the evaporites (Meilijson et al., 2018). Thus, the MSC timing and
418
419 166 events are still debated after more than 50 years of research and over 10,000 publications.

420
421 167 -In recent years, different studies have been leaning towards new and very different ideas
422
423 168 regarding MSC chronology, and thus the mechanisms controlling the deposition of salt giants in deep
424
425 169 sea basins. Ochoa et al. (2015) demonstrated synchronous deposition of evaporites in marginal and
426
427 170 intermediate basins. Simon and Meijer (2017) modeled stratification in the Mediterranean during the
428
429 171 MSC and raised the possibility of a much earlier onset of halite in the deep basins. Finally, García-
430
431 172 Veigas et al. (2018) even went so far as to draw a model for an early onset of halite, yet added a
432
433 173 question mark next to this assumption due to lack of proof for this claim (their ~~Fig~~ fig. 12). Here, we
434
435 174 address this debate on the chronology of MSC events in the Mediterranean by examining the
436
437 175 recovery of deep-basin evaporites from the Levant Basin for stratigraphic indicators that can
438
439 176 promote a better understanding of MSC chronology.
440
441
442
443
444
445
446
447
448

449
450
451 177 The MSC (CIESM, 2008; Roveri et al., 2014a) is expressed in the southeastern Levant Basin
452
453 178 margins as a thick evaporitic sequence (locally named the Mavqiim Formation), as well as clastic
454
455 179 evaporite deposits along local topographical lows (Buchbinder and Zilberman, 1997; Druckman
456
457 180 et al., 1995; Lugli et al., 2013). The MSC deposits in the deep Levant Basin have been identified
458
459 181 through seismic data, and interpreted as mainly consisting of halite, reaching a thicknesses of
460
461 182 ~2 km in the central part of the basin and pinching out upslope towards its southeastern margin
462
463 183 (Bertoni and Cartwright, 2007, 2006; Feng et al., 2016; Gardosh et al., 2008; Netzeband et al.,
464
465 184 2006; Steinberg et al., 2011). The halite sequence base and top are generally imaged as
466
467 185 pronounced high-amplitude seismic reflections, known as the N and M reflectors, respectively
468
469 186 (Ryan, 1978). Up-dip, the evaporitic sequence thins below ~~the~~ seismic resolution and is entirely
470
471 187 represented by the M ~~reflection-reflector~~ (e.g., Steinberg et al., 2010). The nomenclature of the
472
473 188 MSC section in the Levant Basin is currently based on the regional identification of a number of
474
475 189 key markers within seismic sections across the basin, with several divisions presented by
476
477 190 different studies: division of the section into 6 or 7 units (Gvirtzman et al., 2013b, 2017; Lugli et
478
479 191 al., 2013), or into ME 1-4 (Messinian evaporites), and MC 1 and 2 (Messinian clastics; Feng et
480
481 192 al., 2016). In this manuscript we refer to the unit numbers (Gvirtzman et al., 2017, 2013b) and
482
483 193 ME/MC units (Feng et al., 2016), corresponding seismically to the lithostratigraphic descriptions
484
485 194 and division of the Dolphin well sediments.

489
490 195 Several studies have shown that the seismic records of the MSC greatly differ between the
491
492 196 Western and Eastern Mediterranean basins, and argued that it is impossible to properly correlate
493
494 197 individual sub-units (Lofi et al., 2011). Some authors have also questioned the possible
495
496 198 diachronism between both basins (Blanc, 2000; Ryan, 2008). However, the Levant has been for
497
498 199 many years at the center of debate regarding the evolution of the MSC across the entire

505
506
507 Mediterranean ~~basin~~Basin. An example for such a long-term debate includes the formation of the
508
509
510 201 vast drainage systems at the Mediterranean margins and the deposition, or re-deposition, of
511
512 202 gypsum within them. An important type location for this debate is the Afik canyon along the
513
514 203 continental margin of Israel. The presence of evaporite layers at different levels along the Afik
515
516 204 canyons was brought as one of the first evidence for a substantial Messinian sea-level drawdown
517
518 205 (800 m sea-level drop; Druckman et al., 1995). However, these deposits were recently argued to
519
520 206 result ~~of~~ from evaporites recycling through slope mass-wasting, a phenomena suggested to
521
522 207 characterize the upper parts of the MSC throughout the Mediterranean (Lugli et al., 2013). The
523
524 208 wells investigated in this study were drilled in the Levant Basin, and may ~~be argued to~~ represent
525
526 209 local conditions rather than account for the entire Mediterranean Basin. However, by recovering
527
528
529 210 one of the most extensive evaporite deposits of the MSC, the analysis of these wells bears key
530
531 211 implications for unraveling the MSC across the entire Mediterranean.

532 533 212 **3. Methodology**

534
535
536 213 This study is based on the combined analyses of well cuttings, 3D pre-stack depth-migrated
537
538 214 reflection seismics ~~reflection~~, and well-log data of two deep-water industry wells recently
539
540 215 drilled in the Levant Basin (Fig. 1). We have also used a time-migrated 2-D seismic survey
541
542 216 acquired by TGS-NOPEC Geophysical Company in 2000, and the 3-D depth-migrated Pelagic
543
544 217 seismic survey acquired by CGG-Veritas in 2009. Lithological and biostratigraphic data
545
546 218 presented in this study are from the Dolphin well (N 3628144.05 m, E 575444.97 m), drilled by
547
548
549 219 the Leviathan partnership at a water depth of 1,500 m and penetrating the 1,590 m thick
550
551 220 Messinian evaporite section at depths of 2,026-3,616 m below sea level. The second studied well
552
553 221 is the Leviathan-1 well (N 3653455.35 m, E 553663.40 m), also drilled by the Leviathan
554
555 222 partnership at a water depth of 1,644 m and penetrating the 1,694 m thick Messinian evaporite
556

561
562
563 223 section at depths of 2,090-3,784 m below sea level. The record presented in this study
564
565 224 supplements the 350 m section immediately below the base of the halite shown in Meilijson et al.
566
567 225 (2018). Samples were curated and archived in both the Organic Geochemistry Laboratory at the
568
569 226 University of Colorado (organic extracts) and the Department of Marine ~~Geosciences~~
570
571 ~~Geosciences~~, Leon Charney School of Marine Sciences, University of Haifa.
572
573

574 228 Drilled cuttings returns are available starting down from a depth of 2,535 m and 2,497 m in
575
576 229 the Dolphin and Leviathan-1 wells, respectively. The Pre-Evaporites interval of the Dolphin
577
578 230 (Meilijson et al., 2018) and Leviathan wells was sampled every 3 m. The evaporite interval was
579
580 231 sampled every ~9 m, with a total of 123 samples from the Dolphin well. Due to standard drilling
581
582 232 activities, many fallouts of ~~the~~ clastic deposits occur downhole from the lower part of the
583
584 233 ~~interbedded~~ Interbedded evaporite-Evaporite unit to the upper part of the Main Halite unit,
585
586 234 appearing as an interval of clastic deposits in the XRD log of the Dolphin well from 2,560 to
587
588 235 2,675 m. Well-log data does not respond to this high-clastic content (i.e., high RE log values and
589
590 236 low GR log values), and so does not show a shift from halite deposition. This observation
591
592 237 confirms that the clastic material arrives from the ~~Interbedded Evaporites~~ unit above, as drilling
593
594 238 fallouts into the halite interval. While not in-situ, these fallouts, together with the well logs,
595
596 239 allow us to interpret ~~at~~ the distinct lithological transition ~~occurring that occurs~~ at the boundary
597
598 240 between the Main Halite and Interbedded Evaporites unit. However, these fallouts might also
599
600 241 originate from the Argillaceous Evaporites unit above.
601
602
603

604 242 Individual cutting bits were separated by their lithology under a microscope, cleaned with
605
606 243 deionized water and 10% hydrochloric acid, dried, and then crushed in an agate pestle and
607
608 244 mortar. Fine powders were pressed and used for bulk mineralogical X-ray diffractogram (XRD)
609
610 245 analysis using a Rigaku 600 MiniFlex X-Ray Diffractometer with a CuK α source at 30kV / 15-

617
618
619 246 mA from 3° to 70°. Mineralogical compositions of assemblages were determined using the
620
621 247 ICDD PDF2 mineral database references. Next, fine powders were pressed in ~~telephone-~~Teflon
622
623
624 248 crucibles with X-Ray transparent mylar (which was replaced between samples). Each sample
625
626 249 was then analyzed using a Nitton X-Ray XL3 GOLDD+ Fluorescence apparatus for elemental
627
628 250 composition.

629
630 251 Samples found to be bearing microfossils were investigated for their faunal assemblages,
631
632 252 which included washing and picking foraminifera from the Pre-Evaporites (detailed in Meilijson
633
634 253 et al., 2018) and the preparation of smear slides for the study of the diatomites interbedded
635
636 254 within the halite. For the latter, samples were weighed, treated several times with 10% HCl for
637
638 255 carbonate removal, and 30% hydrogen peroxide for organic matter removal, and then loaded
639
640 256 onto glass slides. A total of 50 diatom valves were counted and identified from 10 samples.
641
642 257 Diatoms were characterized by their habitat preferences: planktonic vs. benthic, and marine vs.
643
644 258 freshwater.

645
646
647 259 We also studied the distribution of selected biomarkers (i.e., *n*-alkanes, algal steranes, and
648
649 260 bacterial hopanes) from different intervals to gain insight into variations in organic matter
650
651 261 sources and thermal alteration. Rock cuttings were cleaned and handled with solvent-rinsed
652
653 262 metal tweezers, a Dremmel 8220 wire-brush tip, spatulas, and combusted aluminum foil, and
654
655 263 then powdered with a solvent-rinsed agate mortar and pestle. Approximately 5-10 grams of
656
657 264 sample were extracted using a Dionex Accelerated Solvent Extractor (ASE 200; 100 °C; 2,000
658
659 265 psi) and a mixture of dichloromethylene:methanol 9:1 (v:v) until no more color was observed
660
661 266 (typically 3-6 extractions). Each extraction cycle included heating of the cell for 5 minutes, static
662
663 267 mode for 5 minutes, and flushing for 2 minutes time. A cocktail of internal standards containing
664
665 268 500 ng of D4 C₂₉ ααα (20R)-Ethylcholestane, and 1,000 ng of each 3methyl heneicosane, D14
666
667
668

673
674
675 269 pTerphynyl, 1-nonadecanol, behenic acid methylester (Docosanoic acid), and 2methyl
676
677 270 octadecaonic acid, was added to samples before extraction for quantitation purposes. Total lipid
678
679 271 extracts (TLEs) were combined and evaporated under a gentle nitrogen flow using a Turbovap.
680
681 272 Elemental sulfur was removed using HCl-activated copper shots. TLEs were then filtered
682
683 273 through small Pasteur pipettes filled with combusted glass wool and sand to remove impurities
684
685 274 and any copper-sulfide residues. Asphaltenes were separated from maltenes by precipitation in
686
687 275 hexanes at 4°C for 3 hours, followed by centrifugation at 2000 rpm (3x). Maltenes were later
688
689 276 separated into five different lipid classes by liquid chromatography on small Pasteur pipettes
690
691 277 filled with silica gel. Aliphatic (F1) and aromatic (F2) hydrocarbons were recovered with hexane
692
693 278 (3/4 dead volumes) and hexane:dichloromethylene 8:2 (v:v; 4 dead volumes), respectively. The
694
695 279 more polar fractions (F3, F4, F5) were eluted using dichloromethylene,
696
697 280 dichloromethylene:EtOAc 1:1, and EtOAc (v:v, 4 dead volumes), respectively. Aliphatic
698
699 281 hydrocarbons were analyzed on full scan and selected reaction monitoring (SRM) modes via gas
700
701 282 chromatography – triple quadrupole-mass spectrometry (GC-QQQ-MS) using a Thermo Trace
702
703 283 1310 Gas Chromatograph interfaced to a TSQ Evo 8000 triple quadrupole mass spectrometer
704
705 284 (GC-QQQ-MS) equipped with a split-less PTV injector and electron impact ion source. Helium
706
707 285 was used as a carrier gas with a flow rate of 1.2 ml min⁻¹. Chromeleon 7 was used for data
708
709 286 integration. Aliphatic hydrocarbons were separated using a 60-meter DB-1MS GC column (60
710
711 287 m, 0.25 mm I.D., 0.25 µm film thickness; Agilent Technologies). For FS analysis, samples were
712
713 288 injected at 60°C and then the PTV was heated to 300°C at 14.5°C/second. The GC oven
714
715 289 temperature program was: 60°C (2 min) to 150°C at 15°C min⁻¹, to 315 (held 24 min) at 3°C
716
717 290 min⁻¹. The total GC program was 90 minutes. MS conditions were: 300°C ion source at 70eV
718
719 291 electron energy, 50µA emission current, and 15V electron lens voltage. The mass range was 50-

729
730
731 292 600 m/z with a dwell time of 0.2 seconds per scan. For SRM analysis, the GC oven temperature
732
733 293 program was: 60°C (0 min) to 220°C at 15°C min⁻¹, to 315°C (held 25 min) at 3°C min⁻¹. The
734
735 294 total GC program was 68 minutes. Samples were injected at 65°C and then the PTV temperature
736
737 was heated to 400°C at 3 °C min⁻¹. MS conditions were: ion source temperature of 250°C;
738 295
739 transfer line temperature of 320°C, electron energy of 70eV, electron lens voltage of 35V, and
740 296
741 emission current of 35uA. Peak scanning windows ranged from 0.6 to 1 minute for 147 timed
742 297
743 transitions for regular and methylated steranes and hopanes, and their stereoisomers.
744 298
745

746 299 **4. Evidence from the Levant Basin for an early onset of halite deposition in a deep-water** 747 748 **environment** 749 300

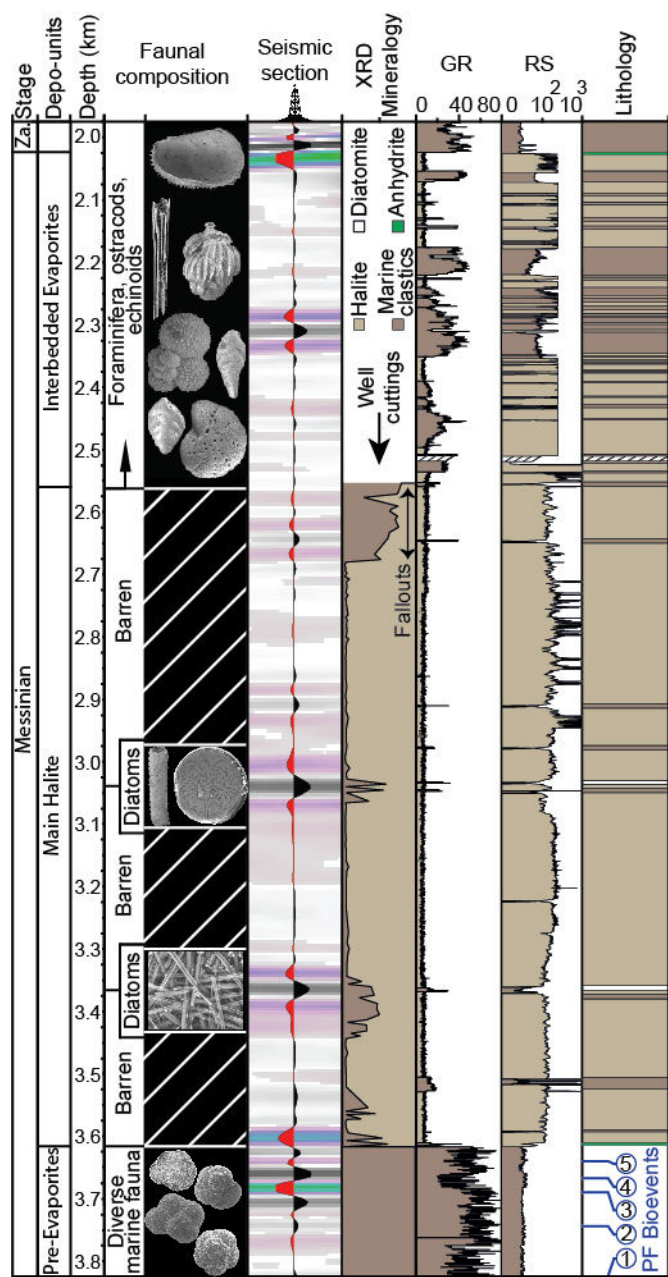
750 751 301 **4.1 Lithologic composition of the Levant deep-sea salt-giant** 752 753

754 302 *4.1.1 Pre-Evaporites* 755

756 303 This interval is detailed in Meilijson et al. (2018). Here we provide a generalized summary,
757
758 304 followed by a more elaborate account of the overlying evaporites of the deep Levant Basin. The
759
760 305 ~~prePre-evaporite-Evaporite~~ interval in the Dolphin well (3850–3616 m; Fig. 2) is seismically
761
762 306 characterized by sub-horizontal and sub-parallel continuous high-amplitude reflections,
763
764 307 implying a stratified and relatively un-deformed marine succession (Meilijson et al., 2018). It is
765
766 308 composed of fine-grained clastic-micritic and carbonate bathypelagic sediments, primarily gray
767
768 309 to dark gray or greenish calcareous soft to hard shale, with several thin layers of white to light
769
770 310 gray hard limestone, and light gray very fine to fine-grained unconsolidated sandstone. Diverse
771
772 311 assemblages of nannofossils, benthic and planktic foraminifera are recognized within this
773
774 312 interval.
775
776
777 313

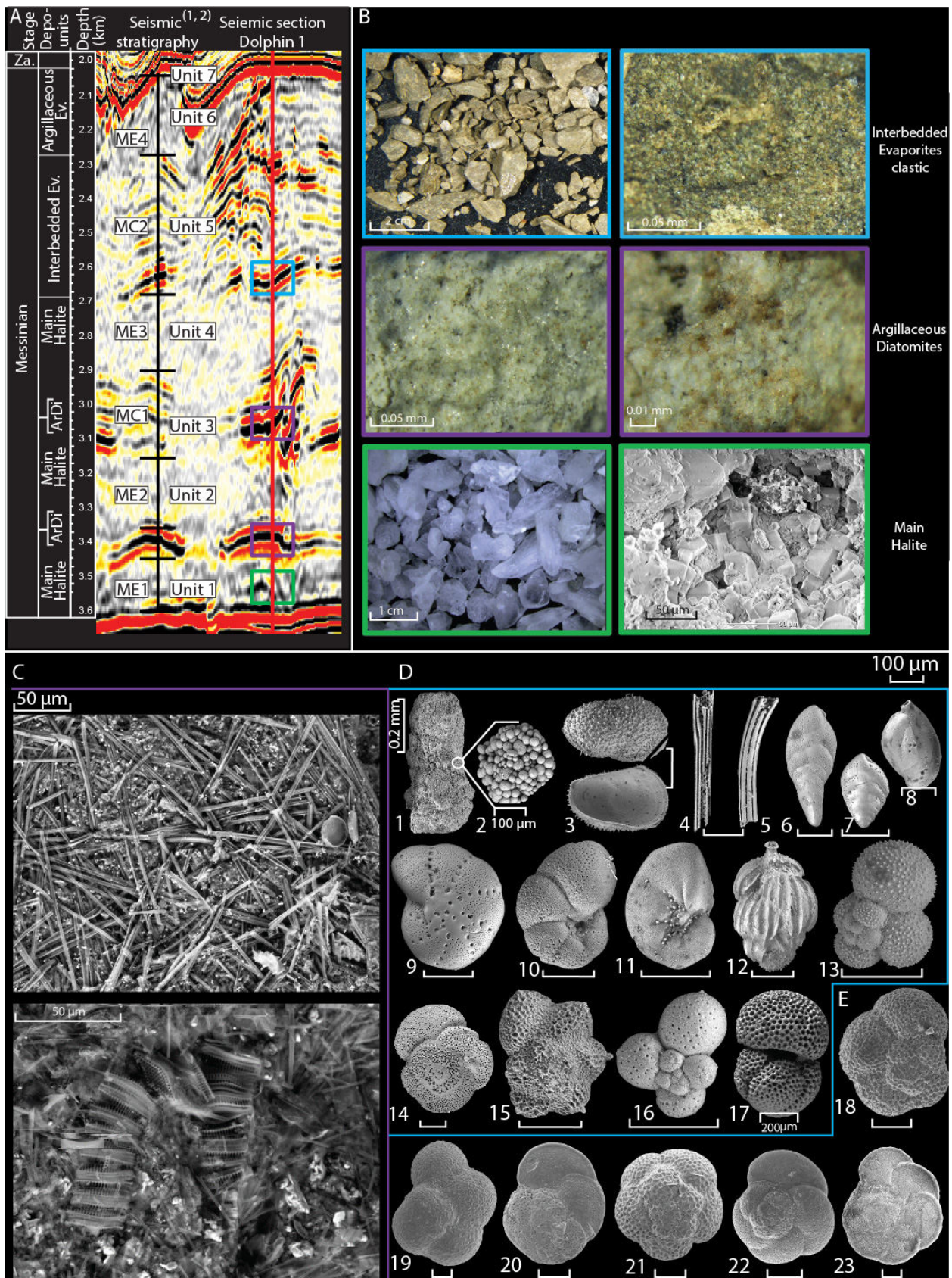
785
786
787
788 314 *Figure 2. The MSC succession of the Dolphin well in the deep Levant ~~basin~~Basin.*
789 315 A juxtaposed simplified display of the primary proxies used to characterize the Dolphin well
790
791 316 section (five central columns), and our depositional (left) and lithological (right) interpretations.
792
793 317 The attributes are (left to right): the faunal composition; the seismic response, with transparent
794
795 318 intervals representing predominantly evaporites and high--amplitude reflections representing
796
797 319 clastic beds (a seismic trace (center) emphasizes relative intensity of the seismic phases); XRD
798
799 320 mineralogy, showing the relative abundance of halite (bright) vs. non-halite (dark; 'marine
800
801
802 321 clastics'), where the uppermost clastic interval (<2,650 m) represents fallouts from the
803
804 322 ~~interbedded~~Interbedded evaporitesEvaporites; the gamma ray (GR -- API units) and resistivity
805
806 323 (RE -- log ohm-m units) logs, color coded based on the characteristic responses to halite and
807
808 324 clastics. The lithological interpretation is color coded as in the attribute columns. Planktonic
809
810 325 foraminiferal (PF) bio-events in blue circles correspond to the following ages: 1- 7.72, 2- 7.24, 3-
811
812 326 6.72, 4- 6.36, and 5- 6.13 Ma (Meilijson et al., 2018).
813
814
815 327
816
817
818
819
820
821
822
823
824
825
826
827
828
829
830
831
832
833
834
835
836
837
838
839
840

841
842
843
844
845
846
847
848
849
850
851
852
853
854
855
856
857
858
859
860
861
862
863
864
865
866
867
868
869
870
871
872
873
874
875
876
877
878
879
880
881
882
883
884
885
886
887
888
889
890
891
892
893
894
895
896



328

897
898
899
900
901
902
903
904
905
906
907
908
909
910
911
912
913
914
915
916
917
918
919
920
921
922
923
924
925
926
927
928
929
930
931
932
933
934
935
936
937
938
939
940
941
942
943
944
945
946
947
948
949
950
951
952



329

953
954
955 330 *Figure 3. Seismic stratigraphy, common lithologies, and SEM imaging of the studied section.*
956
957 331 **A.** The seismic profile crossing the sampled Dolphin well position and its division into the MSC
958 332 depositional units, compared to previously published seismic stratigraphy of the deep Levant
959 333 MSC ((1) Feng et al., 2016; (2) Gvirtzman et al., 2017). ArDi --- Argillaceous Diatomites; Ev. -
960 334 Evaporites. Color coded rectangles corresponding to lithologies described in (B). **B.** images of
961 335 the three main facies recognized in the Levant evaporite section: the homogeneous ~~main~~ Main
962 336 halite Halite (green rectangle) made of pure halite as seen in hand specimen (left) and SEM
963 337 imagery of cubic cleavage (right), corresponding with subdued internal seismic reflectivity in
964 338 (A); Argillaceous Diatomite beds (purple rectangle), represented by high amplitude reflections in
965 339 (A); and Interbedded Evaporites (blue rectangle) identified as brown marine clastics,
966 340 characterized by interchanging low and high amplitude reflections in (A). **C.** Selected SEM
967 341 images from the densely packed and very well preserved diatoms from the diatomite facies. **D.**
968 342 Selected SEM images of the >63 µm size fraction of the washed residue from the Interbedded
969 343 Evaporites unit clastic sediments (P.1-17) showing: large grains of framboidal pyrite (P.1-2),
970 344 well-preserved ostracod valves (P.3), sea urchin spines (P.4-5), benthic foraminifera (P.6-12),
971 345 and planktic foraminifera (P.13-17). **E.** SEM images of the planktic foraminifera used for the
972 346 biostratigraphic age-model (Meilijson et al., 2018) of the ~~pre~~ Pre-E evaporites (P.18-23):
973 347 *Neogloboquadrina* sp. (P.18), *Sphaeroidinellopsis seminulina* (P.19), *Globorotalia miotumida*
974 348 (P.20), *Globoquadrina altispira* (P.21), *Globorotalia scitula* (P.22); *Globorotalia menardii*-4
975 349 (P.23). All scales are 100 µm unless indicated otherwise.

987 350
988
989 351 Shale samples are organic-rich (>1 wt.% TOC) and reach peak values of 4 wt.% TOC
990 352 immediately underlying the base of evaporite deposition (Meilijson et al., 2018). Lower values of
991 353 gamma ray (GR) are associated with silt/carbonate-rich sediments, while higher GR corresponds
992 354 to shale/organic-rich sediments (Fig. 2).

998 355 4.1.2 Main Halite

1000 356 Here we reference our lithologic interpretation to the recently defined seismic stratigraphy of
1001 357 the Levant MSC (units Units 1-6; Gvirtzman et al., 2013), and ME1-4 for the transparent and

1009
1010
1011 358 MC1-2 for the high reflectivity intervals (Feng et al., 2016) (Fig. 3). Different velocity models
1012
1013 359 reported high seismic velocities of 4200-4400 m/s (Gvirtzman et al., 2013a), 3850-4240 m/s
1014
1015
1016 360 (Reiche et al., 2014), and 4400-4600 m/s (Feng et al., 2016) for the seismic transparent layers,
1017
1018 361 interpreted as representing the halite facies. Here we advocate this interpretation by providing the
1019
1020 362 first semi-quantitative XRD analysis (Fig. 4) of well cuttings spanning the transparent high
1021
1022 363 velocity layers.

1024 364 The Main Halite unit in the vicinity of the Dolphin (3616- 2755_m) and Leviathan-1 (3759-
1025
1026 365 2800 m) wells is characterized by low seismic reflectivity, which is internally interrupted by
1027
1028 366 several main high reflectivity bands (Figs- 5, 6). These instances are clearly recognized in the
1029
1030 367 well_-logs (Fig- 2, 5), and represent a different facies within the hyper-saline deposits, described
1031
1032 368 ~~aheadbelow~~. Using XRD analysis coupled with SEM (Fig. 4), we conclude that the transparent
1033
1034 369 intervals are indeed composed of nearly pure (~~←~~(\geq 90%) halite (Fig. 4), with minor quantities of
1035
1036 370 anhydrite, magnesite and barite. Anhydrite ~~appears is also present~~ as a relatively thin bed (<3 m)
1037
1038 371 at the base of the Main Halite section, where it represents the transition to the Main Halite.
1039
1040 372 Anhydrite ~~also further~~ appears in the upper, more clastic ~~Interbedded-Evaporites~~ part of the
1041
1042 373 section (~~2560-2025 m~~; Fig. 2), as is also reported from the same stratigraphic ~~level-interval~~ by
1043
1044 374 Gvirtzman et al. (2017). The halite is clear to milky white with a firm to very hard
1045
1046 375 macrocrystalline structure (Fig. 3), while the anhydrite minerals are white, soft to firm, nodular
1047
1048 376 and amorphous to massive. A sharp transition from the Pre-Evaporites to halite is marked by a
1049
1050 377 decrease in GR well log counts from 53 API to 12 API as well as a sharp increase in the
1051
1052 378 ~~formation-resistivity-(RE)~~ well log reaching 10,000 ohm (Fig. 2; see also Feng et al., 2016).
1053
1054
1055
1056
1057
1058
1059
1060
1061
1062
1063
1064

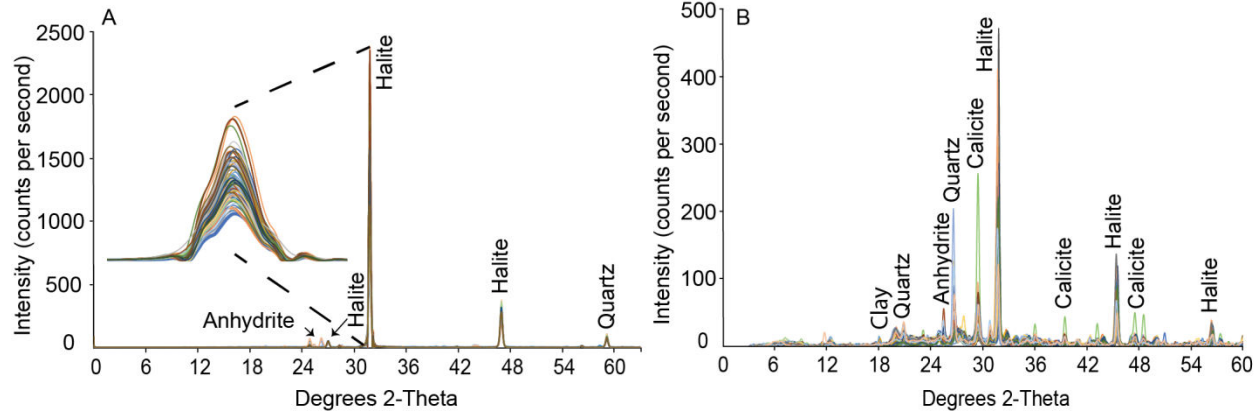


Figure 4. X-ray diffraction results

A. Overlaid (color coded) XRD analysis of 89 halite samples from the Dolphin well produced diffractograms, which are practically identical. The main halite peak is zoomed for emphasis. **B.** Higher variability is recorded both in peaks location and intensity when analyzing samples from the non-evaporitic marine sediments, sampled along the section between the depth of 3,616 m to 2560 m.

These values remain relatively constant within the halite deposits, although inter-halite variations are observed, mainly on the RE log. The pronounced high-amplitude reflection at ca. 3520 m (Dolphin well; Figs- 2, 3), also recognized as an increase in the GR well -logs, represents a short-term return to the clastic Pre-Evaporites facies although with low abundance and poorly preserved foraminiferal content. This interval is not part of the Argillaceous Diatomites facies.

4.1.3 Argillaceous Diatomites

Distinct reflective layers appear within the seismic transparent halite expressions, correlating with relatively lower velocity zones in the seismic velocity models developed for the deep Levant Basin MSC strata (e.g., 3800-4000 m/s in Gvirtzman et al. (2013); 3650-4030 m/s in Reiche et al. (2014)). These reflective layers are easily identified across the study area (Figs- 5, 6).

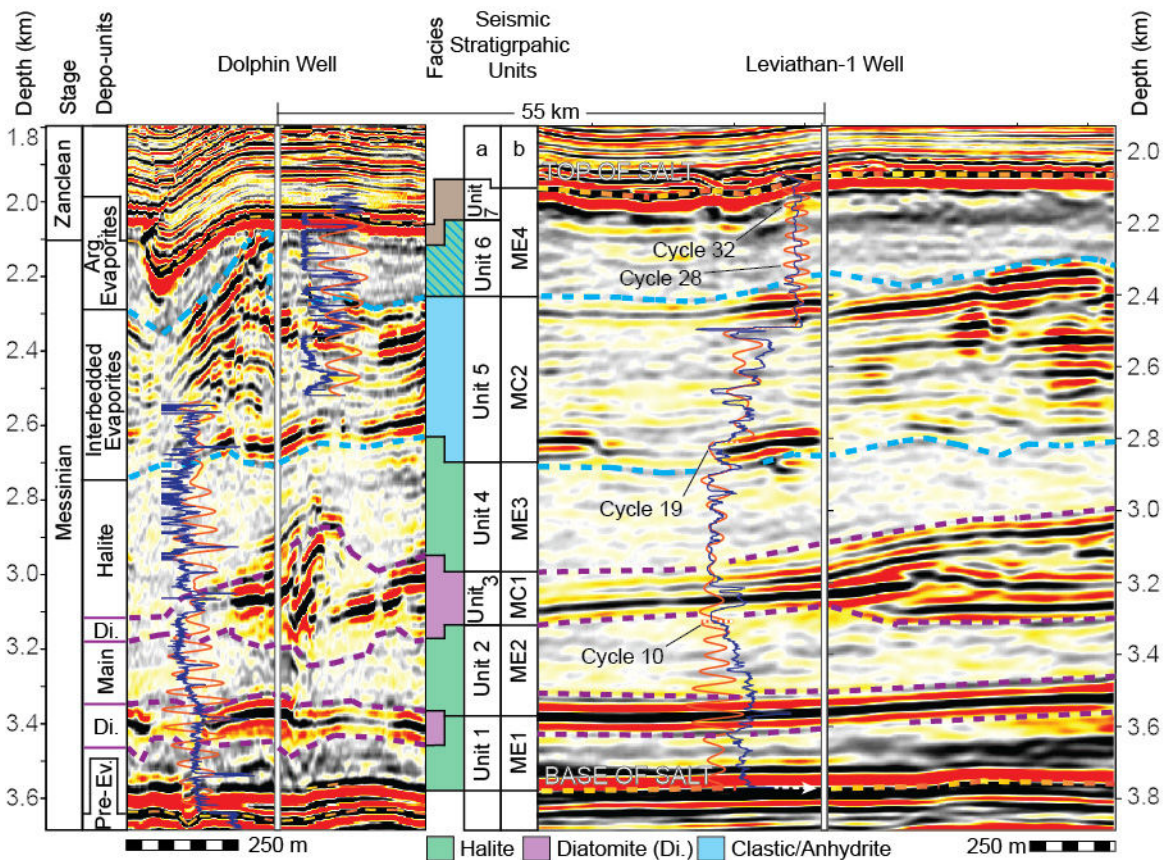
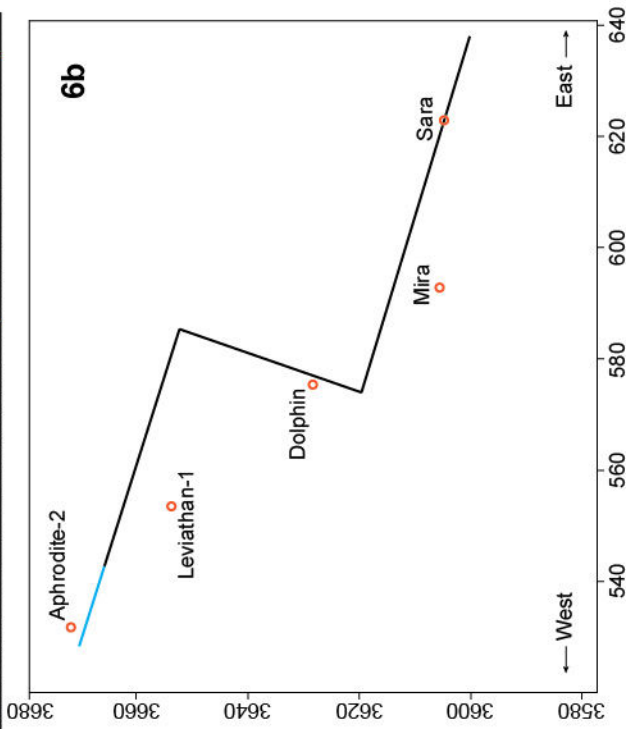
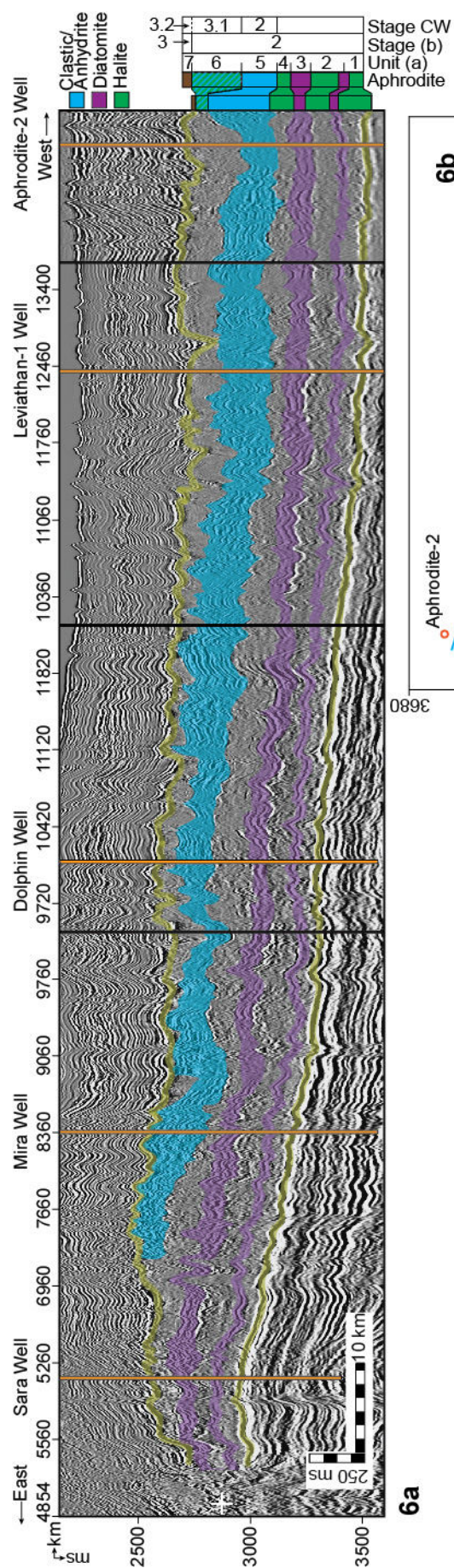


Figure 5. Geophysical data and seismic stratigraphy of the Dolphin and Leviathan-1 wells.

Depth-migrated sections crossing the Dolphin (left) and Leviathan-1 (right) wells (marked by a vertical white line). Overlaid on the sections are the well logs (blue curve left to the well), and the filtered well-log cycles superimposed on the target curves (orange). The depth and lithostratigraphic units (this work) related with the sampled Dolphin well are displayed on the left, and the depth related with the Leviathan-1 well is displayed on the right. Data columns in the middle are seismic-stratigraphic units from (a) Gvirtzman et al. (2013, 2017), and (b) Feng et al. (2016). Note the relatively deformed area of the Dolphin well relative to the more conformal vicinity of the Leviathan-1 well.

1177
 1178
 1179
 1180
 1181
 1182
 1183
 1184
 1185
 1186
 1187
 1188
 1189
 1190
 1191
 1192
 1193
 1194
 1195
 1196
 1197
 1198
 1199
 1200
 1201
 1202
 1203
 1204
 1205
 1206
 1207
 1208
 1209
 1210
 1211
 1212
 1213
 1214
 1215
 1216
 1217
 1218
 1219
 1220
 1221
 1222
 1223
 1224
 1225
 1226
 1227
 1228
 1229
 1230
 1231
 1232



1233
1234
1235 409 *Figure 6. A composite seismic section linking the commercial wells across the Levant Basin.*
1236
1237 410 A composite time-migrated seismic section (a), and location map (b), combining three 2D
1238
1239 411 traverses of the TGS survey (dark line) with a transect through the Pelagic 3D volume (blue line)
1240
1241 412 across the Levant Basin, all plotted at a common scale with a vertical exaggeration of ca. x10.
1242
1243 413 Orange vertical lines note the positions of the wells discussed in the text, while black lines note
1244
1245 414 the section stiches, primarily at turning points. The wells are projected laterally onto the seismic
1246
1247 415 profiles by up to 10 km (in the case of the Leviathan-1 well). Note the similar relative spatial
1248
1249 416 thickness of the diatomite beds (purple) in comparison with the largely varying thickness of the
1250
1251 417 Interbedded Evaporites (blue). Stage CW (current work); Stage (b) (Manzi et al., 2018); Unit (a)
1252
1253 418 (Gvirtzman et al., 2013; 2017).
1254
1255 419

1256
1257
1258 420 In the Dolphin well, this seismic facies includes five seismic high-reflectivity bands,
1259
1260 421 corresponding to peaks in the GR and troughs in the RE well-logs, appearing within the Main
1261
1262 422 Halite interval between 3375 and 2560 m (Fig. 2). Using a GR value of 20 API as an upper
1263
1264 423 cutoff value for determining the location and thickness of these intervals, results in estimated bed
1265
1266 424 thicknesses of 0.9-2.4 m (Fig. 2). Of the 1,056 m Main Halite interval in the Dolphin well, the
1267
1268 425 non-halite sediments form a regional cumulative thickness of 25-40 m (see also Feng et al.,
1269
1270 426 2016; Gvirtzman et al., 2013). At the macro-scale, the content of these layers appears as light
1271
1272 427 gray to white, soft to firm, porous, and occasionally fibrous. SEM imaging and smear-slide
1273
1274 428 analyses indicate that the rock-mass is made of densely packed, very well-preserved, and intact
1275
1276 429 diatoms (Fig. 3), and fine-grained terrigenous sediments (Fig. 4). No other transported or local
1277
1278 430 faunal remains were recognized. Identified diatoms include abundant marine planktonic genera,
1279
1280 431 such as *Coscinodiscus*, *Asteromphalus*, and *Actinoptychus* (*sensu* Tomas, 1996).
1281
1282
1283
1284
1285
1286
1287
1288

1289
1290
1291 432 XRD analysis from available samples of these high-amplitude intervals confirms the log data
1292
1293 433 response and shows an increase in terrigenous grains, mainly composed of quartz, calcite, some
1294
1295 434 clay minerals, and low amounts of anhydrite, dolomite and magnesite. (Fig. 4). Halite appears
1296
1297 435 within these samples in a high relative abundance, reaching 45% (Figs. 2, 4).
1298
1299

1300 436 Due to the nature of well-cuttings, samples from these intervals were only retrieved from the
1301
1302 437 two thickest beds, at 3367.7 m of the Dolphin well with a thickness of 2.4 m, and the two
1303
1304 438 adjacent beds at 3047 and 3034 m with a cumulative thickness of 2.1 m. These intervals are also
1305
1306 439 represented by bands of much higher seismic reflectivity than the thin (1.2-1.4 m), overlying
1307
1308 440 intervals at 2910 and 2646.5 m. Consequently, the two upper intervals might be the same
1309
1310 441 diatomite facies, or only represent marine clastic sediments.
1311
1312

1313 442 *4.1.4 Interbedded Evaporites*

1314
1315 443 This facies is represented in the seismic sections by high-amplitude reflections interbedded
1316
1317 444 with nearly transparent intervals with weak internal reflections (Fig. 3), interpreted in previous
1318
1319 445 studies to represent an alternation of clastic sediments and evaporites (Gvirtzman et al., 2013a;
1320
1321 446 Feng et al., 2016). More recently, Gvirtzman et al. (2017) and Manzi et al. (2018) presented
1322
1323 447 further evidence based on well logs from deep-basin wells in the region (Aphrodite), or by
1324
1325 448 correlation to more proximal well sections (Hannah-1), showing that this interval mostly consists
1326
1327 449 of shale, sand, anhydrite, and halite. The Interbedded Evaporites unit correlates to Unit 5 in
1328
1329 450 Gvirtzman et al. (2013). It covers 2560-2025 m in the Dolphin well, and 2548-2276 m in the
1330
1331 451 Leviathan-1 well. The GR well log in the Leviathan-1 well indicates 3 m to 20 m thick clastic
1332
1333 452 beds, interbedded with evaporites varying in thickness from 6 m to 30 m. A relatively large
1334
1335 453 diameter wellbore used while drilling this interval might have reduced the GR signal and thinner
1336
1337 454 clastic beds might not have been detected.
1338
1339
1340
1341
1342
1343
1344

1345
1346
1347 455 Due to drilling limitations, the material made available from this interval is partial, and the
1348
1349 456 only sampled sequence consists of the lowermost part above 2560 m in the Dolphin well. We
1350
1351 457 consider grains from this interval as fallouts from the Interbedded Evaporites unit, confirmed by
1352
1353 458 the absence of any indications for a clastic interval in the well-log and seismic data from the top
1354
1355 459 of the Main Halite interval, where these grains appear. The samples are made of hard, light to dark
1356
1357 460 brown sandy shales (Fig. 3). The grain composition of the >63 µm washed residue is very
1358
1359 461 different compared to the underlying Main Halite or Argillaceous Diatomite facies. It contains a
1360
1361 462 higher amount of sub-rounded larger sand grains compared to the diatomite facies, different
1362
1363 463 types of pyrite including large agglutination of pyritohedrons reaching several mm in size, and a
1364
1365 464 diverse faunal composition (Fig. 3). The latter includes few mollusk fragments, ostracods,
1366
1367 465 ~~echinoid~~ ~~sea-urchin~~ spines and a relatively rich assemblage of benthic and planktic foraminifera
1368
1369 466 (Fig. 3). The most common foraminifera are different *Globigerinoides* species, *Orbulina*
1370
1371 467 *universa* and *Sphaeroidinellopsis seminulina* (younger than 15 Ma; Berggren et al., 2006). Older
1372
1373 468 Cretaceous to Eocene foraminifera species are also present, indicating reworking processes, most
1374
1375 469 likely from exposed basin margins. These include *Parasubbotina pseudobulloides* (Danian-
1376
1377 470 Selandian; Fig. 3.D.13), *Plummerita hantkeninoides* (Maastrichtian; Fig. 3.D.15), and *Subbotina*
1378
1379 471 *triloculinoides* (Paleocene; Fig. 3.D.17). While no overlying samples exist, this interval was
1380
1381 472 logged and a reliable lithological interpretation is presented by extrapolating the coupling
1382
1383 473 between sample analysis (XRD and micropaleontology) and the log data from the lower to the
1384
1385 474 upper part of the section (Fig. 2). The clastic input is estimated from the geophysical data as
1386
1387 475 ~40% of the 535 m thick unit in the Dolphin well. However, due to local deformations in the
1388
1389 476 Dolphin well area, the Interbedded Evaporites are displaced and ~~reach at~~ is reached at
1390
1391 477 the top of the MSC section.
1392
1393
1394
1395
1396
1397
1398
1399
1400

1401
1402
1403
1404 478 ~~-Comparing Comparison with~~ Manzi et al. (2018) suggests that, Unit 6 is not represented in
1405
1406 479 the Dolphin well but ~~rather that~~ Unit 5 reaches-marks the top of the section (Fig. 5). However,
1407
1408 480 seismic and well-log interpretation indicates that in the Leviathan-1 well another ~200 m of
1409
1410 481 evaporites appear above the Interbedded Evaporites, ~~correlating which corresponds~~ to Unit 6 in
1411
1412 482 Manzi et al. (2018). There, the Interbedded Evaporites (Unit 5) are 260 m thinner than in the
1413
1414 483 Dolphin well (Fig. 5). This discrepancy is presumably the result of post-depositional halokinetic
1415
1416 484 deformation and imbrication of ~~unit~~ Unit 5 in the Dolphin well, as imaged in the seismic data
1417
1418 485 (Fig. 5).

1420 486 *4.1.4-5 Argillaceous Evaporites*

1421
1422
1423 487 This interval was not sampled in any of the Levant Basin studies and ~~any-its~~ interpretation ~~of~~
1424
1425 488 ~~it in the present~~ is only based on the interpretation of seismic and well-log data. In the
1426
1427 489 Leviathan-1 well this interval covers the ~~top uppermost part~~ of the evaporites at-between 2,090-m
1428
1429 490 and to 2,320 m (Fig. 5). The transparent reflective character of this interval in the seismic section
1430
1431 491 includes cyclic darker bands. The unit appears to be composed of clastic sediments, probably
1432
1433 492 clays, silts and sands, which are characterized by GR values of 7_{api} to 15_{api}API. Intervals of ca.
1434
1435 493 zero GR are interpreted as argillaceous anhydrite. Gvirtzman et al. (2013; 2017), Feng et al.
1436
1437 494 (2017), and Manzi et al. (2018) refer to this interval as Unit 6, ~~and it which~~ is generally lumped
1438
1439 495 with the underlying halite as part of the evaporite unit. Regionally, the presence of Unit 6 is
1440
1441 496 limited to the westernmost and deeper areas of the basin, while it is truncated to completely
1442
1443 497 removed landward to the east (Fig. 6). The amount of truncation on Unit 6 gradually increases
1444
1445 498 eastwards, eroding also Units 5-2 at the eastern parts (Gvirtzman et al., 2013, Feng et al., 2017;
1446
1447 499 the current study). Both the Dolphin and the Leviathan wells are within the deeper areas in which
1448
1449 500 Unit 6 is present, but due to local deformations it might be underrepresented in the Dolphin well.
1450
1451
1452
1453
1454
1455
1456

1457
1458
1459 501 A 5 m clastic and ~~anhydrate-anhydrite interval bed~~ defines the top of ~~tops the MSC~~ this unit,
1460
1461 502 marked by a nearly transparent seismic interval in the Leviathan-1 well, as indicated by a sharp
1462
1463
1464 503 drop in GR and drilling penetration rate relative to the overlying Pliocene sediments. This
1465
1466 504 anhydrite interval ~~might be~~ is most likely part of Unit 7 in Gvirtzman et al. (2018), or the Nahal
1467
1468 505 Menashe in Madof et al. (2019).

1470 506 **4.2 Chronology of halite deposition and well log frequency analysis**

1473 507 In order to attain a direct age control on the duration of halite deposition, the halite samples
1474
1475 508 were washed and inspected for microfossils, prepared as smear slides, and examined under SEM
1476
1477 509 in search for the preservation of eukaryotic life in the evaporites, which failed.

1479 510 We also measured the Sr₂-isotopic composition of evaporite samples in order to compare them
1480
1481 511 with the well-established Sr isotope stratigraphy constructed from elsewhere in the
1482
1483 512 Mediterranean (e.g., Topper et al., 2011; Roveri et al., 2014; Flecker et al., 2015). This published
1484
1485 513 dataset shows that Sr₂-isotope data from stage 1 lies mainly within error of the ocean₂-water
1486
1487 514 curve (McArthur et al., 2012), suggesting that the Mediterranean was connected to the global
1488
1489 515 ocean during the initial phases of the MSC (e.g., Roveri et al., 2014; Flecker et al., 2015). During
1490
1491 516 stages 2 and 3 the Mediterranean's Sr record diverges from ocean₂-water values towards much
1492
1493 517 lower ratios that reflect a substantially smaller connection to the global ocean and dominance of
1494
1495 518 fresh₂-water sources such as the Nile, Rhone, and input from the Paratethys, particularly during
1496
1497 519 the Lago Mare phase (e.g., Roveri et al., 2014; Flecker et al., 2015). Sr₂-isotope data from the
1498
1499 520 lowest Pliocene are again within error of ocean₂-water values, indicating an abrupt transition
1500
1501 521 back to full connectivity after the MSC (e.g., Roveri et al., 2014; Flecker et al., 2015). Despite
1502
1503 522 the wide geographical distribution of the Mediterranean samples from which this published Sr₂-
1504
1505 523 isotope stratigraphy has been constructed, the pattern appears to be consistent, indicating that the

1513
1514
1515
1516
1517
1518
1519
1520
1521
1522
1523
1524
1525
1526
1527
1528
1529
1530
1531
1532
1533
1534
1535
1536
1537
1538
1539
1540
1541
1542
1543
1544
1545
1546
1547
1548
1549
1550
1551
1552
1553
1554
1555
1556
1557
1558
1559
1560
1561
1562
1563
1564
1565
1566
1567
1568

524 controlling factor was Mediterranean-Atlantic exchange and that the Mediterranean behaved as a
525 single basin throughout the MSC (Flecker et al., 2015). However, the dataset does not include
526 samples from these deep-water Eastern Mediterranean sites as they were previously not
527 available; ~~and~~ it therefore makes sense to compare new analyses from these locations with the
528 existing Sr-chemostratigraphic scheme.

529 Halite is highly soluble and it is therefore challenging to clean samples prior to analysis. We
530 used the basic method described in Gvirtzman et al. (2017) and Manzi et al. (2018), with
531 additional eleven different techniques (Fig. S1, Table S1) for attempting to isolate the halite
532 ~~grains-crystals~~ from any contaminant phases coating the samples such as clay or industrial
533 drilling additives. The data generated for each of the nine different samples analyzed is highly
534 variable, ranging from a few values within error of Late Miocene ocean water (McArthur et al.,
535 2012), to substantially higher values (Fig. S1, Table S1). There is no consistency between the
536 data generated and the technique used for dissolving the halite (Fig. S1, Table S1), suggesting
537 that we have not been able to reliably isolate the halite from contaminant phases coating the
538 crystals by any of the methods used. We therefore conclude that none of this data should be
539 considered as representing a primary record of Eastern Mediterranean water at this time.

540 Similar high values have been reported for halite from other industrial wells in the Levant
541 Basin (Gvirtzman et al., 2017; Manzi et al., 2018). Manzi et al., (2018) attributed the
542 anomalously high values to “local, diverse, short-term Sr input”, but did not specify what this
543 input might be. One possibility is that these published halite values from industrial cuttings may,
544 like our data, ~~also~~ be contaminated. We conclude that a robust Sr-isotope record for the deep-
545 basin halite deposits will only be achieved either by establishing a reliable method for removing

1569
1570
1571 546 contaminant phases or by recovering halite samples without the use of industrial drilling fluids,
1572
1573 547 e.g., through scientific drilling (Camerlenghi et al., 2014).

1575 548 Next, we attempted to construct a chronostratigraphic framework for the Levant MSC
1576 549 deposits based on astrochronological tuning. We carried out spectral analysis of GR and RE
1577
1578 549 well-logs to correlate the Levant MSC section to astronomical target curves, and the more
1579
1580 550 proximal to onshore Mediterranean MSC deposits. REDFIT spectral analyses (Schulz and
1581
1582 551 Mudelsee, 2002) of the Dolphin and Leviathan-1 well-log data from the base to the top of the
1583
1584 552 evaporite unit (3616-2025 m in the Dolphin well, divided into three intervals for spectral
1585
1586 553 analysis; Fig. S2) indicates statistically significant, periodical signals in the RE and GR logs.
1587
1588 554 However, the GR produces a weaker signal than the RE log within the massive halite intervals.
1589
1590 555 This is expected, as pure halite does not contain the elements U, Th, and K and their decay series
1591
1592 556 responsible for natural GR radiation emitted by rocks. However, several examples indicate how
1593
1594 557 different log responses occur within halite sequences. For example, inner-halite variations such
1595
1596 558 as thin clay ~~laminas~~ laminae caused by microstratification within the brines might occur
1597
1598 559 (Sonnenfeld, 1983). Alternatively, thin sulphate layers (Biehl et al., 2014) have also been shown
1599
1600 560 to produce log-responses.
1601
1602 561

1603
1604 562 Each of the analyzed log segments is characterized by several frequency peaks exceeding the
1605
1606 563 chi 95% confidence interval (Fig. S2). Each segment was bandpass filtered according to these
1607
1608 564 frequencies, and the fit of the filtered version to the original well-log was examined, ultimately
1609
1610 565 selecting the best-fit result for subsequent analysis. Both logs are composed of significant and
1611
1612 566 approximately overlapping periodical frequencies, with an average cycle thickness of ~50 m
1613
1614 567 (Fig. S2). While the RE log appears to be more attuned to inner-halite variations in the Main
1615
1616 568 Halite interval, the GR log is more consistent and provides a more reliable fit to the well log
1617
1618
1619
1620
1621
1622
1623
1624

1625
1626
1627
1628 569 target curve in the Interbedded Evaporites units above 2833 m. Consequently, the Dolphin well
1629
1630 570 cyclostratigraphy is constructed from information derived from the GR and RE logs that cover
1631
1632 571 the lower and upper parts of the section (Fig. S2). The lower part of the Main Halite interval
1633
1634 572 (cycles 1-11; Fig. S2) is not very well represented by the Gaussian filter, with some five cycles
1635
1636 573 that fit well with the target curve. The upper part of the Main Halite interval is best filtered by
1637
1638 574 using the RE log with a bandwidth of 49 m (cycles 12-24; Fig. S2). The cycles within the upper
1639
1640 575 part of the section in the interbedded-Interbedded evaporite-Evaporite interval are picked up
1641
1642 576 relatively clearly by the GR log (cycles 25-32; Fig. S2). However, as the Dolphin well section
1643
1644 577 from the Interbedded Evaporites and above experienced significant deformation (Figs- 5, 6), the
1645
1646 578 well-log cyclostratigraphy of the upper part of the studied section is not reliable in this well.

1648
1649 579 Several frequency peaks exceeding the chi 95% confidence interval were also identified in
1650
1651 580 the Leviathan-1 well-log analysis, where deformation was minimalis reduced and Unit 6 is
1652
1653 581 represented (Figs- 5, 6). The RE log was cleaned from clear-outlier spikes and used for bandpass
1654
1655 582 filtering. The original log includes several short intervals in which values go-range from 10's or
1656
1657 583 100's of ohm*m to extremely high 18,000+ ohm*m values, masking cyclic trends in the data.
1658
1659 584 Fig-ure 5 includes-shows the cleaned RE log overlain on the seismic data. There is a much-
1660
1661 585 improved fit between the log and filtered cycles, relative to the Dolphin well-filtering, with only
1662
1663 586 a few examples of a misfit between the two. A good fit is also generally apparent between the
1664
1665 587 seismic signal and the well-log response. The Main Halite interval includes 19 cycles, in which
1666
1667 588 cycles 4 and 5 are within the first Argillaceous Diatomite beds, and cycles 11-13 are within the
1668
1669 589 second. The cycles within the Interbedded Evaporite interval are picked up relatively clearly by
1670
1671
1672 590 the RE log (cycles 19-27; Fig. 5). The-In the Argillaceous Evaporites toping-in the uppermost

1681
1682
1683
1684 591 part of the studied section in the Leviathan-1 well, the RE log response fits with banding in the
1685
1686 592 seismic data, which is also picked by bandpass filtering (cycles 27-33; Fig. 5).

1687
1688 593 Consequently, bandpass filtering of the well_-logs results in ~33 cycles from the base to the
1689
1690 594 top of the evaporites sequence in the Levant Basin. In the next two sections, we present different
1691
1692 595 findings supporting the occurrence of lithological cycles along the studied section, followed by
1693
1694 596 the astrochronologic interpretation of these cycles in the discussion section.

1695 1696 597 **4.3 Cyclicality of seismic reflective phases**

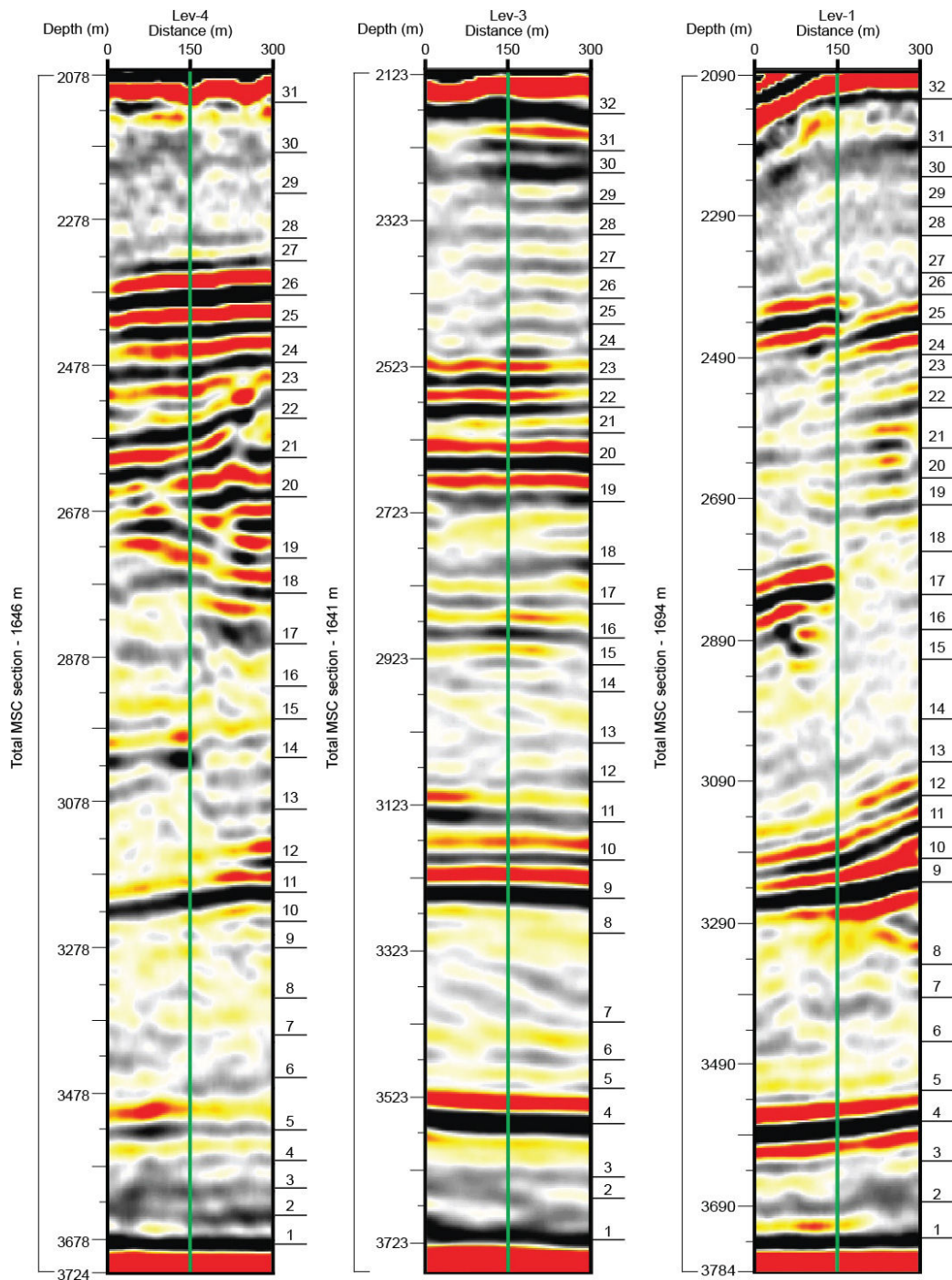
1698
1699 598 Modern high-quality 3D seismic imagery represents a new frontier for astronomical
1700
1701 599 calibration, potentially adding a chronological time-frame for seismic stratigraphy. However, in
1702
1703 600 most marine settings, precession-scaled cycles are registered as-at a thicknesses-to-cycles ratio
1704
1705 601 which has a much higher resolution than the seismic data. Yet, several studies show a good
1706
1707 602 match between the number of precession-induced astronomic cycles and the number of positive
1708
1709 603 vs. negative seismic phases within MSC deposits (Driussi et al., 2015; Geletti et al., 2014). This
1710
1711 604 is explained by the considerably higher sedimentation rates that characterize evaporite deposits,
1712
1713 605 relative to the much lower rates typical of normal-marine clastic or carbonate deposition. The
1714
1715 606 higher sedimentation rates result in an improved alignment between the spacing, or resolution, of
1716
1717 607 lithologic variations and the resolution of the seismic imagery. As orbital forcing was repeatedly
1718
1719 608 identified as determining lithological variations during the MSC (e.g., Krijgsman et al., 1999;
1720
1721 609 Ochoa et al., 2015; Roveri et al., 2014a; Sierro et al., 2001; van den Berg et al., 2015), seismic
1722
1723 610 data recording these variations can be used with caution for strengthening the well-log
1724
1725 611 astronomical tuning-based age models. This is not the case for the Pre-Evaporites in this area,
1726
1727 612 which deposited at an average sedimentation rate of 11.4 cm/kyr and a cycle thickness of around
1728
1729 613 2-3 m, as shown by Meilijson et al. (2018). This thickness is below the resolution of the seismic
1730
1731
1732
1733
1734
1735
1736

1737
1738
1739
1740
1741
1742
1743
1744
1745
1746
1747
1748
1749
1750
1751
1752
1753
1754
1755
1756
1757
1758
1759
1760
1761
1762
1763
1764
1765
1766
1767
1768
1769
1770
1771
1772
1773
1774
1775
1776
1777
1778
1779
1780
1781
1782
1783
1784
1785
1786
1787
1788
1789
1790
1791
1792

614 data. Here, we use the seismic 3D data for additional validation of our results from well-log
615 curves based on REDFIT spectral analysis and bandpass-filtering within the Main hHalite and
616 overlying Interbedded Evaporites intervals.

617 In practice, the seismic tuning analysis was performed by counting the number of reflectivity
618 phases on three different sections where wells were drilled within the 3D geophysical dataset of
619 the study area (Figs. 1, ~~and~~ 7). Yet, as halokinetic deformation affected the Levant deep-basin
620 evaporites, and particularly their upper units (Gvirtzman et al., 2013a), spatial variations are
621 expected even considering a scenario of regionally uniform deposition. Such variations in the
622 number and thickness of cycles are indeed observed when comparing different seismic sections,
623 reflecting the local variabilities (Fig. 7). In total, a consistent number of ~30 reflectivity cycles is
624 identified in different locations (~~Fig. 7~~), which is in agreement with the cyclicity identified
625 through well-log spectral analysis.

1793
1794
1795
1796
1797
1798
1799
1800
1801
1802
1803
1804
1805
1806
1807
1808
1809
1810
1811
1812
1813
1814
1815
1816
1817
1818
1819
1820
1821
1822
1823
1824
1825
1826
1827
1828
1829
1830
1831
1832
1833
1834
1835
1836
1837
1838
1839
1840
1841
1842
1843
1844
1845
1846
1847
1848



626

627 *Figure 7. Seismo-cyclostratigraphy of three seismic profiles around wells in the study area.*

628 Three depth-migrated profiles that are aligned with wells in the central Levant. Black lines
629 with numbers on the right hand side of each seismic profile represents a reflectivity phase (black)
630 cycle count along the section. Left bar shows actual depth for each section and the total depth
631 from base to top of the MSC section in each well.

4.4 Elemental variations within evaporite samples

The wellbore cuttings do not allow recognition of macro-scale sedimentological features, which may reflect the cyclicity identified in the well logs and seismic data within the halite sequence. Tuning of marginal MSC sections has been done based on lithological transitions, such as branching selenite to massive selenite, or chaotic deposits to clastic evaporites in stages 1-3 (e.g., Roveri et al., 2014a), or diatomite-shale-carbonate transitions in the Pre-Evaporites (Ochoa et al., 2015; Sierro et al., 2001). Here, we explore whether minor inner-halite chemical variability down-section can account for the filtered cycles and variable log response within apparently massive and homogenous halite. Other Miocene intervals of homogeneous lithology have also been shown to contain cyclic changes in the chemical composition of the sediments (van den Berg et al., 2015), which are assumed to represent shifts in the depositional environment ~~shifts~~. We hypothesize that these variations, if present in deep Mediterranean basins, could correspond to: 1) disparities-variations in riverine runoff and associated influx of clastic material into the basin, and/or 2) shifts in the degree of evaporation determining the type of deposited evaporites. Both of these drivers can be related to orbital forcing (Marzocchi et al., 2015; Simon et al., 2017).

We observe a relatively low correlation ($R^2=0.46$; Fig. 8A) between Fe and K in the Levant halite samples, which is not in agreement with the occurrence of continentally-derived material transported to the Eastern Mediterranean. In contrast, a high elemental correlation ($R^2=0.91$; Fig. 8B1) is observed between S and Ca, which confirms that low and variable amounts of minerals rich in CaSO_4 (i.e., gypsum and anhydrite) represent an integral part of evaporite deposition in the Main Halite of the deep Levant Basin.

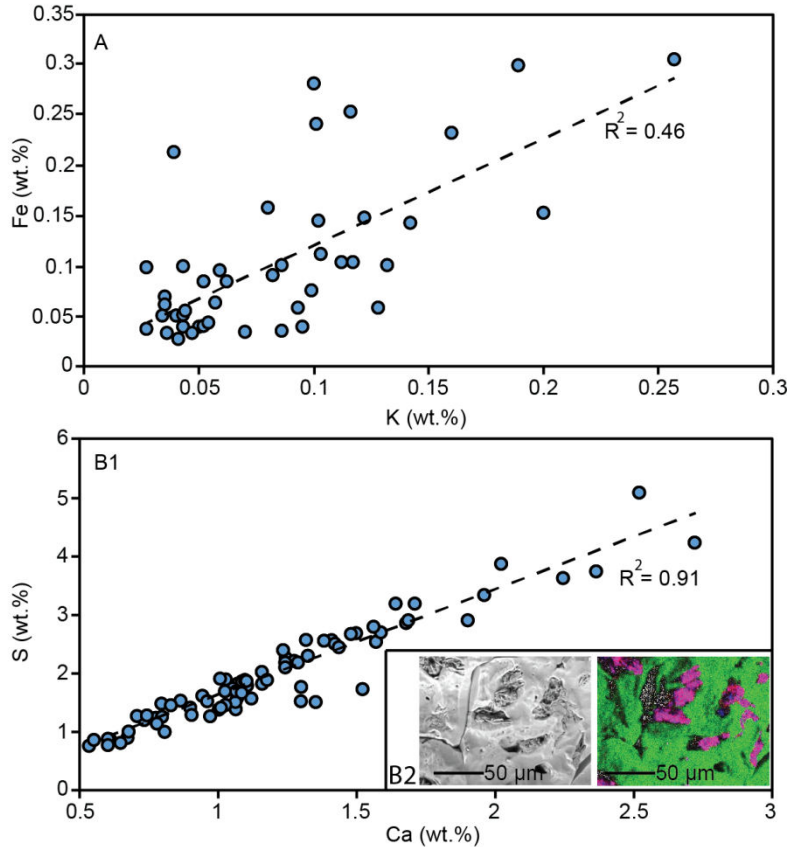


Figure 8. X-ray fluorescence elemental analysis of the Levant evaporites

Results of XRF elemental analysis are shown for 77 halite samples for specific elemental composition. (A) Note the low correlation between iron and potassium, while (B1) shows a high sulfur to calcium correlation. The high correlation between sulfur and calcium is corroborated by SEM-EDS imagery and element maps (halite sample from 3058 m; (B2)) showing the distribution of Na (green), Ca (blue) and S (red). Note that the indicating the occurrence of gypsum microcrystals (purple; B2) within cavities of the larger and much more common halite crystals has a distinct swallowtail twinned microcrystals pattern.

This notion is further confirmed by the recognition of anhydrite-calcium sulfate microcrystals minerals and small-scale but distinct swallowtail twinned microcrystals fabrics within the halite cuttings (Fig. 8B-2). Note that not all halite grains crystals included a similar deposition precipitation of calcium sulfates in small pores. We suggest that shifts in the amount of gypsum

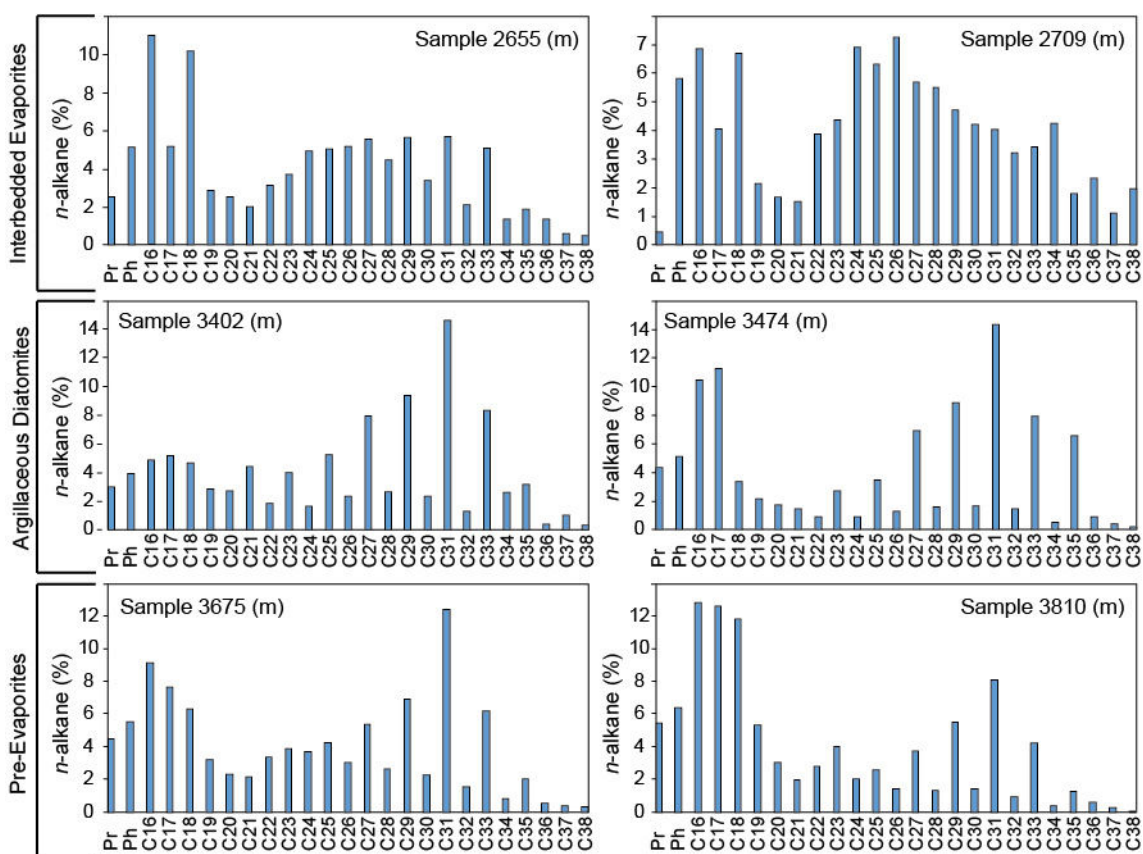
1961
1962
1963
1964 668 or anhydrite deposition~~al~~ along the section might correspond with the cycles obtained by well-
1965
1966 669 log spectral analysis.

1968 670 **4.5 Organic geochemistry as a stratigraphic marker**

1971 671 Biomarker data allow~~s~~ us to identify sources of sedimentary organic matter preserved in the
1972
1973 672 cuttings as well as to gain insights into its thermal history. We observed distinct differences in
1974
1975 673 the biomarker distribution found in the Pre-Evaporites, the Argillaceous Diatomites within the
1976
1977 674 Main Halite deposits, and the overlying Interbedded Evaporites interval. The *n*-alkanes ranged~~d~~
1978
1979 675 from *n*-C₁₆ to *n*-C₃₈ (Table 1, Fig. 9), and their distribution ~~varied~~varies between samples. For
1980
1981 676 example, while short- and long-chain alkanes ~~were~~are more predominant in the Pre-Evaporites
1982
1983 677 and the Argillaceous Diatomites, mid-chain alkanes ~~were~~are more prominent in the Interbedded
1984
1985 678 Evaporites. Additionally, the carbon preference index (CPI) of long-chain *n*-alkanes, which
1986
1987 679 portrays the degree of oddity in the distribution of the different *n*-alkanes, ~~varies~~d around 5-7 in
1988
1989 680 the Pre-Evaporites, 4-12.3 in the Main Halite (Argillaceous Diatomites) interval, and around 1.9-
1990
1991 681 2.9 in the Interbedded Evaporites (Table 1; Fig. 10). ~~The CPI reports on the degree of oddity~~
1992
1993 682 ~~between the distribution of the different *n*-alkanes.~~ The Argillaceous Diatomites also contain the
1994
1995 683 lowest Pr/Ph ratios (Table 1, Fig. 10) compared to other samples. The relative abundance of
1996
1997 684 long-chain *n*-alkanes (C₂₅-C₃₅) ~~was~~is more elevated within the Argillaceous Diatomites and
1998
1999 685 ~~prePre-evaporiteEvaporite~~. This ~~was~~is reflected in the ratio of long chain (C₂₅-C₃₇) to short
2000
2001 686 chain (C₁₆-C₂₁) *n*-alkanes, which ~~maximized~~ in the Argillaceous Diatomites (1.9), followed by
2002
2003 687 the Interbedded Evaporites (1.6) and the Pre-Evaporites (1.2). The C₃₁ *n*-alkane ~~was~~ commonly
2004
2005 688 is the most dominant homologue.

2009 689 Selected hopane- and sterane-based thermal maturity indices (Table 2; Fig. 11; Peters and
2010
2011 690 Moldowan, 1993; Rullkötter and Marzi, 1988; Peters et al., 2005) also indicate major differences

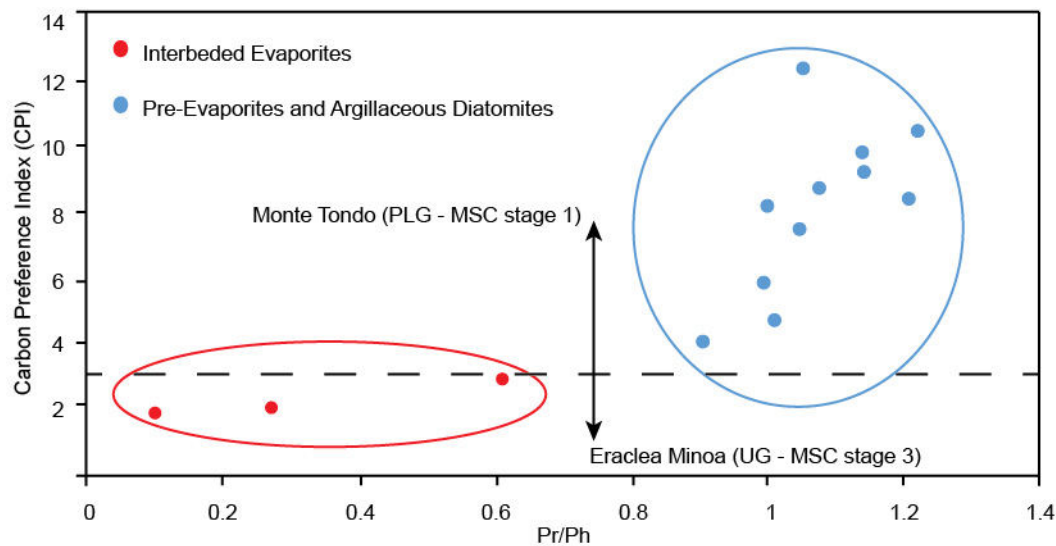
691 between samples from the Pre-Evaporites and Argillaceous Diatomites, relative to those from the
 692 lower part of the Interbedded Evaporites ~~interval~~. As summarized in Table 2, the diatomite facies
 693 exhibit the lowest thermal maturity values, to be followed by the Pre-Evaporites, and while much
 694 more mature ~~indicative~~ indices are reached in the overlying Interbedded Evaporites. This is
 695 clearly indicated by the presence of hopanes with the biological $\beta\beta$ configuration, in addition to
 696 low values of the C_{31} S/R hopanes ratio and the C_{28} $\alpha\alpha$ 20S/20R steranes ratio, and more
 697 elevated values of the C_{30} $\beta\alpha/\alpha\beta$ hopanes ratio in immature samples (Fig. 11). Additionally, the
 698 Argillaceous Diatomites samples exhibits a lack of re-arranged steranes compared to the
 699 overlying and underlying intervals (Fig. 11; Table 2).



700
701 *Figure 9. n-alkane distribution in non-halite intervals.*

702 Two samples from each depositional unit (left and right columns) show the relative abundance of
 703 pristane (Pr), phytane (Ph), and C_{16} - C_{38} n -alkanes. Note the odd-over-even carbon-number

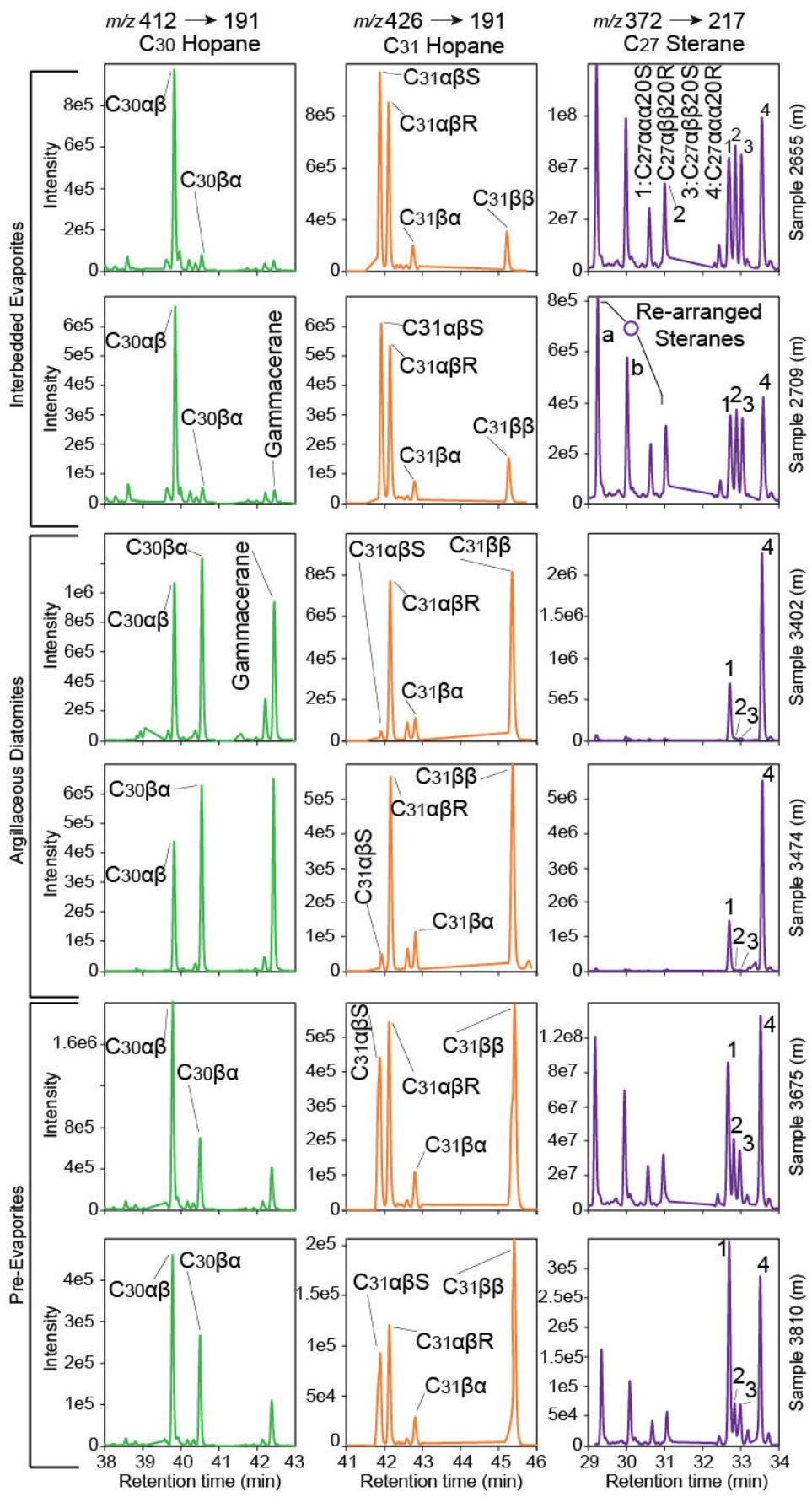
2073
 2074
 2075
 2076 704 predominance of long-chain *n*-alkanes in the Argillaceous Diatomites (center) and ~~pre~~Pre-
 2077 705 ~~evaporites~~Evaporites (lower) relative to the overlying Interbedded Evaporites. Also observe the
 2078
 2079 706 higher CPI, i.e., ~~the distribution~~the distribution of *n*-alkanes, in the Pre-Evaporites and
 2080 707 Argillaceous Diatomites relative to the Interbedded Evaporites, and higher relative abundance of
 2081
 2082 708 medium-long chained compounds.
 2083
 2084 709



2100
 2101 710
 2102 711 *Figure 10. Pristane/phytane ratio to carbon preference index (CPI) plot.*

2103 712 Legend indicates the strata of plotted samples. Horizontal dashed line indicates the separation
 2104
 2105 713 of CPI values of marginal section across the MSC reported by Vasiliev et al. (2017). Note that
 2106 714 the samples from the Interbedded Evaporites plot in the area of values measured in stage 3 of the
 2107
 2108 715 MSC (Vasiliev et al., 2017), while the lower samples from the Levant plot in the area of MSC
 2109
 2110 716 stage 1. Also note the separation in Pr/Ph values between the Interbedded Evaporites relative to
 2111 717 the Pre-Evaporites and Argillaceous Diatomites.
 2112
 2113
 2114
 2115
 2116
 2117
 2118
 2119
 2120
 2121
 2122
 2123
 2124
 2125
 2126
 2127
 2128

2129
 2130
 2131
 2132
 2133
 2134
 2135
 2136
 2137
 2138
 2139
 2140
 2141
 2142
 2143
 2144
 2145
 2146
 2147
 2148
 2149
 2150
 2151
 2152
 2153
 2154
 2155
 2156
 2157
 2158
 2159
 2160
 2161
 2162
 2163
 2164
 2165
 2166
 2167
 2168
 2169
 2170
 2171
 2172
 2173
 2174
 2175
 2176
 2177
 2178
 2179
 2180
 2181
 2182
 2183
 2184



2185
2186
2187
2188
2189
2190
2191
2192
2193
2194
2195
2196
2197
2198
2199
2200
2201
2202
2203
2204
2205
2206
2207
2208
2209
2210
2211
2212
2213
2214
2215
2216
2217
2218
2219
2220
2221
2222
2223
2224
2225
2226
2227
2228
2229
2230
2231
2232
2233
2234
2235
2236
2237
2238
2239
2240

719 *Figure 11. Distribution of selected bacterial hopanes and algal steranes-.*

720 Two samples from each depositional unit (left and right columns) were investigated for the
721 distribution of aliphatic hydrocarbons using selective reaction monitoring (SRM) analysis. Each
722 sample (numbered on the right) includes a chromatogram for three given SRM transitions: 412
723 → 191 (C₃₀ Hopane); 426 → 191 (C₃₁ Hopane); 372 → 217 (C₂₇ Sterane). The C₂₇ rearranged
724 steranes are marked as (a) C₂₇β α 20S and (b) C₂₇β α 20R. High ratios of C₃₁αβS/R hopanes and
725 C₂₇αααS/R steranes, along with low values of C₃₁ββ/αβ and C₃₀ββ/αβ hopane ratios, indicate a
726 higher, yet mixed, maturity of the organic matter preserved in the Interbedded Evaporite shale
727 samples compared to samples from the Pre-Evaporites and Argillaceous Diatomites. The
728 underlying diatomite facies sediments are immature in nature, while the ~~pre~~Pre-evaporite
729 Evaporite shale samples exhibit mixed signatures (e.g., high C₃₁ββ/αβ hopanes and C₂₇ αααS/R
730 steranes).

5. Discussion

5.1 Deep-sea halite depositional environment

The halite in the Dolphin well appears to be a pure, homogeneous layer, indicating a monotonous deposition of halite in the deep Levant Basin. Transmitted-light microscopy and SEM analysis of halite ~~grains-crystals~~ (<0.5 cm) throughout the section reveals no distinct sedimentological variations. XRD analysis also confirms a uniform, halite-dominated mineralogical composition (Fig. 4). ~~Swallowtail-twinnedGypsum microcrystals structures made out of calcium sulfates~~ were observed ~~on-within~~ several halite ~~grains-crystals~~ as seen in SEM-EDS (Fig. 8B-2), and elemental variations ~~s-~~Supporting shifts in the relative amounts of calcium sulfates deposited along the halite part of the section were apparent in XRF analysis (Fig. 8). However, we found no features similar to the lithological variations reported from the Realmonte salt mine (Lugli et al., 1999) or the intermediate depth halite of the Balearic Basin (~~site-Site~~ 134; Lugli et al., 2015), such as cumulates of halite plates settled out from a stratified water column, plate cumulates in a shallowing-upward sequence containing kainite layers, ~~nor~~ cumulates of skeletal hoppers with chevron overgrowths. The above conclusion might be biased due to the usage of well cutting, possibly not allowing to recognize these features. However, the mm-scale variations in the salt deposits shown by Lugli et al. (2015) should have been recognizable ~~on-in~~ the halite well cuttings. The lack of comparative features between the marginal halite and the Levant deep-basin halite is also evident when comparing the halite samples in the Dolphin well and halite deposits penetrated by DSDP drilling. There is a clear distinction between the featureless Dolphin halite and the halite interbedded with detrital sand and small anhydrite nodules recovered at DSDP ~~site-Site~~ 134 offshore Sardinia in the margins of the western Mediterranean (Hsü et al., 1973). The halite sampled in ~~site-Site~~ 134 is banded similarly to the

2297
2298
2299 754 Sicily halite reported by Lugli et al. (1999), with alternative cloudy and translucent beds.
2300
2301 755 Similarly, the banded halite and polyhalite at DSDP Sites 374, 375 and 376 in the Eastern
2302
2303 756 Mediterranean (Garrison et al., 1978) does not resemble the homogenous halite recovered in the
2304
2305 757 Dolphin well. The homogeneous nature of the halite observed in the Dolphin well suggests
2306
2307 758 continuous deep-sea deposition, in comparison to halite deposition in the shallower marginal
2308
2309 759 basins.

2310
2311
2312 760 Modern analogs for ancient deep-water halite depositional environments are scarce. An
2313
2314 761 exception is the hypersaline Dead Sea, in which active precipitation of halite occurs within the
2315
2316 762 deepest parts of the basin (Arnon et al., 2016; Sirota et al., 2016, 2017; Steinhorn, 1983; Stiller et
2317
2318 763 al., 1997). The Dead Sea floor is divided into two principal environments: a deep, hypolimnetic
2319
2320 764 lake floor, and a shallow, epilimnetic lake floor (Sirota et al., 2016, 2017). Halite continuously
2321
2322 765 precipitates with seasonal variations influencing the type of halite formation on the deeper
2323
2324 766 hypolimnetic lake floor. However, the shallow epilimnetic lake floor is also subject to seasonal
2325
2326 767 variations, which produce annual unconformities related to halite deposition and dissolution. The
2327
2328 768 epilimnion part of the lake is under-saturated during the summer and halite is dissolved, while
2329
2330 769 winter is characterized by a heavily supersaturated water column and halite is crystallized (Sirota
2331
2332 770 et al., 2016). Summer is associated with higher loss of water by evaporation from the lake
2333
2334 771 compared to the winter. Sirota et al. (2016) argue that the seasonal halite deposition cycle in the
2335
2336 772 Dead Sea epilimnion is controlled by the decrease in the saturation with increasing temperature,
2337
2338 773 which overcomes the effect of enhanced summer evaporation. The hypolimnion is
2339
2340 774 supersaturated and halite is crystallized throughout the year, with higher super-saturation and
2341
2342 775 higher crystallization rates during winter. During summer, the undersaturated epilimnion
2343
2344 776 dissolves halite, forming highly saturated dense solutions. These solutions flow to the
2345
2346
2347
2348
2349
2350
2351
2352

2353
2354
2355
2356
2357
2358
2359
2360
2361
2362
2363
2364
2365
2366
2367
2368
2369
2370
2371
2372
2373
2374
2375
2376
2377
2378
2379
2380
2381
2382
2383
2384
2385
2386
2387
2388
2389
2390
2391
2392
2393
2394
2395
2396
2397
2398
2399
2400
2401
2402
2403
2404
2405
2406
2407
2408

777 hypolimnion, which becomes supersaturated and crystallizes halite. This process results in
778 focusing of halite deposits in the deep hypolimnetic parts of the evaporitic sea, and thinning of
779 the shallow epilimnetic deposits occurs (Sirota et al., 2016, 2017). The Dead Sea modern
780 analogue provides a mechanism for explaining the great thickness of the deep Mediterranean
781 MSC halite deposit. A similar model might have applied during the MSC, with halite dissolution
782 in the marginal and intermediate basin evaporites, and focusing and thickening of halite
783 deposition in the deeper parts of the basin, as also partly proposed by Roveri et al. (2014c).

784 **5.2 Stratigraphic markers in deep basin MSC deposits**

785 *5.2.1 Deep--basin diatomites as environmental and lithostratigraphic markers*

786 As no chronostratigraphic indicators were found in the studied section, we aim to use the
787 litho-chemical analysis performed on the Dolphin well samples to identify lithostratigraphic and
788 chemostratigraphic markers, that could-may serve as tie-points for establishing an age model for
789 the deep basin MSC deposits (Fig. 12). In this context, the occurrence of diatomites within the
790 Main Halite unit provides a primary observation. Diatomites are known to occur within Pre-
791 Evaporite and PLG intervals in some of the marginal sections (Dela Pierre et al., 2014; Hilgen et
792 al., 2007; Hilgen and Krijgsman, 1999; Krijgsman et al., 2001; Manzi et al., 2011; Roveri et al.,
793 2014a), and more rarely within stage 3 Upper Gypsum deposits (e.g., Eraclea Monia section;
794 Manzi et al., 2009). Diatom-rich aggregates within laminated layers, appearing as mudstone
795 intervals interbedded within the PLG deposits of the Piedmont basin, were used by Dela Pierre et
796 al. (2014) to establish the existence of normal--marine (not brackish or hypersaline) waters
797 during deposition of non-evaporitic intervals during stage 1 of the MSC. Here we show that open
798 --marine planktonic diatom taxa abundant in the Piedmont during the PLG (e.g., *Coscinodiscus*

2465
2466
2467 803 *Figure 12. Astronomical age model and regional correlation of the Levant MSC*
2468
2469 804 *The Levant interpreted lithology (left, from Fig. 2), biostratigraphic reference levels (PF –*
2470
2471 805 *planktic foraminifera, below) and filtered well-log model (Figs. 5) determine a*
2472 806 *cyclostratigraphic model, resulting with 33 cycles for the Levant MSC (shaded cycles). Note the*
2473
2474 807 *significantly lower cycle frequency in the ~~pre~~Pre-evaporites-Evaporites (2.3 m compared to 51 m*
2475 808 *per-cycle), due to the much higher sedimentation rates in the evaporites interval. This*
2476
2477 809 *cyclostratigraphic model is tuned to astronomic target curves (center) of ETP (blue; calculated*
2478
2479 810 *as eccentricity (Ecc; red) + obliquity - precession ((1) Laskar et al., 2004)), 65°N summer*
2480 811 *insolation (65°N SI; green) (Laskar et al., 2004), and marginal MSC deposits (right columns)*
2481
2482 812 *based on astronomical calibrated ages and cycles identified across the Mediterranean ((1)*
2483 813 *Laskar et al., 2004; (3) Roveri et al., 2014a, CIESM (2008); (4) Manzi et al., 2011; (5)*
2484
2485 814 *Krijgsman et al., 2001). The drop in sea level (SLG; sea level Gibraltar; (2) Ohneiser et al.*
2486
2487 815 *2015) corresponding to glacial peaks TG12-14 ($\delta^{18}O$; as summarized in Roveri et al. (2014))*
2488 816 *marks the top of the ~~main~~ Main halite-Halite unit. The shift to post-evaporitic and clastic*
2489
2490 817 *deposits of MSC stage 3 (Hilgen et al., 2007; Krijgsman et al., 2001; Laskar et al., 2004; Roveri*
2491 818 *et al., 2014), through a stepwise deglaciation associated with sea-level rise (TG12-9), is here*
2492
2493 819 *astronomically tuned to enhanced clastic deposition in the Interbedded Evaporites and*
2494
2495 820 *Argillaceous Evaporites units of the Levant.*

2496 821
2497
2498 822 *To date, there are no reports of diatomites, or a diatom-rich assemblage in stages 2 of the MSC*
2499
2500 823 *across the Mediterranean. Based on the taxonomic similarities between the deep and marginal*
2501
2502 824 *planktonic marine diatom assemblages, we propose that the Levant diatomites constitute a*
2503
2504 825 *temporal lithostratigraphic marker. If we follow the interpretation for the occurrence of planktic*
2505
2506 826 *marine diatoms as indicators of partial connectivity with the Atlantic Ocean (Dela Pierre et al.,*
2507
2508 827 *2014; Hüsing et al., 2009; Krijgsman et al., 2000), then their appearance interbedded within the*
2509
2510 828 *halite in the Levant suggests that deposition of the halite layer occurred at a time of at least*
2511
2512 829 *partial, periodic Atlantic connectivity, most likely during deposition of the PLG on the margins*
2513
2514 830 *(5.97-5.6 Ma).*

2521
2522
2523 831 5.2.2 Allochthonous grains in the Interbedded Evaporites-*Argillaceous Evaporites* and stages 2-
2524
2525 832 3 of the MSC
2526

2527
2528 833 The abrupt change that marks the onset of enhanced clastic input in the Interbedded
2529
2530 834 Evaporites in the Levant Basin, together with endemic and reworked Eocene and Cretaceous
2531
2532 835 foraminifera into the basin, matches other similar episodes reported from the MSC in the
2533
2534 836 Mediterranean. Primarily, these are the clastic-rich deposits that result in the deposition of the
2535
2536 837 Reworked Lower Gypsum (stage 2) and the Upper Gypsum and Lago-Mare deposits (stage 3) on
2537
2538 838 the margins. These clastic deposits, including a similar abundance of minerals and reworked
2539
2540 839 fauna, are not only reported from marginal sections (e.g., Lofi et al., 2011; Roveri et al., 2014),
2541
2542 840 but also from cores of deeper parts of the basin (e.g., Sites 124 in the Western Med (Ryan et al.,
2543
2544 841 2007), Site 654 ~~from-in~~ the Tyrrhenian Sea (Borsetti et al., 1990), and from Sites 374 and 376 in
2545
2546 842 the Eastern Mediterranean (Cita et al., 2006; Hsü et al., 1978a, 1978b)).
2547
2548

2549 843 DSDP ~~sites~~ Sites 375 and 376 ~~on-at~~ the Florence Rise in the Eastern Mediterranean recovered
2550
2551 844 nanofossil marlstones and dolomitic marlstones of latest Miocene age, overlying a gypsum with
2552
2553 845 marlstone ~~evaporite~~-sequence; (Hsü, et al., 1978b). The gypsum with marlstone-~~evaporites~~,
2554
2555 846 which are interpreted as deposits of a shallow subaqueous environment, are followed downwards
2556
2557 847 by anhydrite and halite at Site 376 and are collectively recognized as the upper part of the
2558
2559 848 Mediterranean evaporites. The interbedded gypsum contains reworked Cretaceous, Paleogene
2560
2561 849 and lower/middle Miocene foraminifera and nanofossils, similar to the fauna identified in the
2562
2563 850 clastic interval of the Interbedded Evaporites in the Dolphin well. The reworked fauna from ~~the~~
2564
2565 851 Florence Rise are common to abundant in the bedded evaporites and rare to absent in the
2566
2567 852 overlying Pliocene and underlying Tortonian and Serravallian (Hsü, et al., 1978b), indicating a
2568
2569 853 distinctive phase of reworked sediments deposited within the Mediterranean basins. The
2570
2571
2572
2573
2574
2575
2576

2577
2578
2579
2580
2581
2582
2583
2584
2585
2586
2587
2588
2589
2590
2591
2592
2593
2594
2595
2596
2597
2598
2599
2600
2601
2602
2603
2604
2605
2606
2607
2608
2609
2610
2611
2612
2613
2614
2615
2616
2617
2618
2619
2620
2621
2622
2623
2624
2625
2626
2627
2628
2629
2630
2631
2632

854 sedimentary response of the Interbedded Evaporites and Argillaceous Evaporites (Unitse 5 and 6,
855 respectively; Gvirtzman et al., 2013; 2017; Manzi et al., 20018) in the Levant Dolphin and
856 Leviathan-1 wells (from ~2270 m in the Dolphin well, Figs- 5, 12) resembles similar
857 observations reported from shallower deposits in the Levant. For example, the Afiq Formation
858 overlies the anhydrite-siliciclastic stage 2-RLG equivalent Mavqiim Formation (Druckman et al.,
859 1995; Lugli et al., 2013) and was penetrated by the Or-South 1 well. It consists of Eocene-aged
860 lithoclasts made of limestone, dolomite, and chert- and quartz--rich sand, overlying a
861 conglomerate unit with brackish ostracods indicating a plausible correlation to the Lago-Mare
862 stage (Derin, 2000). A fluvial or sabkha environment is attributed to this interval with subaerial
863 exposure, supporting the idea of a considerable desiccation phase and subaerial exposure near the
864 end of the MSC (Cita et al., 1978; Lofi et al., 2011; Madof et al., 2019; Ryan, 1978). Similar
865 lithologies, including clasts of Eocene and Cretaceous age, were described from the marginal
866 Nir-1 well in the Levant Basin above an erosion surface and beneath earliest Pliocene marls
867 (Frey-Martinez et al., 2007). Similar clastic-conglomeratic and sandy lithologies are also
868 reported from the Messinian Qawasim and Rosetta formations offshore Egypt (Leila et al.,
869 2016); the latter correlates with the Afiq Formation in the Levant (Derin, 2000). Unfortunately,
870 no samples are available from above the base of the Interbedded Evaporites in the deep Levant
871 Basin to further confirm the lithological correlation between these sections and the deep Levant
872 Basin. Correlation to more proximal sections and well-log interpretations indicate (~~see also~~
873 ~~Gvirtzman et al., 2013; 2017; Manzi et al., 2018~~) that the overlying Argillaceous Evaporites
874 mark a shift to more clastic and gypsum/anhydrite deposition (see also Gvirtzman et al., 2013;
875 2017; Manzi et al., 2018).

2633
2634
2635 876 We argue that the main change in the halite unit, characterized by mixing of clastic material
2636
2637 877 into the deep-basin deposits at the base of the Interbedded Evaporites, correlates with the
2638
2639 878 beginning of major sea-level drawdown and introduction of clastic material into the entire
2640
2641 879 Mediterranean ~~basin~~Basin, from stage 2 of the MSC (5.61 Ma) through the Upper Gypsum and
2642
2643 880 Lago Mare stages in the marginal basins (5.5355-5.33 Ma; Argillaceous Evaporites in Fig. 12).
2644
2645 881 During stage 2, sea-level drawdown eroded and redeposited the PLG gypsum into the marginal
2646
2647 882 and intermediate parts of the basin (e.g., Lofi et al., 2011). The deep-basin expression ~~to~~of this
2648
2649 883 regression might be the fine-grained clastics, including older reworked fauna, reaching the
2650
2651 884 Mediterranean's depocenters. However, to further test this idea, and try to distinguish between
2652
2653 885 stage 2 and 3 sediments, we compare biomarker distribution across the basin, and identify
2654
2655 886 sedimentary cycles within the MSC of the Levant Basin.

2658 887 5.2.3 Basin-wide transport of organic matter

2661 888 The *n*-alkane distribution and CPI values of the Levant samples (Figs. 7 and 8; Table 1) are
2662
2663 889 similar to some extent to those obtained from marginal and onshore MSC successions (Vasiliev
2664
2665 890 et al., 2017), and provide further support for the introduction of reworked and mixed material
2666
2667 891 into the Levant during the deposition of the Interbedded Evaporites. The *n*-alkane distribution of
2668
2669 892 Mediterranean MSC samples covering the entire 640-kyr-long MSC interval shows distinct
2670
2671 893 dissimilarities between several marginal to intermediate-depth sections (Vasiliev et al., 2017):
2672
2673 894 ~~the~~The Monte Tondo (Primary Lower Gypsum; MSC stage 1), Realmonte salt mine (Halite and
2674
2675 895 Re-sedimented Lower Gypsum; MSC stage 2), and Eraclea Minoa (Upper Gypsum/Lago Mare;
2676
2677 896 MSC stage 3). The Delphine well *n*-alkane distribution shows a higher abundance of short-chain
2678
2679 897 homologues in the Levant relative to marginal sections (Vasiliev et al., 2017), likely due to the
2680
2681 898 lower relative input of terrestrial organic matter in more distal depositional settings. Several
2682
2683
2684
2685
2686
2687
2688

2689
2690
2691 899 similarities exist between both data sets. Vasiliev et al. (2017) reported CPI values of 3.0-7.9 ~~in~~
2692 ~~at~~ Monte Tondo (stage 1), and 1.7-3.7 ~~in-at~~ Eraclea Minoa (stage 3; Fig. 10). While CPI values
2693 900 ~~at~~ Monte Tondo (stage 1), and 1.7-3.7 ~~in-at~~ Eraclea Minoa (stage 3; Fig. 10). While CPI values
2694 901 were not reported from the halite samples of the Realmonte salt mine, Vasiliev et al. (2017) show
2695 902 two different types of organic matter: 1) autochthonous sediment associated with gypsum or
2696 903 halite deposited in place, and 2) allochthonous material associated with clastic sediments and
2697 904 transport. Marked similarities in CPI values are therefore noted between the Levant and marginal
2698 905 locations described by Vasiliev et al. (2017), with CPI values of 4.0-12.3 in the Main Halite
2699 906 interval (indicating stage 1), and 1.9-2.9 in the Interbedded Evaporites interval (indicating stages
2700 907 ~~2/-3~~) (Fig. 10).

2701
2702 908 Vasiliev et al. (2017) also suggest that dissimilarities in the biomarker and isotopic
2703 909 composition of stages 1 and 2, relative to stage 3 sediments, may be attributed to the outflow of
2704 910 Black Sea (i.e., Paratethys) waters and their mixing into the Mediterranean, which paved the way
2705 911 for Paratethyan 'Lago-Mare' type fauna. For instance, the distribution of *n*-alkanes and CPI
2706 912 values in stage 3 ~~in-at~~ Eraclea Minoa are more evenly distributed and lower, relative to those of
2707 913 stage 1 (Fig. 3 in Vasiliev et al., 2017). We report a similar distinction in the *n*-alkane
2708 914 distribution between the ~~upper Interbedded Evaporites~~ clastic samples and underlying sediments
2709 915 (Table 1, Fig. 9). A much stronger odd-over-even predominance (i.e., higher CPI values) is
2710 916 observed in the Argillaceous Diatomites, together with more elevated long-chain over short-
2711 917 chain *n*-alkanes values (LCA/SCA; Table 1) and maturity parameters (Fig. 11; Table 2). This
2712 918 indicates more immature source rocks with significantly different sources of the organic matter
2713 919 in the Main Halite relative to the Interbedded Evaporites sediments (Bray and Evans, 1961;
2714 920 Scalan and Smith, 1970).

2745
2746
2747 921 The distribution of stereoisomers of algal steranes and bacterial hopanes (Fig. 11; Table 2)
2748
2749 922 reflects the transformation, or stereoisomerization from biological epimers to a more stable
2750
2751
2752 923 geological molecular configuration as a consequence of thermal alteration (Peters, 1986; Peters
2753
2754 924 et al., 2005, 1980). The evidence for enhanced thermal maturity in the Interbedded Evaporites
2755
2756 925 relative to the underlying deposits (Fig. 11; Table 2) is counterintuitive, as thermal maturity
2757
2758 926 should increase with depth (Peters et al., 2005, 1980). Furthermore, the Interbedded Evaporites
2759
2760 927 exhibit mixed signals that include high values of the C₃₁ αβ S/R ratio (indicative of thermally
2761
2762 928 mature organic matter) in addition to C₃₁ hopanes with the ββ biological configuration (indicative
2763
2764 929 of immature organic matter) (Fig. 11; Table 2). This aspect further supports the occurrence of
2765
2766 930 organic matter mixtures from differing ages and thermal histories, i.e., a higher proportion of
2767
2768 931 allochthonous, thermally mature organic matter in the Interbedded Evaporites compared with the
2769
2770 932 Main Halite and Pre-Evaporite samples. This interpretation is consistent with similar trends
2771
2772 933 observed in early Paleogene (Sepúlveda et al., 2009) and Quaternary (Rashid and Grosjean,
2773
2774 934 2006) studies. Such trends may reflect an intensification of the hydrological cycle, and thus
2775
2776 935 enhanced precipitation, continental runoff, and the transport of re-worked, and pre-aged,
2777
2778 936 continental or marginally-derived organic matter during the deposition of the Interbedded
2779
2780 937 Evaporites. Another mechanism through which transport can occur is dense shelf-water
2781
2782 938 cascading (DSWC) transport of sediment and associated organic matter from marginal settings to
2783
2784 939 deep Mediterranean basins, as reported to occur in the Mediterranean today (Canals et al., 2009).
2785
2786 940 The interpretation of transport in these intervals is consistent with the occurrence of clastic
2787
2788 941 material, larger sub-rounded minerals, and re-worked Cretaceous and Eocene foraminifera within
2789
2790 942 samples from the Interbedded Evaporites, which also supports the presence of reworked, older
2791
2792 943 sediments. Both Cretaceous and Eocene organic-rich source rocks are known around the
2793
2794
2795
2796
2797
2798
2799
2800

2801
2802
2803 944 Mediterranean ~~basin~~-Basin (e.g., Almogi-Labin et al., 1993; Bayliss, 1973; Meilijson et al.,
2804
2805 945 2014), and might represent sources of pre-aged weathered and transported organic matter,
2806
2807 946 matching the apparent higher maturity measured from the organic--matter extract of the
2808
2809
2810 947 Interbedded Evaporites sediments.

2812 948 In summary, the similarities between our data and ~~that~~-of Vasiliev et al. (2017) suggest that
2813
2814 949 organic geochemical analysis from the Dolphin well ~~can~~-might be used as regional
2815
2816 950 chemostratigraphic markers to distinguish between Pre-Evaporites and Argillaceous Diatomites
2817
2818 951 sediments, and the overlying Interbedded and Argillaceous Evaporites. A correlation between
2819
2820 952 MSC stage 3 and the ~~Interbedded Evaporites~~upper part of the MSC in the Levant Basin has been
2821
2822 953 previously proposed based on seismic interpretation and the sampling of shallower deposits
2823
2824 954 (Druckman et al., 1995; Gvirtzman et al., 2017; Lugli et al., 2013). Here, we present evidence
2825
2826 955 supporting the occurrence of stage 2 sea--level drawdown or stage 3 and ‘Lago-Mare’-type
2827
2828 956 deposits in the deep domains of the Eastern Mediterranean. This includes increased supply of
2829
2830 957 clastic material into the basin, reworked fauna, and chemostratigraphic markers (Figs- 3, 9 and
2831
2832 958 10).

2836 959 **5.3 From cycles to astronomical tuning**

2838 960 Cyclostratigraphy and astronomical tuning of sediment sections, geochemical signals, and
2839
2840 961 well--log responses have been extensively used for stratigraphic interpretations of MSC deposits
2841
2842 962 across the Mediterranean (Dela Pierre et al., 2014; Hilgen et al., 2007, 2000, 1995; Hilgen and
2843
2844 963 Krijgsman, 1999; Hüsing et al., 2010, 2009, Krijgsman et al., 2001, 1999, 1997; Lugli et al.,
2845
2846 964 2015; Manzi et al., 2015, 2013, 2012; Ochoa et al., 2015; Topper et al., 2014). The CIESM
2847
2848 965 stratigraphic model of the MSC has halite deposited in stage 2 of the MSC, during four
2849
2850 966 insolation-precession cycles (e.g., Roveri et al., 2014a, with reference to Laskar et al., 2004; Fig.

2857
2858
2859 967 12). These are part of the 32 precession-controlled cycles (Laskar et al., 2004) identified across
2860
2861 968 the Mediterranean, with a periodicity of about 20 kyr per cycle, amounting to the 640 kyr time
2862
2863 969 frame of the MSC. Manzi et al. (2015) proposed to tune the high-reflectivity intervals in the
2864
2865 970 seismic section of the Levant (interpreted as clastic units; Gvirtzman et al., 2013a) to summer
2866
2867 971 insolation maxima, and the transparent intervals (interpreted as halite) to summer insolation
2868
2869 972 minima, within these four insolation cycles. By contrast, the study of the Pre-Evaporites in the
2870
2871 973 Dolphin well by Meilijson et al. (2018) and the results of this study suggest that salt formation
2872
2873 974 began around 5.97 Ma, i.e., more or less synchronously with the marginal deposition of the PLG.
2874
2875 975 According to this age-model, the evaporitic sequence in the Levant Basin (Fig. 12) was
2876
2877 976 deposited between 5.97 and 5.33 Ma, corresponding to a time span of ~640 kyr rather than 50
2878
2879 977 kyr, and encompassing 32 insolation cycles (Laskar et al., 2004). Our suggested scenario would
2880
2881 978 imply an average cycle thickness of ~50 m, as the studied section is 1590 m thick.
2882
2883
2884

2885 979 Bandpass filtering of the Dolphin well logs resulted in the identification of 31 cycles, closely
2886
2887 980 matching the 32 precession-controlled cycles (Laskar et al., 2004) in the interval between 5.97
2888
2889 981 and 5.33 Ma. However, this age model includes several assumptions: (1) the evaporite record at
2890
2891 982 the studied site is complete with no hiatus, (2) it is largely undisturbed by salt tectonics, and (3)
2892
2893 983 ~~that~~ the sedimentation rate is approximately constant, with no significant changes between the
2894
2895 984 halite-rich intervals and clastic-diatomitic intervals. The Dolphin record lacks
2896
2897 985 chronostratigraphic tie points and contains intervals in which the log data are erratic (Fig-s 5,
2898
2899 986 S2). Furthermore, the Dolphin well area appears deformed in the upper part of the section, and
2900
2901 987 ~~missing~~ Unit 6 is missing (overlying the Interbedded Evaporites; Fig. 6). These sources of
2902
2903 988 uncertainty suggest that the Dolphin well spectral analysis provides a first order approximation
2904
2905 989 of the number of cycles, primarily across the lower part of the section. However, the large
2906
2907
2908
2909
2910
2911
2912

2913
2914
2915
2916
2917
2918
2919
2920
2921
2922
2923
2924
2925
2926
2927
2928
2929
2930
2931
2932
2933
2934
2935
2936
2937
2938
2939
2940
2941
2942
2943
2944
2945
2946
2947
2948
2949
2950
2951
2952
2953
2954
2955
2956
2957
2958
2959
2960
2961
2962
2963
2964
2965
2966
2967
2968

990 number of cycles observed in the Main Halite interval, if assumed to reflect precessional cycles,
991 suggests a longer period of deposition than ~50 kyr. The Leviathan-1 well is much less deformed
992 (Fig-s 5, 6) and has a thick interval of Unit 6 (Gvirtzman et al., 2013; 2017), similar to the
993 sequence at the Aphrodite well (Manzi et al., 2018). It also presents a good fit between the
994 seismic and the RE well-log response. ~~The observed regularity which produced a filtered~~
995 ~~cycles curve (Fig. 5), which the filtered cycles have reveals a good fit to with the well log target~~
996 ~~curve. and a regularity that fits well the produced filtered cycles curve (Fig. 5).~~ We hypothesize
997 that these cycles represent the 32 ~~insolation-precession~~ cycles identified in MSC sections across
998 the Mediterranean. This would imply that the Main Halite interval in the lower part of the
999 studied section is equivalent to stage 1 (PLG) in marginal sections, as also proposed by Meilijson
1000 et al. (2018).

1001 However, lacking chronostratigraphic tie points in the evaporitic section, an alternative
1002 explanation for the cyclicity observed in the well logs of the halite and the seismic profiles
1003 should be considered to reconcile the age model suggested by Manzi et al. (2018) for the Levant
1004 Basin. In this model the FBI unit, ~~which represents the~~ uppermost ~~part of the p~~Pre-Eevaporites ~~in~~
1005 ~~of the Aphrodite well,~~ corresponds to MSC stage 1 (the PLG; Manzi et al., 2018), ~~and while the~~
1006 uppermost part of the section ~~correlates with~~corresponds to stage 3 (Unit 7; Gvirtzman et al.,
1007 2017). Following this model, the ~33 cycles identified within the Leviathan-1 MSC section
1008 (Figs- 5, 7) correspond to the ~50 kyr estimated for the duration of stage 2 of the MSC (Roveri et
1009 al., 2014), and have therefore a cycle duration of ca. 1560 years. If we take into account the
1010 likely different sedimentation rates of the Argillaceous Diatomites facies, this period could
1011 correspond to the period inferred for the Dansgaard-Oeschger events (1470 years), as observed
1012 during the second half of the last glacial (Schulz, 2002) (although see comments by Ditlevsen et

2969
2970
2971 1013 al. (2007) and Lohmann and Ditlevsen (2018) on the validity and interpretation of these cycles).
2972
2973 1014 Alternatively, they could be explained by the Bond cycles, as observed for the North Atlantic
2974
2975 1015 during the Holocene (1500 years; Bond et al., 2001). Another alternative are the periods of ca.
2976
2977 1016 1000 years corresponding to the so-called Eddy cycle observed in the ^{14}C record, which relate to
2978
2979 1017 variations in solar activity (Steinilber et al., 2012). However, this last alternative is unlikely ~~as~~
2980
2981 1018 if the regular alternations in the halite would correspond to Eddy cycles, it implies that stage 2 of
2982
2983 1019 the MSC ~~only~~ lasted only ~32 kyr. This means that the climax stage of the MSC cannot
2984
2985 1020 encompass both glacial stages TG14 and 12 (Fig. 12), as is assumed in the CIESM model.
2986
2987

2988 1021 In the Realmonte salt mine in Sicily, 10-15 cm alternations in the salt have been interpreted as
2989
2990 1022 annual cycles (Manzi et al. 2012). Such sedimentation rates of ca. 10 cm/yr would imply that the
2991
2992 1023 1,060 m thick Main Halite interval in the Levant could have been formed in a short time period
2993
2994 1024 of 10,600 years, although average sedimentation rate may be lower in the Argillaceous
2995
2996 1025 Diatomites. However, it is hard to reconcile such a short duration of deposition with the amounts
2997
2998 1026 of halite required to build up the thickness of the Levant Basin halite layer.
2999
3000

3001 1027 In the absence of a simple explanation for the cyclicity observed in the Dolphin well, we now
3002
3003 1028 consider its interpretation in relation to the different elements of the CIESM model for marginal
3004
3005 1029 MSC deposits. The CIESM (2008) consensus stratigraphic model for the MSC is strongly based
3006
3007 1030 on astronomical tuning of different MSC sections and includes the following division of the 32
3008
3009 1031 orbital-related cycles identified during this time frame (Laskar et al., 2004): cycles 1-18 in stage
3010
3011 1032 1 (PLG), 19-23 in stage 2 (RLG), 24-28 in stage 3.1 (lower part of Upper Gypsum), and 29-32 in
3012
3013 1033 stage 3.2 (the Lago ~~Mare~~). The correlation between the Levant MSC well ~~log-based~~
3014
3015 1034 astrochronology, the orbital target curves, and the chronology of shallow ~~to~~ marginal sections
3016
3017 1035 (CIESM, 2008) of the MSC indicates the following: (1) the Main Halite interval (3759-2800 m
3018
3019
3020
3021
3022
3023
3024

3025
3026
3027 1036 in the Leviathan-1 well) is bound between the Levant filtered cycles 1 through 19 (Fig. 12). A
3028
3029 1037 comparison with the current MSC chronology (CIESM, 2008; Roveri et al., 2014a) shows a
3030
3031 correlation with the number of cycles in the interval between 5.97 and 5.61 Ma from the base of
3032 1038 the PLG (stage 1) to the base of the RLG (stage 2); (2) the Interbedded Evaporites interval
3033
3034 1039 (2800-2320 m) is bound between the Levant filtered cycles 19 through 28 (Fig. 12), which
3035
3036 1040 correlates to the number of cycles in in stage 2 (the RLG; 5.61-5.53-55 Ma; cycles 19-23), with
3037
3038 1041 and its top ~~is~~ known as the 'top salt' horizon, and the lower part of stage 3 (stage 3.1 the Upper
3039
3040 1042 Gypsum who's base is at 5.42 Ma). Thus, the lower part of the Interbedded Evaporites is also
3041
3042 1043 equivalent to stage 2 halite deposits recognized in intermediate basins, such as the Realmonte
3043
3044 1044 salt mine in Sicily; (3) at the upper part of the ~~section--Interbedded Evaporite and~~ the
3045
3046 1045 Argillaceous Evaporites interval is-are equivalent to ~~the-continuation-of~~ stage 3 of the MSC
3047
3048 1046 (2320-2090 m; Fig. 12), ending with the clastic Lago-Mare interval.
3049
3050 1047

3051 1048 Following the suggestion of Meilijson et al. (2018) ~~of-for~~ an early onset of halite deposition in
3052
3053 1049 the deep Mediterranean basins, similar claims were made by García-Veigas et al. (2018) based
3054
3055 1050 on sulfur stable-~~isotopes~~ analysis of marginal and intermediate basin gypsum deposits. They
3056
3057 1051 hypothesize that the deep-~~basin~~ halite deposits are not equivalent to one phase of deposition
3058
3059 1052 during stage 2 of the MSC, but rather comprise two to three phases of halite deposition,
3060
3061 1053 beginning with halite deposition during stage 1 of the MSC. Our astronomical tuning agrees with
3062
3063 1054 this idea by positioning the boundary between stage 1 and 2 of the MSC (2762 m in the Dolphin
3064
3065 1055 well, 2800 m in Leviathan-1) at the top of the Main Halite interval. Consequently, we propose
3066
3067 1056 that the Main Halite is equivalent to stage 1 gypsum deposits of the PLG, as indicated
3068
3069 1057 independently by the diatomite facies. The increase in clastic and re-worked faunal material into
3070
3071 1058 the basin fits well with our astrochronology, placing the Interbedded Evaporites within the time
3072
3073
3074
3075
3076
3077
3078
3079
3080

3081
3082
3083 059 period of the Re-worked Lower Gypsum (stage 2 of the MSC). Sea-level drawdown promoted
3084
3085 060 the scraping of the shelf, re-shaping of drainage and transport systems across the basin, and re-
3086
3087 061 depositing of vast amounts of eroded gypsum-sediment into the intermediate basins. It also
3088
3089 062 delivered vast amounts of fine-grained material to the deep basins, as observed in the
3090
3091 1063 Interbedded Evaporites in the Levant Basin. Lastly, the identification of the *Discoaster*
3092
3093 1064 *quinqueramus* in Unit 5 (the Interbedded Evaporites) by Manzi et al. (2018) supports this
3094
3095 065 conclusion, as this species went extinct towards the end of stage 2.
3096
3097
3098

3099 1066 **5.4 Implications of a new MSC chronology in the Mediterranean**

3100
3101 1067 While not conclusive, the integration of our different stratigraphic proxies supports an early
3102
3103 068 and long-lasting deposition of deep-basin halite. The direct implication of this age-model is that
3104
3105 069 halite was deposited in the deep Eastern Mediterranean when sea level was high and partial,
3106
3107 070 episodic connection with the Atlantic still prevailed (Dela Pierre et al., 2014; Flecker and Ellam,
3108
3109 1071 2006; Krijgsman et al., 2002; Roveri et al., 2014b), synchronously with gypsum deposition along
3110
3111 072 the Mediterranean margins and intermediate basins (Ochoa et al., 2015). Our results do not
3112
3113 1073 exclude an evaporative drawdown (e.g., Lofi, et al., 2011; Rouchy and Caruso, 2006; Ryan,
3114
3115 1074 2008) and lower sea level at the acme of the MSC during stage 2 (Ohneiser et al., 2015). The
3116
3117 1075 lack of sedimentological features within the monotonously clean halite, and our interpretation of
3118
3119 076 long-lasting deep-water evaporite depositional settings, indicate that salt must have started to
3120
3121 077 precipitate within a deep-basin-deep-water environment, and not in shallow-waters. We
3122
3123 078 propose that sea-level drawdown actually prompted enhanced transport of clastic sediments into
3124
3125 079 the deep basin resulting with-in the deposition of the Interbedded Evaporites unit, analog to the
3126
3127 080 marginal deposition of the RLG. Studies of strontium isotopes from the Lower Evaporites (PLG,
3128
3129 081 MSC stage 1) consistently report isotopic values close to those characteristic of the global oceans
3130
3131
3132
3133
3134
3135
3136

3137
3138
3139
3140
3141
3142
3143
3144
3145
3146
3147
3148
3149
3150
3151
3152
3153
3154
3155
3156
3157
3158
3159
3160
3161
3162
3163
3164
3165
3166
3167
3168
3169
3170
3171
3172
3173
3174
3175
3176
3177
3178
3179
3180
3181
3182
3183
3184
3185
3186
3187
3188
3189
3190
3191
3192

1082 (Flecker and Ellam, 2006; Roveri et al., 2014b), and do not support an early desiccation model
1083 (Cita, 1976; Hsü, 1973). While advocating a different chronological model, our study is
1084 consistent with these interpretations and shows that halite deposition started during a time when
1085 Atlantic inflow was still evident.

1086 A coeval initiation of basinal halite and marginal gypsum precipitation calls for a reevaluation
1087 of previous models for MSC development, as well as its effect on global ocean salinity and
1088 climate. We refer to the timing and persistence of halite deposition (which may have been an
1089 order of magnitude larger than previously thought), and also to the substantially lower rates of
1090 deposition of the deep-basin salt unit, from a previous assumption of 3,000 cm/kyr (according to
1091 CIESM chronology) to 250 cm/kyr as deduced ~~by~~ from our new age model. Although this
1092 assumes continuous precipitation and no dissolution, which we consider unlikely if the water is
1093 being relatively refreshed with additional seawater throughout deposition. The Levant
1094 chronostratigraphic model suggests that steady state of halite deposition was achieved and
1095 maintained earlier in the MSC than previously thought. Both halite and gypsum could have been
1096 precipitated ~~be~~-synchronously ~~precipitated~~, with their partitioning possibly governed by their
1097 different solubility product constants (K_{sp}) and ion availability. Furthermore, if we allow for an
1098 order of magnitude change in the time scale of halite precipitation, then the required
1099 sedimentation flux that removes sodium and chlorine from seawater is reduced. This exercise
1100 substantially reduces the total sea-level drawdown (Ryan, 2008) required to explain the
1101 deposition of a ~2 km-thick salt deposit. A further possible mechanism to explain the
1102 synchronous deposition of gypsum and halite in marginal and deeper parts of the basin,
1103 respectively, includes density stratification and down-shelf cascading of brines (Roveri et al.,
1104 2014c; Sirota et al., 2017). While salt-saturated shallow waters seem to have reached gypsum

3193
3194
3195
3196
3197
3198
3199
3200
3201
3202
3203
3204
3205
3206
3207
3208
3209
3210
3211
3212
3213
3214
3215
3216
3217
3218
3219
3220
3221
3222
3223
3224
3225
3226
3227
3228
3229
3230
3231
3232
3233
3234
3235
3236
3237
3238
3239
3240
3241
3242
3243
3244
3245
3246
3247
3248

1105 saturation values, brine formation might have continuously flowed down-shelf, in a similar
1106 manner as dense shelf-water cascading (DSWC) is observed today around the Mediterranean
1107 Basin (Canals et al., 2009, 2006). DSWC is associated with mass-transport complexes and
1108 submarine channels, and has a significant impact on the sediment and organic-matter supply
1109 from continental and shallow-marine settings to deep-sea ecosystems. Mass-balance calculations
1110 suggest that the input of dissolved organic carbon and suspended particulate organic carbon from
1111 ocean margins to the open ocean interior may be more than an order of magnitude greater than
1112 direct inputs of organic carbon produced near the ocean surface today (Bauer and Druffel, 1998).
1113 Similarly, highly saturated waters produced in an evaporitic Mediterranean may have produced
1114 vast quantities of brine accumulating in the deep depocenters. Brine formation may have been at
1115 least partly controlled by precession-induced increases in river runoff (Marzocchi et al., 2015),
1116 and potentially by surface inflow from the Paratethys (Karakitsios et al., 2017; Krijgsman et al.,
1117 2010). Salinity stratification is supported by geochemical evidence for the occurrence of low-
1118 salinity surface waters overlying deep brines at gypsum and halite saturation (Christeleit et al.,
1119 2015), as well as by the presence of brackish-water faunas of Paratethyan origin in the Lago-
1120 Mare phase (Stoica et al., 2016). Our data, including high concentrations of long-chain *n*-alkanes
1121 (Table 1) and high LCA/SCA values (Table 1), also support the occurrence of increased river
1122 runoff into the basin during the deposition of the Interbedded Evaporites.

1123 Our interpretation of a deep-basin-deep-water model and early onset of halite, rejuvenates
1124 an idea that has been a focus of debate in the past (e.g., Garcia-Castellanos and Villaseñor, 2011;
1125 Lofi et al., 2011; Ryan, 2008; Schmalz, 1969). Simon and Meijer (2017) used a box-model setup
1126 to model the MSC events forced by Atlantic exchange and evaporative loss. This model
1127 demonstrated that a significantly stratified Mediterranean water column could have been

3249
3250
3251
3252
3253
3254
3255
3256
3257
3258
3259
3260
3261
3262
3263
3264
3265
3266
3267
3268
3269
3270
3271
3272
3273
3274
3275
3276
3277
3278
3279
3280
3281
3282
3283
3284
3285
3286
3287
3288
3289
3290
3291
3292
3293
3294
3295
3296
3297
3298
3299
3300
3301
3302
3303
3304

1128 established early in the crisis, while the duration of halite deposition must have taken longer than
1129 currently considered in the MSC stratigraphic consensus model. The synchronous formation of
1130 gypsum and halite in proximal and distal basins, respectively, could have occurred at different
1131 levels within the basin, with lower rates of halite sedimentation than previously thought. Our
1132 data supports the model by Simon and Meijer (2017) and calls to reevaluate Mediterranean MSC
1133 sections, while considering a possible early deposition of halite.

1134 Sea-level drop during stage 2 of the MSC may have added more proximal basins to the
1135 regional deep-sea deposition of halite, which might explain why those intermediate-basin halite
1136 deposits correlate to the stage 2 RLG. Such a mechanism can explain the existence of marginal
1137 or intermediate-depth basins with relatively thin halite deposits, which only correlate with the
1138 Interbedded evaporites-Evaporites interval in the Levant (Fig. 12), in which halite is still the
1139 dominant lithology. For example, the marginal Realmonte salt mine has a ~600 m thick halite
1140 sequence (Lugli et al., 1999; Roveri et al., 2014a) compared with the thick (>2 km) halite
1141 deposits in deep Mediterranean basins. In a similar manner, recent studies from the Dead Sea
1142 demonstrate downslope-flowing brines, in which the deep basinal areas accumulate the most
1143 brine and the marginal areas are influenced by fresher waters and hence subject to more
1144 dissolution (Sirota et al., 2016).

1145 Being one of the largest and youngest salt giants formation episodes in Earth's history, the
1146 MSC is repeatedly used as a cornerstone for explaining evaporite deposition. Our new model,
1147 which includes the synchronous deposition of sulfates in the margins of the basin and halite at its
1148 center, calls for a re-evaluation of the mechanisms governing evaporite deposition in other salt-
1149 giant deposits in the geologic record. For example, in the Permian Zechstein-, similar to the
1150 Mediterranean, sulfates appear to have been limited to the margins while halite was deposited in

3305
3306
3307
3308
3309
3310
3311
3312
3313
3314
3315
3316
3317
3318
3319
3320
3321
3322
3323
3324
3325
3326
3327
3328
3329
3330
3331
3332
3333
3334
3335
3336
3337
3338
3339
3340
3341
3342
3343
3344
3345
3346
3347
3348
3349
3350
3351
3352
3353
3354
3355
3356
3357
3358
3359
3360

151 the deeper parts of the basin (Richter-Bernburg, 1985). This is also the case for the Permian ~~aged~~
1152 Delaware Basin in Texas and New Mexico, where clear inter-fingering between sulfates and
1153 halite are observed as brine concentrations oscillate (Anderson and Dean, 1995).

1154 The alternating clastic and evaporitic sediments of the Interbedded Evaporites (Unit 5;
1155 Gvirtzman et al., 2013; 2017) include cycles 19-28, matching in its lower part the time frame of
1156 MSC stage 2, the RLG. Isolation from the Atlantic and significant sea-level drawdown ~~is-are~~
1157 proposed as the formation mechanism for both the onshore deep subaerial canyons and offshore
1158 erosion surfaces across the Mediterranean (Lofi et al., 2011; Ryan, 1976; Ryan and Cita, 1978).

1159 Different models were proposed to explain the mechanisms behind erosion, transport, and re-
1160 deposition, such as early subaqueous large-scale mass-wasting processes occurring at the
1161 beginning of the MSC drawdown, subaerial rivers down-cutting by retrogressive action to adjust
1162 for their new base level, or marine abrasion as possible agent for late erosion (Lofi et al., 2011
1163 and references therein). Regardless of the mechanism, clastic geometries are clear in MSC
1164 seismic sections and are partly controlled by local factors such as the dimension of the drainage
1165 basin, resulting in major differences between the Messinian sedimentary successions in the
1166 different areas of the Mediterranean. The whereabouts of the massive products of ~~this-these~~
1167 basin-wide erosional processes ~~es~~ has been one of the MSC's enigmas (Ryan, 1976; Ryan and Cita,
1168 1978; Lofi et al., 2011). The seismic facies defined as the Complex Unit (CU; Lofi et al., 2011)
1169 in the Western Mediterranean is either chaotic or roughly bedded, and is believed to account for
1170 some of the waste products. CU deposits are absent on the margin shelves, rarely observed on the
1171 upper slopes, and mainly ~~recovered-observed at-along~~ the ~~margin-footbase of the slopes~~, either as
1172 fan-shaped deposits at the Messinian river mouths or as poorly organized bodies elsewhere. This

3361
3362
3363 173 unit ~~makes marks~~ the transition between the eroded slopes and deep-basin deposits (Lofi et al.,
3364 1174 2011). The CU is positioned above or parallel to the Mobile Unit (the halite).
3365
3366
3367 In summary, stage 2 of the MSC is characterized by massive sediment displacement, for
3368 1175 which only a portion is accounted for. We propose that the Interbedded Evaporites (Unit 5;
3369 1176 Gvirtzman et al., 2017) are part of this high-energy system and that the interbedding of clastics
3370 1177 represents the deep-basin depocenters for the fine grained material at the distal part of the
3371 1178 drainage system. These precession~~al~~-controlled clastic incursions ~~were displaced~~reached into an
3372 1179 evaporitic system, which in the deep basins has been depositing halite for ~360 kyr during stage
3373 1180 1 of the MSC. We argue that this idea could not be examined before due to lack of a sedimentary
3374 1181 record from the deep basin and the difficulty of correlating marginal and deep-basin units based
3375 1182 on seismo-stratigraphy. The call for caution regarding the interpretation of MSC-related
3376 1183 offshore data was recently presented by Roveri et al. (2019). They pointed out that MSC units
3377 1184 having with different age, nature and depositional settings, may show similar seismic facies and
3378 1185 geometries. On the other hand, the same units may appear as belonging to different seismic
3379 1186 facies, either with parallel and high-amplitude reflections or even transparent or chaotic
3380 1187 reflectivity due to seismic interference patterns related to the dominant frequency. We therefore
3381 1188 argue against lumping the different facies of the Interbedded Evaporites into a unified deep-basin
3382 1189 halite deposit, disregarding its clastic nature, as done in past interpretations of the Levant
3383 1190 Basin MSC section (e.g., Manzi et al., 2018). Here we offer new sedimentological analysis of the
3384 1191 non-evaporitic facies, interpreted in the past as clastic deposits through seismic and well-log
3385 1192 interpretation (e.g., Feng et al., 2016). We argue that two different ‘non-halite’ deposits exist in
3386 1193 the Levant deep MSC deposits: 1) ~~The~~the mostly biogenic remains of diatoms (the Argillaceous
3387 1194

3417
3418
3419
3420
3421
3422
3423
3424
3425
3426
3427
3428
3429
3430
3431
3432
3433
3434
3435
3436
3437
3438
3439
3440
3441
3442
3443
3444
3445
3446
3447
3448
3449
3450
3451
3452
3453
3454
3455
3456
3457
3458
3459
3460
3461
3462
3463
3464
3465
3466
3467
3468
3469
3470
3471
3472

195 Diatomites) within the stage 1 Main Halite interval, and 2) ~~The~~the clastic and reworked deposits
1196 of the Interbedded Evaporites/Argillaceous Evaporites belonging to stage 2 and 3 of the MSC.

1197 Stage 3 of the MSC is generally characterized by reworking of shelf sediments and their
1198 occasional influx into the basin during renewed gypsum deposition. We position the base of
1199 stage 3 within the Interbedded Evaporites- at cycle 23 (Figs: 5, 6, 712), pointing to a much
1200 thicker stage 3 section in the Levant ~~then~~than in the model of Gvirtzman et al. (2017), Manzi et
1201 al. (2018), or Madof et al. (2019). Relying on the CIESM (2008) stratigraphic model, these
1202 separate studies position the halite into stage 2, and continue stage 2 until almost the top of the
1203 Levant MSC section. They position stage 3 at the topmost part of the section, represented only
1204 by Unit 7 - a thin anhydrite and shale unit (~~as~~ interpreted by well-log data in the deep basin as
1205 no study has recovered samples from this interval thus far). These studies mainly differ in their
1206 interpretation of the stage 3 depositional environment, namely subaerial (Madof et al., 2019) or
1207 subaqueous (Gvirtzman et al., 2017) dissolution/ and truncation. According to our depositional
1208 model (Fig. 12), Unit 6 belongs to stage 3 of the MSC (the Upper Gypsum and Lago Mare;
1209 CIESM, 2008), and the IMTS (Gvirtzman et al., 2017) or IES (Madof et al., 2019)
1210 unconformities in the Levant represent the transition between stage 3.1 (Upper Gypsum) and 3.2
1211 (Lago Mare) of the MSC. The latter stage (3.2) was attributed to Unit 7 and perhaps also to parts
1212 of the overlying brackish Afik Formation (Druckman et al., 1995) by Gvirtzman et al.
1213 (~~2018~~2017). The introduction of Paratethyan waters and sediment, termed Lago Mare deposits
1214 along the Paratethyan side of the Mediterranean, is also likely to have reached the deep basins.
1215 However, while those might have reached the Levant Basin, different local drainage systems are
1216 most likely the sources for the MSC stage 3 transported sediments in the Levant area. A local
1217 source for transported sediments is the Nile drainage and fan systems, identified as reaching

3473
3474
3475 218 further north-west, beyond the Dolphin and Leviathan wells, towards the Eratosthenes Seamount
3476
3477 219 offshore Cyprus (Hawie et al., [2013b](#)[2013a](#), [2013a](#)[2013b](#)). In addition, local drainage systems
3478
3479 220 that may have supplied the transported sediments ~~observed~~ include the Afiq and Ashdod canyons
3480
3481 (Bertoni and Cartwright, 2007; Druckman et al., 1995), and the southern Turkey and western
3482 221
3483
3484 222 Syria drainage systems proposed by Madof et al. (2019).
3485

3486 1223 **6. Conclusions**

3489 1224 Over the past 50 years, models explaining the formation of offshore MSC deposits have
3490
3491 1225 remained hypothetical in the absence of a complete sedimentary record of the deep
3492
3493 226 Mediterranean ~~basin~~[Basin](#). The current study presents ~~results~~[results](#) from the offshore Dolphin
3494
3495 227 and Leviathan-1 wells, which penetrated MSC evaporites ~~at from~~ 2,025 to 3,616 ~~m.b.s.l.m~~, and
3496
3497 ~~from~~ 2,090 to 3,759 ~~m.b.s.l.m~~, respectively. Our results challenge some of the current models for
3498 228
3499 229 the MSC, regarding the synchronicity or diachronism of evaporite deposits across the
3500
3501 Mediterranean ~~basin~~[Basin](#), their composition, and controlling factors. A longer duration for
3502 230
3503 halite deposition [than previously assumed](#) impacts our understanding of the biochemical and
3504 231
3505 spatial constraints of this time period. While similar ideas have been previously raised (e.g., Van
3506 1232
3507 Couvering et al., 1976; Govers, 2009; Hardie and Lowenstein, 2004; Meilijson et al., 2018;
3508 1233
3509 Ryan, 2011; Simon and Meijer, 2017), we provide the first report on sedimentological data from
3510 1234
3511 the deep basin MSC halite deposits supporting the scenario of long-lasting salt deposition. We
3512 1235
3513 call for a re-evaluation of models based on a ~50 kyr-long deposition of halite in the deep basins.
3514 1236
3515 However, samples from the upper part of the deep MSC deposits in the Eastern Mediterranean
3516 1237
3517 are not ~~currently~~[yet](#) available, while the existing sedimentary record drilled by the industry
3518
3519 238
3520 consists of well cuttings and not a continues core. The complexity revealed by this study makes a
3521 1239
3522
3523
3524
3525
3526
3527
3528

3529
3530
3531
3532
3533
3534
3535
3536
3537
3538
3539
3540
3541
3542
3543
3544
3545
3546
3547
3548
3549
3550
3551
3552
3553
3554
3555
3556
3557
3558
3559
3560
3561
3562
3563
3564
3565
3566
3567
3568
3569
3570
3571
3572
3573
3574
3575
3576
3577
3578
3579
3580
3581
3582
3583
3584

1240 strong case for future scientific drilling efforts that can retrieve cores from different parts of the
1241 deep-basin halite deposits of the Mediterranean.

1242 This study aimed at addressing the composition and key stratigraphic questions regarding the
1243 timing and correlation of MSC events in the deep Mediterranean. Our main findings can be
1244 summarized as follows:

1. The formation of thick halite deposits in the Levant Basin occurred in a deep-basin deep-
water environment that began earlier than previously thought, during the PLG phase of
gypsum precipitation ~~on~~in the marginal ~~basins~~basins. This implies that a shallow desiccated
scenario is not necessarily required to generate halite ~~-~~precipitation during the MSC. The
presence of well-preserved marine planktonic diatoms within the massive halite deposits
strongly supports a periodic connectivity between the Atlantic and the Eastern
Mediterranean during halite deposition.

2. The exact timing for the end of deep-~~basin~~ halite precipitation is still unclear. Well-~~log~~
interpretation, cyclostratigraphy, and the astronomical tuning model presented here
suggest that halite deposition continued at least until 5.45 Ma, and interbedded clastic
material and evaporites (probably mainly gypsum/anhydrite) persisted until ca. 5.33 Ma.

3. The transition into the Interbedded Evaporites interval at 2,560 m at Dolphin and 2,800 m
at Leviathan-1 marks a major shift in the mode of deposition. An increase in basin-ward
transport of sediments is indicated by the high abundance of larger sub-rounded clastic
grains such as quartz and plagioclase ~~minerals~~, clay, micrite, and reworked Cretaceous
~~and to~~ Eocene benthic and planktic foraminifera. Variable ~~ranges of organic matter~~
thermal maturity indices also point to mixed sources of organic matter~~sediment~~. In
general, biomarker indices in the Interbedded Evaporites resemble those measured

3585
3586
3587
3588 1263 elsewhere in the Mediterranean Basin from strata with transported material and mixed
3589
3590 264 sources. The transition from the Main Halite to the Interbedded Evaporites at 2,560 m
3591
3592 265 most likely represents the transition between stage 1 and 2 of the MSC. The ~~massive~~-large
3593
3594 1266 amounts of clastic sediments in the Interbedded Evaporites are possibly an answer to one
3595
3596 267 of the MSC enigmas, regarding the location of the transported material related to the sea-
3597
3598 268 level drawdown of stage 2 and the ~~closer~~-interruption of the connection with of the Atlantic
3599
3600 1269 Ocean.

- 3601
3602 270 4. During the MSC, high sea level and partial connectivity with the global oceans promoted
3603
3604 1271 the deposition of deep-basin deep-water halite, while sea-level drawdown promoted
3605
3606 1272 deposition of reworked and transported material from the margins into deep
3607
3608
3609 1273 Mediterranean basins.

3610 3611 1274 **Acknowledgments**

3612
3613
3614 1275 The authors would like to thank Ratio Oil Exploration, Noble Energy, and Delek Energy for
3615
3616 1276 kindly providing data and permission to publish. This work was supported by the State of Israel
3617
3618 1277 Ministry of Energy, the Maurice Hatter Foundation, and by the Marie Curie Career Integration
3619
3620 1278 Grants (CIG) FP7-PEOPLE-2011-CIG under the GASTIME project framework. The work was
3621
3622 1279 also supported by the COST Action “Uncovering the Mediterranean salt giant” (MEDSALT)
3623
3624 1280 supported by COST (European Cooperation in Science and Technology). We are grateful to
3625
3626 1281 Emerson-Paradigm for software sponsorship. We would also like to thank Tanja Kouwenhoven
3627
3628 1282 for her contribution with foraminiferal analysis, Revital Bookman and Beverly Goodman for the
3629
3630 1283 use of laboratory equipment, Nimer Taha and Alexander Surdyaev for laboratory assistance with
3631
3632 1284 the XRD/XRF analysis and seismic interpretation, respectively. Nadia Dildar, Alexander Weber,
3633
3634 1285 and Ian Bishop are thanked for laboratory assistance for biomarker analysis and diatom
3635
3636
3637
3638
3639
3640

3641
3642
3643
3644
3645
3646
3647
3648
3649
3650
3651
3652
3653
3654
3655
3656
3657
3658
3659
3660
3661
3662
3663
3664
3665
3666
3667
3668
3669
3670
3671
3672
3673
3674
3675
3676
3677
3678
3679
3680
3681
3682
3683
3684
3685
3686
3687
3688
3689
3690
3691
3692
3693
3694
3695
3696

286 taxonomy. We thank William B.F. Ryan, Andre Strasser, and an anonymous reviewer for
287 suggestions which significantly improved the manuscript.

3697
3698
3699
3700
3701
3702
3703
3704
3705
3706
3707
3708
3709
3710
3711
3712
3713
3714
3715
3716
3717
3718
3719
3720
3721
3722
3723
3724
3725
3726
3727
3728
3729
3730
3731
3732
3733
3734
3735
3736
3737
3738
3739
3740
3741
3742
3743
3744
3745
3746
3747
3748
3749
3750
3751
3752

1288 **References**

1289 Alinat, J., Cousteau, J., 1962. Accidents de terrain en mer de Ligurie. *Océanographie géologique*
1290 et géophysique de la Méditerranée occidentale, 121. Centre national de la recherche
1291 scientifique, Paris.

1292 Almogi-Labin, A., Bein, A., Sass, E., 1993. Late Cretaceous upwelling system along the
1293 Southern Tethys Margin (Israel): Interrelationship between productivity, bottom water
1294 environments, and organic matter preservation. *Paleoceanography* 8, 671–690.
1295 doi:10.1029/93PA02197

1296 Anderson, R.Y., Dean, W.E., 1995. Filling the Delaware Basin: Hydrologic and Climatic
1297 Controls on the Upper Permian Castile Formation Varved Evaporite, in: Scholle, P.A.,
1298 Peryt, T.M., Ulmer-Scholle, D.S. (Eds.), *The Permian of Northern Pangea: Volume 2:*
1299 *Sedimentary Basins and Economic Resources*. Springer Berlin Heidelberg, Berlin,
1300 Heidelberg, pp. 61–78. doi:10.1007/978-3-642-78590-0_4

1301 Arnon, A., Selker, J.S., Lensky, N.G., 2016. Thermohaline stratification and double diffusion
1302 diapycnal fluxes in the hypersaline Dead Sea. *Limnol. Oceanogr.* 61, 1214–1231.
1303 doi:10.1002/lno.10285

1304 Bauer, J.E., Druffel, E.R.M., 1998. Ocean margins as a significant source of organic matter to
1305 the deep open ocean. *Nature* 392, 20–23. doi:10.1038/33122

1306 Bayliss, D.D., 1973. *Micropalaeontology of sections Cenomanian to Middle Eocene West Bank*
1307 *of Jordan*. London.

1308 Bellaiche, G., Genesseeux, M., Mauffret, A., Rehault, J.P., 1974. Prélèvements systématique et
1309 caractérisation des réflecteurs acoustiques: nouvelle étape dans la compréhension de la
1310 géologie de la Méditerranée occidentale. *Marine Geology* 16, M47–M56.

3753
3754
3755 1311 Berggren, W.A., Kennett, J.P., Srinivasan, M.S., 2006. Neogene Planktonic Foraminifera: A
3756
3757 1312 Phylogenetic Atlas. *Micropaleontology*. doi:10.2307/1485586
3758
3759
3760 1313 Bertoni, C., Cartwright, J.A., 2007. Major erosion at the end of the Messinian Salinity Crisis:
3761
3762 1314 Evidence from the Levant Basin, Eastern Mediterranean. *Basin Res.* 19, 1–18.
3763
3764 1315 doi:10.1111/j.1365-2117.2006.00309.x.
3765
3766 1316 Bertoni, C., Cartwright, J.A., 2006. Controls on the basinwide architecture of late Miocene
3767
3768 1317 (Messinian) evaporites on the Levant margin (Eastern Mediterranean). *Sediment. Geol.*
3769
3770 1318 188–189, 93–114. doi:10.1016/j.sedgeo.2006.03.019.
3771
3772
3773 1319 Biehl, B.C., Reuning, L., Strozyk, F., Kukla, P.A., 2014. Origin and deformation of intra-salt
3774
3775 1320 sulphate layers: An example from the Dutch Zechstein (Late Permian). *Int. J. Earth Sci.*
3776
3777 1321 103, 697–712. doi:10.1007/s00531-014-0999-4
3778
3779
3780 1322 Blanc, P., 2000. Of sills and straits : a quantitative assessment of the Messinian Salinity Crisis.
3781
3782 1323 *Deep. Res. I* 47, 1429–1460.
3783
3784 1324 Bond, G., Kromer, B., Beer, J., Muscheler, R., Evans, M.N., Showers, W., Hoffmann, S., Lotti-
3785
3786 1325 Bond, R., Hajdas, I., Bonani, G., 2001. Persistent Solar Influence on North Atlantic Climate
3787
3788 1326 During the Holocene. *Science* (80-.). 294, 2130–2136.
3789
3790
3791 1327 Borsetti,, A. M., Curzi, P. V., Landuzzi, V., Mutti, M., Ricci Lucchi, F., Sartori, R., Tomadin, L.,
3792
3793 1328 Zuffa, G.G., 1990. Messinian and pre-Messinian sediments from ODP leg 107 Sites 652 and
3794
3795 1329 654 in the Tyrrhenian Sea: sedimentological and petrographic study and possible
3796
3797 1330 comparisons with Italian sequences, in: Kastens, K. A., Mascle, J., et al. (Ed.), *Proc. Ocean*
3798
3799 1331 *Drill. Program, 107 Sci. Results* 107, 169–186. doi:10.2973/odp.proc.sr.107.161.1990.
3800
3801
3802 1332 Bourcart, J., Boillot, G., Cousteau, J.Y., Gennesseaux, M., Klimek, C., 1958. Les sediments
3803
3804
3805
3806
3807
3808

3809
3810
3811 1333 profonds au large de la cote nicoise. Comptes Rendus de l'Academie des Sciences Paris
3812
3813 1334 147, 116.
3814
3815
3816 1335 Bray, E.E., Evans, E.D., 1961. Distribution of n-paraffins as a clue to recognition of source beds.
3817
3818 1336 Geochim. Cosmochim. Acta 22, 2–15. doi:10.1016/0016-7037(61)90069-2
3819
3820 1337 Buchbinder, B., Zilberman, E., 1997. Sequence stratigraphy of Miocene-Pliocene carbonate-
3821
3822 1338 siliciclastic shelf deposits in the eastern Mediterranean margin (Israel): effects of eustasy
3823
3824 1339 and tectonics. Sediment. Geol. 112, 7–32.
3825
3826 1340 Camerlenghi, A., Aosis, V., Lofi, J., Hübscher, C., deLange, G., Flecker, R., Garcia-Castellanos,
3827
3828 1341 D., Gorini, C., Krijgsman, W., Lugli, S., Makovsky, Y., Manzi, V., McGenity, T., Pan, N.,
3829
3830 1342 2014. Uncovering a Salt Giant. Deep-Sea Record of Mediterranean Messinian Events
3831
3832 1343 (DREAM) multi-phase drilling project, in: EGU. Vienna, p. 1.
3833
3834 1344 Canals, M., Danovaro, R., Heussner, S., Lykousis, V., Puig, P., Trincardi, F., Calafat, A.,
3835
3836 1345 Durrieu de Madron, X., Palanques, A., 2009. Cascades in Mediterranean Submarine Grand
3837
3838 1346 Canyons. Oceanography 22, 26–43. doi:10.5670/oceanog.2009.03
3839
3840 1347 Canals, M., Puig, P., de Madron, X.D., Heussner, S., Palanques, A., Fabres, J., 2006. Flushing
3841
3842 1348 submarine canyons. Nature 444, 354–357. doi:10.1038/nature05271
3843
3844 1349 Christeleit, E.C., Brandon, M.T., Zhuang, G., 2015. Evidence for deep-water deposition of
3845
3846 1350 abyssal Mediterranean evaporites during the Messinian salinity crisis. Earth Planet. Sci.
3847
3848 1351 Lett. 427, 226–235. doi:10.1016/j.epsl.2015.06.060
3849
3850 1352 CIESM, 2008. The Messinian Salinity Crisis from mega-deposits to microbiology - A consensus
3851
3852 1353 report. N° 33. CIESM Work. Monogr. 7–10.
3853
3854 1354 Cita, M.B., 1976. Biodynamic effects of the messinian salinity crisis on the evolution of
3855
3856 1355 planktonic foraminifera in the mediterranean. Palaeogeogr. Palaeoclimatol. Palaeoecol. 20,
3857
3858
3859
3860
3861
3862
3863
3864

3865
3866
3867 1356 23–42. doi:10.1016/0031-0182(76)90023-7
3868
3869 1357 Cita, M.B., Ryan, W.B.F., Kidd, R.B., 1978. Sedimentation rates in neogene deep-sea sediments
3870
3871 from the mediterranean and geodynamic implications of their changes, in: Initial Reports of
3872 1358 the Deep Sea Drilling Project. pp. 991–1002.
3873
3874 1359
3875
3876 1360 Cita, M.B., Santambrogio, S., Melillo, B., Rogate, F., 2006. Messinian Paleoenvironments: New
3877
3878 1361 Evidence from the Tyrrhenian Sea (ODP Leg 107). Proc. Ocean Drill. Program, 107 Sci.
3879
3880 1362 Results 107, 211–227. doi:10.2973/odp.proc.sr.107.161.1990.
3881
3882 1363 Clauzon G., Suc, J.P., Gautier, F., Berger, A., Loutre, M.F., 1996. Alternate interpretation of the
3883
3884 1364 Messinian salinity crisis, controversy resolved? *Geology*, 24, 363-366. Doi: 10.1130/0091-
3885
3886 1365 7613
3887
3888
3889 1366 Cornet, C., 1968. Le graben médian (zone A) de la Méditerranée occidentale pourrait être
3890
3891 1367 pontien. *Sommaire Société Géologique de France* 149.
3892
3893 1368 Couto, D. Do, Popescu, S., Suc, J., Melinte-dobrinescu, M.C., Barhoun, N., Gorini, C., Jolivet,
3894
3895 1369 L., Poort, J., Jouannic, G., Auxietre, J., 2014. Lago Mare and the Messinian Salinity Crisis :
3896
3897 1370 Evidence from the Alboran Sea Lago Mare and the Messinian Salinity Crisis : Evidence
3898
3899 1371 from the Alboran Sea (S . Spain). *Mar. Pet. Geol.* 52, 57–76.
3900
3901 1372 doi:10.1016/j.marpetgeo.2014.01.018
3902
3903 1373 Van Couvering, J.A., Berggren, W.A., Drake, R.E., Aguirre, E., Curtis, G.H., 1976. The terminal
3904
3905 1374 Miocene event. *Mar. Micropaleontol.* 1, 263–286.
3906
3907
3908 1375 Debenedetti, A., 1982. The problem of the origin of the salt deposits in the mediterranean and of
3909
3910 1376 their relations to the other salt occurrences in the neogene formations of the contiguous
3911
3912 1377 regions. *Mar. Geol.* 49, 91–114.
3913
3914 1378 Dela Pierre, F., Clari, P., Natalicchio, M., Ferrando, S., Giustetto, R., Lozar, F., Lugli, S., Manzi,

3921
3922
3923 1379 V., Roveri, M., Violanti, D., 2014. Flocculent layers and bacterial mats in the mudstone
3924
3925 1380 interbeds of the Primary Lower Gypsum unit (Tertiary Piedmont basin, NW Italy): Archives
3926
3927
3928 1381 of palaeoenvironmental changes during the Messinian salinity crisis. *Mar. Geol.* 355, 71–
3929
3930 1382 87. doi:10.1016/j.margeo.2014.05.010
3931
3932 1383 Derin, B., 2000. Stratigraphic and environments of deposition of Or South 1075–2090 m. Ramat
3933
3934 1384 Gan, Derin Consulting & Micropaleontological Services LTD, Internal Isramco Consultant
3935
3936 1385 Report 2/00.
3937
3938 1386 Ditlevsen, P.D., Andersen, K.K., Svensson, A., 2007. The DO-climate events are probably noise
3939
3940 1387 induced: Statistical investigation of the claimed 1470 years cycle. *Clim. Past* 3, 129–134.
3941
3942 1388 doi:10.5194/cp-3-129-2007
3943
3944 1389 Driussi, O., Maillard, A., Ochoa, D., Lofi, J., Chanier, F., Gaullier, V., Briaais, A., Sage, F.,
3945
3946 1390 Sierrro, F., Garcia, M., 2015. Messinian Salinity Crisis deposits widespread over the
3947
3948 1391 Balearic Promontory: Insights from new high-resolution seismic data. *Mar. Pet. Geol.* 66,
3949
3950 1392 41–54. doi:10.1016/j.marpetgeo.2014.09.008
3951
3952 1393 Druckman, Y., Buchbinder, B., Martinotti, G.M., Tov, R.S., Aharon, P., 1995. The buried Afik
3953
3954 1394 Canyon (eastern Mediterranean, Israel): a case study of a Tertiary submarine canyon
3955
3956 1395 exposed in Late Messinian times. *Mar. Geol.* 123, 167–185. doi:10.1016/0025-
3957
3958 1396 3227(94)00127-7
3959
3960 1397 Ensminger, A., Joly, G., Albrecht, P., 1978. Rearranged steranes in sediments and crude oils.
3961
3962 1398 *Tetrahedron Letters.* 1575–1578. doi:https://doi.org/10.1016/S0040-4039(01)94608-8
3963
3964 1399 Feng, Y.E., Yankelzon, A., Steinberg, J., Reshef, M., 2016. Lithology and characteristics of the
3965
3966 1400 Messinian evaporite sequence of the deep Levant Basin, Eastern Mediterranean. *Mar. Geol.*
3967
3968 1401 376, 118–131. doi:10.1016/j.margeo.2016.04.004
3969
3970
3971
3972
3973
3974
3975
3976

3977
3978
3979 1402 Flecker, R., Ellam, R.M., 2006. Identifying Late Miocene episodes of connection and isolation in
3980 the Mediterranean-Paratethyan realm using Sr isotopes. *Sediment. Geol.* 188–189, 189–203.
3981 1403 doi:10.1016/j.sedgeo.2006.03.005
3982
3983
3984 1404
3985
3986 1405 Flecker, R., et al., 2015. Evolution of the Late Miocene Mediterranean-Atlantic gateways and
3987 their impact on regional and global environmental change. *Earth-Science Reviews*, 150,
3988 1406 365–392.
3989
3990 1407
3991
3992 1408 Frey-Martinez, J., Hall, B., Cartwright, J., Huuse, M., 2007. Clastic Intrusion at the Base of
3993 Deep-water Sands: A Trap-forming Mechanism in the Eastern Mediterranean. *Sand Inject.*
3994 1409 *Implic. Hydrocarb. Explor. Prod. AAPG Mem.* 87 49–63. doi:10.1306/1209849M873255
3995
3996 1410
3997
3998 1411 Garcia-Castellanos, D., Villaseñor, A., 2011. Messinian salinity crisis regulated by competing
4000 tectonics and erosion at the Gibraltar arc. *Nature* 480, 359–363. doi:10.1038/nature10651
4001 1412
4002
4003 1413 García-Veigas, J., Cendón, D.I., Gibert, L., Lowenstein, T.K., Artiaga, D., 2018. Geochemical
4004 indicators in Western Mediterranean Messinian evaporites: Implications for the salinity
4005 1414 crisis. *Mar. Geol.* 403, 197–214. doi:10.1016/j.margeo.2018.06.005
4006
4007 1415
4008
4009 1416 Gardosh, M., Druckman, Y., Buchbinder, B., Rybakov, M., 2008. The Levant Basin Offshore
4010 Israel: Stratigraphy, Structure, Tectonic Evolution and Implications for Hydrocarbon
4011 1417 Exploration - revised edition. Geological Survey of Israel report GSI/4/2008.
4012
4013 1418
4014
4015
4016 1419 Garrison, R.E., Schreiber, B.C., Bernoulli, D., Fabricius, F.H., Kidd, R.B., Mélières, F., 1978.
4017 Sedimentary Petrology and Structures of Messinian Evaporitic Sediments in the
4018 1420 Mediterranean Sea, Leg 42A, Deep Sea Drilling Project, in: *Initial Reports of the Deep Sea*
4019 Drilling Project 42, No. 1. pp. 571–612.
4020 1421
4021
4022 1422
4023
4024
4025 1423 Geletti, R., Zgur, F., Del Ben, A., Buriola, F., Fais, S., Fedi, M., Forte, E., Mocnik, A., Paoletti,
4026 V., Pipan, M., Ramella, R., Romeo, R., Romi, A., 2014. The Messinian Salinity Crisis: New
4027 1424
4028
4029
4030
4031
4032

4033
4034
4035 1425 seismic evidence in the West-Sardinian Margin and Eastern Sardo-Provencal basin (West
4036
4037 1426 Mediterranean Sea). *Mar. Geol.* 351, 76–90. doi:10.1016/j.margeo.2014.03.019
4038
4039
4040 1427 Gennari, R., Manzi, V., Angeletti, L., Bertini, A., Ceregato, A., Faranda, C., Gliozzi, E.,
4041
4042 1428 Menichetti, E., Rosso, A., Roveri, M., Taviani, M., 2013. A shallow water record of the
4043
4044 1429 onset of the Messinian salinity crisis in the Adriatic foredeep (Legnagnone section,
4045
4046 1430 Northern Apennines). *NU SC. Palaeogeogr. Palaeoclimatol. Palaeoecol.*
4047
4048 1431 doi:10.1016/j.palaeo.2013.05.015
4049
4050 1432 Govers, R., 2009. Choking the Mediterranean to dehydration: The Messinian salinity crisis.
4051
4052 1433 *Geology* 37, 167–170. doi:10.1130/G25141A.1
4053
4054 1434 Gvirtzman, Z., Manzi, V., Calvo, R., Gavrieli, I., Gennari, R., Lugli, S., Reghizzi, M., Roveri,
4055
4056 1435 M., 2017. Intra-Messinian truncation surface in the Levant Basin explained by subaqueous
4057
4058 1436 dissolution. *Geology* 45, 4–7. doi:10.1130/G39113.1
4059
4060
4061 1437 Gvirtzman, Z., Reshef, M., Buch-leviatan, O., Ben-avraham, Z., 2013a. Intense salt deformation
4062
4063 1438 in the Levant Basin in the middle of the Messinian Salinity Crisis. *Earth Planet. Sci. Lett.*
4064
4065 1439 379, 108–119. doi:10.1016/j.epsl.2013.07.018
4066
4067 1440 Gvirtzman, Z., Reshef, M., Buch-Leviatan, O., Ben-Avraham, Z., 2013b. Intense salt
4068
4069 1441 deformation in the Levant Basin in the middle of the Messinian Salinity Crisis. *Earth Planet.*
4070
4071 1442 *Sci. Lett.* 379, 108–119. doi:10.1016/j.epsl.2013.07.018
4072
4073
4074 1443 Hall, J.K., Udintsev, G.B., Odnikov, Y.Y., 1994. The bottom relief of the Levantine Sea, in
4075
4076 1444 *Geologic Structure of the Northeastern Mediterranean*. Krashennnikov, V. A., Hall, J.K.,
4077
4078 1445 pp. 5–32, Historical Productions-Hall Ltd., Jerusalem.
4079
4080 1446 Hall, J.K., Lippman, S., Gardosh, M., Tibor, G., Sade, A.R., Sade, H., 2015. A New Bathymetric
4081
4082 1447 Map for the Israeli EEZ: Preliminary Results. State of Israel, Ministry of National
4083
4084
4085
4086
4087
4088

4089
4090
4091 1448 Infrastructure Energy and Water, Jerusalem.
4092
4093 1449 Hardie, L.A., Lowenstein, T.K., 2004. Did the Mediterranean Sea Dry Out During the Miocene?
4094
4095 a Reassessment of the Evaporite Evidence From Dsdp Legs 13 and 42a Cores. *J. Sediment.*
4096 1450
4097
4098 1451 *Res.* 74, 453–461. doi:10.1306/112003740453
4099
4100 1452 Hawie, N., Deschamps, R., Nader, F.H., Gorini, C., 2013a. Sedimentological and stratigraphic
4101
4102 1453 evolution of northern Lebanon since the Late Cretaceous: implications for the Levant
4103
4104 1454 margin and basin. doi:10.1007/s12517-013-0914-5
4105
4106 1455 Hawie, N., Gorini, C., Deschamps, R., Nader, F.H., Montadert, L., Granjeon, D., Baudin, F.,
4107
4108 1456 2013b. Tectono-stratigraphic evolution of the northern Levant Basin (offshore Lebanon).
4109
4110 1457 *Mar. Pet. Geol.* 48, 392–410. doi:10.1016/j.marpetgeo.2013.08.004
4111
4112
4113 1458 Hernández-Molina F.J, et al., 2014. Onset of Mediterranean outflow into the North Atlantic.
4114
4115 1459 *Science* 344, 1244–1250. doi: 10.1126/science.1251306
4116
4117 1460 Hilgen, F., Kuiper, K., Krijgsman, W., Snel, E., Laan, E. Van Der, van der Laan, E., 2007.
4118
4119 1461 Astronomical tuning as the basis for high resolution chronostratigraphy: The intricate
4120
4121 1462 history of the Messinian Salinity Crisis. *Stratigraphy* 4, 231–238.
4122
4123 1463 Hilgen, F.J., Bissoli, L., Iaccarino, S., Krijgsman, W., Meijer, R., Negri, A., Villa, G., 2000.
4124
4125 1464 Integrated stratigraphy and astrochronology of the Messinian GSSP at Oued Akrech
4126
4127 1465 (Atlantic Morocco). *Earth Planet. Sci. Lett.* 182, 237–251. doi:10.1016/S0012-
4128
4129 1466 821X(00)00247-8
4130
4131
4132 1467 Hilgen, F.J., Krijgsman, W., 1999. Cyclostratigraphy and astrochronology of the Tripoli
4133
4134 1468 diatomite formation (pre-evaporite Messinian, Sicily, Italy). *Terra Nov.* 11, 16–22.
4135
4136 1469 doi:10.1046/j.1365-3121.1999.00221.x
4137
4138 1470 Hilgen, F.J., Krijgsman, W., Langereis, C.G., Lourens, L.J., Santarelli, A., Zachariasse, W.J.,
4139
4140
4141
4142
4143
4144

4145
4146
4147 1471 1995. Extending the astronomical (polarity) time scale into the Miocene. *Earth Planet. Sci.*
4148
4149
4150 1472 *Lett.* 136, 495–510. doi:10.1016/0012-821X(95)00207-S
4151
4152 1473 Hsü, K.J., 1973. The desiccated deep-basin model for the Messinian events, in: Drooger, C.W.
4153
4154 1474 (Ed.), *Messinian Events in the Mediterranean*. North-Holland Publ. Co., Amsterdam, pp.
4155
4156 1475 60–67.
4157
4158 1476 Hsü, K. J., Ryan, W.B.F., Schreiber, B.C., 1973. Petrography of a halite sample from hole 134 -
4159
4160 1477 balearic abyssal plain, in: *Initial Reports of the Deep Sea Drilling Project 13, No. Part 2*. pp.
4161
4162 1478 708–711.
4163
4164
4165 1479 Hsü, K.J., Montadert, L., Bernoulli, D., Bizon, G., Cita, M., Erickson, A., Fabricius, F., Garrison,
4166
4167 1480 R.E., Kidd, R.B., Mélières, F., Müller, C., Wright, R.C., 1978a. Site 374: Messina Abyssal
4168
4169 1481 Plain, in: *Initial Reports of the Deep Sea Drilling Project: DSDP Volume XLII Part 1*. p. 43.
4170
4171 1482 doi:10.2973/dsdp.proc.42-1.105.1978
4172
4173
4174 1483 Hsü, K.J., Montadert, L., Bernoulli, D., Bizon, G., Cita, M., Erickson, A., Fabricius, F., Garrison,
4175
4176 1484 R.E., Kidd, R.B., Mélières, F., Müller, C., Wright, R.C., 1978b. Sites 375 and 376: Florence
4177
4178 1485 Rise, in: *Initial Reports of the Deep Sea Drilling Project: DSDP Volume XLII Part 1*. p. 86.
4179
4180 1486 Hüsing, S.K., Cascella, A., Hilgen, F.J., Krijgsman, W., Kuiper, K.F., Turco, E., Wilson, D.,
4181
4182 1487 2010. Astrochronology of the Mediterranean Langhian between 15 . 29 and 14 . 17 Ma.
4183
4184 1488 *Earth Planet. Sci. Lett.* 290, 254–269. doi:10.1016/j.epsl.2009.12.002
4185
4186 1489 Hüsing, S.K., Kuiper, K.F., Link, W., Hilgen, F.J., Krijgsman, W., 2009. The upper Tortonian-
4188
4189 1490 lower Messinian at Monte dei Corvi (Northern Apennines, Italy): Completing a
4190
4191 1491 Mediterranean reference section for the Tortonian Stage. *Earth Planet. Sci. Lett.* 282, 140–
4192
4193 1492 157. doi:10.1016/j.epsl.2009.03.010
4194
4195 1493 Karakitsios, V., Cornée, J.J., Tsourou, T., Moissette, P., Kontakiotis, G., Agiadi, K.,
4196
4197
4198
4199
4200

4201
4202
4203 1494 Manoutsoglou, E., Triantaphyllou, M., Koskeridou, E., Drinia, H., Roussos, D., 2017.
4204
4205 1495 Messinian salinity crisis record under strong freshwater input in marginal, intermediate, and
4206
4207 deep environments: The case of the North Aegean. *Palaeogeogr. Palaeoclimatol.*
4208 1496
4209
4210 1497 *Palaeoecol.* 485, 316–335. doi:10.1016/j.palaeo.2017.06.023
4211
4212 1498 Keogh, S.M., Butler, R.W.H., 1999. The Mediterranean water body in the late Messinian:
4213
4214 1499 interpreting the record from marginal basins on Sicily. *J. Geol. Soc. London.* 156, 837–846.
4215
4216 doi:10.1144/gsjgs.156.4.0837
4217 1500
4218
4219 1501 Krijgsman, W., Blanc-Valleron, M.M., Flecker, R., Hilgen, F.J., Kouwenhoven, T.J., Merle, D.,
4220
4221 1502 Orszag-Sperber, F., Rouchy, J.M., 2002. The onset of the Messinian salinity crisis in the
4222
4223 1503 Eastern Mediterranean (Pissouri Basin, Cyprus). *Earth Planet. Sci. Lett.* 194, 299–310.
4224
4225 doi:10.1016/S0012-821X(01)00574-X
4226 1504
4227
4228 1505 Krijgsman, W., Fortuin, A.R., Hilgen, F.J., Sierro, F.J., 2001. Astrochronology for the Messinian
4229
4230 1506 Sorbas basin (SE Spain) and orbital (precessional) forcing for evaporite cyclicity. *Sediment.*
4231
4232 1507 *Geol.* 140, 43–60. doi:10.1016/S0037-0738(00)00171-8
4233
4234 1508 Krijgsman, W., Garces, M., Agusti, J., Raffi, I., Taberner, C., Zachariasse, W.J., 2000. The
4235
4236 1509 “Tortonian salinity crisis” of the eastern Betics (Spain). *Earth Planet. Sci. Lett.* 181, 497–
4237
4238 1510 511. doi:10.1016/S0012-821X(00)00224-7
4239
4240 1511 Krijgsman, W., Hilgen, F.J., Negri, A., Wijbrans, J.R., Zachariasse, W.J., 1997. The Monte del
4241
4242 1512 Casino section (Northern Apennines, Italy): A potential Tortonian/Messinian boundary
4243
4244 1513 stratotype? *Palaeogeogr. Palaeoclimatol. Palaeoecol.* 133, 27–47. doi:10.1016/S0031-
4245
4246 1514 0182(97)00039-4
4247
4248
4249 1515 Krijgsman, W., Hilgen, F.J., Raffi, I., Sierro, F.J., Wilson, D.S., 1999. Chronology, causes and
4250
4251 1516 progression of the Messinian salinity crisis. *Nature* 400, 652–655. doi:10.1038/23231.
4252
4253
4254
4255
4256

4257
4258
4259 1517 Krijgsman, W., Meijer, P.T., 2008. Depositional environments of the Mediterranean “Lower
4260
4261 1518 Evaporites” of the Messinian salinity crisis: Constraints from quantitative analyses. *Mar.*
4262
4263
4264 1519 *Geol.* doi:10.1016/j.margeo.2008.04.010
4265
4266 1520 Krijgsman, W., Stoica, M., Vasiliev, I., Popov, V. V., 2010. Rise and fall of the Paratethys Sea
4267
4268 1521 during the Messinian Salinity Crisis. *Earth Planet. Sci. Lett.* 290, 183–191.
4269
4270 1522 doi:10.1016/j.epsl.2009.12.020.
4271
4272
4273 1523 Lange, G.J. De, Krijgsman, W., 2010. Messinian salinity crisis: A novel unifying shallow
4274
4275 1524 gypsum / deep dolomite formation mechanism. *Mar. Geol.* 275, 273–277.
4276
4277 1525 doi:10.1016/j.margeo.2010.05.003
4278
4279 1526 Laskar, J., Robutel, P., Joutel, F., Gastineau, M., Correia, A.C.M., Levrard, B., 2004. A long-
4280
4281 1527 term numerical solution for the insolation quantities of the Earth. *Astron. As-trophys.*
4282
4283 1528 *Astron. Astrophys.* 428, 261–285. doi:10.1051/0004-6361:20041335
4284
4285 1529 Leila, M., Kora, M.A., Ahmed, M.A., Ghanem, A., 2016. Sedimentology and reservoir
4286
4287 1530 characterization of the Upper Miocene Qawasim Formation, El-Tamad Oil Field onshore
4288
4289 1531 Nile Delta, Egypt. *Arab. J. Geosci.* 9, 1–13. doi:10.1007/s12517-015-2088-9
4290
4291
4292 1532 Lofi, J., Camerlenghi, A., 2014. Messinian Salinity Crisis - DREAM (Deep-sea Record of
4293
4294 1533 Mediterranean Messinian events) drilling projects Messinian Salinity Crisis - DREAM
4295
4296 1534 (Deep-sea Record of Mediterranean Messinian events) drilling projects, in: EGU. Vienna, p.
4297
4298 1535 1.
4299
4300 1536 Lofi, J., Sage, F., Deverchere, J., Loncke, L., Maillard, A., Gaullier, V., Thion, I., Gillet, H.,
4301
4302 1537 Guennoc, P., Gorini, C., 2011. Refining our knowledge of the Messinian salinity crisis
4303
4304 1538 records in the offshore domain through multi-site seismic analysis. *Bull. la Soc. Geol. Fr.*
4305
4306 1539 182, 163–180. doi:10.2113/gssgfbull.182.2.163
4307
4308
4309
4310
4311
4312

4313
4314
4315 1540 Lohmann, J., Ditlevsen, P.D., 2018. Random and externally controlled occurrences of
4316
4317 1541 Dansgaard-Oeschger events. *Clim. Past* 14, 609–617. doi:10.5194/cp-14-609-2018
4318
4319 1542 Lugli, S., Gennari, R., Gvirtzman, Z., Manzi, V., Roveri, M., Schreiber, B.C., 2013. Evidence of
4320
4321 clastic evaporites in the canyons of the Levant Basin (Israel): implications for the Messinian
4322 1543 Salinity Crisis. *J. Sediment. Res.* 83, 942–954. doi:10.2110/jsr.2013.72
4323
4324 1544
4325
4326 1545 Lugli, S., Manzi, V., Roveri, M., Schreiber, B.C., 2015. The deep record of the Messinian
4327
4328 1546 salinity crisis: Evidence of a non-desiccated Mediterranean Sea. *Palaeogeogr.*
4329
4330 1547 *Palaeoclimatol. Palaeoecol.* 433, 201–218. doi:10.1016/j.palaeo.2015.05.017
4331
4332 1548 Lugli, S., Schreiber, B.C., Triberti, B., 1999. Giant polygons in the Realmonte Mine (Agrigento,
4333
4334 1549 Sicily); evidence for the desiccation of a Messinian halite basin. *J. Sediment. Res.* 69, 764–
4335
4336 1550 771. doi:10.2110/jsr.69.764
4337
4338
4339 1551 McArthur, J. M., Howarth, R. J., Shield, G. A., 2012. Chapter 7: Strontium Isotope Stratigraphy.
4340
4341 1552 In *The Geologic Time Scale*, eds. F. M. Gredstein, J. G. Ogg, M. D. Schmotz & G. M. Ogg,
4342
4343 1553 1144 Elsevier.
4344
4345 1554 Madof, A.S., Bertoni, C., Lofi, J., 2019. Discovery of vast fluvial deposits provides evidence for
4346
4347 1555 drawdown during the late Miocene Messinian salinity crisis. *Geology* 47, 171–174.
4348
4349 1556 doi:10.1130/G45873.1
4350
4351 1557 Manzi, V., Gennari, R., Hilgen, F., Krijgsman, W., Lugli, S., 2013. Age refinement of the
4352
4353 1558 Messinian salinity crisis onset in the Mediterranean. doi:10.1111/ter.12038
4354
4355
4356 1559 Manzi, V., Gennari, R., Lugli, S., Persico, D., Reghizzi, M., Roveri, M., Schreiber, B.C., Calvo,
4357
4358 1560 R., Gavrieli, I., Gvirtzman, Z., 2018. The onset of the Messinian salinity crisis in the deep
4359
4360 1561 Eastern Mediterranean basin. *Terra Nov.* 38, 42–49. doi:10.1111/ter.12325
4361
4362 1562 Manzi, V., Gennari, R., Lugli, S., Roveri, M., Scafetta, N., Charlotte, B., 2012. High-frequency
4363
4364
4365
4366
4367
4368

4369
4370
4371 1563 cyclicality in the Mediterranean Messinian evaporites: evidence for solar-lunar climate
4372
4373 forcing. *J. Sediment. Res.* 82, 991–1005. doi:10.2110/jsr.2012.81
4374 1564
4375
4376 1565 Manzi, V., Lugli, S., Roveri, M., Dela Pierre, F., Gennari, R., Lozar, F., Natalicchio, M.,
4377
4378 1566 Schreiber, B.C., Taviani, M., Turco, E., 2015. The Messinian salinity crisis in Cyprus: A
4379
4380 1567 further step towards a new stratigraphic framework for Eastern Mediterranean. *Basin Res.*
4381
4382 1568 28, 207–236. doi:10.1111/bre.12107
4383
4384 1569 Manzi, V., Lugli, S., Roveri, M., Schreiber, B.C., 2009. A new facies model for the Upper
4385
4386 1570 Gypsum of Sicily (Italy): Chronological and palaeoenvironmental constraints for the
4387
4388 1571 Messinian salinity crisis in the Mediterranean. *Sedimentology* 56, 1937–1960.
4389
4390 1572 doi:10.1111/j.1365-3091.2009.01063.x
4391
4392
4393 1573 Manzi, V., Lugli, S., Roveri, M., Schreiber, B.C., Gennari, R., 2011. The Messinian “Calcare di
4394
4395 1574 Base” (Sicily, Italy) revisited. *Bull. Geol. Soc. Am.* 123, 347–370. doi:10.1130/B30262.1
4396
4397 1575 Marzocchi, A., Lunt, D.J., Flecker, R., Bradshaw, C.D., Farnsworth, A., Hilgen, F.J., 2015.
4398
4399 1576 Orbital control on late Miocene climate and the North African monsoon: Insight from an
4400
4401 1577 ensemble of sub-precessional simulations. *Clim. Past* 11, 1271–1295. doi:10.5194/cp-11-
4402
4403 1578 1271-2015
4404
4405 1579 Meilijson, A., Ashckenazi-Polivoda, S., Ron-Yankovich, L., Illner, P., Alsenz, H., Speijer, R.P.,
4406
4407 1580 Almogi-Labin, A., Feinstein, S., Berner, Z., Püttmann, W., Abramovich, S., 2014.
4408
4409 1581 Chronostratigraphy of the Upper Cretaceous high productivity sequence of the southern
4410
4411 1582 Tethys, Israel. *Cretac. Res.* 50. doi:10.1016/j.cretres.2014.04.006
4412
4413
4414 1583 Meilijson, A., Steinberg, J., Hilgen, F., Bialik, O.M., Waldmann, N.D., Makovsky, Y., 2018.
4415
4416 1584 Deep-basin evidence resolves a 50-year-old debate and demonstrates synchronous onset of
4417
4418 1585 Messinian evaporite deposition in a non-desiccated Mediterranean. *Geology* 46, 4–7.
4419
4420
4421
4422
4423
4424

4425
4426
4427 1586 Müller, D.W., Mueller, P.A., 1991. Origin and age of the Mediterranean Messinian evaporites:
4428
4429 1587 implications from Sr isotopes. *Earth Planet. Sci. Lett.* doi:10.1016/0012-821X(91)90039-K
4430
4431
4432 1588 Nam, M., Görür, N., Flecker, R., Sak, M., Tüno, C., Ellam, R., Krijgsman, W., Vincent, S.,
4433
4434 1589 Dikba, A., 2006. Paratethyan–Mediterranean connectivity in the Sea of Marmara region
4435
4436 1590 (NW Turkey) during the Messinian. *Sediment. geo* 188–189, 171–187.
4437
4438 1591 doi:10.1016/j.sedgeo.2006.03.004
4439
4440 1592 Netzeband, G.L., Hübscher, C.P., Gajewski, D., 2006. The structural evolution of the Messinian
4441
4442 1593 evaporites in the Levantine Basin. *Mar. Geol.* 230, 249–273.
4443
4444 1594 doi:10.1016/j.margeo.2006.05.004
4445
4446 1595 Ochoa, D., Sierro, F.J., Lofi, J., Maillard, A., Flores, J.A., Suarez, M., 2015. Synchronous onset
4447
4448 1596 of the Messinian evaporite precipitation: First Mediterranean offshore evidence. *Earth*
4449
4450 1597 *Planet. Sci. Lett.* 427, 112–124. doi:10.1016/j.epsl.2015.06.059
4451
4452 1598 Ogniben, L., 1957. Petrografia della Serie Solfifera Siciliana e considerazioni geologiche
4453
4454 1599 relative. *Memorie Descrittive della Carta Geologica d'Italia* 33, 1–275.
4455
4456 1600 Ohneiser, C., Florindo, F., Stocchi, P., Roberts, A.P., DeConto, R.M., Pollard, D., 2015.
4457
4458 1601 Antarctic glacio-eustatic contributions to late Miocene Mediterranean desiccation and
4459
4460 1602 reflooding. *Nat. Commun.* 6, 8765. doi:10.1038/ncomms9765
4461
4462 1603 Peters, K.E., A.E. Kontorovich, J.M.M., 1993. Geochemistry of selected oils and rocks from the
4463
4464 1604 central portion of the west Siberian Basin, Russia. *Am. Assoc. Pet. Geol. Bull.* 77, 87–863.
4465
4466 1605 Peters, K.E., 1986. Guidelines for Evaluating Petroleum Source Rock Using Programmed
4467
4468 1606 Pyrolysis. *Am. Assoc. Pet. Geol. Bull.* 70, 318–329. doi:10.1306/94885688-1704-11D7-
4469
4470 1607 8645000102C1865D
4471
4472 1608 Peters, K.E., Rohrback, B.G., Kaplan, I.R., 1980. Laboratory-simulated thermal maturation of
4473
4474
4475
4476
4477
4478
4479
4480

4481
4482
4483 1609 Recent sediments. *Phys. Chem. Earth* 12, 547–557. doi:10.1016/0079-1946(79)90136-8
4484
4485 1610 Peters, K.E., Walters Clifford C, Moldowan, J.M., 2005. *The Biomarker Guide, Biomarkers and*
4486
4487
4488 1611 *Isotopes in Petroleum Exploration and Earth History, Volume 2.* Cambridge.
4489
4490 1612 doi:10.1017/s0016756806212056
4491
4492 1613 Rashid, H., Grosjean, E., 2006. Detecting the source of Heinrich layers: An organic geochemical
4493
4494 1614 study. *Paleoceanography* 21. doi:10.1029/2005PA001240
4495
4496 1615 Reiche, S., Hübscher, C., Beitz, M., 2014. Fault-controlled evaporite deformation in the Levant
4497
4498 1616 Basin, Eastern Mediterranean. *Mar. Geol.* 354, 53–68. doi:10.1016/j.margeo.2014.05.002
4499
4500 1617 Richter-Bernburg, G., 1996. Zechstein-Anhydrite: Fazies und Genese, *Geologisches Jahrbuch.*
4501
4502 1618 Reihe A, Allgemeine und regionale Geologie Bundesrepublik Deutschland und
4503
4504 1619 Nachbargebiete, Tektonik, Stratigraphie, Paläontologie. Bundesanstalt für
4505
4506 1620 Geowissenschaften und Rohstoffe.
4507
4508
4509 1621 Roberts, G., Peace, D., 2007. Hydrocarbon plays and prospectivity of the Levantine basin,
4510
4511 1622 offshore Lebanon and Syria from modern seismic data. *GeoArabia* 12, 99–124.
4512
4513 1623 Rouchy, J.M., Caruso, A., 2006. The Messinian salinity crisis in the Mediterranean basin : A
4514
4515 1624 reassessment of the data and an integrated scenario. *Sediment. Geol.* 188–189, 35–67.
4516
4517 1625 doi:10.1016/j.sedgeo.2006.02.005
4518
4519 1626 Roveri, M., Flecker, R., Krijgsman, W., Lofi, J., Lugli, S., Manzi, V., Sierro, F.J., Bertini, A.,
4520
4521 1627 Camerlenghi, A., De Lange, G., Govers, R., Hilgen, F.J., Hübscher, C., Meijer, P.T., Stoica,
4522
4523 1628 M., 2014a. The Messinian Salinity Crisis: Past and future of a great challenge for marine
4524
4525 1629 sciences. *Mar. Geol.* 352, 25–58. doi:10.1016/j.margeo.2014.02.002
4526
4527
4528 1630 Roveri, M., Gennari, R., Ligi, M., Lugli, S., Manzi, V., Reghizzi, M., 2019. The synthetic
4529
4530 1631 seismic expression of the Messinian salinity crisis from onshore records: implications for
4531
4532
4533
4534
4535
4536

4537
4538
4539 1632 shallow- to deep-water correlations. *Basin Res.* doi:10.1111/bre.12361
4540
4541
4542 1633 Roveri, M., Lugli, S., Manzi, V., Gennari, R., Schreiber, B.C., 2014b. High-resolution strontium
4543
4544 1634 isotope stratigraphy of the messinian deep Mediterranean basins: Implications for marginal
4545
4546 1635 to central basins correlation. *Mar. Geol.* 349, 113–125. doi:10.1016/j.margeo.2014.01.002
4547
4548 1636 Roveri, M., Manzi, V., Bergamasco, A., Falcieri, F.M., Gennari, R., Lugli, S., Schreiber, B.C.,
4549
4550 1637 2014c. Dense shelf water cascading and messinian canyons: A new scenario for the
4551
4552 1638 mediterranean salinity crisis. *Am. J. Sci.* 314, 751–784. doi:10.2475/05.2014.03
4553
4554
4555 1639 Rullkötter, J., R.M., 1988. Natural and artificial maturation of biological markers in a Toarcian
4556
4557 1640 shale from northern Germany, in: Novelli, L.M. and L. (Ed.), *Advances in Organic*
4558
4559 1641 *Geochemistry* 1987. Oxford Pergamon Press, pp. 639–645.
4560
4561 1642 Ryan, W.B.F., 2011. Geodynamic responses to a two-step model of the Messinian salinity crisis.
4562
4563 1643 *Bull. la Soc. Geol. Fr.* 182, 73–78. doi:10.2113/gssgfbull.182.2.73
4564
4565 1644 Ryan, W.B.F., 2008. Modeling the magnitude and timing of evaporative drawdown during the
4566
4567 1645 Messinian salinity crisis. *Stratigraphy* 5, 227–243.
4568
4569
4570 1646 Ryan, W.B.F., 1978. Messinian badlands on the southeastern margin of the Mediterranean Sea.
4571
4572 1647 *Mar. Geol.* 27, 349–363. doi:10.1016/0025-3227(78)90039-7
4573
4574 1648 Ryan, W.B.F., 1976. Quantitative evaluation of the depth of the western Mediterranean before,
4575
4576 1649 during and after the late Miocene salinity crisis. *Sedimentology* 23, 791–813.
4577
4578
4579 1650 Ryan, W.B.F., 1973. Geodynamic implications of the Messinian crisis of salinity, in: Drooger,
4580
4581 1651 D.W. (Ed.), *Messinian Events in the Mediterranean*. Elsevier, Amsterdam, pp. 26–38.
4582
4583 1652 Ryan, W.B.F., Cita, M.B., 1978. The nature and distribution of Messinian erosional surfaces -
4584
4585 1653 Indicators of a several-kilometer-deep Mediterranean in the Miocene. *Mar. Geol.*
4586
4587 1654 doi:10.1016/0025-3227(78)90032-4
4588
4589
4590
4591
4592

4593
4594
4595 1655 Ryan, W.B.F., Hsü, K.J., Cita, M.B., Dumitrica, P., Lort, J., Maync, W., Nesteroff, W.D., Pautot,
4596
4597 G., Stradner, H., 2007. DSDP Volume XIII: 6. Balearic Rise - Site 124. The Shipboard
4598 1656
4599 Scientific Party. doi:10.2973/dsdp.proc.13.1973
4600 1657
4601
4602 1658 Ryan, W.B.F., Stanley, D.J., Hersey, J.B., Fahlquist, D.A., Allan, T.D., 1971. The tectonics and
4603
4604 geology of the Mediterranean Sea. In: Maxwell, A.E. (Ed.), *The Sea*. Wiley- Interscience,
4605 1659
4606 New York, pp. 387–492.
4607 1660
4608
4609 1661 Scafetta, N., Milani, F., Bianchini, A., Ortolani, S., 2016. On the astronomical origin of the
4610
4611 Hallstatt oscillation found in radiocarbon and climate records throughout the Holocene.
4612
4613 Earth-Science Rev. 162, 24–43. doi:10.1016/j.earscirev.2016.09.004
4614 1663
4615 1664 Scalán, E.S., Smith, J.E., 1970. An improved measure of the odd-even predominance in the
4616
4617 normal alkanes of sediment extracts and petroleum. *Geochim. Cosmochim. Acta* 34, 611–
4618 1665
4619 620. doi:10.1016/0016-7037(70)90019-0
4620 1666
4621 1667 Schmalz, R.F., 1969. Deep-Water Evaporite Deposition: A Genetic Model. *Am. Assoc. Pet.*
4622
4623 *Geol. Bull.* 53, 798–823. doi:10.1306/5D25C7FD-16C1-11D7-8645000102C1865D
4624 1668
4625
4626 1669 Schulz, M., 2002. On the 1470-year pacing of Dansgaard-Oeschger warm events.
4627
4628 *Paleoceanography* 17, 4-1-4–9. doi:10.1029/2000PA000571
4629 1670
4630 1671 Schulz, M., Mudelsee, M., 2002. REDFIT: Estimating red-noise spectra directly from unevenly
4631
4632 spaced paleoclimatic time series. *Comput. Geosci.* 28, 421–426. doi:10.1016/S0098-
4633 1672
4634 3004(01)00044-9
4635 1673
4636 1674 Selli, R., 1954. Il Bacino del Metauro. *Giornale di Geologia* 24, 1–294.
4637
4638
4639 1675 Sepúlveda, J., Wendler, J.E., Summons, R.E., Hinrichs, K.U., 2009. Rapid Resurgence of Marine
4640
4641 Productivity After the Cretaceous-Paleogene Mass Extinction. *Science* (80-.). 326, 129–
4642 1676
4643 132.
4644 1677
4645
4646
4647
4648

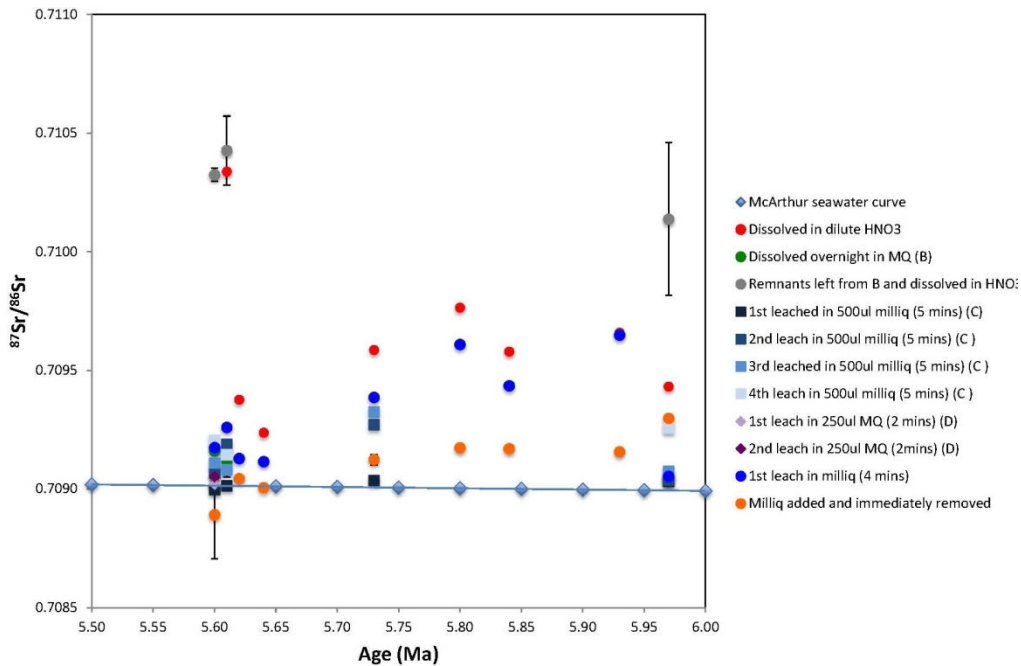
4649
4650
4651 1678 Sierro, F.J., Hilgen, F.J., Krijgsman, W., Flores, J.A., 2001. The Abad composite (SE Spain): A
4652
4653 1679 Messinian reference section for the Mediterranean and the APTS. *Palaeogeogr.*
4654
4655
4656 1680 *Palaeoclimatol. Palaeoecol.* 168, 141–169. doi:10.1016/S0031-0182(00)00253-4
4657
4658 1681 Simon, D., Marzocchi, A., Flecker, R., Lunt, D.J., Hilgen, F.J., Meijer, P.T., 2017. Quantifying
4659
4660 1682 the Mediterranean freshwater budget throughout the late Miocene: New implications for
4661
4662 1683 sapropel formation and the Messinian Salinity Crisis. *Earth Planet. Sci. Lett.* 472, 25–37.
4663
4664 1684 doi:10.1016/j.epsl.2017.05.013
4665
4666 1685 Simon, D., Meijer, P.T., 2017. Salinity stratification of the Mediterranean Sea during the
4667
4668 1686 Messinian crisis: A first model analysis. *Earth Planet. Sci. Lett.* 479, 366–376.
4669
4670 1687 doi:10.1016/j.epsl.2017.09.045
4671
4672
4673 1688 Sirota, I., Ali, A., Lensky, N.G., 2016. Seasonal variations of halite saturation in the Dead Sea.
4674
4675 1689 *Water Resour. Res.* 52. doi:10.1002/2014WR016618
4676
4677 1690 Sirota, I., Enzel, Y., Lensky, N.G., 2017. Temperature seasonality control on modern halite
4678
4679 1691 layers in the Dead Sea: In situ observations. *Bull. Geol. Soc. Am.* 129, 1181–1194.
4680
4681 1692 doi:10.1130/B31661.1
4682
4683 1693 Sonnenfeld, P., Finetti, I., 2011. Messinian Evaporites in the Mediterranean: A Model of
4684
4685 1694 Continuous Inflow and Outflow, in: *Geological Evolution of the Mediterranean Basin.*
4686
4687 1695 doi:10.1007/978-1-4613-8572-1-17
4688
4689
4690 1696 Sonnenfeld, P., Hudec, P.P., 1983. Clay laminations in Halite: Their Cause and Effect, in: *Sixth*
4691
4692 1697 *International Symposium on Salt.* pp. 51–56.
4693
4694 1698 Steinberg, J., Gvirtzman, Z., Folkman, Y., 2010. New age constraints on the evolution of the Mt
4695
4696 1699 Carmel structure and its implications on a Late Miocene extensional phase of the Levant
4697
4698 1700 continental margin. *J. Geol. Soc. London.* 167, 203–216. doi:10.1144/0016-76492009-089
4699
4700
4701
4702
4703
4704

4705
4706
4707 1701 Steinberg, J., Gvirtzman, Z., Folkman, Y., Garfunkel, Z., 2011. Origin and nature of the rapid
4708
4709 1702 late Tertiary filling of the Levant Basin. *Geology* 39, 355–358. doi:10.1130/G31615.1
4710
4711
4712 1703 Steinhilber, F., Abreu, J.A., Beer, J., Brunner, I., Christl, M., Fischer, H., Heikkila, U., Kubik,
4713
4714 1704 P.W., Mann, M., McCracken, K.G., Miller, H., Miyahara, H., Oerter, H., Wilhelms, F.,
4715
4716 1705 2012. 9,400 Years of Cosmic Radiation and Solar Activity From Ice Cores and Tree Rings.
4717
4718 1706 *Proc. Natl. Acad. Sci.* 109, 5967–5971. doi:10.1073/pnas.1118965109
4719
4720 1707 Steinhorn, I., 1983. In situ salt precipitation at the Dead Sea. *Limnol. Oceanogr.* 28, 580–583.
4721
4722 1708 doi:10.4319/lo.1983.28.3.0580
4723
4724 1709 Stiller, M., Gat, J.R., Kaushansky, P., 1997. Halite Precipitation and Sediment Deposition As
4725
4726 1710 Measured in Sediment Traps Deployed in the Dead Sea: 1981-1983. *Dead Sea lake its*
4727
4728 settings 161–170.
4729
4730 1712 Stoica, M., Krijgsman, W., Fortuin, A., Gliozzi, E., 2016. Paratethyan ostracods in the Spanish
4731
4732 Lago-Mare: More evidence for interbasinal exchange at high Mediterranean sea level.
4733 1713
4734 *Palaeogeogr. Palaeoclimatol. Palaeoecol.* 441, 854–870. doi:10.1016/j.palaeo.2015.10.034
4735 1714
4736
4737 1715 ten Haven, H.L., de Leeuw, J.W., Schenck, P.A., 1985. Organic geochemical studies of a
4738
4739 1716 Messinian evaporitic basin, northern Apennines (Italy) I: Hydrocarbon biological markers
4740
4741 1717 for a hypersaline environment. *Geochim. Cosmochim. Acta* 49, 2181–2191.
4742
4743 1718 Tomas, C.R., 1996. *Identifying Marine Phytoplankton*, Academic Press Inc. San Diego.
4744
4745 1719 doi:10.1016/S0025-3227(97)81154-1
4746
4747
4748 1720 Topper, R. P. M., Flecker, R., Meijer, P., Wortel, M. J. R., 2011. A box model of the Late
4749
4750 1721 Miocene Mediterranean Sea: implications from combined $87\text{Sr}/86\text{Sr}$ and salinity data.
4751
4752 1722 *Paleoceanography*, 26.
4753
4754 1723 Topper, R.P.M., Lugli, S., Manzi, V., Roveri, M., Meijer, P.T., 2014. Precessional control of Sr
4755
4756
4757
4758
4759
4760

4761
4762
4763 1724 ratios in marginal basins during the Messinian Salinity Crisis? *Geochemistry, Geophys.*
4764
4765 *Geosystems* 15, 1926–1944. doi:10.1002/2013GC005192
4766 1725
4767
4768 1726 van den Berg, B.C.J., Sierro, F.J., Hilgen, F.J., Flecker, R., Larrasoña, J.C., Krijgsman, W.,
4769
4770 1727 Flores, J.A., Mata, M.P., Bellido Martín, E., Civis, J., González-Delgado, J.A., 2015.
4771
4772 1728 Astronomical tuning for the upper Messinian Spanish Atlantic margin: Disentangling basin
4773
4774 1729 evolution, climate cyclicity and MOW. *Glob. Planet. Change* 135, 89–103.
4775
4776 1730 doi:10.1016/j.gloplacha.2015.10.009
4777
4778 1731 Vasiliev, I., Mezger, E.M., Lugli, S., Reichert, G., Manzi, V., Roveri, M., 2017. How dry was the
4779
4780 1732 Mediterranean during the Messinian salinity crisis ? *Palaeogeogr. Palaeoclimatol.*
4781
4782 *Palaeoecol.* 471, 120–133. doi:10.1016/j.palaeo.2017.01.032
4783 1733
4784
4785 1734
4786
4787
4788
4789
4790
4791
4792
4793
4794
4795
4796
4797
4798
4799
4800
4801
4802
4803
4804
4805
4806
4807
4808
4809
4810
4811
4812
4813
4814
4815
4816

4817
4818
4819
4820
4821
4822
4823
4824
4825
4826
4827
4828
4829
4830
4831
4832
4833
4834
4835
4836
4837
4838
4839
4840
4841
4842
4843
4844
4845
4846
4847
4848
4849
4850
4851
4852
4853
4854
4855
4856
4857
4858
4859
4860
4861
4862
4863
4864
4865
4866
4867
4868
4869
4870
4871
4872

1735 **Supplementary Figures**



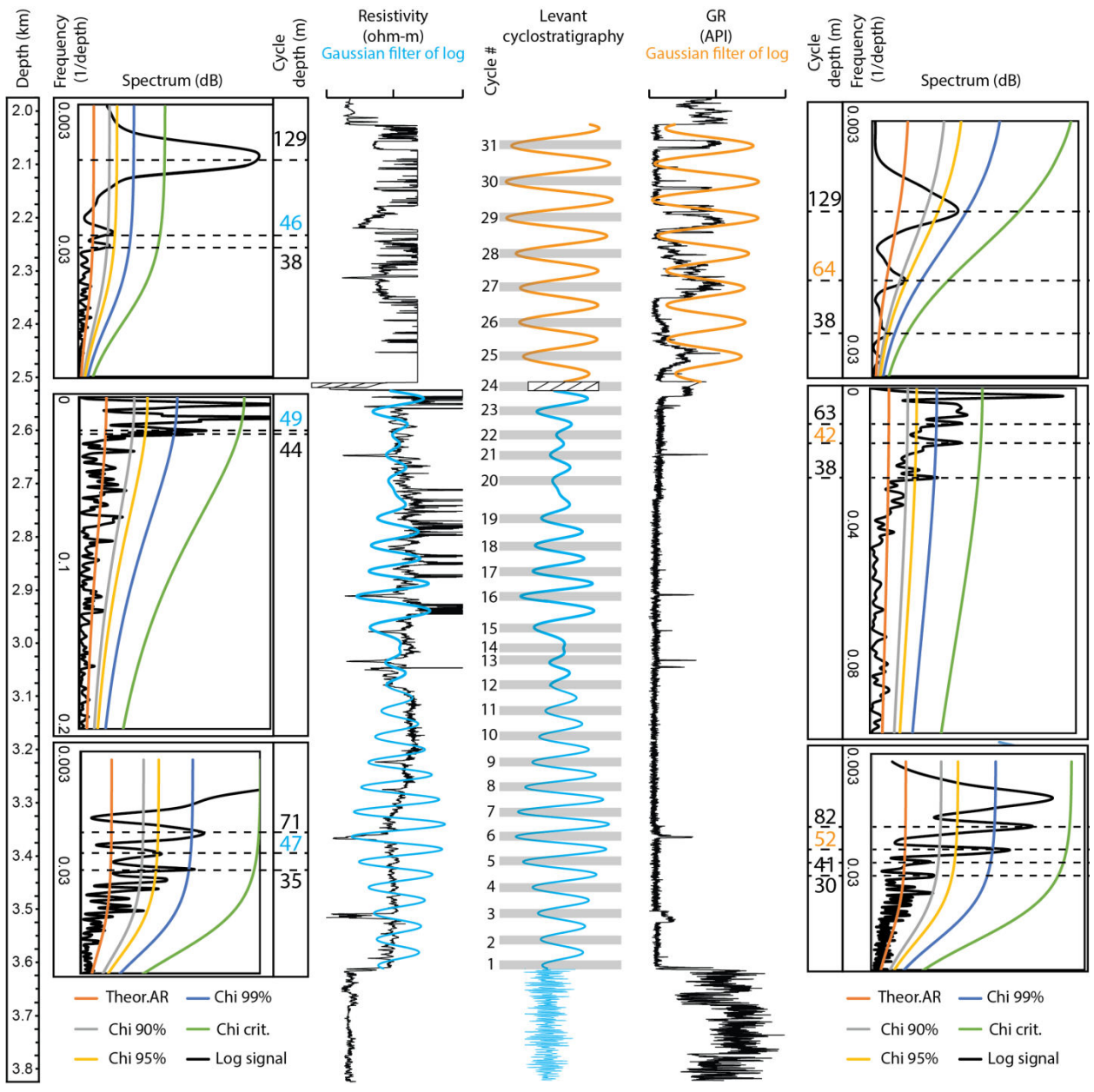
1736

1737 *Figure S1. Strontium stable isotope analysis*

1738 Results obtained by the different protocols used for strontium stable isotope analysis with respect
1739 to the McArthur et al. (2012) seawater curve. Note the large discrepancies between the results
1740 obtained by the different methods used, indicating a highly probable contamination from the
1741 drilling mud used during the retrieval of the halite cuttings samples.

1742

4873
 4874
 4875 1743
 4876
 4877 1744
 4878
 4879
 4880
 4881
 4882
 4883
 4884
 4885
 4886
 4887
 4888
 4889
 4890
 4891
 4892
 4893
 4894
 4895
 4896
 4897
 4898
 4899
 4900
 4901
 4902
 4903
 4904
 4905
 4906
 4907
 4908
 4909
 4910
 4911
 4912
 4913
 4914



1745
 4915 1746
 4916
 4917 1747
 4918 1748
 4919
 4920 1749
 4921 1750
 4922
 4923 1751
 4924
 4925
 4926
 4927
 4928

Figure S2. Spectral analysis of *the Dolphin* well-log curves.

Data shown are the spectral analysis of the resistivity (blue, left) and gamma ray (orange, right) well log curves using REDFIT spectral analysis procedure in Matlab, PAST and Analyseries software. Each log is bounded by respective REDFIT (left of resistivity and right of gamma ray logs) and the combined optimal cyclostratigraphy (center). The REDFIT procedure fits the time series to a red noise model null hypothesis (Theor. AR), produces 'false-alarm' parametric

4929
4930
4931
4932
4933
4934
4935
4936
4937
4938
4939
4940
4941
4942
4943
4944
4945
4946
4947
4948
4949
4950
4951
4952
4953
4954
4955
4956
4957
4958
4959
4960
4961
4962
4963
4964
4965
4966
4967
4968
4969
4970
4971
4972
4973
4974
4975
4976
4977
4978
4979
4980
4981
4982
4983
4984

1752 approximations (chi² of 90%, 95%, and 99%) and a 'critical false-alarm' level (chi crit.). REDFIT
1753 analyses were run by intervals, defined according to the logs expression as follows: from the
1754 base to 3175 m, from 3175 to 2560 m, and from 2560 m to the top of the evaporitic bed.

Chronology with a pinch of salt: integrated stratigraphy of Messinian evaporites in the deep Eastern Mediterranean reveals long-lasting halite deposition during Atlantic connectivity

Aaron Meilijson^{a,b,*}, Frits Hilgen^c, Julio Sepúlveda^b, Josh Steinberg^d, Vanessa Fairbank^e, Rachel Flecker^e, Nicolas D. Waldmann^f, Sarah A. Spaulding^{g,h}, Or M. Bialik^f, F. Garrett Boudinot^b, [Peter Illnerⁱ](#), and Yizhaq Makovsky^{a,f}

^aThe Hatter Department of Marine Technologies, Charney School of Marine Sciences, University of Haifa, Mount Carmel, 31905 Haifa, Israel.

^bOrganic Geochemistry Laboratory, Department of Geological Sciences and Institute of Arctic and Alpine Research (INSTAAR), University of Colorado Boulder, Boulder, Colorado 80309, USA.

^cStratigraphy/Paleontology, Faculty of Geosciences, Utrecht University, Budapestlaan 4, 3584 CD Utrecht, the Netherlands.

^dRatio Oil Exploration, Tel Aviv, Israel.

^eBRIDGE, School of Geographical Sciences, Bristol University, University Road, Bristol BS8 1SS, United Kingdom.

^fThe Dr. Moses Strauss Department of Marine Geosciences, Charney School of Marine Sciences, University of Haifa, Mount Carmel, 31905 Haifa, Israel.

^gInstitute of Arctic and Alpine Research (INSTAAR), University of Colorado Boulder, Boulder Colorado 80309, USA.

^hUnited States Geological Survey, University of Colorado Boulder, Boulder Colorado 80309, USA.

[Institute for Mineralogy and Geochemistry, Karlsruhe University, 76131 Karlsruhe, Germany](#)

*Correspondence to: Dr. Aaron Meilijson email: aaron.meilijson@colorado.edu Tel: +972-505666926

Abstract

The Messinian Salinity Crisis (MSC; 5.97-5.33 Ma) is considered ~~to be~~ an extreme environmental event driven by changes in climate and tectonics, which affected global ocean salinity and shaped the biogeochemical composition of the Mediterranean Sea. Yet, after more than 50 years of research, MSC stratigraphy remains controversial. Recent studies agree that the transition from the underlying pre-evaporite sediments to thick halite deposits is conformal in the deep Eastern Mediterranean basin. However, the age of the base and the duration of halite deposition are still unclear. Also disputed is the nature of the intermediate and upper MSC units, which are characterized as periods of increased clastic deposition into the Eastern Mediterranean based on marginal outcrops and seismic data. We provide a multidisciplinary study of sedimentary, geochemical, and geophysical data from industrial offshore wells in the Levant Basin, which recovered a sedimentary record of deep-basin Mediterranean evaporites deposited during the MSC. In combination with previous observations of the MSC throughout the Mediterranean Basin, our results promote the need for a new chronological model. Remarkably, the one-kilometer-thick lower part of the evaporitic unit is composed of essentially pure halite, ~~other than~~except for a thin transitional anhydrite layer at its base. The halite is undisturbed and homogeneous, lacking diverse features apparent in more proximal sections, indicating a deep-sea depositional environment. We ~~confirm~~find that distinct, meters-thick non-evaporitic intervals interbedded with the halite, previously thought to be clastic layers, are indeed diatomites. While XRD analysis confirms an increase in clastic components in these sediments, they are composed

primarily of well-preserved marine and freshwater planktonic diatoms. The occurrence of marine planktonic diatoms in these intervals indicates the input of Atlantic waters into the Mediterranean Basin during the deposition of the massive halite unit. Seismic [stratigraphy](#) and well-log cyclostratigraphy further support deep basin halite deposition, which started about 300 kyr earlier than widely assumed (~5.97 Ma). We propose that halite deposition in the deep Mediterranean took place during stage 1 of the MSC, rather than being limited to the short 50 kyr MSC acme when sea-level was presumably at its lowest. Thus, brine formation, salt precipitation, and faunal extinction occurred at least in part in a deep, non-desiccated basin, with a restricted yet open Mediterranean-Atlantic connection that allowed inflow of oceanic water. We observe an increase in heavy minerals and reworked fauna within the clastic-evaporitic, Interbedded Evaporites of the basinal MSC section, and argue that these settings correspond in the deep basins with a significant sea-level drawdown during stage 2 of the MSC, as observed in the marginal sections. This correlation is corroborated by astrochronology and chemostratigraphic markers, such as the distribution of *n*-alkanes and biomarker-based thermal maturity indices.

The Levant deposits indicate that high sea-level and partial connectivity with global oceans promoted the deposition of deep-basin deep-water halite, while sea-level drawdown promoted deposition of reworked and transported material from the margins into deep Mediterranean basins. This [review study](#) modifies the current understanding of the mechanisms governing salt deposition throughout the MSC with implications for other evaporitic events in the geologic record.

Keywords: Messinian Salinity Crisis, Mediterranean, deep-basin, evaporites, stratigraphy, sedimentology

Highlights

- After 50 years of research and over 10,000 publications, Messinian Salinity Crisis chronology is still debated
- We analyze a detailed sedimentary and geophysical record from the deep Levant Messinian halite
- Lithological, stratigraphic, and chemical signals indicate precipitation of halite 300 kyr earlier than presumed
- Halite was deposited in a deep-basin deep-water environment synchronously with gypsum deposition ~~in~~on the margins
- Sea-level drawdown during the MSC acme in the Mediterranean promoted the deposition of reworked material in deep basins

Chronology with a pinch of salt: integrated stratigraphy of Messinian evaporites in the deep Eastern Mediterranean reveals long-lasting halite deposition during Atlantic connectivity

Aaron Meilijson^{a,b,*}, Frits Hilgen^c, Julio Sepúlveda^b, Josh Steinberg^d, Vanessa Fairbank^e, Rachel Flecker^e, Nicolas D. Waldmann^f, Sarah A. Spaulding^{g,h}, Or M. Bialik^f, F. Garrett Boudinot^b, Peter Illnerⁱ, and Yizhaq Makovsky^{a,f}

^aThe Hatter Department of Marine Technologies, Charney School of Marine Sciences, University of Haifa, Mount Carmel, 31905 Haifa, Israel.

^bOrganic Geochemistry Laboratory, Department of Geological Sciences and Institute of Arctic and Alpine Research (INSTAAR), University of Colorado Boulder, Boulder, Colorado 80309, USA.

^cStratigraphy/Paleontology, Faculty of Geosciences, Utrecht University, Budapestlaan 4, 3584 CD Utrecht, the Netherlands.

^dRatio Oil Exploration, Tel Aviv, Israel.

^eBRIDGE, School of Geographical Sciences, Bristol University, University Road, Bristol BS8 1SS, United Kingdom.

^fThe Dr. Moses Strauss Department of Marine Geosciences, Charney School of Marine Sciences, University of Haifa, Mount Carmel, 31905 Haifa, Israel.

^gInstitute of Arctic and Alpine Research (INSTAAR), University of Colorado Boulder, Boulder Colorado 80309, USA.

^hUnited States Geological Survey, University of Colorado Boulder, Boulder Colorado 80309, USA.

ⁱInstitute for Mineralogy and Geochemistry, Karlsruhe University, 76131 Karlsruhe, Germany

*Correspondence to: Dr. Aaron Meilijson email: aaron.meilijson@colorado.edu Tel: +972-505666926

Abstract

The Messinian Salinity Crisis (MSC; 5.97-5.33 Ma) is considered an extreme environmental event driven by changes in climate and tectonics, which affected global ocean salinity and shaped the biogeochemical composition of the Mediterranean Sea. Yet, after more than 50 years of research, MSC stratigraphy remains controversial. Recent studies agree that the transition from the underlying pre-evaporite sediments to thick halite deposits is conformal in the deep Eastern Mediterranean basin. However, the age of the base and the duration of halite deposition are still unclear. Also disputed is the nature of the intermediate and upper MSC units, which are characterized as periods of increased clastic deposition into the Eastern Mediterranean based on marginal outcrops and seismic data. We provide a multidisciplinary study of sedimentary, geochemical, and geophysical data from industrial offshore wells in the Levant Basin, which recovered a sedimentary record of deep-basin Mediterranean evaporites deposited during the MSC. In combination with previous observations of the MSC throughout the Mediterranean Basin, our results promote the need for a new chronological model. Remarkably, the one-kilometer-thick lower part of the evaporitic unit is composed of essentially pure halite, except for a thin transitional anhydrite layer at its base. The halite is undisturbed and homogeneous, lacking diverse features apparent in more proximal sections, indicating a deep-sea depositional environment. We find that distinct, meters-thick non-evaporitic intervals interbedded with the halite, previously thought to be clastic layers, are indeed diatomites. While XRD analysis confirms an increase in clastic components in these sediments, they are composed primarily of

well-preserved marine and freshwater planktonic diatoms. The occurrence of marine planktonic diatoms in these intervals indicates the input of Atlantic waters into the Mediterranean Basin during the deposition of the massive halite unit. Seismic stratigraphy and well-log cyclostratigraphy further support deep basin halite deposition, which started about 300 kyr earlier than widely assumed (~5.97 Ma). We propose that halite deposition in the deep Mediterranean took place during stage 1 of the MSC, rather than being limited to the short 50 kyr MSC acme when sea level was presumably at its lowest. Thus, brine formation, salt precipitation, and faunal extinction occurred at least in part in a deep, non-desiccated basin, with a restricted yet open Mediterranean-Atlantic connection that allowed inflow of oceanic water. We observe an increase in heavy minerals and reworked fauna within the clastic-evaporitic, Interbedded Evaporites of the basal MSC section, and argue that these settings correspond in the deep basins with a significant sea-level drawdown during stage 2 of the MSC, as observed in the marginal sections. This correlation is corroborated by astrochronology and chemostratigraphic markers, such as the distribution of *n*-alkanes and biomarker-based thermal maturity indices.

The Levant deposits indicate that high sea level and partial connectivity with global oceans promoted the deposition of deep-basin deep-water halite, while sea-level drawdown promoted deposition of reworked and transported material from the margins into deep Mediterranean basins. This study modifies the current understanding of the mechanisms governing salt deposition throughout the MSC with implications for other evaporitic events in the geologic record.

Keywords: Messinian Salinity Crisis, Mediterranean, deep-basin, evaporites, stratigraphy, sedimentology

Highlights

- After 50 years of research and over 10,000 publications, Messinian Salinity Crisis chronology is still debated
- We analyze a detailed sedimentary and geophysical record from the deep Levant Messinian halite
- Lithological, stratigraphic, and chemical signals indicate precipitation of halite 300 kyr earlier than presumed
- Halite was deposited in a deep-basin deep-water environment synchronously with gypsum deposition on the margins
- Sea-level drawdown during the MSC acme in the Mediterranean promoted the deposition of reworked material in deep basins

1. Introduction

An international and multidisciplinary group of scientists have recently joined efforts to organize the challenging endeavor of drilling through the thick Messinian evaporites found in deep Mediterranean basins (IODP pre-Proposal P857B DREAM; Camerlenghi et al., 2014; Lofi and Camerlenghi, 2014). The targeted deep basin evaporites reach up to 3 km in thickness (Hsü, 1973) and are thought to have resulted from restricted connectivity of the Mediterranean Basin to the Atlantic Ocean that led to the Messinian Salinity Crisis (MSC). It has been suggested that deposition of the MSC salt giant has greatly affected the global oceans by sequestering 5% (Ryan, 1973; 2008) to 10% (Garcia-Castellanos and Villaseñor, 2011) of their salt content into the Mediterranean. Also, by contributing warm, saline water to northern latitudes, the MSC influenced Atlantic Meridional Overturning Circulation and, consequently, global climatic shifts (Hernández-Molina et al., 2014). Among the major stratigraphically-driven findings of modern geoscience, the MSC stands alone as being supported by an 'outrageously under-sampled stratigraphic record' (CIESM, 2008). For several decades, focused investigation of the MSC within various interdisciplinary studies was aimed at understanding the mechanisms governing its timing, paleogeography, and the inter-relationship between external forcing and physical systems response. However, while the deep-basin halite was penetrated in its uppermost part (Fig. 1), the prohibitive risk and high drilling cost of recovering cores through the entire deep-basin MSC unit has resulted in a critical lack of data. Scientific drilling of the deep Mediterranean basins has been repeatedly called for in order to test and validate different hypotheses regarding the MSC in the deep Mediterranean basins (CIESM, 2008; Dela Pierre et al., 2014; Gvirtzman et al., 2017; Manzi et al., 2015, 2018; Meilijson et al., 2018), but has yet to be achieved.

57
58
59 24 The MSC came into awareness and was documented as early as the 1950's, when massive
60
61 25 evaporite outcrops in the peri-Mediterranean were identified as co-occurring around the end of
62
63 26 the Miocene (Selli, 1954; Ogniben, 1957). However, the MSC magnitude and extent became
64
65 27 clear only when seismic imaging penetrated the massive diapiric and stratified salt bodies of the
66
67 28 Mediterranean Sea, reaching more than 2 km in thickness and stretching across vast parts of the
68
69 29 basin (e.g., Bourcart et al., 1958; Alinat and Cousteau, 1962; Cornet, 1968; Ryan et al., 1971;
70
71 30 Bellaiche et al. 1974; Ryan, 1976). One of the oldest controversies related to the MSC concerns
72
73 31 the magnitude and timing of sea-level lowering and desiccation, where several models for
74
75 32 evaporite formation have been suggested. Some have proposed that salt was precipitated in deep
76
77 33 basins under a deep-water environment (Schmalz, 1969; Debenedetti, 1982; Sonnenfeld and
78
79 34 Finetti, 2011), while other scenarios promoted a desiccated shallow-water environment (Hsu,
80
81 35 1973). A hybrid model was proposed, with early brine formation in the deep Mediterranean,
82
83 36 preceding substantial drawdown, followed by massive salt precipitation during gateway closure
84
85 37 (Ryan, 2008; Garcia-Castellanos and Villaseñor, 2011; Lofi et al., 2011). Clauzon et al. (1996)
86
87 38 recognized the occurrence of shallow-water first cycle gypsum beds of the same age in many
88
89 39 localities in the western and eastern Mediterranean. Based on this observation they presented a 2-
90
91 40 step model, in which the surface of the Mediterranean Sea remained close to the global ocean
92
93 41 level during the early part of the crisis, and deep-basin evaporites formed following sea-level
94
95 42 drop of the subsequent step. Based on this model, Ryan (2011) described the geodynamic
96
97 43 response of the basin to each of these steps: 1) Significant deepening of the basins by isostatic
98
99 44 load due to an increase in weight of the brine layer. 2) As the basins dried out, the loss of weight
100
101 45 of the water led to regional isostatic uplift that permanently closed the prior inlets.
102
103
104
105
106
107
108
109
110
111
112

113
114
115 46 Van Couvering et al. (1976) were the first to propose a similar 2-step model, which also
116
117 47 portrays an early deposition of halite in the deep basins: (1) An initial deep-water phase marked
118
119 48 by refluxive concentration of brines and controlled by a tectonically elevated sill, during which
120
121 49 evaporites and associated sediments accumulated simultaneously near the surface in marginal
122
123 50 areas (gypsum) and within great saline water bodies in the depths of the basin (halite). (2) A
124
125 51 terminal phase of total isolation, caused by an eustatic sea-level drop, during which erosion and
126
127 52 desiccation features were developed that fit the "deep-basin, shallow-water" model. However,
128
129 53 this model was later abandoned in favor of what developed into the CIESM (2008) workshop
130
131 54 consensus stratigraphic model, which was elaborated in the extensive review of the MSC by
132
133 55 Roveri et al. (2014a) and widely cited.
134
135

136
137 56 The CIESM (2008) stratigraphic model of the MSC is based on correlation of Mediterranean
138
139 57 evaporite sequences deposited in marginal to intermediate basins, and their isotopic signatures
140
141 58 (Keogh and Butler, 1999; Müller and Mueller, 1991; Flecker and Ellam, 2006). While the
142
143 59 division of MSC units differs slightly in terminology between the CIESM (2008) model and the
144
145 60 widely used review of the MSC presented by Roveri et al. (2014a), they both stem from the same
146
147 61 stratigraphic concepts, and are jointly referred to here as the 'consensus model' for MSC
148
149 62 chronology. These studies demonstrate that partial connectivity with the Atlantic Ocean persisted
150
151 63 throughout the first phase of gypsum deposition, lasting for ~370 kyr and known as MSC phase
152
153 64 1: Primary Lower Gypsum [PLG], 5.97–5.6 Ma.
154
155
156
157
158
159
160
161
162
163
164
165
166
167
168

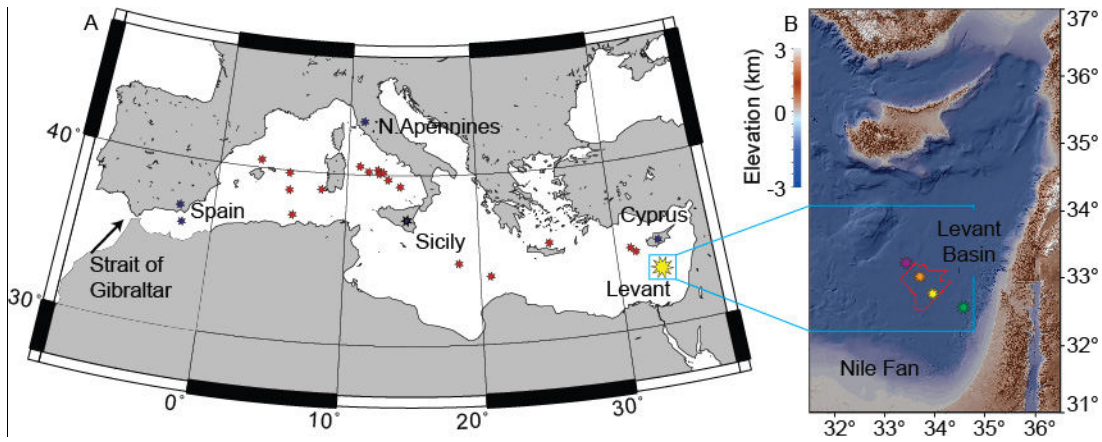


Figure 1. Map of the Mediterranean Sea marking the study area and referenced sections.

A. Map of Mediterranean Sea marking study area (yellow star); main referenced sections (blue stars); and Deep Sea Drilling Project and Ocean Drilling Program wells (red stars), which penetrated MSC halite deposits only at their uppermost part. **B.** A shaded relief map of the Levant Basin and surrounding area (Hall et al., 1994, 2015). Red polygon outlines the three-dimensional seismic cube referred to in this study. Well locations marked by stars: Aphrodite-1 (purple star), Leviathan-1 (orange), Dolphin (yellow), and Sara (Green).

During the PLG, euxinic shales and dolostones were thought to have been deposited in the deep basins in parallel to gypsum deposition in the proximal settings (Lange and Krijgsman, 2010). However, using sonic and resistivity logs and samples from cuttings of the 497-Muchamiel oil-industry well, Ochoa et al. (2015) observed all 14 of the known first-stage gypsum beds present in the Sorbas Basin, offshore southeast Spain, deep (875 -965 m) below the present-day sea level. This observation was regarded opposite to previous assumptions that only shales would be present in this interval of the deep basins (CIESM, 2008; Roveri et al., 2014a).

The thick salt unit was interpreted as being accumulated during the succeeding MSC acme, a short period of ~50 kyr known as MSC phase 2: Resedimented Lower Gypsum [RLG], 5.6–5.55 Ma (although its top is often marked at 5.53 Ma in different cyclostratigraphic schemes (e.g., Roveri et al., 2014a; Manzi et al., 2015) due to the ‘Messinian gap’, during which Messinian

225
226
227 85 erosion and/or deposition of resedimented gypsum and halite occurred). A model depicting the
228
229 86 desiccation of the Mediterranean during stage 2 was proposed to explain its formation over such
230
231 87 a short period of time. This model entails a massive sea-level drawdown and consequent removal
232
233 88 and re-deposition of the PLG gypsum, and a seasonal or long-term deposition of halite in
234
235 89 intermediate to deep-water basins. Lastly, the third phase of the MSC was defined within the
236
237 90 Upper Evaporites or Gypsum sequences (UG), which include clastic or brackish sediments
238
239 91 culminating in the Lago-Mare deposits (5.55-5.33 Ma). The latter consist of several units with 7-
240
241 92 10 sedimentary cycles identified in the Upper Gypsum of Italy overlying erosional surfaces and
242
243 93 angular unconformities, and underlying Pliocene sediments (Hilgen et al., 2007; Krijgsman et al.,
244
245 94 2010; Roveri et al., 2014a). A recent review of different Lago-Mare deposits depicts that three
246
247 95 main pulses of seaward-transport occurred within the time-interval 5.64-5.33 Ma, and suggests
248
249 96 abandonment of previous concepts dealing with a unique chronostratigraphic unit, favoring
250
251 97 several episodes of flooding (Couto et al., 2014). Nonetheless, the first influx of Paratethyan
252
253 98 organisms, identified through the dinoflagellate cyst record near Malaga within a fan delta, was
254
255 99 found overlying the intra-Messinian truncation surface (IMTS) (Couto et al., 2014).

256
257
258
259 100 Recent industrial activities targeting hydrocarbon reservoirs in the Eastern Mediterranean
260
261 101 Basin provide the scientific community with unparalleled seismics, well logs, and cuttings across
262
263 102 the salt interval. The current work takes advantage of these industrial data to address two critical
264
265 103 issues regarding Messinian stratigraphy in the deep Eastern Mediterranean Basin, which impact
266
267 104 our basic understanding of this event: (1) To evaluate the composition, age and duration of
268
269 105 evaporite deposition in the Eastern Mediterranean. (2) To characterize, interpret, and
270
271 106 stratigraphically position the sediments overlying the IMTS (as in Gvirtzman et al., 2017),
272
273 107 termed here the Interbedded and Argillaceous Evaporites. Here, we report previously unknown
274
275
276
277
278
279
280

281
282
283 108 features and lithology of the deep basin MSC and, by using a multi-disciplinary approach, we
284
285 109 provide further interpretation of their stratigraphy.
286
287

288 110 **2. MSC deposits in the Levant**

289 111 Feng et al. (2016) analyzed jointly well-log measurements and a pervasive seismic dataset,
290
291
292 112 and demonstrated that the seismically transparent layers composing the majority of the
293
294 113 Messinian evaporite deposits across the deep Levant Basin are composed of pure halite. The
295
296 114 reflective layers appearing within the halite (Figs 2, 3) were interpreted as bundles of thin clay
297
298 115 layers interbedded in the halite background, having a cumulative thickness of 25-40 m. Feng et
299
300 116 al. (2016) also reported high-amplitude fan structures on the deepest internal reflectors, which
301
302 117 may suggest transport mechanisms. Later, Gvirtzman et al. (2017) argued against a complete
303
304 118 desiccation of the Eastern Mediterranean, following the seismic identification of the IMTS at
305
306 119 ~100 m below the Messinian-Zanclean boundary in the Levant Basin. Based on interpretation of
307
308 120 well logs and correlation to shallower-water wells, Gvirtzman et al. (2017) suggested that the
309
310 121 post-truncation Messinian unit is different from the underlying salt deposits and mostly consists
311
312 122 of shale, sand and anhydrite. Lastly, two separate studies (Manzi et al., 2018; Meilijson et al.,
313
314 123 2018) have investigated the sediments underlying the evaporites, based on data from different
315
316 124 wells within the Levant Basin. Both studies address the stratigraphy of the Pre-Evaporites and
317
318 125 are aimed at providing an indication for the age of the base of the halite in the deep Eastern
319
320 126 Mediterranean, represented on seismic data in the region as the 'N' reflection (Ryan, 1978;
321
322 127 Bertoni and Cartwright, 2007). Establishing the age and duration of the deep-basin halite is
323
324 128 perhaps the most enigmatic aspect of MSC research. Both recent studies test the CIESM
325
326 129 stratigraphic model of the MSC (CIESM, 2008; Dela Pierre et al., 2014; Roveri et al., 2014a).
327
328
329
330
331
332
333
334
335
336

337
338
339 130 Manzi et al. (2018) and Meilijson et al. (2018) report several similar findings, such as the
340
341 131 seismic interpretations regarding the conformity of the base of the evaporites, and thus refuting
342
343 132 the occurrence of a long hiatus at the base of the evaporites. In addition, both studies indicate
344
345 133 little deformation of the Levant Pre-Evaporite interval and a continuous record of the Tortonian
346
347 134 to Messinian sediments. Still, different observations reported in these studies have led to
348
349 135 continued uncertainty concerning the age and duration of salt deposition.
350

351
352 136 Meilijson et al. (2018) considered two alternatives for the age of the base evaporites in the
353
354 137 deep basins: (1) during stage 1 (PLG) of the MSC at around 5.9 Ma, or (2) at around 5.6 Ma
355
356 138 during stage 2 (RLG) of the MSC, as is described in the CIESM stratigraphic model (CIESM,
357
358 139 2008; Roveri et al., 2014a). The latter would imply a major hiatus of ~370 kyr (missing the PLG
360
361 140 equivalent unit) at the base of the salt, or alternatively that the PLG is expressed as a very thin
362
363 141 interval in the uppermost Pre-Evaporites unit. A hiatus in the deep basin has not been identified,
364
365 142 but rather a visible lateral continuity of seismic reflectors below and at the boundary itself
366
367 143 (Meilijson et al., 2018). This finding is consistent with published regional seismic sections (Feng
368
369 144 et al., 2016; Manzi et al., 2018; Roberts and Peace, 2007) and elsewhere in the deep domain of
370
371 145 the Mediterranean (Lofi et al., 2011). Thus, Meilijson et al. (2018) concluded that the studied
372
373 146 section is in fact conformal and halite began to precipitate around the onset of the PLG in the
374
375 147 marginal basins, predating the CIESM consensus for halite deposition by ~300 kyr.
376

377
378 148 Manzi et al. (2018) reported that in the Aphrodite-2 well (Fig. 1), which is the deepest
379
380 149 location along their four-well cross-section, a complete absence of foraminifera occurs from
381
382 150 3959 m upwards, 28 m below the first occurrence of anhydrite, and 33 m from the base of halite
383
384 151 deposition. They interpret this foraminifera barren interval (FBI) as corresponding to the Non-
385
386 152 Distinctive Zone (NDZ) marking the onset of the MSC (5.971 Ma) in marginal settings (Gennari et
387
388
389
390
391
392

393
394
395
396
397
398
399
400
401
402
403
404
405
406
407
408
409
410
411
412
413
414
415
416
417
418
419
420
421
422
423
424
425
426
427
428
429
430
431
432
433
434
435
436
437
438
439
440
441
442
443
444
445
446
447
448

153 al., 2013; Manzi et al., 2013). Manzi et al. (2018) proposed that this interval represents the deep basin
154 expression of the PLG, followed by halite deposition during stage 2 of the MSC at around 5.6 Ma.
155 This FBI is argued by them to be further substantiated by a prominent peak of *Sphenolitus abies* at
156 3961 m, closely followed by a decrease in the number of species of calcareous nannofossils. The
157 FBI was also identified by Manzi et al. (2018) in the Myra well, which is situated in a more proximal
158 position, 90 km SW to the Aphrodite well. Farther landward to the west, the FBI is no longer
159 recognized in the Sara well, where the Aphrodite well equivalence of about 60 m underlying the base
160 of the evaporites is missing. This observation indicates that the Dolphin well should also include an
161 equivalent FBI, as it is positioned between the Myra well, and closer to the latter (Fig. 1). However,
162 such an FBI is not present in the Dolphin well, in which the samples include a relatively open-marine
163 foraminiferal assemblage up to the uppermost sample available for analysis, representing the interval
164 0-9 m below the base of the evaporites (Meilijson et al., 2018). Thus, the MSC timing and events are
165 still debated after more than 50 years of research and over 10,000 publications.

166 In recent years, different studies have been leaning towards new and very different ideas
167 regarding MSC chronology, and thus the mechanisms controlling the deposition of salt giants in deep
168 sea basins. Ochoa et al. (2015) demonstrated synchronous deposition of evaporites in marginal and
169 intermediate basins. Simon and Meijer (2017) modeled stratification in the Mediterranean during the
170 MSC and raised the possibility of a much earlier onset of halite in the deep basins. Finally, García-
171 Veigas et al. (2018) even went so far as to draw a model for an early onset of halite, yet added a
172 question mark next to this assumption due to lack of proof for this claim (their fig. 12). Here, we
173 address this debate on the chronology of MSC events in the Mediterranean by examining the
174 recovery of deep-basin evaporites from the Levant Basin for stratigraphic indicators that can promote
175 a better understanding of MSC chronology.

449
450
451 176 The MSC (CIESM, 2008; Roveri et al., 2014a) is expressed in the southeastern Levant Basin
452
453 177 margins as a thick evaporitic sequence (locally named the Mavqiim Formation), as well as clastic
454
455 178 evaporite deposits along local topographical lows (Buchbinder and Zilberman, 1997; Druckman
456
457 179 et al., 1995; Lugli et al., 2013). The MSC deposits in the deep Levant Basin have been identified
458
459 180 through seismic data, and interpreted as mainly consisting of halite, reaching a thickness of
460
461 181 ~2 km in the central part of the basin and pinching out upslope towards its southeastern margin
462
463 182 (Bertoni and Cartwright, 2007, 2006; Feng et al., 2016; Gardosh et al., 2008; Netzeband et al.,
464
465 183 2006; Steinberg et al., 2011). The halite sequence base and top are generally imaged as
466
467 184 pronounced high-amplitude seismic reflections, known as the N and M reflectors, respectively
468
469 185 (Ryan, 1978). Up-dip, the evaporitic sequence thins below seismic resolution and is entirely
470
471 186 represented by the M reflector (e.g., Steinberg et al., 2010). The nomenclature of the MSC
472
473 187 section in the Levant Basin is currently based on the regional identification of a number of key
474
475 188 markers within seismic sections across the basin, with several divisions presented by different
476
477 189 studies: division of the section into 6 or 7 units (Gvirtzman et al., 2013b, 2017; Lugli et al.,
478
479 190 2013), or into ME 1-4 (Messinian evaporites) and MC 1 and 2 (Messinian clastics; Feng et al.,
480
481 191 2016). In this manuscript we refer to the unit numbers (Gvirtzman et al., 2017, 2013b) and
482
483 192 ME/MC units (Feng et al., 2016), corresponding seismically to the lithostratigraphic descriptions
484
485 193 and division of the Dolphin well sediments.

489 194 Several studies have shown that the seismic records of the MSC greatly differ between the
490
491 195 Western and Eastern Mediterranean basins, and argued that it is impossible to properly correlate
492
493 196 individual sub-units (Lofi et al., 2011). Some authors have also questioned the possible
494
495 197 diachronism between both basins (Blanc, 2000; Ryan, 2008). However, the Levant has been for
496
497 198 many years at the center of debate regarding the evolution of the MSC across the entire
498
499
500
501
502
503
504

505
506
507
508
509
510
511
512
513
514
515
516
517
518
519
520
521
522
523
524
525
526
527
528
529
530
531
532
533
534
535
536
537
538
539
540
541
542
543
544
545
546
547
548
549
550
551
552
553
554
555
556
557
558
559
560

199 Mediterranean Basin. An example for such a long-term debate includes the formation of the vast
200 drainage systems at the Mediterranean margins and the deposition, or re-deposition, of gypsum
201 within them. An important type location for this debate is the Afiq canyon along the continental
202 margin of Israel. The presence of evaporite layers at different levels along the Afiq canyon was
203 brought as one of the first evidence for a substantial Messinian sea-level drawdown (800 m sea-
204 level drop; Druckman et al., 1995). However, these deposits were recently argued to result from
205 evaporite recycling through slope mass-wasting, a phenomena suggested to characterize the
206 upper parts of the MSC throughout the Mediterranean (Lugli et al., 2013). The wells investigated
207 in this study were drilled in the Levant Basin, and may represent local conditions rather than
208 account for the entire Mediterranean Basin. However, by recovering one of the most extensive
209 evaporite deposits of the MSC, the analysis of these wells bears key implications for unraveling
210 the MSC across the entire Mediterranean.

211 **3. Methodology**

212 This study is based on the combined analyses of well cuttings, 3D pre-stack depth-migrated
213 reflection seismics, and well-log data of two deep-water industry wells recently drilled in the
214 Levant Basin (Fig. 1). We have also used a time-migrated 2-D seismic survey acquired by TGS-
215 Nopec Geophysical Company in 2000, and the 3-D depth-migrated Pelagic seismic survey
216 acquired by CGG-Veritas in 2009. Lithological and biostratigraphic data presented in this study
217 are from the Dolphin well (N 3628144.05 m, E 575444.97 m), drilled by the Leviathan
218 partnership at a water depth of 1500 m and penetrating the 1590 m thick Messinian evaporite
219 section at depths of 2026-3616 m below sea level. The second studied well is the Leviathan-1 (N
220 3653455.35 m, E 553663.40 m), also drilled by the Leviathan partnership at a water depth of
221 1644 m and penetrating the 1694 m thick Messinian evaporite section at depths of 2090-3784 m

561
562
563
564
565
566
567
568
569
570
571
572
573
574
575
576
577
578
579
580
581
582
583
584
585
586
587
588
589
590
591
592
593
594
595
596
597
598
599
600
601
602
603
604
605
606
607
608
609
610
611
612
613
614
615
616

222 below sea level. The record presented in this study supplements the 350 m section immediately
223 below the base of the halite shown in Meilijson et al. (2018). Samples were curated and archived
224 in both the Organic Geochemistry Laboratory at the University of Colorado (organic extracts)
225 and the Department of Marine Geosciences, Leon Charney School of Marine Sciences,
226 University of Haifa.

227 Drilled cutting returns are available starting down from a depth of 2535 m and 2497 m in the
228 Dolphin and Leviathan-1 wells, respectively. The Pre-Evaporites interval of the Dolphin
229 (Meilijson et al., 2018) and Leviathan wells was sampled every 3 m. The evaporite interval was
230 sampled every ~9 m, with a total of 123 samples from the Dolphin well. Due to standard drilling
231 activities, many fallouts of clastic deposits occur downhole from the lower part of the
232 Interbedded Evaporite unit to the upper part of the Main Halite unit, appearing as an interval of
233 clastic deposits in the XRD log of the Dolphin well from 2560 to 2675 m. Well-log data does not
234 respond to this high-clastic content (i.e., high RE log values and low GR log values), and so does
235 not show a shift from halite deposition. This observation confirms that the clastic material arrive
236 from the unit above, as drilling fallouts into the halite interval. While not in-situ, these fallouts,
237 together with the well logs, allow us to interpret the distinct lithological transition that occurs at
238 the boundary between the Main Halite and Interbedded Evaporites unit. However, these fallouts
239 might also originate from the Argillaceous Evaporites unit above.

240 Individual cutting bits were separated by their lithology under a microscope, cleaned with
241 deionized water and 10% hydrochloric acid, dried, and then crushed in an agate pestle and
242 mortar. Fine powders were pressed and used for bulk mineralogical X-ray diffractogram (XRD)
243 analysis using a Rigaku 600 MiniFlex X-Ray Diffractometer with a CuK α source at 30kV / 15-
244 mA from 3° to 70°. Mineralogical compositions of assemblages were determined using the

617
618
619 245 ICDD PDF2 mineral database references. Next, fine powders were pressed in Teflon crucibles
620
621 246 with X-Ray transparent mylar (which was replaced between samples). Each sample was then
622
623 247 analyzed using a Nitton X-Ray XL3 GOLDD+ Fluorescence apparatus for elemental
624
625
626 248 composition.

627
628 249 Samples found to be bearing microfossils were investigated for their faunal assemblages,
629
630 250 which included washing and picking foraminifera from the Pre-Evaporites (detailed in Meilijson
631
632 251 et al., 2018) and the preparation of smear slides for the study of the diatomites interbedded
633
634 252 within the halite. For the latter, samples were weighed, treated several times with 10% HCl for
635
636 253 carbonate removal, and 30% hydrogen peroxide for organic matter removal, and then loaded
637
638 254 onto glass slides. A total of 50 diatom valves were counted and identified from 10 samples.
639
640 255 Diatoms were characterized by their habitat preferences: planktonic vs. benthic, and marine vs.
641
642 256 freshwater.

643
644
645 257 We also studied the distribution of selected biomarkers (i.e., *n*-alkanes, algal steranes, and
646
647 258 bacterial hopanes) from different intervals to gain insight into variations in organic matter
648
649 259 sources and thermal alteration. Rock cuttings were cleaned and handled with solvent-rinsed
650
651 260 metal tweezers, a Dremmel 8220 wire-brush tip, spatulas, and combusted aluminum foil, and
652
653 261 then powdered with a solvent-rinsed agate mortar and pestle. Approximately 5-10 grams of
654
655 262 sample were extracted using a Dionex Accelerated Solvent Extractor (ASE 200; 100 °C; 2,000
656
657 263 psi) and a mixture of dichloromethylene:methanol 9:1 (v:v) until no more color was observed
658
659 264 (typically 3-6 extractions). Each extraction cycle included heating of the cell for 5 minutes, static
660
661 265 mode for 5 minutes, and flushing for 2 minutes time. A cocktail of internal standards containing
662
663 266 500 ng of D4 C₂₉ ααα (20R)-Ethylcholestane, and 1,000 ng of each 3methyl heneicosane, D14
664
665 267 pTerphenyl, 1-nonadecanol, behenic acid methylester (Docosanoic acid), and 2methyl
666
667
668
669
670
671
672

673
674
675 268 octadecaonic acid, was added to samples before extraction for quantitation purposes. Total lipid
676
677 269 extracts (TLEs) were combined and evaporated under a gentle nitrogen flow using a Turbovap.
678
679 270 Elemental sulfur was removed using HCl-activated copper shots. TLEs were then filtered
680
681 271 through small Pasteur pipettes filled with combusted glass wool and sand to remove impurities
682
683 272 and any copper-sulfide residues. Asphaltenes were separated from maltenes by precipitation in
684
685 273 hexanes at 4⁰C for 3 hours, followed by centrifugation at 2000 rpm (3x). Maltenes were later
686
687 274 separated into five different lipid classes by liquid chromatography on small Pasteur pipettes
688
689 275 filled with silica gel. Aliphatic (F1) and aromatic (F2) hydrocarbons were recovered with hexane
690
691 276 (3/4 dead volumes) and hexane:dichloromethylene 8:2 (v:v; 4 dead volumes), respectively. The
692
693 277 more polar fractions (F3, F4, F5) were eluted using dichloromethylene,
694
695 278 dichloromethylene:EtOAc 1:1, and EtOAc (v:v, 4 dead volumes), respectively. Aliphatic
696
697 279 hydrocarbons were analyzed on full scan and selected reaction monitoring (SRM) modes via gas
698
699 280 chromatography – triple quadrupole-mass spectrometry (GC-QQQ-MS) using a Thermo Trace
700
701 281 1310 Gas Chromatograph interfaced to a TSQ Evo 8000 triple quadrupole mass spectrometer
702
703 282 (GC-QQQ-MS) equipped with a split-less PTV injector and electron impact ion source. Helium
704
705 283 was used as a carrier gas with a flow rate of 1.2 ml min⁻¹. Chromeleon 7 was used for data
706
707 284 integration. Aliphatic hydrocarbons were separated using a 60-meter DB-1MS GC column (60
708
709 285 m, 0.25 mm I.D., 0.25 μm film thickness; Agilent Technologies). For FS analysis, samples were
710
711 286 injected at 60°C and then the PTV was heated to 300°C at 14.5°C/second. The GC oven
712
713 287 temperature program was: 60°C (2 min) to 150°C at 15°C min⁻¹, to 315 (held 24 min) at 3°C
714
715 288 min⁻¹. The total GC program was 90 minutes. MS conditions were: 300°C ion source at 70eV
716
717 289 electron energy, 50uA emission current, and 15V electron lens voltage. The mass range was 50-
718
719 290 600 m/z with a dwell time of 0.2 seconds per scan. For SRM analysis, the GC oven temperature
720
721
722
723
724
725
726
727
728

729
730
731 291 program was: 60°C (0 min) to 220°C at 15°C min⁻¹, to 315°C (held 25 min) at 3°C min⁻¹. The
732
733 292 total GC program was 68 minutes. Samples were injected at 65°C and then the PTV temperature
734
735 293 was heated to 400°C at 3 °C min⁻¹. MS conditions were: ion source temperature of 250°C;
736
737 294 transfer line temperature of 320°C, electron energy of 70eV, electron lens voltage of 35V, and
738
739 295 emission current of 35uA. Peak scanning windows ranged from 0.6 to 1 minute for 147 timed
740
741 296 transitions for regular and methylated steranes and hopanes, and their stereoisomers.
742
743

744 297 **4. Evidence from the Levant Basin for an early onset of halite deposition in a deep-water** 745 746 **environment** 747 298

748 749 299 **4.1 Lithologic composition of the Levant deep-sea salt-giant** 750

751 752 300 *4.1.1 Pre-Evaporites* 753

754 301 This interval is detailed in Meilijson et al. (2018). Here we provide a generalized summary,
755
756 302 followed by a more elaborate account of the overlying evaporites of the deep Levant Basin. The
757
758 303 Pre-Evaporite interval in the Dolphin well (3850-3616 m; Fig. 2) is seismically characterized by
759
760 304 sub-horizontal and sub-parallel continuous high-amplitude reflections, implying a stratified and
761
762 305 relatively undeformed marine succession (Meilijson et al., 2018). It is composed of fine-grained
763
764 306 clastic-micritic and carbonate bathypelagic sediments, primarily gray to dark gray or greenish
765
766 307 calcareous soft to hard shale, with several thin layers of white to light gray hard limestone, and
767
768 308 light gray very fine to fine-grained unconsolidated sandstone. Diverse assemblages of
769
770 309 nannofossils, benthic and planktic foraminifera are recognized within this interval.
771
772

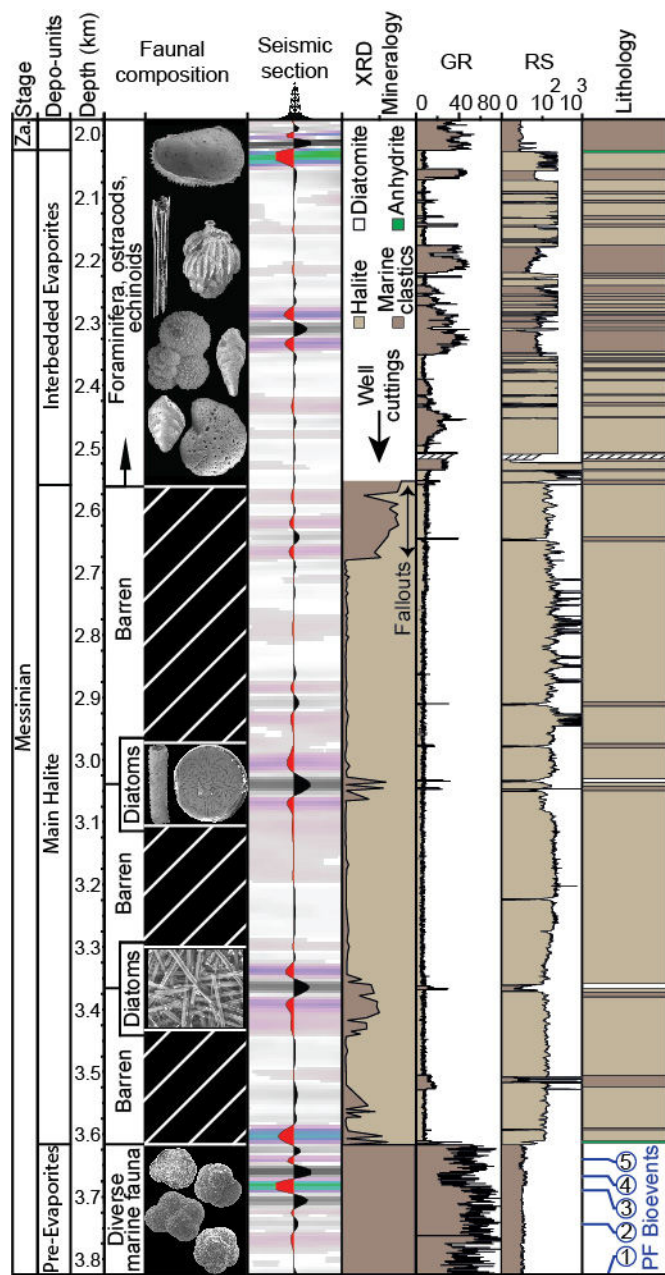
773 310
774
775 311 *Figure 2. The MSC succession of the Dolphin well in the deep Levant Basin.*
776

777 312 A juxtaposed simplified display of the primary proxies used to characterize the Dolphin well
778
779 313 section (five central columns), and our depositional (left) and lithological (right) interpretations.
780
781
782
783
784

785
786
787
788 314 The attributes are (left to right): the faunal composition; the seismic response, with transparent
789
790 315 intervals representing predominantly evaporites and high-amplitude reflections representing
791
792 316 clastic beds (a seismic trace (center) emphasizes relative intensity of the seismic phases); XRD
793
794 317 mineralogy, showing the relative abundance of halite (bright) vs. non-halite (dark; 'marine
795
796 318 clastics'), where the uppermost clastic interval (<2650 m) represents fallouts from the
797
798 319 Interbedded Evaporites; the gamma ray (GR - API units) and resistivity (RE - log ohm-m units)
799
800 320 logs, color coded based on the characteristic responses to halite and clastics. The lithological
801
802 321 interpretation is color coded as in the attribute columns. Planktonic foraminiferal (PF) bio-events
803
804 322 in blue circles correspond to the following ages: 1- 7.72, 2- 7.24, 3- 6.72, 4- 6.36, and 5- 6.13 Ma
805
806 323 (Meilijson et al., 2018).

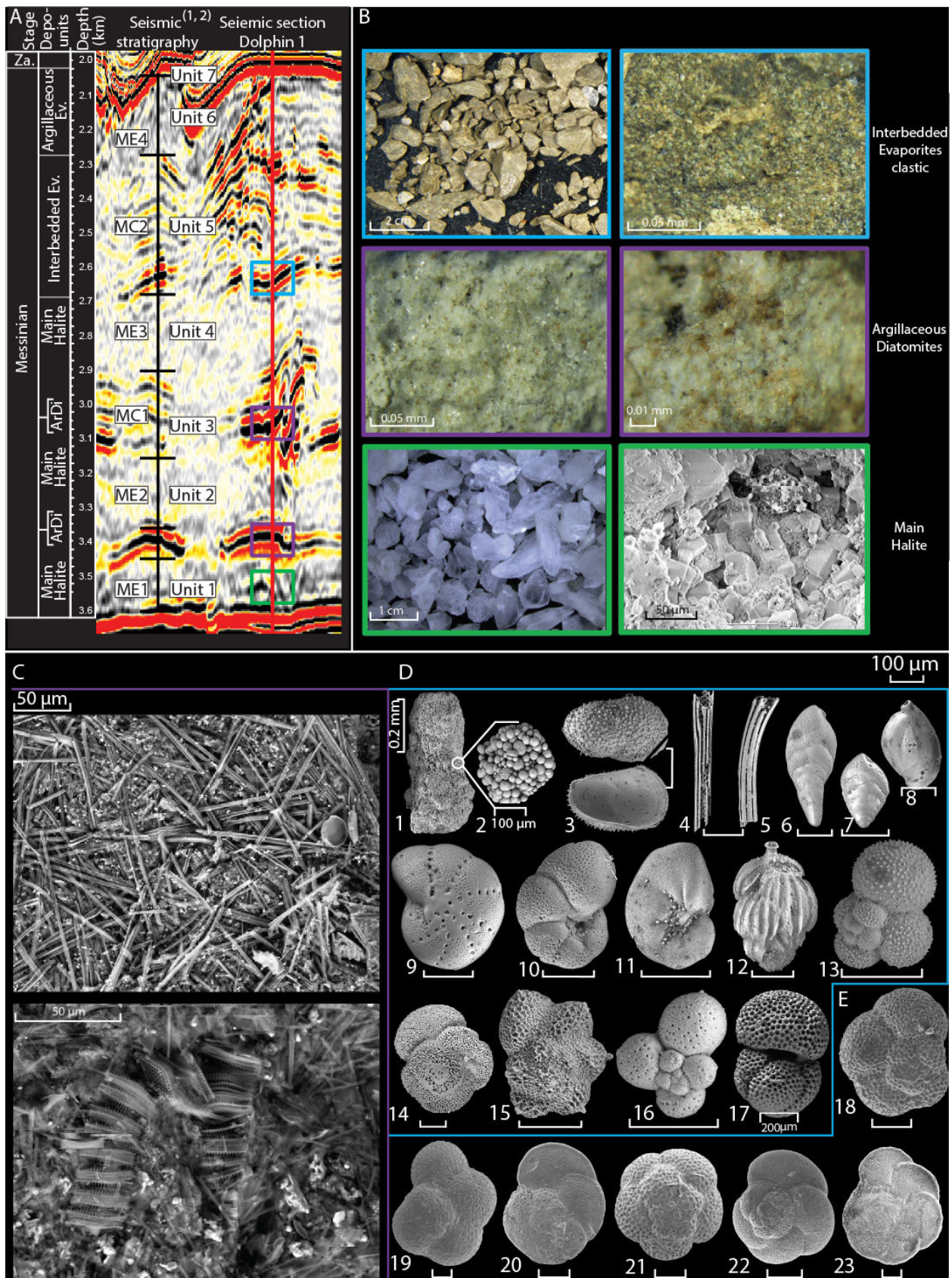
808
809 324
810
811
812
813
814
815
816
817
818
819
820
821
822
823
824
825
826
827
828
829
830
831
832
833
834
835
836
837
838
839
840

841
842
843
844
845
846
847
848
849
850
851
852
853
854
855
856
857
858
859
860
861
862
863
864
865
866
867
868
869
870
871
872
873
874
875
876
877
878
879
880
881
882
883
884
885
886
887
888
889
890
891
892
893
894
895
896



325

897
898
899
900
901
902
903
904
905
906
907
908
909
910
911
912
913
914
915
916
917
918
919
920
921
922
923
924
925
926
927
928
929
930
931
932
933
934
935
936
937
938
939
940
941
942
943
944
945
946
947
948
949
950
951
952



326

953
954
955 327 *Figure 3. Seismic stratigraphy, common lithologies, and SEM imaging of the studied section.*
956
957 328 **A.** The seismic profile crossing the sampled Dolphin well position and its division into the MSC
958 329 depositional units, compared to previously published seismic stratigraphy of the deep Levant
959 330 MSC ((1) Feng et al., 2016; (2) Gvirtzman et al., 2017). ArDi - Argillaceous Diatomites; Ev. -
960 331 Evaporites. Color coded rectangles corresponding to lithologies described in (B). **B.** images of
961 332 the three main facies recognized in the Levant evaporite section: the homogeneous Main Halite
962 333 (green rectangle) made of pure halite as seen in hand specimen (left) and SEM imagery of cubic
963 334 cleavage (right), corresponding with subdued internal seismic reflectivity in (A); Argillaceous
964 335 Diatomite beds (purple rectangle), represented by high amplitude reflections in (A); and
965 336 Interbedded Evaporites (blue rectangle) identified as brown marine clastics, characterized by
966 337 interchanging low and high amplitude reflections in (A). **C.** Selected SEM images from the
967 338 densely packed and very well preserved diatoms from the diatomite facies. **D.** Selected SEM
968 339 images of the >63 µm size fraction of the washed residue from the Interbedded Evaporites unit
969 340 clastic sediments (P.1-17) showing: large grains of framboidal pyrite (P.1-2), well-preserved
970 341 ostracod valves (P.3), sea urchin spines (P.4-5), benthic foraminifera (P.6-12), and planktic
971 342 foraminifera (P.13-17). **E.** SEM images of the planktic foraminifera used for the biostratigraphic
972 343 age model (Meilijson et al., 2018) of the Pre-Evaporites (P.18-23): *Neogloboquadrina* sp. (P.18),
973 344 *Sphaeroidinellopsis seminulina* (P.19), *Globorotalia miotumida* (P.20), *Globoquadrina altispira*
974 345 (P.21), *Globorotalia scitula* (P.22); *Globorotalia menardii*-4 (P.23). All scales are 100 µm unless
975 346 indicated otherwise.

987 347
988
989 348 Shale samples are organic-rich (>1 wt.% TOC) and reach peak values of 4 wt.% TOC
990 349 immediately underlying the base of evaporite deposition (Meilijson et al., 2018). Lower values of
991 350 gamma ray (GR) are associated with silt/carbonate-rich sediments, while higher GR corresponds
992 351 to shale/organic-rich sediments (Fig. 2).

998 352 *4.1.2 Main Halite*

1000 353 Here we reference our lithologic interpretation to the recently defined seismic stratigraphy of
1001 354 the Levant MSC (Units 1-6; Gvirtzman et al., 2013), and ME1-4 for the transparent and MC1-2

1009
1010
1011 355 for the high reflectivity intervals (Feng et al., 2016) (Fig. 3). Different velocity models reported
1012
1013 356 high seismic velocities of 4200-4400 m/s (Gvirtzman et al., 2013a), 3850-4240 m/s (Reiche et
1014
1015 357 al., 2014), and 4400-4600 m/s (Feng et al., 2016) for the seismic transparent layers, interpreted
1016
1017
1018 358 as representing the halite facies. Here we advocate this interpretation by providing the first semi-
1019
1020 359 quantitative XRD analysis (Fig. 4) of well cuttings spanning the transparent high velocity layers.
1021

1022 360 The Main Halite unit in the vicinity of the Dolphin (3616- 2755 m) and Leviathan-1 (3759-
1023
1024 361 2800 m) wells is characterized by low seismic reflectivity, which is internally interrupted by
1025
1026 362 several main high reflectivity bands (Figs 5, 6). These instances are clearly recognized in the
1027
1028 363 well logs (Fig 2, 5), and represent a different facies within the hypersaline deposits described
1029
1030 364 below. Using XRD analysis coupled with SEM (Fig. 4), we conclude that the transparent
1031
1032 365 intervals are indeed composed of nearly pure (>90%) halite (Fig. 4), with minor quantities of
1033
1034 366 anhydrite, magnesite and barite. Anhydrite is also present as a relatively thin bed (<3 m) at the
1035
1036 367 base of the Main Halite section, where it represents the transition to the Main Halite. Anhydrite
1037
1038 368 further appears in the upper, more elastic part of the section (Fig. 2), as is also reported from the
1039
1040 369 same stratigraphic interval by Gvirtzman et al. (2017). The halite is clear to milky white with a
1041
1042 370 firm to very hard macrocrystalline structure (Fig. 3), while the anhydrite minerals are white, soft
1043
1044 371 to firm, nodular and amorphous to massive. A sharp transition from the Pre-Evaporites to halite
1045
1046 372 is marked by a decrease in GR well log counts from 53 API to 12 API as well as a sharp increase
1047
1048 373 in the RE well log reaching 10,000 ohm (Fig. 2; see also Feng et al., 2016).
1049
1050
1051
1052
1053
1054
1055
1056
1057
1058
1059
1060
1061
1062
1063
1064

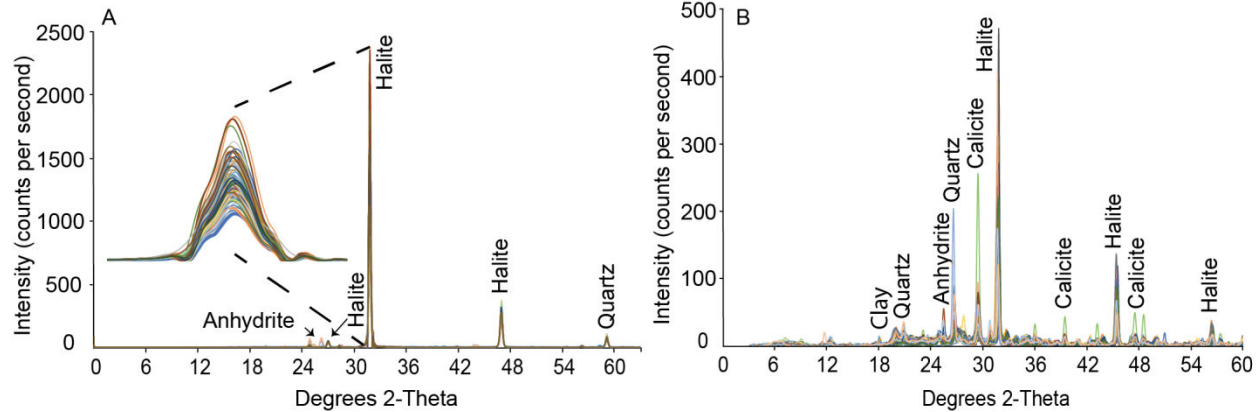


Figure 4. X-ray diffraction results

A. Overlaid (color coded) XRD analysis of 89 halite samples from the Dolphin well produced diffractograms, which are practically identical. The main halite peak is zoomed for emphasis. **B.** Higher variability is recorded both in peak location and intensity when analyzing samples from the non-evaporitic marine sediments, sampled along the section between the depth of 3,616 m to 2560 m.

These values remain relatively constant within the halite deposits, although inter-halite variations are observed, mainly on the RE log. The pronounced high-amplitude reflection at ca. 3520 m (Dolphin well; Figs 2, 3), also recognized as an increase in the GR well logs, represents a short-term return to the clastic Pre-Evaporites facies although with low abundance and poorly preserved foraminiferal content. This interval is not part of the Argillaceous Diatomites facies.

4.1.3 Argillaceous Diatomites

Distinct reflective layers appear within the seismic transparent halite expressions, correlating with relatively lower velocity zones in the seismic velocity models developed for the deep Levant Basin MSC strata (e.g., 3800-4000 m/s in Gvirtzman et al. (2013); 3650-4030 m/s in Reiche et al. (2014)). These reflective layers are easily identified across the study area (Figs 5, 6).

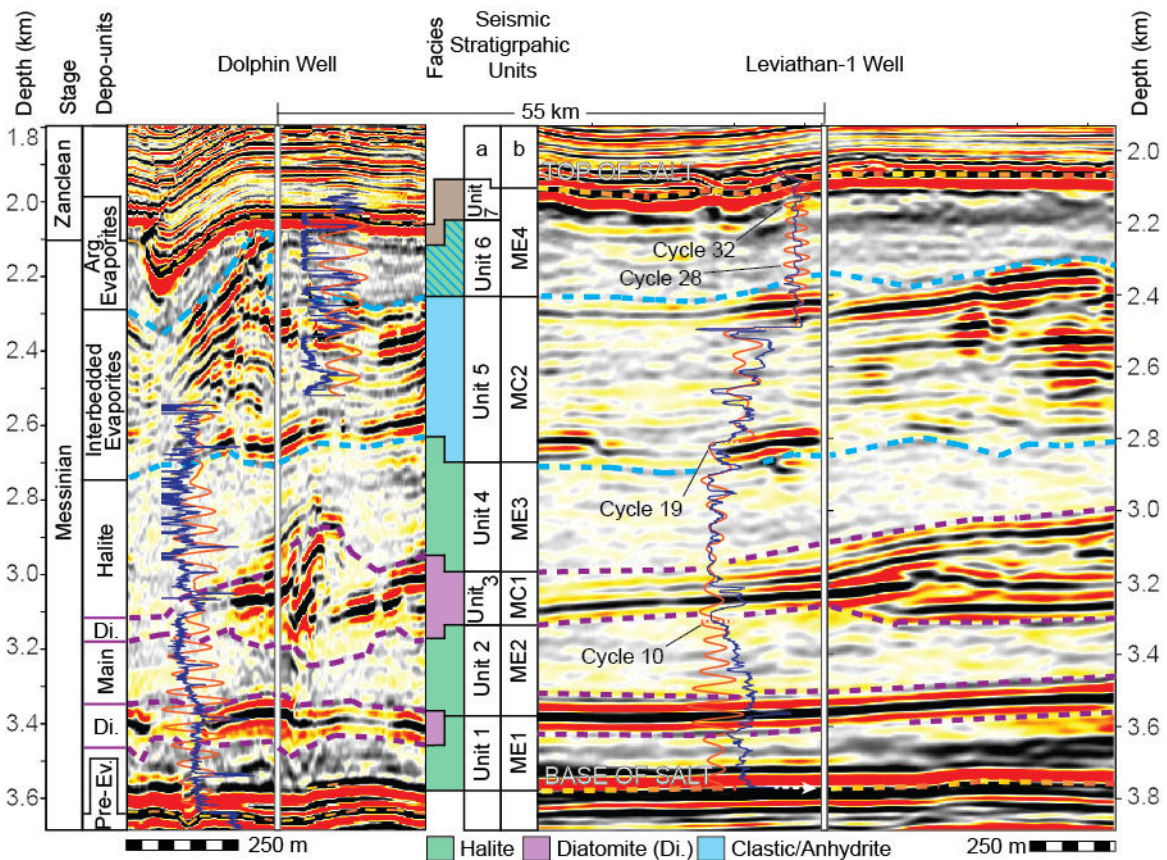
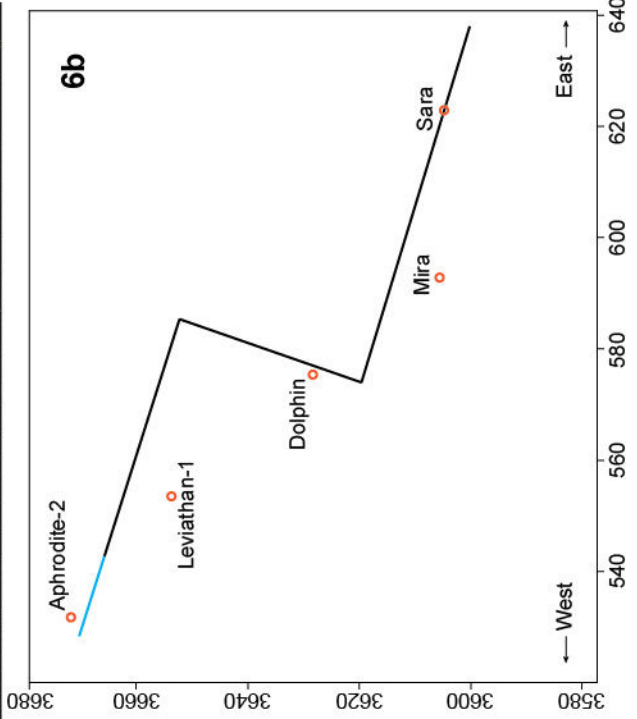
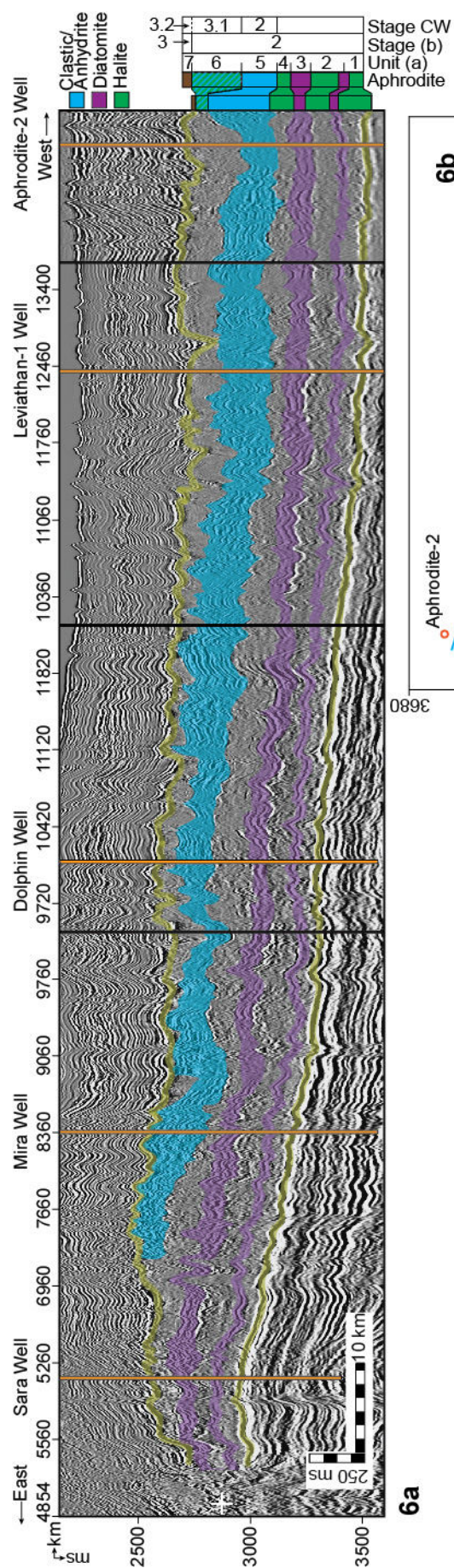


Figure 5. Geophysical data and seismic stratigraphy of the Dolphin and Leviathan-1 wells.

Depth-migrated sections crossing the Dolphin (left) and Leviathan-1 (right) wells (marked by a vertical white line). Overlaid on the sections are the well logs (blue curve left to the well), and the filtered well-log cycles superimposed on the target curves (orange). The depth and lithostratigraphic units (this work) related with the sampled Dolphin well are displayed on the left, and the depth related with the Leviathan-1 well is displayed on the right. Data columns in the middle are seismic-stratigraphic units from (a) Gvirtzman et al. (2013, 2017), and (b) Feng et al. (2016). Note the relatively deformed area of the Dolphin well relative to the more conformal vicinity of the Leviathan-1 well.

1177
 1178
 1179
 1180
 1181
 1182
 1183
 1184
 1185
 1186
 1187
 1188
 1189
 1190
 1191
 1192
 1193
 1194
 1195
 1196
 1197
 1198
 1199
 1200
 1201
 1202
 1203
 1204
 1205
 1206
 1207
 1208
 1209
 1210
 1211
 1212
 1213
 1214
 1215
 1216
 1217
 1218
 1219
 1220
 1221
 1222
 1223
 1224
 1225
 1226
 1227
 1228
 1229
 1230
 1231
 1232



403

1233
1234
1235
1236
1237
1238
1239
1240
1241
1242
1243
1244
1245
1246
1247
1248
1249
1250
1251
1252
1253
1254
1255
1256
1257
1258
1259
1260
1261
1262
1263
1264
1265
1266
1267
1268
1269
1270
1271
1272
1273
1274
1275
1276
1277
1278
1279
1280
1281
1282
1283
1284
1285
1286
1287
1288

404 *Figure 6. A composite seismic section linking the commercial wells across the Levant Basin.*

405 A composite time-migrated seismic section (a), and location map (b), combining three 2D
406 traverses of the TGS survey (dark line) with a transect through the Pelagic 3D volume (blue line)
407 across the Levant Basin, all plotted at a common scale with a vertical exaggeration of ca. x10.
408 Orange vertical lines note the positions of the wells discussed in the text, while black lines note
409 the section stiches, primarily at turning points. The wells are projected laterally onto the seismic
410 profiles by up to 10 km (in the case of the Leviathan-1 well). Note the similar relative spatial
411 thickness of the diatomite beds (purple) in comparison with the largely varying thickness of the
412 Interbedded Evaporites (blue). Stage CW (current work); Stage (b) (Manzi et al., 2018); Unit (a)
413 (Gvirtzman et al., 2013; 2017).

414
415 In the Dolphin well, this seismic facies includes five seismic high-reflectivity bands,
416 corresponding to peaks in the GR and troughs in the RE well logs, appearing within the Main
417 Halite interval between 3375 and 2560 m (Fig. 2). Using a GR value of 20 API as an upper
418 cutoff value for determining the location and thickness of these intervals results in estimated bed
419 thicknesses of 0.9-2.4 m (Fig. 2). Of the 1,056 m Main Halite interval in the Dolphin well, the
420 non-halite sediments form a regional cumulative thickness of 25-40 m (see also Feng et al.,
421 2016; Gvirtzman et al., 2013). At the macro-scale, the content of these layers appears as light
422 gray to white, soft to firm, porous, and occasionally fibrous. SEM imaging and smear-slide
423 analyses indicate that the rock-mass is made of densely packed, very well-preserved, and intact
424 diatoms (Fig. 3), and fine-grained terrigenous sediments (Fig. 4). No other transported or local
425 faunal remains were recognized. Identified diatoms include abundant marine planktonic genera,
426 such as *Coscinodiscus*, *Asteromphalus*, and *Actinoptychus* (*sensu* Tomas, 1996).

1289
1290
1291 427 XRD analysis from available samples of these high-amplitude intervals confirms the log data
1292
1293 428 response and shows an increase in terrigenous grains, mainly composed of quartz, calcite, some
1294
1295 429 clay minerals, and low amounts of anhydrite, dolomite and magnesite (Fig. 4). Halite appears
1296
1297
1298 430 within these samples in a high relative abundance, reaching 45% (Figs 2, 4).
1299

1300 431 Due to the nature of well cuttings, samples from these intervals were only retrieved from the
1301
1302 432 two thickest beds, at 3367.7 m of the Dolphin well with a thickness of 2.4 m, and the two
1303
1304 433 adjacent beds at 3047 and 3034 m with a cumulative thickness of 2.1 m. These intervals are also
1305
1306 434 represented by bands of much higher seismic reflectivity than the thin (1.2-1.4 m), overlying
1307
1308 435 intervals at 2910 and 2646.5 m. Consequently, the two upper intervals might be the same
1309
1310 436 diatomite facies, or only represent marine clastic sediments.
1311
1312

1313 437 *4.1.4 Interbedded Evaporites*

1315 438 This facies is represented in the seismic sections by high-amplitude reflections interbedded
1316
1317 439 with nearly transparent intervals with weak internal reflections (Fig. 3), interpreted in previous
1318
1319 440 studies to represent an alternation of clastic sediments and evaporites (Gvirtzman et al., 2013a;
1320
1321 441 Feng et al., 2016). More recently, Gvirtzman et al. (2017) and Manzi et al. (2018) presented
1322
1323 442 further evidence based on well logs from deep-basin wells in the region (Aphrodite), or by
1324
1325 443 correlation to more proximal well sections (Hannah-1), showing that this interval mostly consists
1326
1327 444 of shale, sand, anhydrite, and halite. The Interbedded Evaporites unit correlates to Unit 5 in
1328
1329
1330 445 Gvirtzman et al. (2013). It covers 2560-2025 m in the Dolphin well, and 2548-2276 m in the
1331
1332 446 Leviathan-1 well. The GR well log in the Leviathan-1 well indicates 3 to 20 m thick clastic beds,
1333
1334 447 interbedded with evaporites varying in thickness from 6 to 30 m. A relatively large diameter
1335
1336 448 wellbore used while drilling this interval might have reduced the GR signal and thinner clastic
1337
1338 449 beds might not have been detected.
1339
1340
1341
1342
1343
1344

1345
1346
1347 450 Due to drilling limitations, the material made available from this interval is partial, and the
1348
1349 451 only sampled sequence consists of the lowermost part above 2560 m in the Dolphin well. We
1350
1351 452 consider grains from this interval as fallouts from the Interbedded Evaporites unit, confirmed by
1352
1353 453 the absence of any indications for a clastic interval in the well-log and seismic data from the top
1354
1355 454 of the Main Halite interval, where these grains appear. The samples are made of hard, light to dark
1356
1357 455 brown sandy shales (Fig. 3). The grain composition of the >63 µm washed residue is very
1358
1359 456 different compared to the underlying Main Halite or Argillaceous Diatomite facies. It contains a
1360
1361 457 higher amount of sub-rounded larger sand grains compared to the diatomite facies, different
1362
1363 458 types of pyrite including large agglutination of pyritohedrons reaching several mm in size, and a
1364
1365 459 diverse faunal composition (Fig. 3). The latter includes few mollusk fragments, ostracods,
1366
1367 460 echinoid spines and a relatively rich assemblage of benthic and planktic foraminifera (Fig. 3).
1368
1369 461 The most common foraminifera are different *Globigerinoides* species, *Orbulina universa* and
1370
1371 462 *Sphaeroidinellopsis seminulina* (younger than 15 Ma; Berggren et al., 2006). Older Cretaceous
1372
1373 463 to Eocene foraminifera species are also present, indicating reworking processes, most likely from
1374
1375 464 exposed basin margins. These include *Parasubbotina pseudobulloides* (Daninian-Selandian; Fig.
1376
1377 465 3.D.13), *Plummerita hantkeninoides* (Maastrichtian; Fig. 3.D.15), and *Subbotina triloculinoides*
1378
1379 466 (Paleocene; Fig. 3.D.17). While no overlying samples exist, this interval was logged and a
1380
1381 467 reliable lithological interpretation is presented by extrapolating the coupling between sample
1382
1383 468 analysis (XRD and micropaleontology) and the log data from the lower to the upper part of the
1384
1385 469 section (Fig. 2). The clastic input is estimated from the geophysical data as ~40% of the 535 m
1386
1387 470 thick unit in the Dolphin well. However, due to local deformations in the Dolphin well area, the
1388
1389 471 Interbedded Evaporites are displaced and their top is reached at the top of the MSC section.
1390
1391
1392
1393
1394
1395
1396
1397
1398
1399
1400

1401
1402
1403 472 Comparison with Manzi et al. (2018) suggests that Unit 6 is not represented in the Dolphin
1404 well but that Unit 5 marks the top of the section (Fig. 5). However, seismic and well-log
1405 473
1406 interpretation indicates that in the Leviathan-1 well another ~200 m of evaporites appear above
1407 474
1408 the Interbedded Evaporites, which corresponds to Unit 6 in Manzi et al. (2018). There, the
1409 475
1410 Interbedded Evaporites (Unit 5) are 260 m thinner than in the Dolphin well (Fig. 5). This
1411 476
1412 discrepancy is presumably the result of post-depositional halokinetic deformation and
1413 477
1414 imbrication of Unit 5 in the Dolphin well, as imaged in the seismic data (Fig. 5).
1415 478
1416
1417

1418 479 *4.1.5 Argillaceous Evaporites*

1420 480 This interval was not sampled in any of the Levant Basin studies and its interpretation is only
1421 based on the interpretation of seismic and well-log data. In the Leviathan-1 well this interval
1422 481
1423 covers the uppermost part of the evaporites between 2090 and 2320 m (Fig. 5). The transparent
1424 482
1425 reflective character of this interval in the seismic section includes cyclic darker bands. The unit
1426 483
1427 appears to be composed of clastic sediments, probably clays, silts and sands, which are
1428 484
1429 characterized by GR values of 7 to 15 API. Intervals of ca. zero GR are interpreted as
1430 485
1431 argillaceous anhydrite. Gvirtzman et al. (2013; 2017), Feng et al. (2017), and Manzi et al. (2018)
1432 486
1433 refer to this interval as Unit 6, which is generally lumped with the underlying halite as part of the
1434 487
1435 evaporite unit. Regionally, the presence of Unit 6 is limited to the westernmost and deeper areas
1436 488
1437 of the basin, while it is truncated to completely removed landward to the east (Fig. 6). The
1438 489
1439 amount of truncation on Unit 6 gradually increases eastwards, eroding also Units 5-2 at the
1440 490
1441 eastern parts (Gvirtzman et al., 2013, Feng et al., 2017; the current study). Both the Dolphin and
1442 491
1443 the Leviathan wells are within the deeper areas in which Unit 6 is present, but due to local
1444 492
1445 deformations it might be underrepresented in the Dolphin well. A 5 m clastic and anhydrite bed
1446 493
1447 defines the top of this unit, marked by a nearly transparent seismic interval in the Leviathan-1
1448 494
1449
1450
1451
1452
1453
1454
1455
1456

1457
1458
1459 495 well, as indicated by a sharp drop in GR and drilling penetration rate relative to the overlying
1460
1461 496 Pliocene sediments. This anhydrite interval is most likely part of Unit 7 in Gvirtzman et al.
1462
1463
1464 497 (2018), or the Nahal Menashe in Madof et al. (2019).
1465

1466 498 **4.2 Chronology of halite deposition and well log frequency analysis**

1467

1468
1469 499 In order to attain a direct age control on the duration of halite deposition, the halite samples
1470
1471 500 were washed and inspected for microfossils, prepared as smear slides, and examined under SEM
1472
1473 501 in search for the preservation of eukaryotic life in the evaporites, which failed.
1474

1475 502 We also measured the Sr-isotopic composition of evaporite samples in order to compare them
1476
1477 503 with the well-established Sr isotope stratigraphy constructed from elsewhere in the
1478
1479 504 Mediterranean (e.g., Topper et al., 2011; Roveri et al., 2014; Flecker et al., 2015). This published
1480
1481 505 dataset shows that Sr-isotope data from stage 1 lie mainly within error of the ocean-water curve
1482
1483 506 (McArthur et al., 2012), suggesting that the Mediterranean was connected to the global ocean
1484
1485 507 during the initial phases of the MSC (e.g., Roveri et al., 2014; Flecker et al., 2015). During
1486
1487 508 stages 2 and 3 the Mediterranean's Sr record diverges from ocean-water values towards much
1488
1489 509 lower ratios that reflect a substantially smaller connection to the global ocean and dominance of
1490
1491 510 fresh-water sources such as the Nile, Rhone, and input from the Paratethys, particularly during
1492
1493 511 the Lago Mare phase (e.g., Roveri et al., 2014; Flecker et al., 2015). Sr-isotope data from the
1494
1495 512 lowest Pliocene are again within error of ocean-water values, indicating an abrupt transition back
1496
1497 513 to full connectivity after the MSC (e.g., Roveri et al., 2014; Flecker et al., 2015). Despite the
1498
1499 514 wide geographical distribution of the Mediterranean samples from which this published Sr-
1500
1501 515 isotope stratigraphy has been constructed, the pattern appears to be consistent, indicating that the
1502
1503 516 controlling factor was Mediterranean-Atlantic exchange and that the Mediterranean behaved as a
1504
1505 517 single basin throughout the MSC (Flecker et al., 2015). However, the dataset does not include
1506
1507
1508
1509
1510
1511
1512

1513
1514
1515 518 samples from these deep-water Eastern Mediterranean sites as they were previously not
1516
1517 519 available; it therefore makes sense to compare new analyses from these locations with the
1518
1519
1520 520 existing Sr-chemostratigraphic scheme.

1521
1522 521 Halite is highly soluble and it is therefore challenging to clean samples prior to analysis. We
1523
1524 522 used the basic method described in Gvirtzman et al. (2017) and Manzi et al. (2018), with
1525
1526 523 additional eleven different techniques (Fig. S1, Table S1) for attempting to isolate the halite
1527
1528 524 crystals from any contaminant phases coating the samples such as clay or industrial drilling
1529
1530 525 additives. The data generated for each of the nine different samples analyzed is highly variable,
1531
1532 526 ranging from a few values within error of Late Miocene ocean water (McArthur et al., 2012), to
1533
1534 527 substantially higher values (Fig. S1, Table S1). There is no consistency between the data
1535
1536 528 generated and the technique used for dissolving the halite (Fig. S1, Table S1), suggesting that we
1537
1538 529 have not been able to reliably isolate the halite from contaminant phases coating the crystals by
1539
1540 530 any of the methods used. We therefore conclude that none of this data should be considered as
1541
1542 531 representing a primary record of Eastern Mediterranean water at this time.

1543
1544 532 Similar high values have been reported for halite from other industrial wells in the Levant
1545
1546 533 Basin (Gvirtzman et al., 2017; Manzi et al., 2018). Manzi et al. (2018) attributed the
1547
1548 534 anomalously high values to “local, diverse, short-term Sr input”, but did not specify what this
1549
1550 535 input might be. One possibility is that these published halite values from industrial cuttings may,
1551
1552 536 like our data, be contaminated. We conclude that a robust Sr-isotope record for the deep-basin
1553
1554 537 halite deposits will only be achieved either by establishing a reliable method for removing
1555
1556 538 contaminant phases or by recovering halite samples without the use of industrial drilling fluids,
1557
1558 539 e.g., through scientific drilling (Camerlenghi et al., 2014).

1569
1570
1571 540 Next, we attempted to construct a chronostratigraphic framework for the Levant MSC
1572
1573 541 deposits based on astrochronological tuning. We carried out spectral analysis of GR and RE
1574
1575 542 well-logs to correlate the Levant MSC section to astronomical target curves, and the more
1576
1577 543 proximal to onshore Mediterranean MSC deposits. REDFIT spectral analyses (Schulz and
1578
1579 544 Mudelsee, 2002) of the Dolphin and Leviathan-1 well-log data from the base to the top of the
1580
1581 545 evaporite unit (3616-2025 m in the Dolphin well, divided into three intervals for spectral
1582
1583 546 analysis; Fig. S2) indicates statistically significant, periodical signals in the RE and GR logs.
1584
1585 547 However, the GR produces a weaker signal than the RE log within the massive halite intervals.
1586
1587 548 This is expected, as pure halite does not contain the elements U, Th, and K and their decay series
1588
1589 549 responsible for natural GR radiation emitted by rocks. However, several examples indicate how
1590
1591 550 different log responses occur within halite sequences. For example, inner-halite variations such
1592
1593 551 as thin clay laminae caused by microstratification within the brines might occur (Sonnenfeld,
1594
1595 552 1983). Alternatively, thin sulphate layers (Biehl et al., 2014) have also been shown to produce
1596
1597 553 log-responses.

1600
1601 554 Each of the analyzed log segments is characterized by several frequency peaks exceeding the
1602
1603 555 chi 95% confidence interval (Fig. S2). Each segment was bandpass filtered according to these
1604
1605 556 frequencies, and the fit of the filtered version to the original well-log was examined, ultimately
1606
1607 557 selecting the best-fit result for subsequent analysis. Both logs are composed of significant and
1608
1609 558 approximately overlapping periodical frequencies, with an average cycle thickness of ~50 m
1610
1611 559 (Fig. S2). While the RE log appears to be more attuned to inner-halite variations in the Main
1612
1613 560 Halite interval, the GR log is more consistent and provides a more reliable fit to the well log
1614
1615 561 target curve in the units above 2833 m. Consequently, the Dolphin well cyclostratigraphy is
1616
1617 562 constructed from information derived from the GR and RE logs that cover the lower and upper
1618
1619
1620
1621
1622
1623
1624

1625
1626
1627 563 parts of the section (Fig. S2). The lower part of the Main Halite interval (cycles 1-11; Fig. S2) is
1628
1629 564 not very well represented by the Gaussian filter, with some five cycles that fit well with the
1630
1631 565 target curve. The upper part of the Main Halite interval is best filtered by using the RE log with a
1632
1633 bandwidth of 49 m (cycles 12-24; Fig. S2). The cycles within the upper part of the section in the
1634 566 Interbedded Evaporite interval are picked up relatively clearly by the GR log (cycles 25-32; Fig.
1635
1636 567 S2). However, as the Dolphin well section from the Interbedded Evaporites and above
1637
1638 568 experienced significant deformation (Figs 5, 6), the well-log cyclostratigraphy of the upper part
1639
1640 569 of the studied section is not reliable in this well.
1641
1642 570

1644 571 Several frequency peaks exceeding the chi 95% confidence interval were also identified in
1645
1646 572 the Leviathan-1 well-log analysis, where deformation is reduced and Unit 6 is represented (Figs
1647
1648 573 5, 6). The RE log was cleaned from outlier spikes and used for bandpass filtering. The original
1649
1650 574 log includes several short intervals in which values range from 10's or 100's of ohm*m to
1651
1652 575 extremely high 18,000+ ohm*m values, masking cyclic trends in the data. Figure 5 shows the
1653
1654 576 cleaned RE log overlain on the seismic data. There is a much-improved fit between the log and
1655
1656 577 filtered cycles, relative to the Dolphin well, with only a few examples of a misfit between the
1657
1658 578 two. A good fit is also generally apparent between the seismic signal and the well-log response.
1659
1660 579 The Main Halite interval includes 19 cycles, in which cycles 4 and 5 are within the first
1661
1662 580 Argillaceous Diatomite beds, and cycles 11-13 are within the second. The cycles within the
1663
1664 581 Interbedded Evaporite interval are picked up relatively clearly by the RE log (cycles 19-27; Fig.
1665
1666 582 5). In the Argillaceous Evaporites in the uppermost part of the studied section in the Leviathan-1
1667
1668 583 well, the RE log response fits with banding in the seismic data, which is also picked by bandpass
1669
1670 584 filtering (cycles 27-33; Fig. 5).
1671
1672
1673
1674
1675
1676
1677
1678
1679
1680

1681
1682
1683
1684 585 Consequently, bandpass filtering of the well logs results in ~33 cycles from the base to the top
1685
1686 586 of the evaporite sequence in the Levant Basin. In the next two sections, we present different
1687
1688 587 findings supporting the occurrence of lithological cycles along the studied section, followed by
1689
1690 588 the astrochronologic interpretation of these cycles in the discussion section.

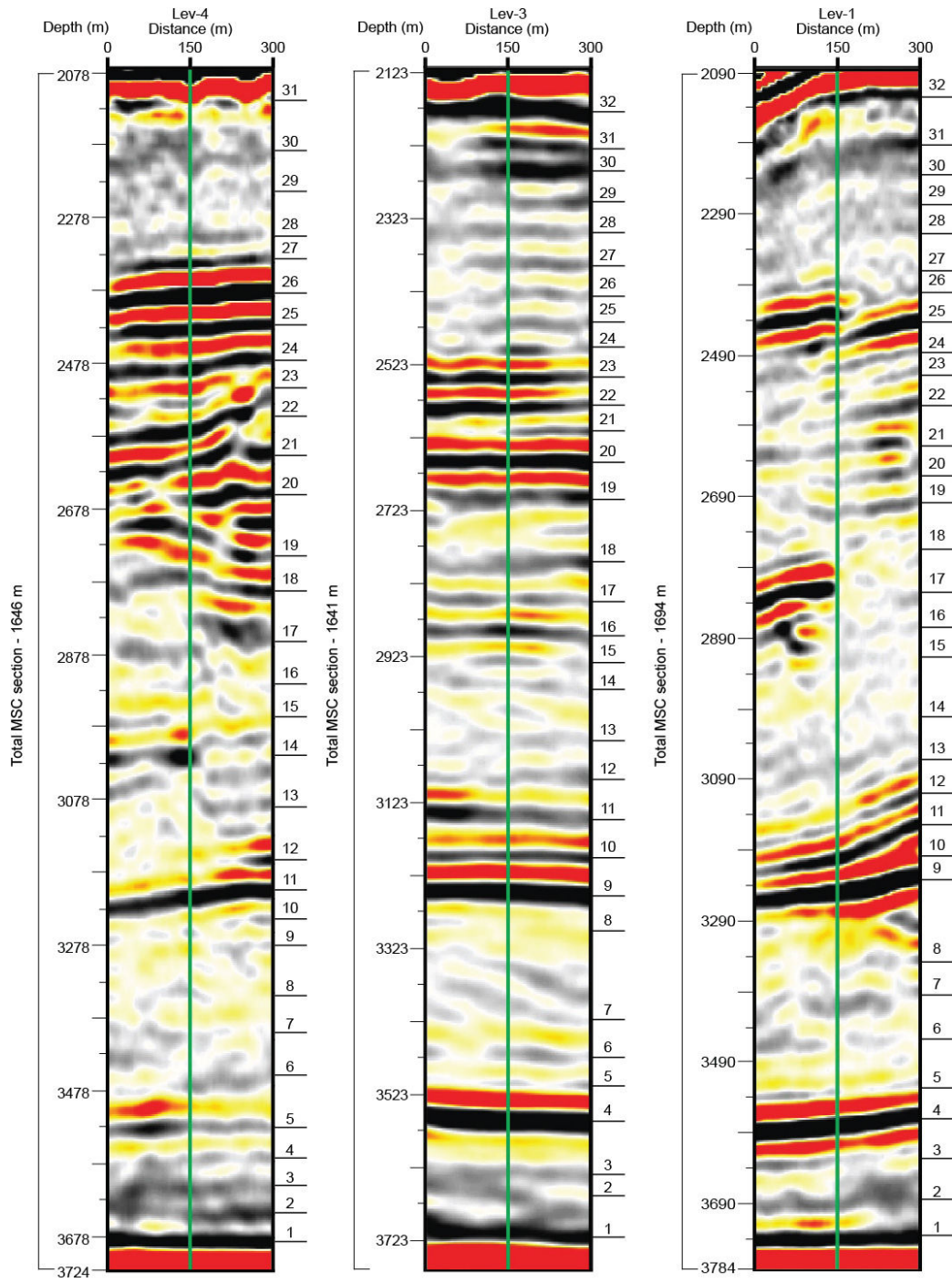
1692 589 **4.3 Cyclicity of seismic reflective phases**

1694
1695 590 Modern high-quality 3D seismic imagery represents a new frontier for astronomical
1696
1697 591 calibration, potentially adding a chronological time-frame for seismic stratigraphy. However, in
1698
1699 592 most marine settings, precession-scaled cycles are registered at a thicknesses-to-cycles ratio
1700
1701 593 which has a much higher resolution than the seismic data. Yet, several studies show a good
1702
1703 594 match between the number of precession-induced astronomic cycles and the number of positive
1704
1705 595 vs. negative seismic phases within MSC deposits (Driussi et al., 2015; Geletti et al., 2014). This
1706
1707 596 is explained by the considerably higher sedimentation rates that characterize evaporite deposits,
1708
1709 597 relative to the much lower rates typical of normal-marine clastic or carbonate deposition. The
1710
1711 598 higher sedimentation rates result in an improved alignment between the spacing, or resolution, of
1712
1713 599 lithologic variations and the resolution of the seismic imagery. As orbital forcing was repeatedly
1714
1715 600 identified as determining lithological variations during the MSC (e.g., Krijgsman et al., 1999;
1716
1717 601 Ochoa et al., 2015; Roveri et al., 2014a; Sierrro et al., 2001; van den Berg et al., 2015), seismic
1718
1719 602 data recording these variations can be used with caution for strengthening the well-log
1720
1721 603 astronomical tuning-based age models. This is not the case for the Pre-Evaporites in this area,
1722
1723 604 which deposited at an average sedimentation rate of 11.4 cm/kyr and a cycle thickness of around
1724
1725 605 2-3 m, as shown by Meilijson et al. (2018). This thickness is below the resolution of the seismic
1726
1727 606 data. Here, we use the seismic 3D data for additional validation of our results from well-log
1728
1729
1730
1731
1732
1733
1734
1735
1736

1737
1738
1739
1740
1741
1742
1743
1744
1745
1746
1747
1748
1749
1750
1751
1752
1753
1754
1755
1756
1757
1758
1759
1760
1761
1762
1763
1764
1765
1766
1767
1768
1769
1770
1771
1772
1773
1774
1775
1776
1777
1778
1779
1780
1781
1782
1783
1784
1785
1786
1787
1788
1789
1790
1791
1792

607 curves based on REDFIT spectral analysis and bandpass-filtering within the Main Halite and
608 overlying intervals.

609 In practice, the seismic tuning analysis was performed by counting the number of reflectivity
610 phases on three different sections where wells were drilled within the 3D geophysical dataset of
611 the study area (Figs 1, 7). Yet, as halokinetic deformation affected the Levant deep-basin
612 evaporites, and particularly their upper units (Gvirtzman et al., 2013a), spatial variations are
613 expected even considering a scenario of regionally uniform deposition. Such variations in the
614 number and thickness of cycles are indeed observed when comparing different seismic sections,
615 reflecting the local variabilities (Fig. 7). In total, a consistent number of ~30 reflectivity cycles is
616 identified in different locations, which is in agreement with the cyclicity identified through well-
617 log spectral analysis.



618

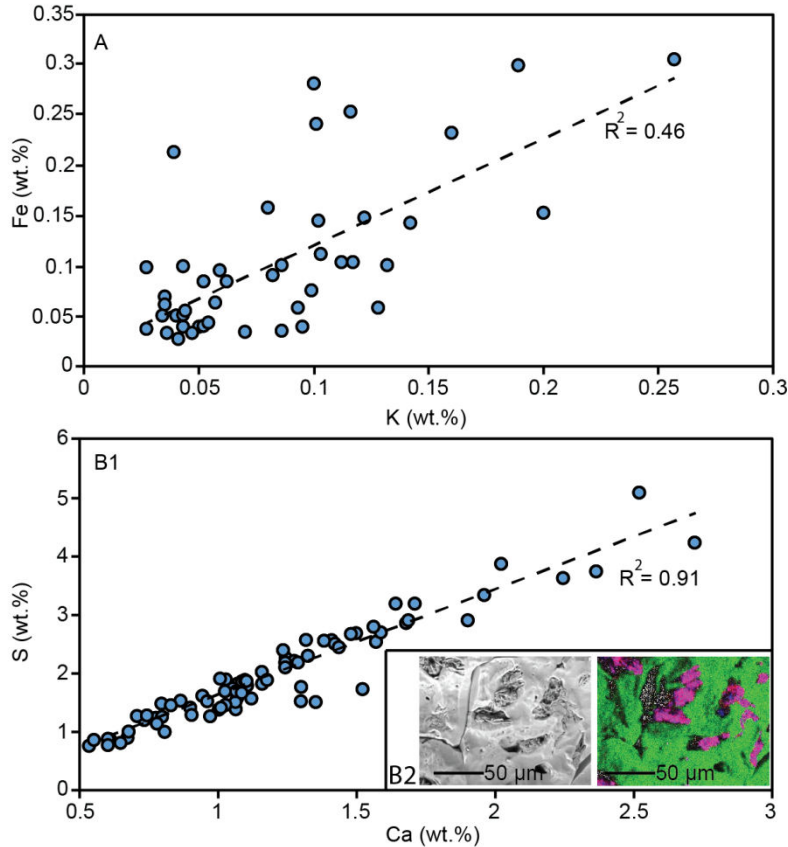
619 *Figure 7. Seismo-cyclostratigraphy of three seismic profiles around wells in the study area.*

620 Three depth-migrated profiles that are aligned with wells in the central Levant. Black lines
 621 with numbers on the right hand side of each seismic profile represents a reflectivity phase (black)
 622 cycle count along the section. Left bar show actual depth for each section and the total depth
 623 from base to top of the MSC section in each well.

4.4 Elemental variations within evaporite samples

The wellbore cuttings do not allow recognition of macro-scale sedimentological features, which may reflect the cyclicity identified in the well logs and seismic data within the halite sequence. Tuning of marginal MSC sections has been done based on lithological transitions, such as branching selenite to massive selenite, or chaotic deposits to clastic evaporites in stages 1-3 (e.g., Roveri et al., 2014a), or diatomite-shale-carbonate transitions in the Pre-Evaporites (Ochoa et al., 2015; Sierro et al., 2001). Here, we explore whether minor inner-halite chemical variability down-section can account for the filtered cycles and variable log response within apparently massive and homogenous halite. Other Miocene intervals of homogeneous lithology have also been shown to contain cyclic changes in the chemical composition of the sediments (van den Berg et al., 2015), which are assumed to represent shifts in the depositional environment. We hypothesize that these variations, if present in deep Mediterranean basins, could correspond to: 1) variations in riverine runoff and associated influx of clastic material into the basin, and/or 2) shifts in the degree of evaporation determining the type of deposited evaporites. Both of these drivers can be related to orbital forcing (Marzocchi et al., 2015; Simon et al., 2017).

We observe a relatively low correlation ($R^2=0.46$; Fig. 8A) between Fe and K in the Levant halite samples, which is not in agreement with the occurrence of continentally-derived material transported to the Eastern Mediterranean. In contrast, a high elemental correlation ($R^2=0.91$; Fig. 8B1) is observed between S and Ca, which confirms that low and variable amounts of minerals rich in CaSO_4 (i.e., gypsum and anhydrite) represent an integral part of evaporite deposition in the Main Halite of the deep Levant Basin.



646
647 *Figure 8. X-ray fluorescence elemental analysis of the Levant evaporites*

648 Results of XRF elemental analysis are shown for 77 halite samples for specific elemental
649 composition. (A) Note the low correlation between iron and potassium, while (B1) shows a high
650 sulfur to calcium correlation. The high correlation between sulfur and calcium is corroborated by
651 SEM-EDS imagery and element maps (halite sample from 3058 m; (B2)) showing the
652 distribution of Na (green), Ca (blue) and S (red), indicating the occurrence of gypsum
653 microcrystals (purple; B2) within cavities of the larger and much more common halite crystals.

654
655 This notion is further confirmed by the recognition of calcium sulfate microcrystals minerals
656 within the halite cuttings (Fig. 8B-2). Note that not all halite crystals include a similar
657 precipitation of calcium sulfates in small pores. We suggest that shifts in the amount of gypsum
658 or anhydrite deposition along the section might correspond with the cycles obtained by well-log
659 spectral analysis.

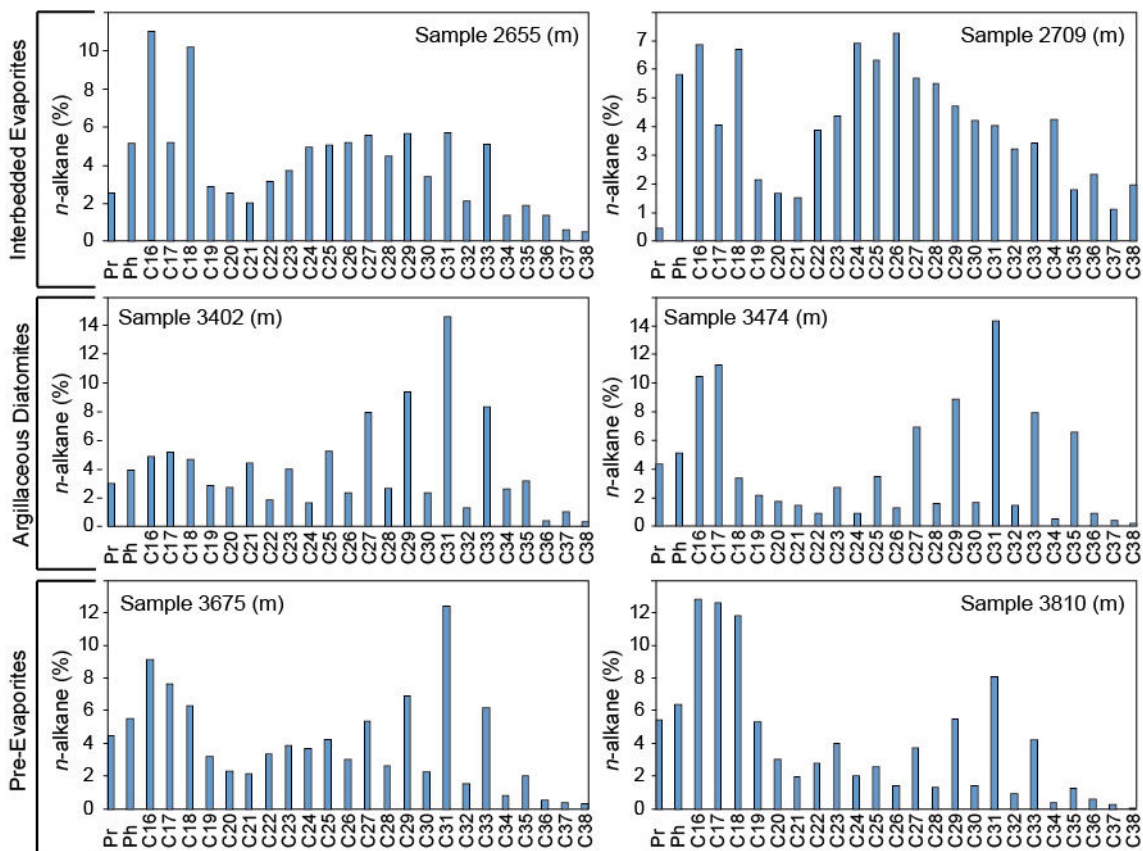
4.5 Organic geochemistry as a stratigraphic marker

Biomarker data allow us to identify sources of sedimentary organic matter preserved in the cuttings as well as to gain insights into its thermal history. We observed distinct differences in the biomarker distribution found in the Pre-Evaporites, the Argillaceous Diatomites within the Main Halite deposits, and the overlying Interbedded Evaporites interval. The *n*-alkanes range from *n*-C₁₆ to *n*-C₃₈ (Table 1, Fig. 9), and their distribution varies between samples. For example, while short- and long-chain alkanes are more predominant in the Pre-Evaporites and the Argillaceous Diatomites, mid-chain alkanes are more prominent in the Interbedded Evaporites. Additionally, the carbon preference index (CPI) of long-chain *n*-alkanes, which portrays the degree of oddity in the distribution of the different *n*-alkanes, varies around 5-7 in the Pre-Evaporites, 4-12.3 in the Main Halite (Argillaceous Diatomites) interval, and around 1.9-2.9 in the Interbedded Evaporites (Table 1; Fig. 10). The Argillaceous Diatomites also contain the lowest Pr/Ph ratios (Table 1, Fig. 10) compared to other samples. The relative abundance of long-chain *n*-alkanes (C₂₅-C₃₅) is more elevated within the Argillaceous Diatomites and Pre-Evaporite. This is reflected in the ratio of long chain (C₂₅-C₃₇) to short chain (C₁₆-C₂₁) *n*-alkanes, which maximize in the Argillaceous Diatomites (1.9), followed by the Interbedded Evaporites (1.6) and the Pre-Evaporites (1.2). The C₃₁ *n*-alkane commonly is the most dominant homologue.

Selected hopane- and sterane-based thermal maturity indices (Table 2; Fig. 11; Peters and Moldowan, 1993; Rullkötter and Marzi, 1988; Peters et al., 2005) also indicate major differences between samples from the Pre-Evaporites and Argillaceous Diatomites, relative to those from the lower part of the Interbedded Evaporites. As summarized in Table 2, the diatomite facies exhibit the lowest thermal maturity values, to be followed by the Pre-Evaporites, while much more mature indices are reached in the overlying Interbedded Evaporites. This is clearly indicated by

2017
2018
2019
2020
2021
2022
2023
2024
2025
2026
2027
2028
2029
2030
2031
2032
2033
2034
2035
2036
2037
2038
2039
2040
2041
2042
2043
2044
2045
2046
2047
2048
2049
2050
2051
2052
2053
2054
2055
2056
2057
2058
2059
2060
2061
2062
2063
2064
2065
2066
2067
2068
2069
2070
2071
2072

683 the presence of hopanes with the biological $\beta\beta$ configuration, in addition to low values of the C_{31}
684 S/R hopanes ratio and the C_{28} $\alpha\alpha\alpha$ 20S/20R steranes ratio, and more elevated values of the C_{30}
685 $\beta\alpha/\alpha\beta$ hopanes ratio in immature samples (Fig. 11). Additionally, the Argillaceous Diatomites
686 samples exhibit a lack of re-arranged steranes compared to the overlying and underlying
687 intervals (Fig. 11; Table 2).

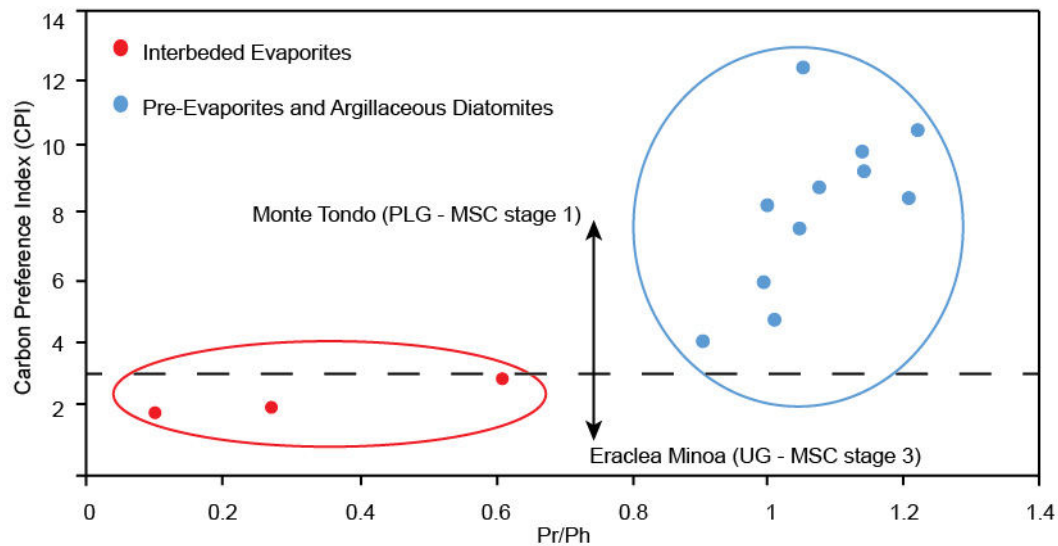


688

689 *Figure 9. n-alkane distribution in non-halite intervals.*

690 Two samples from each depositional unit (left and right columns) show the relative abundance of
691 pristane (Pr), phytane (Ph), and C_{16} - C_{38} n -alkanes. Note the odd-over-even carbon-number
692 predominance of long-chain n -alkanes in the Argillaceous Diatomites (center) and Pre-
693 Evaporites (lower) relative to the overlying Interbedded Evaporites. Also observe the higher CPI,
694 i.e., the distribution of n -alkanes, in the Pre-Evaporites and Argillaceous Diatomites relative to
695 the Interbedded Evaporites, and higher relative abundance of medium-long chained compounds.

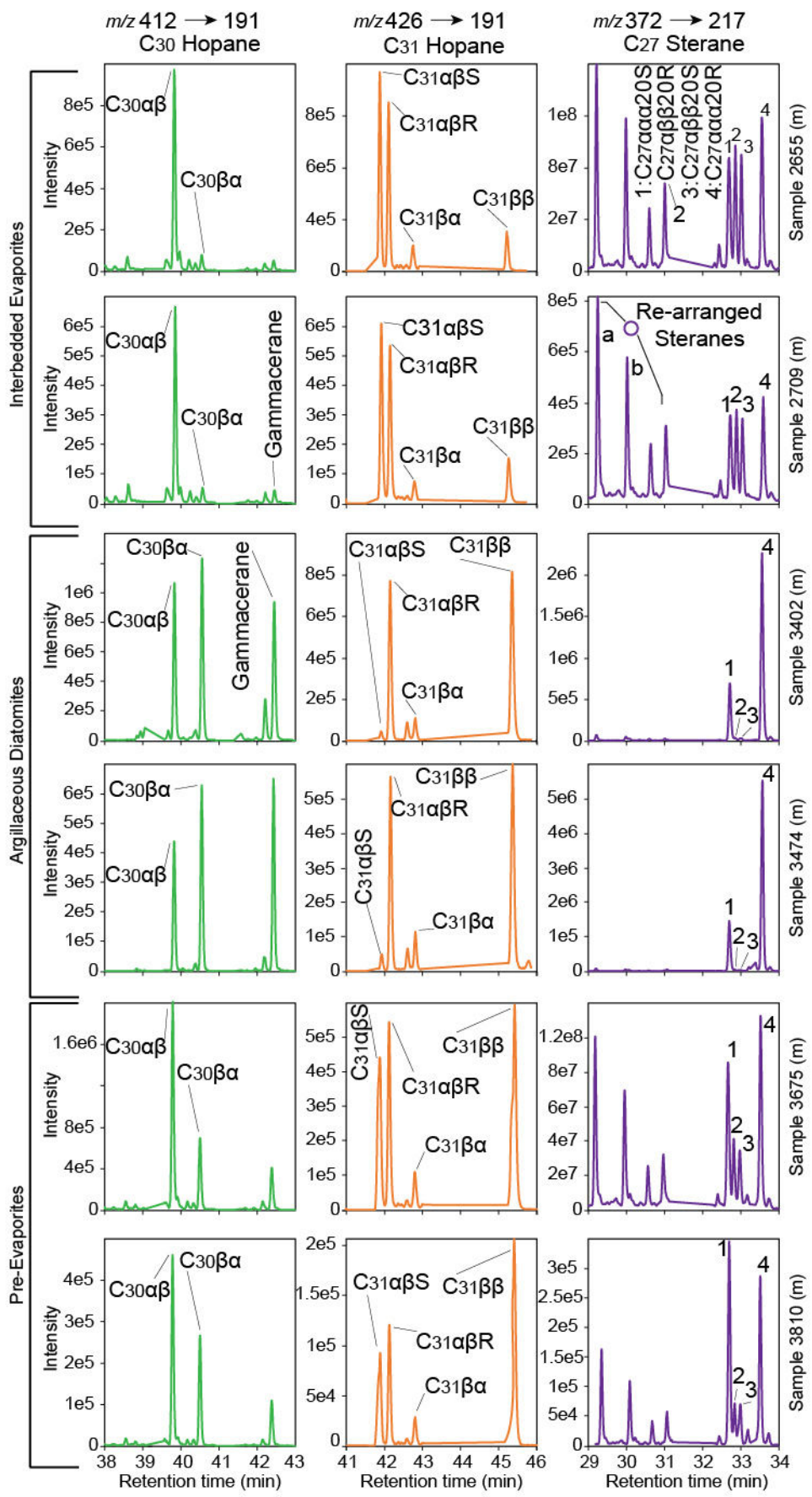
696



697
698 *Figure 10. Pristane/phytane ratio to carbon preference index (CPI) plot.*

699 Legend indicates the strata of plotted samples. Horizontal dashed line indicates the separation
700 of CPI values of marginal section across the MSC reported by Vasiliev et al. (2017). Note that
701 the samples from the Interbedded Evaporites plot in the area of values measured in stage 3 of the
702 MSC (Vasiliev et al., 2017), while the lower samples from the Levant plot in the area of MSC
703 stage 1. Also note the separation in Pr/Ph values between the Interbedded Evaporites relative to
704 the Pre-Evaporites and Argillaceous Diatomites.

2129
 2130
 2131
 2132
 2133
 2134
 2135
 2136
 2137
 2138
 2139
 2140
 2141
 2142
 2143
 2144
 2145
 2146
 2147
 2148
 2149
 2150
 2151
 2152
 2153
 2154
 2155
 2156
 2157
 2158
 2159
 2160
 2161
 2162
 2163
 2164
 2165
 2166
 2167
 2168
 2169
 2170
 2171
 2172
 2173
 2174
 2175
 2176
 2177
 2178
 2179
 2180
 2181
 2182
 2183
 2184



2185
2186
2187
2188
2189
2190
2191
2192
2193
2194
2195
2196
2197
2198
2199
2200
2201
2202
2203
2204
2205
2206
2207
2208
2209
2210
2211
2212
2213
2214
2215
2216
2217
2218
2219
2220
2221
2222
2223
2224
2225
2226
2227
2228
2229
2230
2231
2232
2233
2234
2235
2236
2237
2238
2239
2240

706 *Figure 11. Distribution of selected bacterial hopanes and algal steranes.*

707 Two samples from each depositional unit (left and right columns) were investigated for the
708 distribution of aliphatic hydrocarbons using selective reaction monitoring (SRM) analysis. Each
709 sample (numbered on the right) includes a chromatogram for three given SRM transitions: 412
710 → 191 (C₃₀ Hopane); 426 → 191 (C₃₁ Hopane); 372 → 217 (C₂₇ Sterane). The C₂₇ rearranged
711 steranes are marked as (a) C₂₇β α 20S and (b) C₂₇β α 20R. High ratios of C₃₁αβS/R hopanes and
712 C₂₇αααS/R steranes, along with low values of C₃₁ββ/αβ and C₃₀ββ/αβ hopane ratios, indicate a
713 higher, yet mixed, maturity of the organic matter preserved in the Interbedded Evaporite shale
714 samples compared to samples from the Pre-Evaporites and Argillaceous Diatomites. The
715 underlying diatomite facies sediments are immature in nature, while the Pre-Evaporite shale
716 samples exhibit mixed signatures (e.g., high C₃₁ββ/αβ hopanes and C₂₇ αααS/R steranes).

2241
2242
2243 **717 5. Discussion**
2244
2245

2246 **718 5.1 Deep-sea halite depositional environment**
2247

2248
2249 719 The halite in the Dolphin well appears to be a pure, homogeneous layer, indicating a
2250
2251 720 monotonous deposition of halite in the deep Levant Basin. Transmitted-light microscopy and
2252
2253 721 SEM analysis of halite crystals (<0.5 cm) throughout the section reveals no distinct
2254
2255 722 sedimentological variations. XRD analysis also confirms a uniform, halite-dominated
2256
2257 723 mineralogical composition (Fig. 4). Gypsum microcrystal were observed within several halite
2258
2259 724 crystals as seen in SEM-EDS (Fig. 8B-2), and elemental variations supporting shifts in the
2260
2261 725 relative amounts of calcium sulfates deposited along the halite part of the section were apparent
2262
2263 726 in XRF analysis (Fig. 8). However, we found no features similar to the lithological variations
2264
2265 727 reported from the Realmonte salt mine (Lugli et al., 1999) or the intermediate depth halite of the
2266
2267 728 Balearic Basin (Site 134; Lugli et al., 2015), such as cumulates of halite plates settled out from a
2268
2269 729 stratified water column, plate cumulates in a shallowing-upward sequence containing kainite
2270
2271 730 layers, or cumulates of skeletal hoppers with chevron overgrowths. The above conclusion might
2272
2273 731 be biased due to the usage of well cutting, possibly not allowing to recognize these features.
2274
2275 732 However, the mm-scale variations in the salt deposits shown by Lugli et al. (2015) should have
2276
2277 733 been recognizable in the halite well cuttings. The lack of comparative features between the
2278
2279 734 marginal halite and the Levant deep-basin halite is also evident when comparing the halite
2280
2281 735 samples in the Dolphin well and halite deposits penetrated by DSDP drilling. There is a clear
2282
2283 736 distinction between the featureless Dolphin halite and the halite interbedded with detrital sand
2284
2285 737 and small anhydrite nodules recovered at DSDP Site 134 offshore Sardinia in the margins of the
2286
2287 738 western Mediterranean (Hsü et al., 1973). The halite sampled in Site 134 is banded similarly to
2288
2289 739 the Sicily halite reported by Lugli et al. (1999), with alternative cloudy and translucent beds.
2290
2291
2292
2293
2294
2295
2296

2297
2298
2299
2300
2301
2302
2303
2304
2305
2306
2307
2308
2309
2310
2311
2312
2313
2314
2315
2316
2317
2318
2319
2320
2321
2322
2323
2324
2325
2326
2327
2328
2329
2330
2331
2332
2333
2334
2335
2336
2337
2338
2339
2340
2341
2342
2343
2344
2345
2346
2347
2348
2349
2350
2351
2352

740 Similarly, the banded halite and polyhalite at DSDP Sites 374, 375 and 376 in the Eastern
741 Mediterranean (Garrison et al., 1978) does not resemble the homogenous halite recovered in the
742 Dolphin well. The homogeneous nature of the halite observed in the Dolphin well suggests
743 continuous deep-sea deposition, in comparison to halite deposition in the shallower marginal
744 basins.

745 Modern analogs for ancient deep-water halite depositional environments are scarce. An
746 exception is the hypersaline Dead Sea, in which active precipitation of halite occurs within the
747 deepest parts of the basin (Arnon et al., 2016; Sirota et al., 2016, 2017; Steinhorn, 1983; Stiller et
748 al., 1997). The Dead Sea floor is divided into two principal environments: a deep, hypolimnetic
749 lake floor, and a shallow, epilimnetic lake floor (Sirota et al., 2016, 2017). Halite continuously
750 precipitates with seasonal variations influencing the type of halite formation on the deeper
751 hypolimnetic lake floor. However, the shallow epilimnetic lake floor is also subject to seasonal
752 variations, which produce annual unconformities related to halite deposition and dissolution. The
753 epilimnion part of the lake is undersaturated during the summer and halite is dissolved, while
754 winter is characterized by a heavily supersaturated water column and halite is crystallized (Sirota
755 et al., 2016). Summer is associated with higher loss of water by evaporation from the lake
756 compared to the winter. Sirota et al. (2016) argue that the seasonal halite deposition cycle in the
757 Dead Sea epilimnion is controlled by the decrease in the saturation with increasing temperature,
758 which overcomes the effect of enhanced summer evaporation. The hypolimnion is supersaturated
759 and halite is crystallized throughout the year, with higher supersaturation and higher
760 crystallization rates during winter. During summer, the undersaturated epilimnion dissolves
761 halite, forming highly saturated dense solutions. These solutions flow to the hypolimnion, which
762 becomes supersaturated and crystallizes halite. This process results in focusing of halite deposits

2353
2354
2355
2356
2357
2358
2359
2360
2361
2362
2363
2364
2365
2366
2367
2368
2369
2370
2371
2372
2373
2374
2375
2376
2377
2378
2379
2380
2381
2382
2383
2384
2385
2386
2387
2388
2389
2390
2391
2392
2393
2394
2395
2396
2397
2398
2399
2400
2401
2402
2403
2404
2405
2406
2407
2408

763 in the deep hypolimnetic parts of the evaporitic sea, and thinning of the shallow epilimnetic
764 deposits occurs (Sirota et al., 2016, 2017). The Dead Sea modern analogue provides a
765 mechanism for explaining the great thickness of the deep Mediterranean MSC halite deposit. A
766 similar model might have applied during the MSC, with halite dissolution in the marginal and
767 intermediate basin evaporites, and focusing and thickening of halite deposition in the deeper
768 parts of the basin, as also partly proposed by Roveri et al. (2014c).

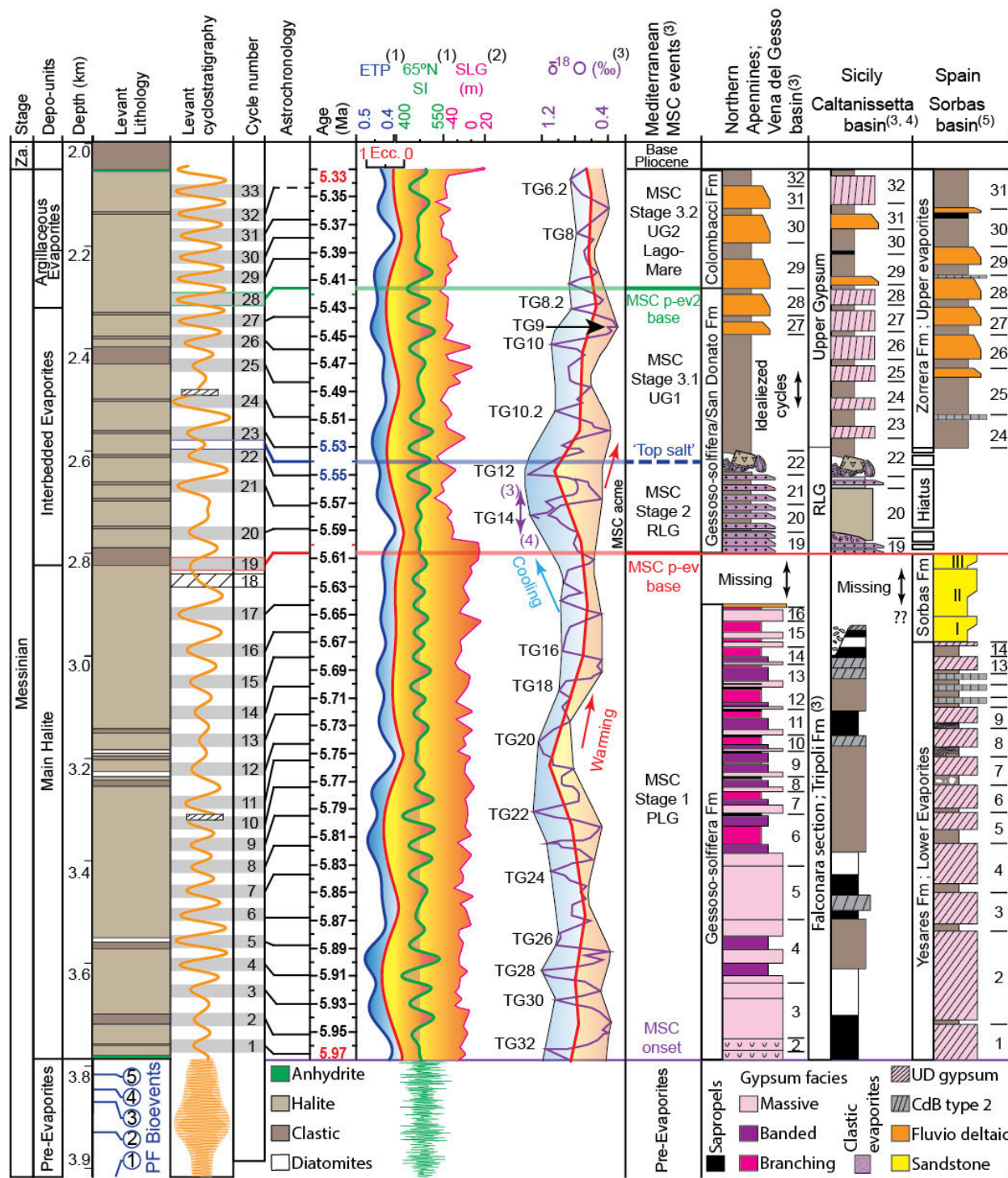
769 **5.2 Stratigraphic markers in deep basin MSC deposits**

770 *5.2.1 Deep-basin diatomites as environmental and lithostratigraphic markers*

771 As no chronostratigraphic indicators were found in the studied section, we aim to use the
772 litho-chemical analysis performed on the Dolphin well samples to identify lithostratigraphic and
773 chemostratigraphic markers that may serve as tie-points for establishing an age model for the
774 deep basin MSC deposits (Fig. 12). In this context, the occurrence of diatomites within the Main
775 Halite unit provides a primary observation. Diatomites are known to occur within Pre-Evaporite
776 and PLG intervals in some of the marginal sections (Dela Pierre et al., 2014; Hilgen et al., 2007;
777 Hilgen and Krijgsman, 1999; Krijgsman et al., 2001; Manzi et al., 2011; Roveri et al., 2014a),
778 and more rarely within stage 3 Upper Gypsum deposits (e.g., Eraclea Monia section; Manzi et
779 al., 2009). Diatom-rich aggregates within laminated layers, appearing as mudstone intervals
780 interbedded within the PLG deposits of the Piedmont basin, were used by Dela Pierre et al.
781 (2014) to establish the existence of normal-marine (not brackish or hypersaline) waters during
782 deposition of non-evaporitic intervals during stage 1 of the MSC. Here we show that open-
783 marine planktonic diatom taxa abundant in the Piedmont during the PLG (e.g., *Coscinodiscus* sp.
784 and *Thalassionema longissimi*) are also abundant or closely related to abundant species within
785 the Dolphin assemblage.

2409
2410
2411
2412
2413
2414
2415
2416
2417
2418
2419
2420
2421
2422
2423
2424
2425
2426
2427
2428
2429
2430
2431
2432
2433
2434
2435
2436
2437
2438
2439
2440
2441
2442
2443
2444
2445
2446
2447
2448
2449
2450
2451
2452
2453
2454
2455
2456
2457
2458
2459
2460
2461
2462
2463
2464

786



787

788 *Figure 12. Astronomical age model and regional correlation of the Levant MSC*
 789 *The Levant interpreted lithology (left, from Fig. 2), biostratigraphic reference levels (PF –*
 790 *planktic foraminifera, below) and filtered well-log model (Fig. 5) determine a cyclostratigraphic*

2465
2466
2467
2468
2469
2470
2471
2472
2473
2474
2475
2476
2477
2478
2479
2480
2481
2482
2483
2484
2485
2486
2487
2488
2489
2490
2491
2492
2493
2494
2495
2496
2497
2498
2499
2500
2501
2502
2503
2504
2505
2506
2507
2508
2509
2510
2511
2512
2513
2514
2515
2516
2517
2518
2519
2520

791 *model, resulting with 33 cycles for the Levant MSC (shaded cycles). Note the significantly lower*
792 *cycle frequency in the Pre-Evaporites (2.3 m compared to 51 m per-cycle), due to the much*
793 *higher sedimentation rates in the evaporites interval. This cyclostratigraphic model is tuned to*
794 *astronomic target curves (center) of ETP (blue; calculated as eccentricity (Ecc; red) + obliquity*
795 *- precession ((1) Laskar et al., 2004), 65°N summer insolation (65°N SI; green) (Laskar et al.,*
796 *2004), and marginal MSC deposits (right columns) based on astronomical calibrated ages and*
797 *cycles identified across the Mediterranean ((1) Laskar et al., 2004; (3) Roveri et al., 2014a,*
798 *CIESM (2008); (4) Manzi et al., 2011; (5) Krijgsman et al., 2001). The drop in sea level (SLG;*
799 *sea level Gibraltar; (2) Ohneiser et al. 2015) corresponding to glacial peaks TG12-14 ($\delta^{18}O$; as*
800 *summarized in Roveri et al. (2014)) marks the top of the Main Halite unit. The shift to post-*
801 *evaporitic and clastic deposits of MSC stage 3 (Hilgen et al., 2007; Krijgsman et al., 2001;*
802 *Laskar et al., 2004; Roveri et al., 2014), through a stepwise deglaciation associated with sea-*
803 *level rise (TG12-9), is here astronomically tuned to enhanced clastic deposition in the*
804 *Interbedded Evaporites and Argillaceous Evaporites units of the Levant.*

805
806 To date, there are no reports of diatomites, or a diatom-rich assemblage in stage 2 of the MSC
807 across the Mediterranean. Based on the taxonomic similarities between the deep and marginal
808 planktonic marine diatom assemblages, we propose that the Levant diatomites constitute a
809 temporal lithostratigraphic marker. If we follow the interpretation for the occurrence of planktic
810 marine diatoms as indicators of partial connectivity with the Atlantic Ocean (Dela Pierre et al.,
811 2014; Hüsing et al., 2009; Krijgsman et al., 2000), then their appearance interbedded within the
812 halite in the Levant suggests that deposition of the halite layer occurred at a time of at least
813 partial, periodic Atlantic connectivity, most likely during deposition of the PLG on the margins
814 (5.97-5.6 Ma).

2521
2522
2523 815 *5.2.2 Allochthonous grains in the Interbedded Evaporites-Argillaceous Evaporites and stages 2-*
2524
2525 816 *3 of the MSC*
2526

2527
2528 817 The abrupt change that marks the onset of enhanced clastic input in the Interbedded
2529
2530 818 Evaporites in the Levant Basin, together with endemic and reworked Eocene and Cretaceous
2531
2532 819 foraminifera into the basin, matches other similar episodes reported from the MSC in the
2533
2534 820 Mediterranean. Primarily, these are the clastic-rich deposits that result in the deposition of the
2535
2536 821 Reworked Lower Gypsum (stage 2) and the Upper Gypsum and Lago-Mare deposits (stage 3) on
2537
2538 822 the margins. These clastic deposits, including a similar abundance of minerals and reworked
2539
2540 823 fauna, are not only reported from marginal sections (e.g., Lofi et al., 2011; Roveri et al., 2014),
2541
2542 824 but also from cores of deeper parts of the basin (e.g., Site 124 in the Western Med (Ryan et al.,
2543
2544 2007), Site 654 in the Tyrrhenian Sea (Borsetti et al., 1990), and from Sites 374 and 376 in the
2545
2546 825 Eastern Mediterranean (Cita et al., 2006; Hsü et al., 1978a, 1978b)).
2547
2548

2549 827 DSDP Sites 375 and 376 at the Florence Rise in the Eastern Mediterranean recovered
2550
2551 828 nannofossil marlstones and dolomitic marlstones of latest Miocene age, overlying a gypsum with
2552
2553 829 marlstone sequence (Hsü, et al., 1978b). The gypsum with marlstone, which are interpreted as
2554
2555 830 deposits of a shallow subaqueous environment, are followed downwards by anhydrite and halite
2556
2557 831 at Site 376 and are collectively recognized as the upper part of the Mediterranean evaporites. The
2558
2559 832 interbedded gypsum contains reworked Cretaceous, Paleogene and lower/middle Miocene
2560
2561 833 foraminifera and nannofossils, similar to the fauna identified in the clastic interval of the
2562
2563 834 Interbedded Evaporites in the Dolphin well. The reworked fauna from Florence Rise are
2564
2565 835 common to abundant in the bedded evaporites and rare to absent in the overlying Pliocene and
2566
2567 836 underlying Tortonian and Serravallian (Hsü, et al., 1978b), indicating a distinctive phase of
2568
2569 837 reworked sediments deposited within the Mediterranean basins. The sedimentary response of the
2570
2571
2572

2577
2578
2579 838 Interbedded Evaporites and Argillaceous Evaporites (Units 5 and 6, respectively; Gvirtzman et
2580
2581 839 al., 2013; 2017; Manzi et al., 20018) in the Levant Dolphin and Leviathan-1 wells (from ~2270
2582
2583 840 m in the Dolphin well, Figs 5, 12) resembles similar observations reported from shallower
2584
2585 841 deposits in the Levant. For example, the Afiq Formation overlies the anhydrite-siliciclastic stage
2586
2587 842 2-RLG equivalent Mavqiim Formation (Druckman et al., 1995; Lugli et al., 2013) and was
2588
2589 843 penetrated by the Or-South 1 well. It consists of Eocene-aged lithoclasts made of limestone,
2590
2591 844 dolomite, and chert- and quartz-rich sand, overlying a conglomerate unit with brackish ostracods
2592
2593 845 indicating a plausible correlation to the Lago-Mare stage (Derin, 2000). A fluvial or sabkha
2594
2595 846 environment is attributed to this interval with subaerial exposure, supporting the idea of a
2596
2597 847 considerable desiccation phase and subaerial exposure near the end of the MSC (Cita et al.,
2598
2599 848 1978; Lofi et al., 2011; Madof et al., 2019; Ryan, 1978). Similar lithologies, including clasts of
2600
2601 849 Eocene and Cretaceous age, were described from the marginal Nir-1 well in the Levant Basin
2602
2603 850 above an erosion surface and beneath earliest Pliocene marls (Frey-Martinez et al., 2007).
2604
2605 851 Similar clastic-conglomeratic and sandy lithologies are also reported from the Messinian
2606
2607 852 Qawasim and Rosetta formations offshore Egypt (Leila et al., 2016); the latter correlates with the
2608
2609 853 Afiq Formation in the Levant (Derin, 2000). Unfortunately, no samples are available from above
2610
2611 854 the base of the Interbedded Evaporites in the deep Levant Basin to further confirm the
2612
2613 855 lithological correlation between these sections and the deep Levant Basin. Correlation to more
2614
2615 856 proximal sections and well-log interpretations indicate that the overlying Argillaceous Evaporites
2616
2617 857 mark a shift to more clastic and gypsum/anhydrite deposition (see also Gvirtzman et al., 2013;
2618
2619 858 2017; Manzi et al., 2018).

2620
2621
2622
2623
2624 859 We argue that the main change in the halite unit, characterized by mixing of clastic material
2625
2626 860 into the deep-basin deposits at the base of the Interbedded Evaporites correlates with the
2627
2628
2629
2630
2631
2632

2633
2634
2635
2636
2637
2638
2639
2640
2641
2642
2643
2644
2645
2646
2647
2648
2649
2650
2651
2652
2653
2654
2655
2656
2657
2658
2659
2660
2661
2662
2663
2664
2665
2666
2667
2668
2669
2670
2671
2672
2673
2674
2675
2676
2677
2678
2679
2680
2681
2682
2683
2684
2685
2686
2687
2688

861 beginning of major sea-level drawdown and introduction of clastic material into the entire
862 Mediterranean Basin, from stage 2 of the MSC (5.6 Ma) through the Upper Gypsum and Lago
863 Mare stages in the marginal basins (5.55-5.33 Ma; Argillaceous Evaporites in Fig. 12). During
864 stage 2, sea-level drawdown eroded and redeposited the PLG gypsum into the marginal and
865 intermediate parts of the basin (e.g., Lofi et al., 2011). The deep-basin expression of this
866 regression might be the fine-grained clastics, including older reworked fauna, reaching the
867 Mediterranean depocenters. However, to further test this idea and try to distinguish between
868 stage 2 and 3 sediments, we compare biomarker distribution across the basin, and identify
869 sedimentary cycles within the MSC of the Levant Basin.

870 *5.2.3 Basin-wide transport of organic matter*

871 The *n*-alkane distribution and CPI values of the Levant samples (Figs 7 and 8; Table 1) are
872 similar to some extent to those obtained from marginal and onshore MSC successions (Vasiliev
873 et al., 2017), and provide further support for the introduction of reworked and mixed material
874 into the Levant during the deposition of the Interbedded Evaporites. The *n*-alkane distribution of
875 Mediterranean MSC samples covering the entire 640-kyr-long MSC interval shows distinct
876 dissimilarities between several marginal to intermediate-depth sections (Vasiliev et al., 2017):
877 The Monte Tondo (Primary Lower Gypsum; MSC stage 1), Realmonte salt mine (Halite and Re-
878 sedimented Lower Gypsum; MSC stage 2), and Eraclea Minoa (Upper Gypsum/Lago Mare;
879 MSC stage 3). The Delphine well *n*-alkane distribution shows a higher abundance of short-chain
880 homologues in the Levant relative to marginal sections (Vasiliev et al., 2017), likely due to the
881 lower relative input of terrestrial organic matter in more distal depositional settings. Several
882 similarities exist between both data sets. Vasiliev et al. (2017) reported CPI values of 3.0-7.9 at
883 Monte Tondo (stage 1), and 1.7-3.7 at Eraclea Minoa (stage 3; Fig. 10). While CPI values were

2689
2690
2691 884 not reported from the halite samples of the Realmonte salt mine, Vasiliev et al. (2017) show two
2692
2693 885 different types of organic matter: 1) autochthonous sediment associated with gypsum or halite
2694
2695 886 deposited in place, and 2) allochthonous material associated with clastic sediments and transport.
2696
2697 887 Marked similarities in CPI values are therefore noted between the Levant and marginal locations
2698
2699 888 described by Vasiliev et al. (2017), with CPI values of 4.0-12.3 in the Main Halite interval
2700
2701 889 (indicating stage 1), and 1.9-2.9 in the Interbedded Evaporites interval (indicating stages 2-3)
2702
2703 890 (Fig. 10).
2704
2705

2706 891 Vasiliev et al. (2017) also suggest that dissimilarities in the biomarker and isotopic
2707
2708 892 composition of stages 1 and 2, relative to stage 3 sediments, may be attributed to the outflow of
2709
2710 893 Black Sea (i.e., Paratethys) waters and their mixing into the Mediterranean, which paved the way
2711
2712 894 for Paratethyan ‘Lago-Mare’ type fauna. For instance, the distribution of *n*-alkanes and CPI
2713
2714 895 values in stage 3 at Eraclea Minoa are more evenly distributed and lower relative to those of
2715
2716 896 stage 1 (fig. 3 in Vasiliev et al., 2017). We report a similar distinction in the *n*-alkane distribution
2717
2718 897 between the upper clastic samples and underlying sediments (Table 1, Fig. 9). A much stronger
2719
2720 898 odd-over-even predominance (i.e., higher CPI values) is observed in the Argillaceous
2721
2722 899 Diatomites, together with more elevated long-chain over short-chain *n*-alkanes values
2723
2724 900 (LCA/SCA; Table 1) and maturity parameters (Fig. 11; Table 2). This indicates more immature
2725
2726 901 source rocks with significantly different sources of the organic matter in the Main Halite relative
2727
2728 902 to the Interbedded Evaporites sediments (Bray and Evans, 1961; Scalan and Smith, 1970).
2729
2730

2731 903 The distribution of stereoisomers of algal steranes and bacterial hopanes (Fig. 11; Table 2)
2732
2733 904 reflects the transformation, or stereoisomerization from biological epimers to a more stable
2734
2735 905 geological molecular configuration as a consequence of thermal alteration (Peters, 1986; Peters
2736
2737 906 et al., 2005, 1980). The evidence for enhanced thermal maturity in the Interbedded Evaporites
2738
2739
2740
2741
2742
2743
2744

2745
2746
2747 907 relative to the underlying deposits (Fig. 11; Table 2) is counterintuitive, as thermal maturity
2748
2749 908 should increase with depth (Peters et al., 2005, 1980). Furthermore, the Interbedded Evaporites
2750
2751 909 exhibit mixed signals that include high values of the $C_{31} \alpha\beta$ S/R ratio (indicative of thermally
2752
2753 910 mature organic matter) in addition to C_{31} hopanes with the $\beta\beta$ biological configuration (indicative
2754
2755 911 of immature organic matter) (Fig. 11; Table 2). This aspect further supports the occurrence of
2756
2757 912 organic matter mixtures from differing ages and thermal histories, i.e., a higher proportion of
2758
2759 913 allochthonous, thermally mature organic matter in the Interbedded Evaporites compared with the
2760
2761 914 Main Halite and Pre-Evaporite samples. This interpretation is consistent with similar trends
2762
2763 915 observed in early Paleogene (Sepúlveda et al., 2009) and Quaternary (Rashid and Grosjean,
2764
2765 916 2006) studies. Such trends may reflect an intensification of the hydrological cycle, and thus
2766
2767 917 enhanced precipitation, continental runoff, and the transport of reworked, and pre-aged,
2768
2769 918 continental or marginally-derived organic matter during the deposition of the Interbedded
2770
2771 919 Evaporites. Another mechanism through which transport can occur is dense shelf-water
2772
2773 920 cascading (DSWC) transport of sediment and associated organic matter from marginal settings to
2774
2775 921 deep Mediterranean basins, as reported to occur in the Mediterranean today (Canals et al., 2009).
2776
2777 922 The interpretation of transport in these intervals is consistent with the occurrence of clastic
2778
2779 923 material, larger sub-rounded minerals, and re-worked Cretaceous and Eocene foraminifera within
2780
2781 924 samples from the Interbedded Evaporites, which also supports the presence of reworked, older
2782
2783 925 sediments. Both Cretaceous and Eocene organic-rich source rocks are known around the
2784
2785 926 Mediterranean Basin (e.g., Almogi-Labin et al., 1993; Bayliss, 1973; Meilijson et al., 2014), and
2786
2787 927 might represent sources of pre-aged weathered and transported organic matter, matching the
2788
2789 928 apparent higher maturity measured from the organic-matter extract of the Interbedded Evaporites
2790
2791 929 sediments.
2792
2793
2794
2795
2796
2797
2798
2799
2800

2801
2802
2803 930 In summary, the similarities between our data and of Vasiliev et al. (2017) suggest that
2804
2805 931 organic geochemical analysis from the Dolphin well might be used as regional
2806
2807 932 chemostratigraphic markers to distinguish between Pre-Evaporites and Argillaceous Diatomites
2808
2809 933 sediments, and the overlying Interbedded and Argillaceous Evaporites. A correlation between
2810
2811 934 MSC stage 3 and the upper part of the MSC in the Levant Basin has been previously proposed
2812
2813 935 based on seismic interpretation and the sampling of shallower deposits (Druckman et al., 1995;
2814
2815 936 Gvirtzman et al., 2017; Lugli et al., 2013). Here, we present evidence supporting the occurrence
2816
2817 937 of stage 2 sea-level drawdown or stage 3 and ‘Lago-Mare’-type deposits in the deep domains of
2818
2819 938 the Eastern Mediterranean. This includes increased supply of clastic material into the basin,
2820
2821 939 reworked fauna, and chemostratigraphic markers (Figs 3, 9 and 10).
2822
2823
2824

2825 940 **5.3 From cycles to astronomical tuning**

2826
2827
2828 941 Cyclostratigraphy and astronomical tuning of sediment sections, geochemical signals, and
2829
2830 942 well-log responses have been extensively used for stratigraphic interpretations of MSC deposits
2831
2832 943 across the Mediterranean (Dela Pierre et al., 2014; Hilgen et al., 2007, 2000, 1995; Hilgen and
2833
2834 944 Krijgsman, 1999; Hüsing et al., 2010, 2009, Krijgsman et al., 2001, 1999, 1997; Lugli et al.,
2835
2836 945 2015; Manzi et al., 2015, 2013, 2012; Ochoa et al., 2015; Topper et al., 2014). The CIESM
2837
2838 946 stratigraphic model of the MSC has halite deposited in stage 2 of the MSC, during four
2839
2840 947 precession cycles (e.g., Roveri et al., 2014a, with reference to Laskar et al., 2004; Fig. 12). These
2841
2842 948 are part of the 32 precession-controlled cycles (Laskar et al., 2004) identified across the
2843
2844 949 Mediterranean, with a periodicity of about 20 kyr per cycle, amounting to the 640 kyr time frame
2845
2846 950 of the MSC. Manzi et al. (2015) proposed to tune the high-reflectivity intervals in the seismic
2847
2848 951 section of the Levant (interpreted as clastic units; Gvirtzman et al., 2013a) to summer insolation
2849
2850 952 maxima, and the transparent intervals (interpreted as halite) to summer insolation minima, within
2851
2852
2853
2854
2855
2856

2857
2858
2859 953 these four insolation cycles. By contrast, the study of the Pre-Evaporites in the Dolphin well by
2860
2861 954 Meilijson et al. (2018) and the results of this study suggest that salt formation began around 5.97
2862
2863 955 Ma, i.e., more or less synchronously with the marginal deposition of the PLG. According to this
2864
2865 956 age model, the evaporitic sequence in the Levant Basin (Fig. 12) was deposited between 5.97 and
2866
2867 957 5.33 Ma, corresponding to a time span of ~640 kyr rather than 50 kyr, and encompassing 32
2868
2869 958 insolation cycles (Laskar et al., 2004). Our suggested scenario would imply an average cycle
2870
2871 959 thickness of ~50 m, as the studied section is 1590 m thick.
2872
2873

2874 960 Bandpass filtering of the Dolphin well logs resulted in the identification of 31 cycles, closely
2875
2876 961 matching the 32 precession-controlled cycles (Laskar et al., 2004) in the interval between 5.97
2877
2878 962 and 5.33 Ma. However, this age model includes several assumptions: (1) the evaporite record at
2879
2880 963 the studied site is complete with no hiatus, (2) it is largely undisturbed by salt tectonics, and (3)
2881
2882 964 the sedimentation rate is approximately constant, with no significant changes between the halite-
2883
2884 965 rich intervals and clastic-diatomitic intervals. The Dolphin record lacks chronostratigraphic tie
2885
2886 966 points and contains intervals in which the log data are erratic (Figs 5, S2). Furthermore, the
2887
2888 967 Dolphin well area appears deformed in the upper part of the section, and Unit 6 is missing
2889
2890 968 (overlying the Interbedded Evaporites; Fig. 6). These sources of uncertainty suggest that the
2891
2892 969 Dolphin well spectral analysis provides a first order approximation of the number of cycles,
2893
2894 970 primarily across the lower part of the section. However, the large number of cycles observed in
2895
2896 971 the Main Halite interval, if assumed to reflect precessional cycles, suggests a longer period of
2897
2898 972 deposition than ~50 kyr. The Leviathan-1 well is much less deformed (Figs 5, 6) and has a thick
2899
2900 973 interval of Unit 6 (Gvirtzman et al., 2013; 2017), similar to the sequence at the Aphrodite well
2901
2902 974 (Manzi et al., 2018). It also presents a good fit between the seismic and the RE well-log
2903
2904 975 response. The observed regularity produced a filtered cycles curve (Fig. 5), which reveals a good
2905
2906
2907
2908
2909
2910
2911
2912

2913
2914
2915 976 fit with the well log curve. We hypothesize that these cycles represent the 32 precession cycles
2916
2917 977 identified in MSC sections across the Mediterranean. This would imply that the Main Halite
2918
2919 978 interval in the lower part of the studied section is equivalent to stage 1 (PLG) in marginal
2920
2921
2922 979 sections, as also proposed by Meilijson et al. (2018).
2923

2924 980 However, lacking chronostratigraphic tie points in the evaporitic section, an alternative
2925
2926 981 explanation for the cyclicity observed in the well logs of the halite and the seismic profiles
2927
2928 982 should be considered to reconcile the age model suggested by Manzi et al. (2018) for the Levant
2929
2930 983 Basin. In this model the FBI unit, which represents the uppermost part of the Pre-Evaporites in
2931
2932 984 the Aphrodite well, corresponds to MSC stage 1 (the PLG; Manzi et al., 2018), while the
2933
2934 985 uppermost part of the section corresponds to stage 3 (Unit 7; Gvirtzman et al., 2017). Following
2935
2936 986 this model, the ~33 cycles identified within the Leviathan-1 MSC section (Figs 5, 7) correspond
2937
2938 987 to the ~50 kyr estimated for the duration of stage 2 of the MSC (Roveri et al., 2014), and have
2939
2940 988 therefore a cycle duration of ca. 1560 years. If we take into account the likely different
2941
2942 989 sedimentation rates of the Argillaceous Diatomites facies, this period could correspond to the
2943
2944 990 period inferred for the Dansgaard-Oeschger events (1470 years), as observed during the second
2945
2946 991 half of the last glacial (Schulz, 2002) (although see comments by Ditlevsen et al. (2007) and
2947
2948 992 Lohmann and Ditlevsen (2018) on the validity and interpretation of these cycles). Alternatively,
2949
2950 993 they could be explained by the Bond cycles, as observed for the North Atlantic during the
2951
2952 994 Holocene (1500 years; Bond et al., 2001). Another alternative are the periods of ca. 1000 years
2953
2954 995 corresponding to the so-called Eddy cycle observed in the ¹⁴C record, which relate to variations
2955
2956 996 in solar activity (Steinhilber et al., 2012). However, this last alternative is unlikely: if the regular
2957
2958 997 alternations in the halite would correspond to Eddy cycles, it implies that stage 2 of the MSC
2959
2960
2961
2962
2963
2964
2965
2966
2967
2968

2969
2970
2971
2972
2973
2974
2975
2976
2977
2978
2979
2980
2981
2982
2983
2984
2985
2986
2987
2988
2989
2990
2991
2992
2993
2994
2995
2996
2997
2998
2999
3000
3001
3002
3003
3004
3005
3006
3007
3008
3009
3010
3011
3012
3013
3014
3015
3016
3017
3018
3019
3020
3021
3022
3023
3024

998 lasted only ~32 kyr. This means that the climax stage of the MSC cannot encompass both glacial
999 stages TG14 and 12 (Fig. 12), as is assumed in the CIESM model.

1000 In the Realmonte salt mine in Sicily, 10-15 cm alternations in the salt have been interpreted as
1001 annual cycles (Manzi et al. 2012). Such sedimentation rates of ca. 10 cm/yr would imply that the
1002 1,060 m thick Main Halite interval in the Levant could have been formed in a short time period
1003 of 10,600 years, although average sedimentation rate may be lower in the Argillaceous
1004 Diatomites. However, it is hard to reconcile such a short duration of deposition with the amounts
1005 of halite required to build up the thickness of the Levant Basin halite layer.

1006 In the absence of a simple explanation for the cyclicity observed in the Dolphin well, we now
1007 consider its interpretation in relation to the different elements of the CIESM model for marginal
1008 MSC deposits. The CIESM (2008) consensus stratigraphic model for the MSC is strongly based
1009 on astronomical tuning of different MSC sections and includes the following division of the 32
1010 orbital-related cycles identified during this time frame (Laskar et al., 2004): cycles 1-18 in stage
1011 1 (PLG), 19-23 in stage 2 (RLG), 24-28 in stage 3.1 (lower part of Upper Gypsum), and 29-32 in
1012 stage 3.2 (the Lago Mare). The correlation between the Levant MSC well-log-based
1013 astrochronology, the orbital target curves, and the chronology of shallow to marginal sections
1014 (CIESM, 2008) of the MSC indicates the following: (1) the Main Halite interval (3759-2800 m
1015 in the Leviathan-1 well) is bound between the Levant filtered cycles 1 through 19 (Fig. 12). A
1016 comparison with the current MSC chronology (CIESM, 2008; Roveri et al., 2014a) shows a
1017 correlation with the number of cycles in the interval between 5.97 and 5.6 Ma from the base of
1018 the PLG (stage 1) to the base of the RLG (stage 2); (2) the Interbedded Evaporites interval
1019 (2800-2320 m) is bound between the Levant filtered cycles 19 through 28 (Fig. 12), which
1020 correlates to the number of cycles in in stage 2 (the RLG; 5.6-5.55 Ma; cycles 19-23), with its

3025
3026
3027 1021 top known as the ‘top salt’ horizon, and the lower part of stage 3 (stage 3.1 the Upper Gypsum
3028
3029 1022 who’s base is at 5.42 Ma). Thus, the lower part of the Interbedded Evaporites is also equivalent
3030
3031
3032 1023 to stage 2 halite deposits recognized in intermediate basins, such as the Realmonte salt mine in
3033
3034 1024 Sicily; (3) at the upper part of the Interbedded Evaporite and the Argillaceous Evaporites interval
3035
3036 1025 are equivalent to stage 3 of the MSC (2320-2090 m; Fig. 12), ending with the clastic Lago-Mare
3037
3038 1026 interval.

3039
3040 1027 Following the suggestion of Meilijson et al. (2018) for an early onset of halite deposition in
3041
3042 1028 the deep Mediterranean basins, similar claims were made by García-Veigas et al. (2018) based
3043
3044 1029 on sulfur stable-isotopes analysis of marginal and intermediate basin gypsum deposits. They
3045
3046 1030 hypothesize that the deep-basin halite deposits are not equivalent to one phase of deposition
3047
3048
3049 1031 during stage 2 of the MSC, but rather comprise two to three phases of halite deposition,
3050
3051 1032 beginning with halite deposition during stage 1 of the MSC. Our astronomical tuning agrees with
3052
3053 1033 this idea by positioning the boundary between stage 1 and 2 of the MSC (2762 m in the Dolphin
3054
3055 1034 well, 2800 m in Leviathan-1) at the top of the Main Halite interval. Consequently, we propose
3056
3057 1035 that the Main Halite is equivalent to stage 1 gypsum deposits of the PLG, as indicated
3058
3059 1036 independently by the diatomite facies. The increase in clastic and reworked faunal material into
3060
3061 1037 the basin fits well with our astrochronology, placing the Interbedded Evaporites within the time
3062
3063 1038 period of the Reworked Lower Gypsum (stage 2 of the MSC). Sea-level drawdown promoted the
3064
3065
3066 1039 scraping of the shelf, reshaping of drainage and transport systems across the basin, and
3067
3068 1040 redepositing of vast amounts of eroded sediment into the intermediate basins. It also delivered
3069
3070 1041 vast amounts of fine-grained material to the deep basins, as observed in the Interbedded
3071
3072 1042 Evaporites in the Levant Basin. Lastly, the identification of the *Discoaster quinqueramus* in Unit
3073
3074
3075
3076
3077
3078
3079
3080

3081
3082
3083 1043 5 (the Interbedded Evaporites) by Manzi et al. (2018) supports this conclusion, as this species
3084
3085 1044 went extinct towards the end of stage 2.
3086
3087

3088 1045 **5.4 Implications of a new MSC chronology in the Mediterranean**

3089
3090

3091 1046 While not conclusive, the integration of our different stratigraphic proxies supports an early
3092
3093 1047 and long-lasting deposition of deep-basin halite. The direct implication of this age model is that
3094
3095 1048 halite was deposited in the deep Eastern Mediterranean when sea level was high and partial,
3096
3097 1049 episodic connection with the Atlantic still prevailed (Dela Pierre et al., 2014; Flecker and Ellam,
3098
3099 1050 2006; Krijgsman et al., 2002; Roveri et al., 2014b), synchronously with gypsum deposition along
3100
3101 1051 the Mediterranean margins and intermediate basins (Ochoa et al., 2015). Our results do not
3102
3103 1052 exclude an evaporative drawdown (e.g., Lofi, et al., 2011; Rouchy and Caruso, 2006; Ryan,
3104
3105 1053 2008) and lower sea level at the acme of the MSC during stage 2 (Ohneiser et al., 2015). The
3106
3107 1054 lack of sedimentological features within the monotonously clean halite, and our interpretation of
3108
3109 1055 long-lasting deep-water evaporite depositional settings, indicate that salt must have started to
3110
3111 1056 precipitate within a deep-basin deep-water environment, and not in shallow waters. We propose
3112
3113 1057 that sea-level drawdown prompted enhanced transport of clastic sediments into the deep basin
3114
3115 1058 resulting in the deposition of the Interbedded Evaporites unit, analog to the marginal deposition
3116
3117 1059 of the RLG. Studies of strontium isotopes from the Lower Evaporites (PLG, MSC stage 1)
3118
3119 1060 consistently report isotopic values close to those characteristic of the global ocean (Flecker and
3120
3121 1061 Ellam, 2006; Roveri et al., 2014b), and do not support an early desiccation model (Cita, 1976;
3122
3123 1062 Hsü, 1973). While advocating a different chronological model, our study is consistent with these
3124
3125 1063 interpretations and shows that halite deposition started during a time when Atlantic inflow was
3126
3127 1064 still evident.
3128
3129
3130
3131
3132
3133
3134
3135
3136

3137
3138
3139
3140
3141
3142
3143
3144
3145
3146
3147
3148
3149
3150
3151
3152
3153
3154
3155
3156
3157
3158
3159
3160
3161
3162
3163
3164
3165
3166
3167
3168
3169
3170
3171
3172
3173
3174
3175
3176
3177
3178
3179
3180
3181
3182
3183
3184
3185
3186
3187
3188
3189
3190
3191
3192

1065 A coeval initiation of basinal halite and marginal gypsum precipitation calls for a reevaluation
1066 of previous models for MSC development, as well as its effect on global ocean salinity and
1067 climate. We refer to the timing and persistence of halite deposition (which may have been an
1068 order of magnitude larger than previously thought), and also to the substantially lower rates of
1069 deposition of the deep-basin salt unit, from a previous assumption of 3,000 cm/kyr (according to
1070 CIESM chronology) to 250 cm/kyr as deduced from our new age model. Although this assumes
1071 continuous precipitation and no dissolution, which we consider unlikely if the water is being
1072 relatively refreshed with additional seawater throughout deposition. The Levant
1073 chronostratigraphic model suggests that steady state of halite deposition was achieved and
1074 maintained earlier in the MSC than previously thought. Both halite and gypsum could have been
1075 precipitated synchronously, with their partitioning possibly governed by their different solubility
1076 product constants (K_{sp}) and ion availability. Furthermore, if we allow for an order of magnitude
1077 change in the time scale of halite precipitation, then the required sedimentation flux that removes
1078 sodium and chlorine from seawater is reduced. This exercise substantially reduces the total sea-
1079 level drawdown (Ryan, 2008) required to explain the deposition of a ~2 km-thick salt deposit. A
1080 further possible mechanism to explain the synchronous deposition of gypsum and halite in
1081 marginal and deeper parts of the basin, respectively, includes density stratification and down-
1082 shelf cascading of brines (Roveri et al., 2014c; Sirota et al., 2017). While salt-saturated shallow
1083 waters seem to have reached gypsum saturation values, brine formation might have continuously
1084 flowed down-shelf, in a similar manner as dense shelf-water cascading (DSWC) is observed
1085 today around the Mediterranean Basin (Canals et al., 2009, 2006). DSWC is associated with
1086 mass-transport complexes and submarine channels, and has a significant impact on the sediment
1087 and organic-matter supply from continental and shallow-marine settings to deep-sea ecosystems.

3193
3194
3195 1088 Mass-balance calculations suggest that the input of dissolved organic carbon and suspended
3196
3197 1089 particulate organic carbon from ocean margins to the open ocean interior may be more than an
3198
3199
3200 1090 order of magnitude greater than direct inputs of organic carbon produced near the ocean surface
3201
3202 1091 today (Bauer and Druffel, 1998). Similarly, highly saturated waters produced in an evaporitic
3203
3204 1092 Mediterranean may have produced vast quantities of brine accumulating in the deep depocenters.
3205
3206 1093 Brine formation may have been at least partly controlled by precession-induced increases in river
3207
3208 1094 runoff (Marzocchi et al., 2015), and potentially by surface inflow from the Paratethys
3209
3210 1095 (Karakitsios et al., 2017; Krijgsman et al., 2010). Salinity stratification is supported by
3211
3212 1096 geochemical evidence for the occurrence of low-salinity surface waters overlying deep brines at
3213
3214 1097 gypsum and halite saturation (Christeleit et al., 2015), as well as by the presence of brackish-
3215
3216 1098 water faunas of Paratethyan origin in the Lago-Mare phase (Stoica et al., 2016). Our data,
3217
3218 1099 including high concentrations of long-chain *n*-alkanes (Table 1) and high LCA/SCA values
3219
3220 1100 (Table 1), also support the occurrence of increased river runoff into the basin during the
3221
3222 1101 deposition of the Interbedded Evaporites.

3223
3224
3225 1102 Our interpretation of a deep-basin deep-water model and early onset of halite, rejuvenates an
3226
3227 1103 idea that has been a focus of debate in the past (e.g., Garcia-Castellanos and Villaseñor, 2011;
3228
3229 1104 Lofi et al., 2011; Ryan, 2008; Schmalz, 1969). Simon and Meijer (2017) used a box-model setup
3230
3231 1105 to model the MSC events forced by Atlantic exchange and evaporative loss. This model
3232
3233 1106 demonstrated that a significantly stratified Mediterranean water column could have been
3234
3235 1107 established early in the crisis, while the duration of halite deposition must have taken longer than
3236
3237 1108 currently considered in the MSC stratigraphic consensus model. The synchronous formation of
3238
3239 1109 gypsum and halite in proximal and distal basins, respectively, could have occurred at different
3240
3241 1110 levels within the basin, with lower rates of halite sedimentation than previously thought. Our
3242
3243
3244
3245
3246
3247
3248

3249
3250
3251
3252
3253
3254
3255
3256
3257
3258
3259
3260
3261
3262
3263
3264
3265
3266
3267
3268
3269
3270
3271
3272
3273
3274
3275
3276
3277
3278
3279
3280
3281
3282
3283
3284
3285
3286
3287
3288
3289
3290
3291
3292
3293
3294
3295
3296
3297
3298
3299
3300
3301
3302
3303
3304

1111 data support the model by Simon and Meijer (2017) and calls to reevaluate Mediterranean MSC
1112 sections, while considering a possible early deposition of halite.

1113 Sea-level drop during stage 2 of the MSC may have added more proximal basins to the
1114 regional deep-sea deposition of halite, which might explain why those intermediate-basin halite
1115 deposits correlate to the stage 2 RLG. Such a mechanism can explain the existence of marginal
1116 or intermediate-depth basins with relatively thin halite deposits, which only correlate with the
1117 Interbedded Evaporites interval in the Levant (Fig. 12), in which halite is still the dominant
1118 lithology. For example, the marginal Realmonte salt mine has a ~600 m thick halite sequence
1119 (Lugli et al., 1999; Roveri et al., 2014a) compared with the thick (>2 km) halite deposits in deep
1120 Mediterranean basins. In a similar manner, recent studies from the Dead Sea demonstrate
1121 downslope-flowing brines, in which the deep basal areas accumulate the most brine and the
1122 marginal areas are influenced by fresher waters and hence subject to more dissolution (Sirota et
1123 al., 2016).

1124 Being one of the largest and youngest salt giant formation episodes in Earth's history, the
1125 MSC is repeatedly used as a cornerstone for explaining evaporite deposition. Our new model,
1126 which includes the synchronous deposition of sulfates in the margins of the basin and halite at its
1127 center, calls for a re-evaluation of the mechanisms governing evaporite deposition in other salt-
1128 giant deposits in the geologic record. For example, in the Permian Zechstein, similar to the
1129 Mediterranean, sulfates appear to have been limited to the margins while halite was deposited in
1130 the deeper parts of the basin (Richter-Bernburg, 1985). This is also the case for the Permian
1131 Delaware Basin in Texas and New Mexico, where clear inter-fingering between sulfates and
1132 halite are observed as brine concentrations oscillate (Anderson and Dean, 1995).

3305
3306
3307 1133 The alternating clastic and evaporitic sediments of the Interbedded Evaporites (Unit 5;
3308
3309 1134 Gvirtzman et al., 2013; 2017) include cycles 19-28, matching in its lower part the time frame of
3310
3311
3312 1135 MSC stage 2, the RLG. Isolation from the Atlantic and significant sea-level drawdown are
3313
3314 1136 proposed as the formation mechanism for both the onshore deep subaerial canyons and offshore
3315
3316 1137 erosion surfaces across the Mediterranean (Lofi et al., 2011; Ryan, 1976; Ryan and Cita, 1978).
3317
3318 1138 Different models were proposed to explain the mechanisms behind erosion, transport, and re-
3319
3320 1139 deposition, such as early subaqueous large-scale mass-wasting processes occurring at the
3321
3322 1140 beginning of the MSC drawdown, subaerial rivers down-cutting by retrogressive action to adjust
3323
3324 1141 for their new base level, or marine abrasion as possible agent for late erosion (Lofi et al., 2011
3325
3326 1142 and references therein). Regardless of the mechanism, clastic geometries are clear in MSC
3327
3328
3329 1143 seismic sections and are partly controlled by local factors such as the dimension of the drainage
3330
3331 1144 basin, resulting in major differences between the Messinian sedimentary successions in the
3332
3333 1145 different areas of the Mediterranean. The whereabouts of the massive products of these basin-
3334
3335 1146 wide erosional processes has been one of the MSC's enigmas (Ryan, 1976; Ryan and Cita, 1978;
3336
3337 1147 Lofi et al., 2011). The seismic facies defined as the Complex Unit (CU; Lofi et al., 2011) in the
3338
3339 1148 Western Mediterranean is either chaotic or roughly bedded, and is believed to account for some
3340
3341 1149 of the waste products. CU deposits are absent on the margin shelves, rarely observed on the
3342
3343 1150 upper slopes, and mainly observed along the base of the slopes, either as fan-shaped deposits at
3344
3345
3346 1151 the Messinian river mouths or as poorly organized bodies elsewhere. This unit marks the
3347
3348 1152 transition between the eroded slopes and deep-basin deposits (Lofi et al., 2011). The CU is
3349
3350 1153 positioned above or parallel to the Mobile Unit (the halite).

3351
3352 1154 In summary, stage 2 of the MSC is characterized by massive sediment displacement, for
3353
3354 1155 which only a portion is accounted for. We propose that the Interbedded Evaporites (Unit 5;
3355
3356
3357
3358
3359
3360

3361
3362
3363 1156 Gvirtzman et al., 2017) are part of this high-energy system and that the interbedding of clastics
3364
3365 1157 represents the deep-basin depocenters for the fine grained material at the distal part of the
3366
3367
3368 1158 drainage system. These precession-controlled clastic incursions reached into an evaporitic
3369
3370 1159 system, which in the deep basins has been depositing halite for ~360 kyr during stage 1 of the
3371
3372 1160 MSC. We argue that this idea could not be examined before due to lack of a sedimentary record
3373
3374 1161 from the deep basin and the difficulty of correlating marginal and deep-basin units based on
3375
3376 1162 seismostratigraphy. The call for caution regarding the interpretation of MSC-related offshore
3377
3378 1163 data was recently presented by Roveri et al. (2019). They pointed out that MSC units with
3379
3380 1164 different age, nature and depositional setting, may show similar seismic facies and geometries.
3381
3382 1165 On the other hand, the same unit may appear as belonging to different seismic facies, either with
3383
3384 1166 parallel and high-amplitude reflections or even transparent or chaotic reflectivity due to seismic
3385
3386 1167 interference patterns related to the dominant frequency. We therefore argue against lumping the
3387
3388 1168 different facies of the Interbedded Evaporites into a unified deep-basin halite deposit,
3389
3390 1169 disregarding its clastic nature, as done in past interpretations of the Levant Basin MSC section
3391
3392 1170 (e.g., Manzi et al., 2018). Here we offer new sedimentological analysis of the non-evaporitic
3393
3394 1171 facies, interpreted in the past as clastic deposits through seismic and well-log interpretation (e.g.,
3395
3396 1172 Feng et al., 2016). We argue that two different ‘non-halite’ deposits exist in the Levant deep
3397
3398 1173 MSC deposits: 1) the mostly biogenic remains of diatoms (the Argillaceous Diatomites) within
3399
3400 1174 the stage 1 Main Halite interval, and 2) the clastic and reworked deposits of the Interbedded
3401
3402 1175 Evaporites/Argillaceous Evaporites belonging to stage 2 and 3 of the MSC.
3403
3404
3405

3406 1176 Stage 3 of the MSC is generally characterized by reworking of shelf sediments and their
3407
3408 1177 occasional influx into the basin during renewed gypsum deposition. We position the base of
3409
3410 1178 stage 3 within the Interbedded Evaporites at cycle 23 (Figs 5, 6, 12), pointing to a much thicker
3411
3412
3413
3414
3415
3416

3417
3418
3419 1179 stage 3 section in the Levant than in the model of Gvirtzman et al. (2017), Manzi et al. (2018), or
3420
3421 1180 Madof et al. (2019). Relying on the CIESM (2008) stratigraphic model, these separate studies
3422
3423 position the halite into stage 2, and continue stage 2 until almost the top of the Levant MSC
3424 1181
3425 section. They position stage 3 at the topmost part of the section, represented only by Unit 7 - a
3426 1182
3427 thin anhydrite and shale unit (interpreted by well-log data in the deep basin as no study has
3428 1183
3429 recovered samples from this interval thus far). These studies mainly differ in their interpretation
3430 1184
3431 of the stage 3 depositional environment, namely subaerial (Madof et al., 2019) or subaqueous
3432 1185
3433 (Gvirtzman et al., 2017) dissolution and truncation. According to our depositional model (Fig.
3434 1186
3435 12), Unit 6 belongs to stage 3 of the MSC (the Upper Gypsum and Lago Mare; CIESM, 2008),
3436 1187
3437 and the IMTS (Gvirtzman et al., 2017) or IES (Madof et al., 2019) unconformities in the Levant
3438 1188
3439 represent the transition between stage 3.1 (Upper Gypsum) and 3.2 (Lago Mare) of the MSC.
3440 1189
3441 The latter stage (3.2) was attributed to Unit 7 and perhaps also to parts of the overlying brackish
3442 1190
3443 Afq Formation (Druckman et al., 1995) by Gvirtzman et al. (2017). The introduction of
3444 1191
3445 Paratethyan waters and sediment, termed Lago Mare deposits along the Paratethyan side of the
3446 1192
3447 Mediterranean, is also likely to have reached the deep basins. However, while those might have
3448 1193
3449 reached the Levant Basin, different local drainage systems are most likely the sources for the
3450 1194
3451 MSC stage 3 transported sediments in the Levant area. A local source for transported sediments
3452 1195
3453 is the Nile drainage and fan systems, identified as reaching further northwest, beyond the
3454 1196
3455 Dolphin and Leviathan wells, towards the Eratosthenes Seamount offshore Cyprus (Hawie et al.,
3456 1197
3457 2013a, 2013b). In addition, local drainage systems that may have supplied the transported
3458 1198
3459 sediments include the Afq and Ashdod canyons (Bertoni and Cartwright, 2007; Druckman et al.,
3460 1199
3461 1995), and the southern Turkey and western Syria drainage systems proposed by Madof et al.
3462 1200
3463 (2019).
3464 1201
3465
3466
3467
3468
3469
3470
3471
3472

3473
3474
3475 1202 **6. Conclusions**
3476
3477

3478 1203 Over the past 50 years, models explaining the formation of offshore MSC deposits have
3479
3480 1204 remained hypothetical in the absence of a complete sedimentary record of the deep
3481
3482 1205 Mediterranean Basin. The current study presents results from the offshore Dolphin and
3483
3484 1206 Leviathan-1 wells, which penetrated MSC evaporites from 2025 to 3616 m, and from 2090 to
3485
3486 1207 3759 m, respectively. Our results challenge some of the current models for the MSC regarding
3487
3488 1208 the synchronicity or diachronism of evaporite deposits across the Mediterranean Basin, their
3489
3490 1209 composition, and controlling factors. A longer duration for halite deposition than previously
3491
3492 1210 assumed impacts our understanding of the biochemical and spatial constraints of this time period.
3493
3494 1211 While similar ideas have been previously raised (e.g., Van Couvering et al., 1976; Govers, 2009;
3495
3496 1212 Hardie and Lowenstein, 2004; Meilijson et al., 2018; Ryan, 2011; Simon and Meijer, 2017), we
3497
3498 1213 provide the first report on sedimentological data from the deep basin MSC halite deposits
3499
3500 1214 supporting the scenario of long-lasting salt deposition. We call for a re-evaluation of models
3501
3502 1215 based on a ~50 kyr-long deposition of halite in the deep basins. However, samples from the
3503
3504 1216 upper part of the deep MSC deposits in the Eastern Mediterranean are not yet available, while
3505
3506 1217 the existing sedimentary record drilled by the industry consists of well cuttings and not a
3507
3508 1218 continues core. The complexity revealed by this study makes a strong case for future scientific
3509
3510 1219 drilling efforts that can retrieve cores from different parts of the deep-basin halite deposits of the
3511
3512 1220 Mediterranean.
3513
3514

3515
3516 1221 This study aimed at addressing the composition and key stratigraphic questions regarding the
3517
3518 1222 timing and correlation of MSC events in the deep Mediterranean. Our main findings can be
3519
3520 1223 summarized as follows:
3521
3522
3523
3524
3525
3526
3527
3528

3529
3530
3531
3532
3533
3534
3535
3536
3537
3538
3539
3540
3541
3542
3543
3544
3545
3546
3547
3548
3549
3550
3551
3552
3553
3554
3555
3556
3557
3558
3559
3560
3561
3562
3563
3564
3565
3566
3567
3568
3569
3570
3571
3572
3573
3574
3575
3576
3577
3578
3579
3580
3581
3582
3583
3584

- 1224 1. The formation of thick halite deposits in the Levant Basin occurred in a deep-basin deep-
- 1225 water environment that began earlier than previously thought, during the PLG phase of
- 1226 gypsum precipitation in the marginal basins. This implies that a shallow desiccated
- 1227 scenario is not necessarily required to generate halite precipitation during the MSC. The
- 1228 presence of well-preserved marine planktonic diatoms within the massive halite deposits
- 1229 strongly supports a periodic connectivity between the Atlantic and the Eastern
- 1230 Mediterranean during halite deposition.
- 1231 2. The exact timing for the end of deep-basin halite precipitation is still unclear. Well-log
- 1232 interpretation, cyclostratigraphy, and the astronomical tuning model presented here
- 1233 suggest that halite deposition continued at least until 5.45 Ma, and interbedded clastic
- 1234 material and evaporites (probably mainly gypsum/anhydrite) persisted until ca. 5.33 Ma.
- 1235 3. The transition into the Interbedded Evaporites interval at 2560 m at Dolphin and 2800 m
- 1236 at Leviathan-1 marks a major shift in the mode of deposition. An increase in basin-ward
- 1237 transport of sediments is indicated by the high abundance of larger sub-rounded clastic
- 1238 grains such as quartz and plagioclase, clay, micrite, and reworked Cretaceous to Eocene
- 1239 benthic and planktic foraminifera. Variable thermal maturity indices also point to mixed
- 1240 sources of organic matter. In general, biomarker indices in the Interbedded Evaporites
- 1241 resemble those measured elsewhere in the Mediterranean Basin from strata with
- 1242 transported material and mixed sources. The transition from the Main Halite to the
- 1243 Interbedded Evaporites at 2560 m most likely represents the transition between stage 1
- 1244 and 2 of the MSC. The large amounts of clastic sediments in the Interbedded Evaporites
- 1245 are possibly an answer to one of the MSC enigmas regarding the location of the

3585
3586
3587 1246 transported material related to the sea-level drawdown of stage 2 and the interruption of the
3588
3589 1247 connection with of the Atlantic Ocean.

- 3591
3592 1248 4. During the MSC, high sea level and partial connectivity with the global ocean promoted
3593
3594 1249 the deposition of deep-basin deep-water halite, while sea-level drawdown promoted
3595
3596 1250 deposition of reworked and transported material from the margins into deep
3597
3598 1251 Mediterranean basins.

3600
3601 1252 **Acknowledgments**

3603 1253 The authors would like to thank Ratio Oil Exploration, Noble Energy, and Delek Energy for
3604
3605 1254 kindly providing data and permission to publish. This work was supported by the State of Israel
3606
3607 1255 Ministry of Energy, the Maurice Hatter Foundation, and by the Marie Curie Career Integration
3608
3609 1256 Grants (CIG) FP7-PEOPLE-2011-CIG under the GASTIME project framework. The work was
3610
3611 1257 also supported by the COST Action “Uncovering the Mediterranean salt giant” (MEDSALT)
3612
3613 1258 supported by COST (European Cooperation in Science and Technology). We are grateful to
3614
3615 1259 Emerson-Paradigm for software sponsorship. We would also like to thank Tanja Kouwenhoven
3616
3617 1260 for her contribution with foraminiferal analysis, Revital Bookman and Beverly Goodman for the
3618
3619 1261 use of laboratory equipment, Nimer Taha and Alexander Surdyaev for laboratory assistance with
3620
3621 1262 the XRD/XRF analysis and seismic interpretation, respectively. Nadia Dildar, Alexander Weber,
3622
3623 1263 and Ian Bishop are thanked for laboratory assistance for biomarker analysis and diatom
3624
3625 1264 taxonomy. We thank William B.F. Ryan, Andre Strasser, and an anonymous reviewer for
3626
3627 1265 suggestions which significantly improved the manuscript.
3628
3629
3630
3631
3632
3633
3634
3635
3636
3637
3638
3639
3640

3641
3642
3643
3644
3645
3646
3647
3648
3649
3650
3651
3652
3653
3654
3655
3656
3657
3658
3659
3660
3661
3662
3663
3664
3665
3666
3667
3668
3669
3670
3671
3672
3673
3674
3675
3676
3677
3678
3679
3680
3681
3682
3683
3684
3685
3686
3687
3688
3689
3690
3691
3692
3693
3694
3695
3696

1266 **References**

1267 Alinat, J., Cousteau, J., 1962. Accidents de terrain en mer de Ligurie. Océanographie géologique
1268 et géophysique de la Méditerranée occidentale, 121. Centre national de la recherche
1269 scientifique, Paris.

1270 Almogi-Labin, A., Bein, A., Sass, E., 1993. Late Cretaceous upwelling system along the
1271 Southern Tethys Margin (Israel): Interrelationship between productivity, bottom water
1272 environments, and organic matter preservation. *Paleoceanography* 8, 671–690.
1273 doi:10.1029/93PA02197

1274 Anderson, R.Y., Dean, W.E., 1995. Filling the Delaware Basin: Hydrologic and Climatic
1275 Controls on the Upper Permian Castile Formation Varved Evaporite, in: Scholle, P.A.,
1276 Peryt, T.M., Ulmer-Scholle, D.S. (Eds.), *The Permian of Northern Pangea: Volume 2:*
1277 *Sedimentary Basins and Economic Resources*. Springer Berlin Heidelberg, Berlin,
1278 Heidelberg, pp. 61–78. doi:10.1007/978-3-642-78590-0_4

1279 Arnon, A., Selker, J.S., Lensky, N.G., 2016. Thermohaline stratification and double diffusion
1280 diapycnal fluxes in the hypersaline Dead Sea. *Limnol. Oceanogr.* 61, 1214–1231.
1281 doi:10.1002/lno.10285

1282 Bauer, J.E., Druffel, E.R.M., 1998. Ocean margins as a significant source of organic matter to
1283 the deep open ocean. *Nature* 392, 20–23. doi:10.1038/33122

1284 Bayliss, D.D., 1973. *Micropalaeontology of sections Cenomanian to Middle Eocene West Bank*
1285 *of Jordan*. London.

1286 Bellaiche, G., Genesseeux, M., Mauffret, A., Rehault, J.P., 1974. Prélèvements systématique et
1287 caractérisation des réflecteurs acoustiques: nouvelle étape dans la compréhension de la
1288 géologie de la Méditerranée occidentale. *Marine Geology* 16, M47–M56.

3697
3698
3699 1289 Berggren, W.A., Kennett, J.P., Srinivasan, M.S., 2006. Neogene Planktonic Foraminifera: A
3700
3701 Phylogenetic Atlas. *Micropaleontology*. doi:10.2307/1485586
3702 1290
3703
3704 1291 Bertoni, C., Cartwright, J.A., 2007. Major erosion at the end of the Messinian Salinity Crisis:
3705
3706 Evidence from the Levant Basin, Eastern Mediterranean. *Basin Res.* 19, 1–18.
3707
3708 1293 doi:10.1111/j.1365-2117.2006.00309.x.
3709
3710 1294 Bertoni, C., Cartwright, J.A., 2006. Controls on the basinwide architecture of late Miocene
3711
3712 (Messinian) evaporites on the Levant margin (Eastern Mediterranean). *Sediment. Geol.*
3713 1295
3714 188–189, 93–114. doi:10.1016/j.sedgeo.2006.03.019.
3715 1296
3716
3717 1297 Biehl, B.C., Reuning, L., Strozyk, F., Kukla, P.A., 2014. Origin and deformation of intra-salt
3718
3719 sulphate layers: An example from the Dutch Zechstein (Late Permian). *Int. J. Earth Sci.*
3720 1298
3721 103, 697–712. doi:10.1007/s00531-014-0999-4
3722 1299
3723
3724 1300 Blanc, P., 2000. Of sills and straits : a quantitative assessment of the Messinian Salinity Crisis.
3725
3726 *Deep. Res. I* 47, 1429–1460.
3727
3728 1302 Bond, G., Kromer, B., Beer, J., Muscheler, R., Evans, M.N., Showers, W., Hoffmann, S., Lotti-
3729
3730 Bond, R., Hajdas, I., Bonani, G., 2001. Persistent Solar Influence on North Atlantic Climate
3731
3732 During the Holocene. *Science* (80-.). 294, 2130–2136.
3733
3734
3735 1305 Borsetti,, A. M., Curzi, P. V., Landuzzi, V., Mutti, M., Ricci Lucchi, F., Sartori, R., Tomadin, L.,
3736
3737 Zuffa, G.G., 1990. Messinian and pre-Messinian sediments from ODP leg 107 Sites 652 and
3738
3739 654 in the Tyrrhenian Sea: sedimentological and petrographic study and possible
3740
3741 comparisons with Italian sequences, in: Kastens, K. A., Mascle, J., et al. (Ed.), *Proc. Ocean*
3742 1308
3743 *Drill. Program, 107 Sci. Results* 107, 169–186. doi:10.2973/odp.proc.sr.107.161.1990.
3744 1309
3745
3746 1310 Bourcart, J., Boillot, G., Cousteau, J.Y., Gennesseaux, M., Klimek, C., 1958. Les sediments
3747
3748
3749
3750
3751
3752

3753
3754
3755 1311 profonds au large de la cote nicoise. Comptes Rendus de l'Academie des Sciences Paris
3756
3757 1312 147, 116.
3758
3759 1313 Bray, E.E., Evans, E.D., 1961. Distribution of n-paraffins as a clue to recognition of source beds.
3760
3761 Geochim. Cosmochim. Acta 22, 2–15. doi:10.1016/0016-7037(61)90069-2
3762 1314
3763
3764 1315 Buchbinder, B., Zilberman, E., 1997. Sequence stratigraphy of Miocene-Pliocene carbonate-
3765
3766 1316 siliciclastic shelf deposits in the eastern Mediterranean margin (Israel): effects of eustasy
3767
3768 1317 and tectonics. Sediment. Geol. 112, 7–32.
3769
3770 1318 Camerlenghi, A., Aosis, V., Lofi, J., Hübscher, C., deLange, G., Flecker, R., Garcia-Castellanos,
3771
3772 1319 D., Gorini, C., Krijgsman, W., Lugli, S., Makovsky, Y., Manzi, V., McGenity, T., Pan, N.,
3773
3774 1320 2014. Uncovering a Salt Giant. Deep-Sea Record of Mediterranean Messinian Events
3775
3776 1321 (DREAM) multi-phase drilling project, in: EGU. Vienna, p. 1.
3777
3778 1322 Canals, M., Danovaro, R., Heussner, S., Lykousis, V., Puig, P., Trincardi, F., Calafat, A.,
3779
3780 Durrieu de Madron, X., Palanques, A., 2009. Cascades in Mediterranean Submarine Grand
3781 1323
3782 Canyons. Oceanography 22, 26–43. doi:10.5670/oceanog.2009.03
3783 1324
3784
3785 1325 Canals, M., Puig, P., de Madron, X.D., Heussner, S., Palanques, A., Fabres, J., 2006. Flushing
3786
3787 1326 submarine canyons. Nature 444, 354–357. doi:10.1038/nature05271
3788
3789 1327 Christeleit, E.C., Brandon, M.T., Zhuang, G., 2015. Evidence for deep-water deposition of
3790
3791 1328 abyssal Mediterranean evaporites during the Messinian salinity crisis. Earth Planet. Sci.
3792
3793 Lett. 427, 226–235. doi:10.1016/j.epsl.2015.06.060
3794 1329
3795
3796 1330 CIESM, 2008. The Messinian Salinity Crisis from mega-deposits to microbiology - A consensus
3797
3798 1331 report. N° 33. CIESM Work. Monogr. 7–10.
3799
3800 1332 Cita, M.B., 1976. Biodynamic effects of the messinian salinity crisis on the evolution of
3801
3802 1333 planktonic foraminifera in the mediterranean. Palaeogeogr. Palaeoclimatol. Palaeoecol. 20,
3803
3804
3805
3806
3807
3808

3809
3810
3811 1334 23–42. doi:10.1016/0031-0182(76)90023-7
3812
3813 1335 Cita, M.B., Ryan, W.B.F., Kidd, R.B., 1978. Sedimentation rates in neogene deep-sea sediments
3814
3815 from the mediterranean and geodynamic implications of their changes, in: Initial Reports of
3816 1336 the Deep Sea Drilling Project. pp. 991–1002.
3817
3818 1337
3819
3820 1338 Cita, M.B., Santambrogio, S., Melillo, B., Rogate, F., 2006. Messinian Paleoenvironments: New
3821
3822 1339 Evidence from the Tyrrhenian Sea (ODP Leg 107). Proc. Ocean Drill. Program, 107 Sci.
3823
3824 1340 Results 107, 211–227. doi:10.2973/odp.proc.sr.107.161.1990.
3825
3826 1341 Clauzon G., Suc, J.P., Gautier, F., Berger, A., Loutre, M.F., 1996. Alternate interpretation of the
3827
3828 1342 Messinian salinity crisis, controversy resolved? *Geology*, 24, 363-366. Doi: 10.1130/0091-
3829
3830 1343 7613
3831
3832
3833 1344 Cornet, C., 1968. Le graben médian (zone A) de la Méditerranée occidentale pourrait être
3834
3835 1345 pontien. *Sommaire Société Géologique de France* 149.
3836
3837 1346 Couto, D. Do, Popescu, S., Suc, J., Melinte-dobrinescu, M.C., Barhoun, N., Gorini, C., Jolivet,
3838
3839 1347 L., Poort, J., Jouannic, G., Auxietre, J., 2014. Lago Mare and the Messinian Salinity Crisis :
3840
3841 1348 Evidence from the Alboran Sea Lago Mare and the Messinian Salinity Crisis : Evidence
3842
3843 1349 from the Alboran Sea (S . Spain). *Mar. Pet. Geol.* 52, 57–76.
3844
3845 1350 doi:10.1016/j.marpetgeo.2014.01.018
3846
3847
3848 1351 Van Couvering, J.A., Berggren, W.A., Drake, R.E., Aguirre, E., Curtis, G.H., 1976. The terminal
3849
3850 1352 Miocene event. *Mar. Micropaleontol.* 1, 263–286.
3851
3852 1353 Debenedetti, A., 1982. The problem of the origin of the salt deposits in the mediterranean and of
3853
3854 1354 their relations to the other salt occurrences in the neogene formations of the contiguous
3855
3856 1355 regions. *Mar. Geol.* 49, 91–114.
3857
3858 1356 Dela Pierre, F., Clari, P., Natalicchio, M., Ferrando, S., Giustetto, R., Lozar, F., Lugli, S., Manzi,
3859
3860
3861
3862
3863
3864

3865
3866
3867 1357 V., Roveri, M., Violanti, D., 2014. Flocculent layers and bacterial mats in the mudstone
3868
3869 1358 interbeds of the Primary Lower Gypsum unit (Tertiary Piedmont basin, NW Italy): Archives
3870
3871 of palaeoenvironmental changes during the Messinian salinity crisis. *Mar. Geol.* 355, 71–
3872 1359 87. doi:10.1016/j.margeo.2014.05.010
3873
3874 1360
3875
3876 1361 Derin, B., 2000. Stratigraphic and environments of deposition of Or South 1075–2090 m. Ramat
3877
3878 1362 Gan, Derin Consulting & Micropaleontological Services LTD, Internal Isramco Consultant
3879
3880 1363 Report 2/00.
3881
3882 1364 Ditlevsen, P.D., Andersen, K.K., Svensson, A., 2007. The DO-climate events are probably noise
3883
3884 1365 induced: Statistical investigation of the claimed 1470 years cycle. *Clim. Past* 3, 129–134.
3885
3886 1366 doi:10.5194/cp-3-129-2007
3887
3888
3889 1367 Driussi, O., Maillard, A., Ochoa, D., Lofi, J., Chanier, F., Gaullier, V., Briaais, A., Sage, F.,
3890
3891 1368 Sierro, F., Garcia, M., 2015. Messinian Salinity Crisis deposits widespread over the
3892
3893 1369 Balearic Promontory: Insights from new high-resolution seismic data. *Mar. Pet. Geol.* 66,
3894
3895 1370 41–54. doi:10.1016/j.marpetgeo.2014.09.008
3896
3897 1371 Druckman, Y., Buchbinder, B., Martinotti, G.M., Tov, R.S., Aharon, P., 1995. The buried Afik
3898
3899 1372 Canyon (eastern Mediterranean, Israel): a case study of a Tertiary submarine canyon
3900
3901 1373 exposed in Late Messinian times. *Mar. Geol.* 123, 167–185. doi:10.1016/0025-
3902
3903 1374 3227(94)00127-7
3904
3905
3906 1375 Ensminger, A., Joly, G., Albrecht, P., 1978. Rearranged steranes in sediments and crude oils.
3907
3908 1376 *Tetrahedron Letters.* 1575–1578. doi:https://doi.org/10.1016/S0040-4039(01)94608-8
3909
3910 1377 Feng, Y.E., Yankelzon, A., Steinberg, J., Reshef, M., 2016. Lithology and characteristics of the
3911
3912 1378 Messinian evaporite sequence of the deep Levant Basin, Eastern Mediterranean. *Mar. Geol.*
3913
3914 1379 376, 118–131. doi:10.1016/j.margeo.2016.04.004
3915
3916
3917
3918
3919
3920

3921
3922
3923 1380 Flecker, R., Ellam, R.M., 2006. Identifying Late Miocene episodes of connection and isolation in
3924
3925 1381 the Mediterranean-Paratethyan realm using Sr isotopes. *Sediment. Geol.* 188–189, 189–203.
3926
3927 doi:10.1016/j.sedgeo.2006.03.005
3928 1382
3929
3930 1383 Flecker, R., et al., 2015. Evolution of the Late Miocene Mediterranean-Atlantic gateways and
3931
3932 1384 their impact on regional and global environmental change. *Earth-Science Reviews*, 150,
3933
3934 1385 365–392.
3935
3936 1386 Frey-Martinez, J., Hall, B., Cartwright, J., Huuse, M., 2007. Clastic Intrusion at the Base of
3937
3938 1387 Deep-water Sands: A Trap-forming Mechanism in the Eastern Mediterranean. *Sand Inject.*
3939
3940 1388 *Implic. Hydrocarb. Explor. Prod. AAPG Mem.* 87 49–63. doi:10.1306/1209849M873255
3941
3942 1389 Garcia-Castellanos, D., Villaseñor, A., 2011. Messinian salinity crisis regulated by competing
3943
3944 1390 tectonics and erosion at the Gibraltar arc. *Nature* 480, 359–363. doi:10.1038/nature10651
3945
3946 1391 García-Veigas, J., Cendón, D.I., Gibert, L., Lowenstein, T.K., Artiaga, D., 2018. Geochemical
3947
3948 1392 indicators in Western Mediterranean Messinian evaporites: Implications for the salinity
3949
3950 1393 crisis. *Mar. Geol.* 403, 197–214. doi:10.1016/j.margeo.2018.06.005
3951
3952 1394 Gardosh, M., Druckman, Y., Buchbinder, B., Rybakov, M., 2008. The Levant Basin Offshore
3953
3954 1395 Israel: Stratigraphy, Structure, Tectonic Evolution and Implications for Hydrocarbon
3955
3956 1396 Exploration - revised edition. Geological Survey of Israel report GSI/4/2008.
3957
3958 1397 Garrison, R.E., Schreiber, B.C., Bernoulli, D., Fabricius, F.H., Kidd, R.B., Mélières, F., 1978.
3959
3960 1398 Sedimentary Petrology and Structures of Messinian Evaporitic Sediments in the
3961
3962 1399 Mediterranean Sea, Leg 42A, Deep Sea Drilling Project, in: *Initial Reports of the Deep Sea*
3963
3964 1400 *Drilling Project 42, No. 1.* pp. 571–612.
3965
3966
3967
3968 1401 Geletti, R., Zgur, F., Del Ben, A., Buriola, F., Fais, S., Fedi, M., Forte, E., Mocnik, A., Paoletti,
3969
3970 1402 V., Pipan, M., Ramella, R., Romeo, R., Romi, A., 2014. The Messinian Salinity Crisis: New
3971
3972
3973
3974
3975
3976

3977
3978
3979 1403 seismic evidence in the West-Sardinian Margin and Eastern Sardo-Provencal basin (West
3980
3981 1404 Mediterranean Sea). *Mar. Geol.* 351, 76–90. doi:10.1016/j.margeo.2014.03.019
3982
3983
3984 1405 Gennari, R., Manzi, V., Angeletti, L., Bertini, A., Ceregato, A., Faranda, C., Gliozzi, E.,
3985
3986 1406 Menichetti, E., Rosso, A., Roveri, M., Taviani, M., 2013. A shallow water record of the
3987
3988 1407 onset of the Messinian salinity crisis in the Adriatic foredeep (Legnagnone section,
3989
3990 1408 Northern Apennines). *NU SC. Palaeogeogr. Palaeoclimatol. Palaeoecol.*
3991
3992 1409 doi:10.1016/j.palaeo.2013.05.015
3993
3994 1410 Govers, R., 2009. Choking the Mediterranean to dehydration: The Messinian salinity crisis.
3995
3996 1411 *Geology* 37, 167–170. doi:10.1130/G25141A.1
3997
3998
3999 1412 Gvirtzman, Z., Manzi, V., Calvo, R., Gavrieli, I., Gennari, R., Lugli, S., Reghizzi, M., Roveri,
4000
4001 1413 M., 2017. Intra-Messinian truncation surface in the Levant Basin explained by subaqueous
4002
4003 1414 dissolution. *Geology* 45, 4–7. doi:10.1130/G39113.1
4004
4005 1415 Gvirtzman, Z., Reshef, M., Buch-leviatan, O., Ben-avraham, Z., 2013a. Intense salt deformation
4006
4007 1416 in the Levant Basin in the middle of the Messinian Salinity Crisis. *Earth Planet. Sci. Lett.*
4008
4009 1417 379, 108–119. doi:10.1016/j.epsl.2013.07.018
4010
4011 1418 Gvirtzman, Z., Reshef, M., Buch-Leviatan, O., Ben-Avraham, Z., 2013b. Intense salt
4012
4013 1419 deformation in the Levant Basin in the middle of the Messinian Salinity Crisis. *Earth Planet.*
4014
4015 1420 *Sci. Lett.* 379, 108–119. doi:10.1016/j.epsl.2013.07.018
4016
4017
4018 1421 Hall, J.K., Udintsev, G.B., Odnikov, Y.Y., 1994. The bottom relief of the Levantine Sea, in
4019
4020 1422 *Geologic Structure of the Northeastern Mediterranean.* Krashennnikov, V. A., Hall, J.K.,
4021
4022 1423 pp. 5–32, Historical Productions-Hall Ltd., Jerusalem.
4023
4024 1424 Hall, J.K., Lippman, S., Gardosh, M., Tibor, G., Sade, A.R., Sade, H., 2015. A New Bathymetric
4025
4026 1425 Map for the Israeli EEZ: Preliminary Results. State of Israel, Ministry of National
4027
4028
4029
4030
4031
4032

4033
4034
4035 1426 Infrastructure Energy and Water, Jerusalem.
4036
4037 1427 Hardie, L.A., Lowenstein, T.K., 2004. Did the Mediterranean Sea Dry Out During the Miocene?
4038
4039 a Reassessment of the Evaporite Evidence From Dsdp Legs 13 and 42a Cores. *J. Sediment.*
4040 1428
4041
4042 1429 *Res.* 74, 453–461. doi:10.1306/112003740453
4043
4044 1430 Hawie, N., Deschamps, R., Nader, F.H., Gorini, C., 2013a. Sedimentological and stratigraphic
4045
4046 1431 evolution of northern Lebanon since the Late Cretaceous: implications for the Levant
4047
4048 1432 margin and basin. doi:10.1007/s12517-013-0914-5
4049
4050 1433 Hawie, N., Gorini, C., Deschamps, R., Nader, F.H., Montadert, L., Granjeon, D., Baudin, F.,
4051
4052 1434 2013b. Tectono-stratigraphic evolution of the northern Levant Basin (offshore Lebanon).
4053
4054 1435 *Mar. Pet. Geol.* 48, 392–410. doi:10.1016/j.marpetgeo.2013.08.004
4055
4056 1436 Hernández-Molina F.J, et al., 2014. Onset of Mediterranean outflow into the North Atlantic.
4057
4058 1437 *Science* 344, 1244–1250. doi: 10.1126/science.1251306
4059
4060 1438 Hilgen, F., Kuiper, K., Krijgsman, W., Snel, E., Laan, E. Van Der, van der Laan, E., 2007.
4061
4062 1439 Astronomical tuning as the basis for high resolution chronostratigraphy: The intricate
4063
4064 1440 history of the Messinian Salinity Crisis. *Stratigraphy* 4, 231–238.
4065
4066 1441 Hilgen, F.J., Bissoli, L., Iaccarino, S., Krijgsman, W., Meijer, R., Negri, A., Villa, G., 2000.
4067
4068 1442 Integrated stratigraphy and astrochronology of the Messinian GSSP at Oued Akrech
4069
4070 1443 (Atlantic Morocco). *Earth Planet. Sci. Lett.* 182, 237–251. doi:10.1016/S0012-
4071
4072 1444 821X(00)00247-8
4073
4074 1445 Hilgen, F.J., Krijgsman, W., 1999. Cyclostratigraphy and astrochronology of the Tripoli
4075
4076 1446 diatomite formation (pre-evaporite Messinian, Sicily, Italy). *Terra Nov.* 11, 16–22.
4077
4078 1447 doi:10.1046/j.1365-3121.1999.00221.x
4079
4080 1448 Hilgen, F.J., Krijgsman, W., Langereis, C.G., Lourens, L.J., Santarelli, A., Zachariasse, W.J.,
4081
4082
4083
4084
4085
4086
4087
4088

4089
4090
4091 1449 1995. Extending the astronomical (polarity) time scale into the Miocene. *Earth Planet. Sci.*
4092
4093 1450 *Lett.* 136, 495–510. doi:10.1016/0012-821X(95)00207-S
4094
4095
4096 1451 Hsü, K.J., 1973. The desiccated deep-basin model for the Messinian events, in: Drooger, C.W.
4097
4098 1452 (Ed.), *Messinian Events in the Mediterranean*. North-Holland Publ. Co., Amsterdam, pp.
4099
4100 1453 60–67.
4101
4102 1454 Hsü, K. J., Ryan, W.B.F., Schreiber, B.C., 1973. Petrography of a halite sample from hole 134 -
4103
4104 1455 balearic abyssal plain, in: *Initial Reports of the Deep Sea Drilling Project 13, No. Part 2*. pp.
4105
4106 1456 708–711.
4107
4108
4109 1457 Hsü, K.J., Montadert, L., Bernoulli, D., Bizon, G., Cita, M., Erickson, A., Fabricius, F., Garrison,
4110
4111 1458 R.E., Kidd, R.B., Mélières, F., Müller, C., Wright, R.C., 1978a. Site 374: Messina Abyssal
4112
4113 1459 Plain, in: *Initial Reports of the Deep Sea Drilling Project: DSDP Volume XLII Part 1*. p. 43.
4114
4115 1460 doi:10.2973/dsdp.proc.42-1.105.1978
4116
4117
4118 1461 Hsü, K.J., Montadert, L., Bernoulli, D., Bizon, G., Cita, M., Erickson, A., Fabricius, F., Garrison,
4119
4120 1462 R.E., Kidd, R.B., Mélières, F., Müller, C., Wright, R.C., 1978b. Sites 375 and 376: Florence
4121
4122 1463 Rise, in: *Initial Reports of the Deep Sea Drilling Project: DSDP Volume XLII Part 1*. p. 86.
4123
4124 1464 Hüsing, S.K., Cascella, A., Hilgen, F.J., Krijgsman, W., Kuiper, K.F., Turco, E., Wilson, D.,
4125
4126 1465 2010. Astrochronology of the Mediterranean Langhian between 15 . 29 and 14 . 17 Ma.
4127
4128 1466 *Earth Planet. Sci. Lett.* 290, 254–269. doi:10.1016/j.epsl.2009.12.002
4129
4130
4131 1467 Hüsing, S.K., Kuiper, K.F., Link, W., Hilgen, F.J., Krijgsman, W., 2009. The upper Tortonian-
4132
4133 1468 lower Messinian at Monte dei Corvi (Northern Apennines, Italy): Completing a
4134
4135 1469 Mediterranean reference section for the Tortonian Stage. *Earth Planet. Sci. Lett.* 282, 140–
4136
4137 1470 157. doi:10.1016/j.epsl.2009.03.010
4138
4139 1471 Karakitsios, V., Cornée, J.J., Tsourou, T., Moissette, P., Kontakiotis, G., Agiadi, K.,
4140
4141
4142
4143
4144

4145
4146
4147 1472 Manoutsoglou, E., Triantaphyllou, M., Koskeridou, E., Drinia, H., Roussos, D., 2017.
4148
4149 1473 Messinian salinity crisis record under strong freshwater input in marginal, intermediate, and
4150
4151 deep environments: The case of the North Aegean. *Palaeogeogr. Palaeoclimatol.*
4152 1474
4153
4154 1475 *Palaeoecol.* 485, 316–335. doi:10.1016/j.palaeo.2017.06.023
4155
4156 1476 Keogh, S.M., Butler, R.W.H., 1999. The Mediterranean water body in the late Messinian:
4157
4158 interpreting the record from marginal basins on Sicily. *J. Geol. Soc. London.* 156, 837–846.
4159 1477
4160
4161 1478 doi:10.1144/gsjgs.156.4.0837
4162
4163 1479 Krijgsman, W., Blanc-Valleron, M.M., Flecker, R., Hilgen, F.J., Kouwenhoven, T.J., Merle, D.,
4164
4165 1480 Orszag-Sperber, F., Rouchy, J.M., 2002. The onset of the Messinian salinity crisis in the
4166
4167 Eastern Mediterranean (Pissouri Basin, Cyprus). *Earth Planet. Sci. Lett.* 194, 299–310.
4168 1481
4169
4170 1482 doi:10.1016/S0012-821X(01)00574-X
4171
4172 1483 Krijgsman, W., Fortuin, A.R., Hilgen, F.J., Sierro, F.J., 2001. Astrochronology for the Messinian
4173
4174 1484 Sorbas basin (SE Spain) and orbital (precessional) forcing for evaporite cyclicity. *Sediment.*
4175
4176 1485 *Geol.* 140, 43–60. doi:10.1016/S0037-0738(00)00171-8
4177
4178 1486 Krijgsman, W., Garces, M., Agusti, J., Raffi, I., Taberner, C., Zachariasse, W.J., 2000. The
4179
4180 1487 “Tortonian salinity crisis” of the eastern Betics (Spain). *Earth Planet. Sci. Lett.* 181, 497–
4181
4182 1488 511. doi:10.1016/S0012-821X(00)00224-7
4183
4184 1489 Krijgsman, W., Hilgen, F.J., Negri, A., Wijbrans, J.R., Zachariasse, W.J., 1997. The Monte del
4185
4186 1490 Casino section (Northern Apennines, Italy): A potential Tortonian/Messinian boundary
4187
4188 stratotype? *Palaeogeogr. Palaeoclimatol. Palaeoecol.* 133, 27–47. doi:10.1016/S0031-
4189 1491
4190 1492 0182(97)00039-4
4191
4192
4193 1493 Krijgsman, W., Hilgen, F.J., Raffi, I., Sierro, F.J., Wilson, D.S., 1999. Chronology, causes and
4194
4195 1494 progression of the Messinian salinity crisis. *Nature* 400, 652–655. doi:10.1038/23231.
4196
4197
4198
4199
4200

4201
4202
4203 1495 Krijgsman, W., Meijer, P.T., 2008. Depositional environments of the Mediterranean “Lower
4204
4205 1496 Evaporites” of the Messinian salinity crisis: Constraints from quantitative analyses. *Mar.*
4206
4207
4208 1497 *Geol.* doi:10.1016/j.margeo.2008.04.010
4209
4210 1498 Krijgsman, W., Stoica, M., Vasiliev, I., Popov, V. V., 2010. Rise and fall of the Paratethys Sea
4211
4212 1499 during the Messinian Salinity Crisis. *Earth Planet. Sci. Lett.* 290, 183–191.
4213
4214 1500 doi:10.1016/j.epsl.2009.12.020.
4215
4216 1501 Lange, G.J. De, Krijgsman, W., 2010. Messinian salinity crisis: A novel unifying shallow
4217
4218 gypsum / deep dolomite formation mechanism. *Mar. Geol.* 275, 273–277.
4219 1502
4220 doi:10.1016/j.margeo.2010.05.003
4221 1503
4222
4223 1504 Laskar, J., Robutel, P., Joutel, F., Gastineau, M., Correia, A.C.M., Levrard, B., 2004. A long-
4224
4225 1505 term numerical solution for the insolation quantities of the Earth. *Astron. As-trophys.*
4226
4227 1506 *Astron. Astrophys.* 428, 261–285. doi:10.1051/0004-6361:20041335
4228
4229 1507 Leila, M., Kora, M.A., Ahmed, M.A., Ghanem, A., 2016. Sedimentology and reservoir
4230
4231 1508 characterization of the Upper Miocene Qawasim Formation, El-Tamad Oil Field onshore
4232
4233 1509 Nile Delta, Egypt. *Arab. J. Geosci.* 9, 1–13. doi:10.1007/s12517-015-2088-9
4234
4235
4236 1510 Lofi, J., Camerlenghi, A., 2014. Messinian Salinity Crisis - DREAM (Deep-sea Record of
4237
4238 1511 Mediterranean Messinian events) drilling projects Messinian Salinity Crisis - DREAM
4239
4240 1512 (Deep-sea Record of Mediterranean Messinian events) drilling projects, in: EGU. Vienna, p.
4241
4242 1513 1.
4243
4244 1514 Lofi, J., Sage, F., Deverchere, J., Loncke, L., Maillard, A., Gaullier, V., Thion, I., Gillet, H.,
4245
4246 1515 Guennoc, P., Gorini, C., 2011. Refining our knowledge of the Messinian salinity crisis
4247
4248 1516 records in the offshore domain through multi-site seismic analysis. *Bull. la Soc. Geol. Fr.*
4249
4250 1517 182, 163–180. doi:10.2113/gssgfbull.182.2.163
4251
4252
4253
4254
4255
4256

4257
4258
4259 1518 Lohmann, J., Ditlevsen, P.D., 2018. Random and externally controlled occurrences of
4260
4261 1519 Dansgaard-Oeschger events. *Clim. Past* 14, 609–617. doi:10.5194/cp-14-609-2018
4262
4263
4264 1520 Lugli, S., Gennari, R., Gvirtzman, Z., Manzi, V., Roveri, M., Schreiber, B.C., 2013. Evidence of
4265
4266 1521 clastic evaporites in the canyons of the Levant Basin (Israel): implications for the Messinian
4267
4268 1522 Salinity Crisis. *J. Sediment. Res.* 83, 942–954. doi:10.2110/jsr.2013.72
4269
4270 1523 Lugli, S., Manzi, V., Roveri, M., Schreiber, B.C., 2015. The deep record of the Messinian
4271
4272 1524 salinity crisis: Evidence of a non-desiccated Mediterranean Sea. *Palaeogeogr.*
4273
4274 1525 *Palaeoclimatol. Palaeoecol.* 433, 201–218. doi:10.1016/j.palaeo.2015.05.017
4275
4276 1526 Lugli, S., Schreiber, B.C., Triberti, B., 1999. Giant polygons in the Realmonte Mine (Agrigento,
4277
4278 1527 Sicily); evidence for the desiccation of a Messinian halite basin. *J. Sediment. Res.* 69, 764–
4279
4280
4281 1528 771. doi:10.2110/jsr.69.764
4282
4283 1529 McArthur, J. M., Howarth, R. J., Shield, G. A., 2012. Chapter 7: Strontium Isotope Stratigraphy.
4284
4285 1530 In *The Geologic Time Scale*, eds. F. M. Gredstein, J. G. Ogg, M. D. Schmotz & G. M. Ogg,
4286
4287 1531 1144 Elsevier.
4288
4289 1532 Madof, A.S., Bertoni, C., Lofi, J., 2019. Discovery of vast fluvial deposits provides evidence for
4290
4291 1533 drawdown during the late Miocene Messinian salinity crisis. *Geology* 47, 171–174.
4292
4293 1534 doi:10.1130/G45873.1
4294
4295 1535 Manzi, V., Gennari, R., Hilgen, F., Krijgsman, W., Lugli, S., 2013. Age refinement of the
4296
4297 1536 Messinian salinity crisis onset in the Mediterranean. doi:10.1111/ter.12038
4298
4299
4300 1537 Manzi, V., Gennari, R., Lugli, S., Persico, D., Reghizzi, M., Roveri, M., Schreiber, B.C., Calvo,
4301
4302 1538 R., Gavrieli, I., Gvirtzman, Z., 2018. The onset of the Messinian salinity crisis in the deep
4303
4304 1539 Eastern Mediterranean basin. *Terra Nov.* 38, 42–49. doi:10.1111/ter.12325
4305
4306 1540 Manzi, V., Gennari, R., Lugli, S., Roveri, M., Scafetta, N., Charlotte, B., 2012. High-frequency
4307
4308
4309
4310
4311
4312

4313
4314
4315 1541 cyclicity in the Mediterranean Messinian evaporites: evidence for solar-lunar climate
4316
4317 1542 forcing. *J. Sediment. Res.* 82, 991–1005. doi:10.2110/jsr.2012.81
4318
4319
4320 1543 Manzi, V., Lugli, S., Roveri, M., Dela Pierre, F., Gennari, R., Lozar, F., Natalicchio, M.,
4321
4322 1544 Schreiber, B.C., Taviani, M., Turco, E., 2015. The Messinian salinity crisis in Cyprus: A
4323
4324 1545 further step towards a new stratigraphic framework for Eastern Mediterranean. *Basin Res.*
4325
4326 1546 28, 207–236. doi:10.1111/bre.12107
4327
4328 1547 Manzi, V., Lugli, S., Roveri, M., Schreiber, B.C., 2009. A new facies model for the Upper
4329
4330 1548 Gypsum of Sicily (Italy): Chronological and palaeoenvironmental constraints for the
4331
4332 1549 Messinian salinity crisis in the Mediterranean. *Sedimentology* 56, 1937–1960.
4333
4334 1550 doi:10.1111/j.1365-3091.2009.01063.x
4335
4336 1551 Manzi, V., Lugli, S., Roveri, M., Schreiber, B.C., Gennari, R., 2011. The Messinian “Calcare di
4337
4338 1552 Base” (Sicily, Italy) revisited. *Bull. Geol. Soc. Am.* 123, 347–370. doi:10.1130/B30262.1
4339
4340 1553 Marzocchi, A., Lunt, D.J., Flecker, R., Bradshaw, C.D., Farnsworth, A., Hilgen, F.J., 2015.
4341
4342 1554 Orbital control on late Miocene climate and the North African monsoon: Insight from an
4343
4344 1555 ensemble of sub-precessional simulations. *Clim. Past* 11, 1271–1295. doi:10.5194/cp-11-
4345
4346 1556 1271-2015
4347
4348 1557 Meilijson, A., Ashckenazi-Polivoda, S., Ron-Yankovich, L., Illner, P., Alsenz, H., Speijer, R.P.,
4349
4350 1558 Almogi-Labin, A., Feinstein, S., Berner, Z., Püttmann, W., Abramovich, S., 2014.
4351
4352 1559 Chronostratigraphy of the Upper Cretaceous high productivity sequence of the southern
4353
4354 1560 Tethys, Israel. *Cretac. Res.* 50. doi:10.1016/j.cretres.2014.04.006
4355
4356 1561 Meilijson, A., Steinberg, J., Hilgen, F., Bialik, O.M., Waldmann, N.D., Makovsky, Y., 2018.
4357
4358 1562 Deep-basin evidence resolves a 50-year-old debate and demonstrates synchronous onset of
4359
4360 1563 Messinian evaporite deposition in a non-desiccated Mediterranean. *Geology* 46, 4–7.
4361
4362
4363
4364
4365
4366
4367
4368

4369
4370
4371 1564 Müller, D.W., Mueller, P.A., 1991. Origin and age of the Mediterranean Messinian evaporites:
4372
4373 1565 implications from Sr isotopes. *Earth Planet. Sci. Lett.* doi:10.1016/0012-821X(91)90039-K
4374
4375
4376 1566 Nam, M., Görür, N., Flecker, R., Sak, M., Tüno, C., Ellam, R., Krijgsman, W., Vincent, S.,
4377
4378 1567 Dikba, A., 2006. Paratethyan–Mediterranean connectivity in the Sea of Marmara region
4379
4380 1568 (NW Turkey) during the Messinian. *Sediment. geo* 188–189, 171–187.
4381
4382 1569 doi:10.1016/j.sedgeo.2006.03.004
4383
4384 1570 Netzeband, G.L., Hübscher, C.P., Gajewski, D., 2006. The structural evolution of the Messinian
4385
4386 1571 evaporites in the Levantine Basin. *Mar. Geol.* 230, 249–273.
4387
4388 1572 doi:10.1016/j.margeo.2006.05.004
4389
4390 1573 Ochoa, D., Sierro, F.J., Lofi, J., Maillard, A., Flores, J.A., Suarez, M., 2015. Synchronous onset
4391
4392 1574 of the Messinian evaporite precipitation: First Mediterranean offshore evidence. *Earth*
4393
4394 1575 *Planet. Sci. Lett.* 427, 112–124. doi:10.1016/j.epsl.2015.06.059
4395
4396 1576 Ogniben, L., 1957. Petrografia della Serie Solfifera Siciliana e considerazioni geologiche
4397
4398 1577 relative. *Memorie Descrittive della Carta Geologica d'Italia* 33, 1–275.
4399
4400 1578 Ohneiser, C., Florindo, F., Stocchi, P., Roberts, A.P., DeConto, R.M., Pollard, D., 2015.
4401
4402 1579 Antarctic glacio-eustatic contributions to late Miocene Mediterranean desiccation and
4403
4404 1580 reflooding. *Nat. Commun.* 6, 8765. doi:10.1038/ncomms9765
4405
4406 1581 Peters, K.E., A.E. Kontorovich, J.M.M., 1993. Geochemistry of selected oils and rocks from the
4407
4408 1582 central portion of the west Siberian Basin, Russia. *Am. Assoc. Pet. Geol. Bull.* 77, 87–863.
4409
4410 1583 Peters, K.E., 1986. Guidelines for Evaluating Petroleum Source Rock Using Programmed
4411
4412 1584 Pyrolysis. *Am. Assoc. Pet. Geol. Bull.* 70, 318–329. doi:10.1306/94885688-1704-11D7-
4413
4414 1585 8645000102C1865D
4415
4416 1586 Peters, K.E., Rohrback, B.G., Kaplan, I.R., 1980. Laboratory-simulated thermal maturation of
4417
4418
4419
4420
4421
4422
4423
4424

4425
4426
4427 1587 Recent sediments. *Phys. Chem. Earth* 12, 547–557. doi:10.1016/0079-1946(79)90136-8
4428
4429 1588 Peters, K.E., Walters Clifford C, Moldowan, J.M., 2005. *The Biomarker Guide, Biomarkers and*
4430
4431 *Isotopes in Petroleum Exploration and Earth History, Volume 2.* Cambridge.
4432 1589
4433 doi:10.1017/s0016756806212056
4434 1590
4435
4436 1591 Rashid, H., Grosjean, E., 2006. Detecting the source of Heinrich layers: An organic geochemical
4437
4438 1592 study. *Paleoceanography* 21. doi:10.1029/2005PA001240
4439
4440 1593 Reiche, S., Hübscher, C., Beitz, M., 2014. Fault-controlled evaporite deformation in the Levant
4441
4442 1594 Basin, Eastern Mediterranean. *Mar. Geol.* 354, 53–68. doi:10.1016/j.margeo.2014.05.002
4443
4444 1595 Richter-Bernburg, G., 1996. *Zechstein-Anhydrite: Fazies und Genese, Geologisches Jahrbuch.*
4445
4446 1596 Reihe A, Allgemeine und regionale Geologie Bundesrepublik Deutschland und
4447
4448 1597 Nachbargebiete, Tektonik, Stratigraphie, Paläontologie. Bundesanstalt für
4449
4450 1598 Geowissenschaften und Rohstoffe.
4451
4452
4453 1599 Roberts, G., Peace, D., 2007. Hydrocarbon plays and prospectivity of the Levantine basin,
4454
4455 1600 offshore Lebanon and Syria from modern seismic data. *GeoArabia* 12, 99–124.
4456
4457 1601 Rouchy, J.M., Caruso, A., 2006. The Messinian salinity crisis in the Mediterranean basin : A
4458
4459 1602 reassessment of the data and an integrated scenario. *Sediment. Geol.* 188–189, 35–67.
4460
4461 1603 doi:10.1016/j.sedgeo.2006.02.005
4462
4463 1604 Roveri, M., Flecker, R., Krijgsman, W., Lofi, J., Lugli, S., Manzi, V., Sierro, F.J., Bertini, A.,
4464
4465 1605 Camerlenghi, A., De Lange, G., Govers, R., Hilgen, F.J., Hübscher, C., Meijer, P.T., Stoica,
4466
4467 1606 M., 2014a. The Messinian Salinity Crisis: Past and future of a great challenge for marine
4468
4469 1607 sciences. *Mar. Geol.* 352, 25–58. doi:10.1016/j.margeo.2014.02.002
4470
4471
4472 1608 Roveri, M., Gennari, R., Ligi, M., Lugli, S., Manzi, V., Reghizzi, M., 2019. The synthetic
4473
4474 1609 seismic expression of the Messinian salinity crisis from onshore records: implications for
4475
4476
4477
4478
4479
4480

4481
4482
4483 1610 shallow- to deep-water correlations. *Basin Res.* doi:10.1111/bre.12361
4484
4485
4486 1611 Roveri, M., Lugli, S., Manzi, V., Gennari, R., Schreiber, B.C., 2014b. High-resolution strontium
4487
4488 1612 isotope stratigraphy of the messinian deep Mediterranean basins: Implications for marginal
4489
4490 1613 to central basins correlation. *Mar. Geol.* 349, 113–125. doi:10.1016/j.margeo.2014.01.002
4491
4492 1614 Roveri, M., Manzi, V., Bergamasco, A., Falcieri, F.M., Gennari, R., Lugli, S., Schreiber, B.C.,
4493
4494 1615 2014c. Dense shelf water cascading and messinian canyons: A new scenario for the
4495
4496 1616 mediterranean salinity crisis. *Am. J. Sci.* 314, 751–784. doi:10.2475/05.2014.03
4497
4498
4499 1617 Rullkötter, J., R.M., 1988. Natural and artificial maturation of biological markers in a Toarcian
4500
4501 1618 shale from northern Germany, in: Novelli, L.M. and L. (Ed.), *Advances in Organic*
4502
4503 1619 *Geochemistry* 1987. Oxford Pergamon Press, pp. 639–645.
4504
4505 1620 Ryan, W.B.F., 2011. Geodynamic responses to a two-step model of the Messinian salinity crisis.
4506
4507 1621 *Bull. la Soc. Geol. Fr.* 182, 73–78. doi:10.2113/gssgfbull.182.2.73
4508
4509 1622 Ryan, W.B.F., 2008. Modeling the magnitude and timing of evaporative drawdown during the
4510
4511 1623 Messinian salinity crisis. *Stratigraphy* 5, 227–243.
4512
4513 1624 Ryan, W.B.F., 1978. Messinian badlands on the southeastern margin of the Mediterranean Sea.
4514
4515 1625 *Mar. Geol.* 27, 349–363. doi:10.1016/0025-3227(78)90039-7
4516
4517
4518 1626 Ryan, W.B.F., 1976. Quantitative evaluation of the depth of the western Mediterranean before,
4519
4520 1627 during and after the late Miocene salinity crisis. *Sedimentology* 23, 791–813.
4521
4522
4523 1628 Ryan, W.B.F., 1973. Geodynamic implications of the Messinian crisis of salinity, in: Drooger,
4524
4525 1629 D.W. (Ed.), *Messinian Events in the Mediterranean*. Elsevier, Amsterdam, pp. 26–38.
4526
4527 1630 Ryan, W.B.F., Cita, M.B., 1978. The nature and distribution of Messinian erosional surfaces -
4528
4529 1631 Indicators of a several-kilometer-deep Mediterranean in the Miocene. *Mar. Geol.*
4530
4531 1632 doi:10.1016/0025-3227(78)90032-4
4532
4533
4534
4535
4536

4537
4538
4539 1633 Ryan, W.B.F., Hsü, K.J., Cita, M.B., Dumitrica, P., Lort, J., Maync, W., Nesteroff, W.D., Pautot,
4540
4541 1634 G., Stradner, H., 2007. DSDP Volume XIII: 6. Balearic Rise - Site 124. The Shipboard
4542
4543 Scientific Party. doi:10.2973/dsdp.proc.13.1973
4544 1635
4545
4546 1636 Ryan, W.B.F., Stanley, D.J., Hersey, J.B., Fahlquist, D.A., Allan, T.D., 1971. The tectonics and
4547
4548 1637 geology of the Mediterranean Sea. In: Maxwell, A.E. (Ed.), *The Sea*. Wiley- Interscience,
4549
4550 1638 New York, pp. 387–492.
4551
4552 1639 Scafetta, N., Milani, F., Bianchini, A., Ortolani, S., 2016. On the astronomical origin of the
4553
4554 1640 Hallstatt oscillation found in radiocarbon and climate records throughout the Holocene.
4555
4556 1641 Earth-Science Rev. 162, 24–43. doi:10.1016/j.earscirev.2016.09.004
4557
4558 1642 Scalán, E.S., Smith, J.E., 1970. An improved measure of the odd-even predominance in the
4559
4560 1643 normal alkanes of sediment extracts and petroleum. *Geochim. Cosmochim. Acta* 34, 611–
4561
4562 1644 620. doi:10.1016/0016-7037(70)90019-0
4563
4564 1645 Schmalz, R.F., 1969. Deep-Water Evaporite Deposition: A Genetic Model. *Am. Assoc. Pet.*
4565
4566 1646 *Geol. Bull.* 53, 798–823. doi:10.1306/5D25C7FD-16C1-11D7-8645000102C1865D
4567
4568 1647 Schulz, M., 2002. On the 1470-year pacing of Dansgaard-Oeschger warm events.
4569
4570 1648 *Paleoceanography* 17, 4-1-4–9. doi:10.1029/2000PA000571
4571
4572 1649 Schulz, M., Mudelsee, M., 2002. REDFIT: Estimating red-noise spectra directly from unevenly
4573
4574 1650 spaced paleoclimatic time series. *Comput. Geosci.* 28, 421–426. doi:10.1016/S0098-
4575
4576 1651 3004(01)00044-9
4577
4578 1652 Selli, R., 1954. Il Bacino del Metauro. *Giornale di Geologia* 24, 1–294.
4579
4580 1653 Sepúlveda, J., Wendler, J.E., Summons, R.E., Hinrichs, K.U., 2009. Rapid Resurgence of Marine
4581
4582 1654 Productivity After the Cretaceous-Paleogene Mass Extinction. *Science* (80-.). 326, 129–
4583
4584 1655 132.
4585
4586
4587
4588
4589
4590
4591
4592

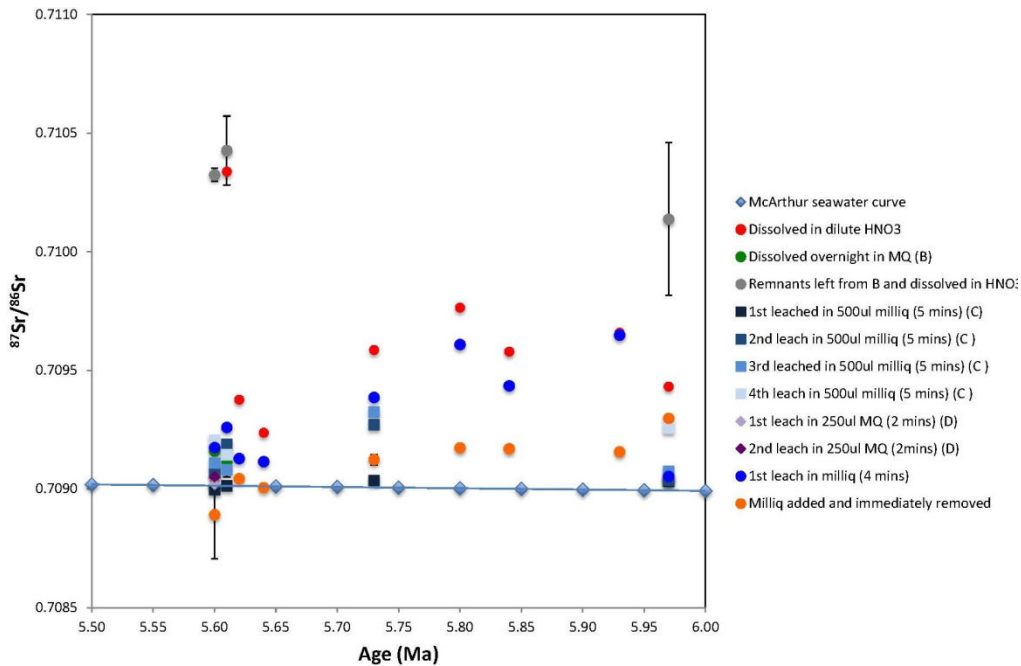
4593
4594
4595 1656 Sierro, F.J., Hilgen, F.J., Krijgsman, W., Flores, J.A., 2001. The Abad composite (SE Spain): A
4596
4597 1657 Messinian reference section for the Mediterranean and the APTS. *Palaeogeogr.*
4598
4599
4600 1658 *Palaeoclimatol. Palaeoecol.* 168, 141–169. doi:10.1016/S0031-0182(00)00253-4
4601
4602 1659 Simon, D., Marzocchi, A., Flecker, R., Lunt, D.J., Hilgen, F.J., Meijer, P.T., 2017. Quantifying
4603
4604 1660 the Mediterranean freshwater budget throughout the late Miocene: New implications for
4605
4606 1661 sapropel formation and the Messinian Salinity Crisis. *Earth Planet. Sci. Lett.* 472, 25–37.
4607
4608 1662 doi:10.1016/j.epsl.2017.05.013
4609
4610 1663 Simon, D., Meijer, P.T., 2017. Salinity stratification of the Mediterranean Sea during the
4611
4612 1664 Messinian crisis: A first model analysis. *Earth Planet. Sci. Lett.* 479, 366–376.
4613
4614 1665 doi:10.1016/j.epsl.2017.09.045
4615
4616 1666 Sirota, I., Ali, A., Lensky, N.G., 2016. Seasonal variations of halite saturation in the Dead Sea.
4617
4618 1667 *Water Resour. Res.* 52. doi:10.1002/2014WR016618
4619
4620
4621 1668 Sirota, I., Enzel, Y., Lensky, N.G., 2017. Temperature seasonality control on modern halite
4622
4623 1669 layers in the Dead Sea: In situ observations. *Bull. Geol. Soc. Am.* 129, 1181–1194.
4624
4625 1670 doi:10.1130/B31661.1
4626
4627 1671 Sonnenfeld, P., Finetti, I., 2011. Messinian Evaporites in the Mediterranean: A Model of
4628
4629 1672 Continuous Inflow and Outflow, in: *Geological Evolution of the Mediterranean Basin.*
4630
4631 1673 doi:10.1007/978-1-4613-8572-1-17
4632
4633
4634 1674 Sonnenfeld, P., Hudec, P.P., 1983. Clay laminations in Halite: Their Cause and Effect, in: *Sixth*
4635
4636 1675 *International Symposium on Salt.* pp. 51–56.
4637
4638 1676 Steinberg, J., Gvirtzman, Z., Folkman, Y., 2010. New age constraints on the evolution of the Mt
4639
4640 1677 Carmel structure and its implications on a Late Miocene extensional phase of the Levant
4641
4642 1678 continental margin. *J. Geol. Soc. London.* 167, 203–216. doi:10.1144/0016-76492009-089
4643
4644
4645
4646
4647
4648

4649
4650
4651 1679 Steinberg, J., Gvirtzman, Z., Folkman, Y., Garfunkel, Z., 2011. Origin and nature of the rapid
4652
4653 1680 late Tertiary filling of the Levant Basin. *Geology* 39, 355–358. doi:10.1130/G31615.1
4654
4655
4656 1681 Steinhilber, F., Abreu, J.A., Beer, J., Brunner, I., Christl, M., Fischer, H., Heikkila, U., Kubik,
4657
4658 1682 P.W., Mann, M., McCracken, K.G., Miller, H., Miyahara, H., Oerter, H., Wilhelms, F.,
4659
4660 1683 2012. 9,400 Years of Cosmic Radiation and Solar Activity From Ice Cores and Tree Rings.
4661
4662 1684 *Proc. Natl. Acad. Sci.* 109, 5967–5971. doi:10.1073/pnas.1118965109
4663
4664 1685 Steinhorn, I., 1983. In situ salt precipitation at the Dead Sea. *Limnol. Oceanogr.* 28, 580–583.
4665
4666 1686 doi:10.4319/lo.1983.28.3.0580
4667
4668 1687 Stiller, M., Gat, J.R., Kaushansky, P., 1997. Halite Precipitation and Sediment Deposition As
4669
4670 1688 Measured in Sediment Traps Deployed in the Dead Sea: 1981-1983. *Dead Sea lake its*
4671
4672 1689 *settings* 161–170.
4673
4674
4675 1690 Stoica, M., Krijgsman, W., Fortuin, A., Gliozzi, E., 2016. Paratethyan ostracods in the Spanish
4676
4677 1691 Lago-Mare: More evidence for interbasinal exchange at high Mediterranean sea level.
4678
4679 1692 *Palaeogeogr. Palaeoclimatol. Palaeoecol.* 441, 854–870. doi:10.1016/j.palaeo.2015.10.034
4680
4681 1693 ten Haven, H.L., de Leeuw, J.W., Schenck, P.A., 1985. Organic geochemical studies of a
4682
4683 1694 Messinian evaporitic basin, northern Apennines (Italy) I: Hydrocarbon biological markers
4684
4685 1695 for a hypersaline environment. *Geochim. Cosmochim. Acta* 49, 2181–2191.
4686
4687 1696 Tomas, C.R., 1996. *Identifying Marine Phytoplankton*, Academic Press Inc. San Diego.
4688
4689 1697 doi:10.1016/S0025-3227(97)81154-1
4690
4691
4692 1698 Topper, R. P. M., Flecker, R., Meijer, P., Wortel, M. J. R., 2011. A box model of the Late
4693
4694 1699 Miocene Mediterranean Sea: implications from combined $^{87}\text{Sr}/^{86}\text{Sr}$ and salinity data.
4695
4696 1700 *Paleoceanography*, 26.
4697
4698 1701 Topper, R.P.M., Lugli, S., Manzi, V., Roveri, M., Meijer, P.T., 2014. Precessional control of Sr
4699
4700
4701
4702
4703
4704

4705
4706
4707 1702 ratios in marginal basins during the Messinian Salinity Crisis? *Geochemistry, Geophys.*
4708
4709 *Geosystems* 15, 1926–1944. doi:10.1002/2013GC005192
4710 1703
4711
4712 1704 van den Berg, B.C.J., Sierro, F.J., Hilgen, F.J., Flecker, R., Larrasoña, J.C., Krijgsman, W.,
4713
4714 1705 Flores, J.A., Mata, M.P., Bellido Martín, E., Civis, J., González-Delgado, J.A., 2015.
4715
4716 1706 Astronomical tuning for the upper Messinian Spanish Atlantic margin: Disentangling basin
4717
4718 1707 evolution, climate cyclicity and MOW. *Glob. Planet. Change* 135, 89–103.
4719
4720 1708 doi:10.1016/j.gloplacha.2015.10.009
4721
4722 1709 Vasiliev, I., Mezger, E.M., Lugli, S., Reichart, G., Manzi, V., Roveri, M., 2017. How dry was the
4723
4724 1710 Mediterranean during the Messinian salinity crisis ? *Palaeogeogr. Palaeoclimatol.*
4725
4726 1711 *Palaeoecol.* 471, 120–133. doi:10.1016/j.palaeo.2017.01.032
4727
4728
4729 1712
4730
4731
4732
4733
4734
4735
4736
4737
4738
4739
4740
4741
4742
4743
4744
4745
4746
4747
4748
4749
4750
4751
4752
4753
4754
4755
4756
4757
4758
4759
4760

4761
4762
4763
4764
4765
4766
4767
4768
4769
4770
4771
4772
4773
4774
4775
4776
4777
4778
4779
4780
4781
4782
4783
4784
4785
4786
4787
4788
4789
4790
4791
4792
4793
4794
4795
4796
4797
4798
4799
4800
4801
4802
4803
4804
4805
4806
4807
4808
4809
4810
4811
4812
4813
4814
4815
4816

1713 **Supplementary Figures**



1714
1715
1716
1717
1718
1719
1720

Figure S1. Strontium stable isotope analysis

Results obtained by the different protocols used for strontium stable isotope analysis with respect to the McArthur et al. (2012) seawater curve. Note the large discrepancies between the results obtained by the different methods used, indicating a highly probable contamination from the drilling mud used during the retrieval of the halite cuttings samples.

4817
 4818
 4819
 4820 1721
 4821 1722
 4822
 4823
 4824
 4825
 4826
 4827
 4828
 4829
 4830
 4831
 4832
 4833
 4834
 4835
 4836
 4837
 4838
 4839
 4840
 4841
 4842
 4843
 4844
 4845
 4846
 4847
 4848
 4849
 4850
 4851
 4852
 4853
 4854
 4855
 4856
 4857
 4858 1723
 4859 1724
 4860
 4861 1725
 4862 1726
 4863
 4864 1727
 4865 1728
 4866
 4867 1729
 4868
 4869
 4870
 4871
 4872

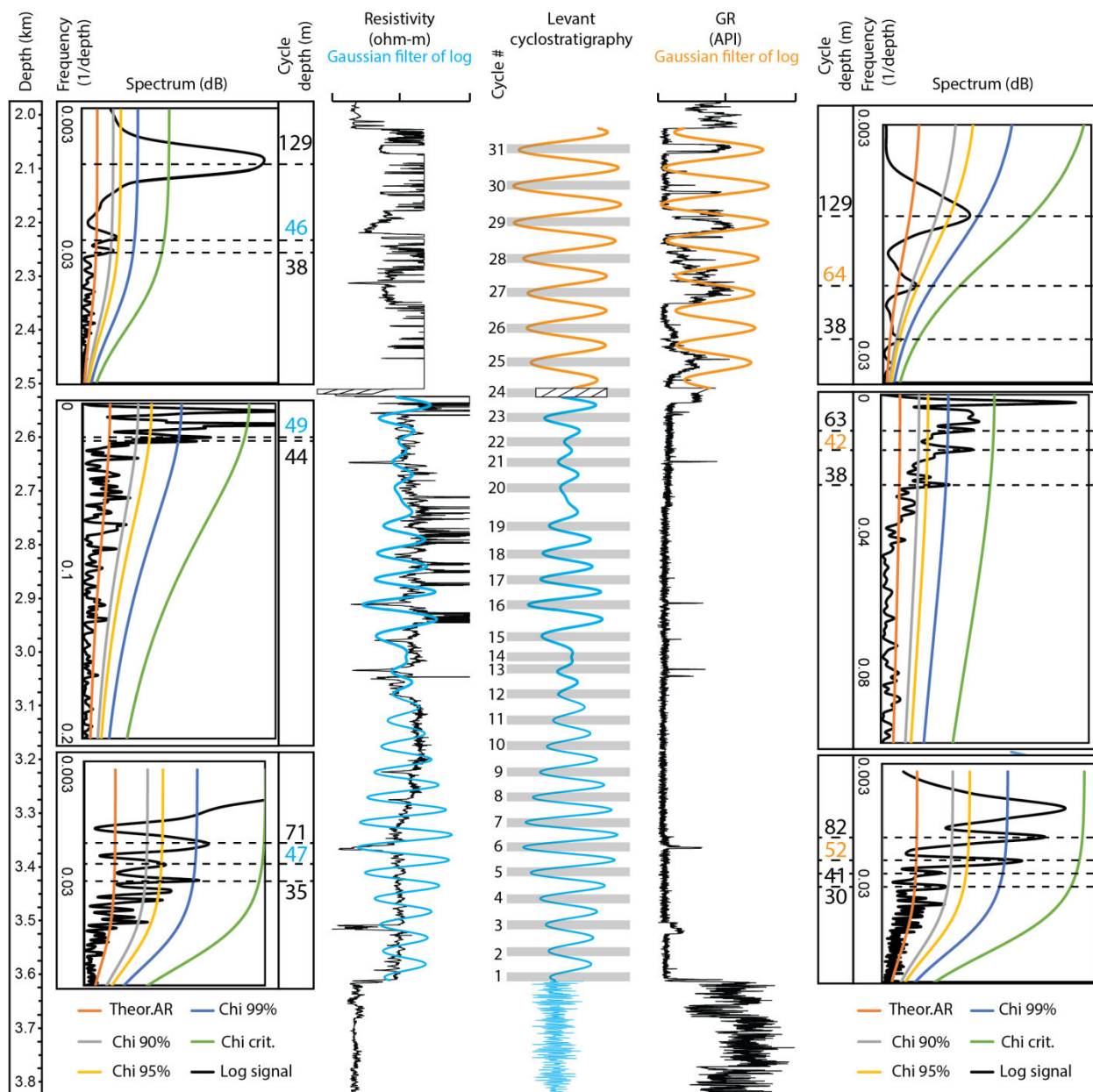


Figure S2. Spectral analysis of the Dolphin well-log curves.

Data shown are the spectral analysis of the resistivity (blue, left) and gamma ray (orange, right) well log curves using REDFIT spectral analysis procedure in Matlab, PAST and Analyseries software. Each log is bounded by respective REDFIT (left of resistivity and right of gamma ray logs) and the combined optimal cyclostratigraphy (center). The REDFIT procedure fits the time series to a red noise model null hypothesis (Theor. AR), produces 'false-alarm' parametric

4873
4874
4875
4876
4877
4878
4879
4880
4881
4882
4883
4884
4885
4886
4887
4888
4889
4890
4891
4892
4893
4894
4895
4896
4897
4898
4899
4900
4901
4902
4903
4904
4905
4906
4907
4908
4909
4910
4911
4912
4913
4914
4915
4916
4917
4918
4919
4920
4921
4922
4923
4924
4925
4926
4927
4928

1730 approximations (chi² of 90%, 95%, and 99%) and a 'critical false-alarm' level (chi crit.). REDFIT
1731 analyses were run by intervals, defined according to the logs expression as follows: from the
1732 base to 3175 m, from 3175 to 2560 m, and from 2560 m to the top of the evaporitic bed.

Sample depth (m)	Depositional units, Dolphin-1, Levant Basin	<i>n</i> -alkane distribution					
		ng SCA/g rock	ng LCA/g rock	LCA/SCA	ACL	CPI	Pr/Ph
2655	Interbedded Evaporites	5.3	8.3	1.6	25	2.9	0.6
2709		9.9	17.0	1.7	25	1.9	0.1
3402	Argillaceous Diatomites	15.9	32.3	2.1	25	4.1	0.9
3474		29.2	52.2	1.8	25	12.3	1.1
3675	Pre-Evaporites	16.4	26.9	1.6	25	5.8	1.0
3810		7.5	5.5	0.7	23	7.4	1.1

Table 1. Indices and distribution of *n*-alkanes as measured from the aliphatic hydrocarbons, Levant Basin MSC lipid extract. Depositional units are described in the text and presented in Figs- 2 and 3. SCA – short chain alkanes (C₁₅₋₂₁), LCA – long chain alkanes (C₂₇₋₃₅), ACL – average chain length, CPI – carbon preference index (Bray and Evans, 1961), expressed as the following relation (*sensu* Vasiliev et al., 2017): $CPI = (((N_{25} + N_{27} + N_{29} + N_{31} + N_{33}) / (N_{24} + N_{26} + N_{28} + N_{30} + N_{32})) + ((N_{25} + N_{27} + N_{29} + N_{31} + N_{33}) / (N_{26} + N_{28} + N_{30} + N_{32} + N_{34}))) * 0.5$, where N represents the relative abundance for individual *n*-alkanes. Pr/Ph is the ratio between the pristane and phytane measured from the extracts.

Sample depth (m)	Depositional units, Dolphin-1, Levant Basin	Steranes				Hopanes		
		C ₂₇		C ₂₈		C ₃₀	C ₃₁	
		C ₂₇ ααα20S/ C ₂₇ ααα20R	Amount of rearranged steranes	C ₂₈ αββ20S/ C ₂₈ αββ20R	C ₂₈ ααα 20S/ C ₂₈ ααα 20R	C ₃₀ βα/ C ₃₀ αβ	C ₃₁ αβS/ C ₃₁ αβR	C ₃₁ βα/ C ₃₁ ββ
2655	Interbedded Evaporites	0.74	High	1.37	0.43	0.02	1.19	0.64
2709		0.82	High	1.39	0.50	0.07	1.15	0.39
3402	Argillaceous Diatomites	0.26	Low	0.01	0.04	1.16	0.07	0.16
3474		0.29	Low	0.03	0.08	1.40	0.03	0.10
3675	Pre-Evaporites	1.66	Moderate	0.06	0.28	0.32	0.79	0.16
3810		0.72	Moderate	1.14	0.43	0.22	0.73	0.02

Table 2. Indices and distribution of steranes and hopanes measured by selective reaction monitoring (SRM) of the aliphatic hydrocarbons, Levant Basin MSC lipid extract. Depositional units as in Table 1. Selected samples and thermal maturity-dependent ratios from SRM analysis include C₂₇ steranes (Ensminger et al., 1978; Peters et al., 2005, 1980), and C₃₀ and C₃₁ hopanes (Peters and Moldowan, 1993; Rullkötter and Marzi, 1988). Note the higher maturity values in the Interbedded Evaporites relative to the over- and underlying intervals.

Sample depth (m)	Depositional units, Dolphin-1, Levant Basin	<i>n</i> -alkane distribution					
		ng SCA/g rock	ng LCA/g rock	LCA/SCA	ACL	CPI	Pr/Ph
2655	Interbedded Evaporites	5.3	8.3	1.6	25	2.9	0.6
2709		9.9	17.0	1.7	25	1.9	0.1
3402	Argillaceous Diatomites	15.9	32.3	2.1	25	4.1	0.9
3474		29.2	52.2	1.8	25	12.3	1.1
3675	Pre-Evaporites	16.4	26.9	1.6	25	5.8	1.0
3810		7.5	5.5	0.7	23	7.4	1.1

Table 1. Indices and distribution of *n*-alkanes as measured from the aliphatic hydrocarbons, Levant Basin MSC lipid extract. Depositional units are described in the text and presented in Figs 2 and 3. SCA – short chain alkanes (C₁₅₋₂₁), LCA – long chain alkanes (C₂₇₋₃₅), ACL – average chain length, CPI – carbon preference index (Bray and Evans, 1961), expressed as the following relation (*sensu* Vasiliev et al., 2017): $CPI = (((N_{25} + N_{27} + N_{29} + N_{31} + N_{33}) / (N_{24} + N_{26} + N_{28} + N_{30} + N_{32})) + ((N_{25} + N_{27} + N_{29} + N_{31} + N_{33}) / (N_{26} + N_{28} + N_{30} + N_{32} + N_{34}))) * 0.5$, where N represents the relative abundance for individual *n*-alkanes. Pr/Ph is the ratio between the pristane and phytane measured from the extracts.

Sample depth (m)	Depositional units, Dolphin-1, Levant Basin	Steranes				Hopanes		
		C ₂₇		C ₂₈		C ₃₀	C ₃₁	
		C ₂₇ ααα20S/ C ₂₇ ααα20R	Amount of rearranged steranes	C ₂₈ αββ20S/ C ₂₈ αββ20R	C ₂₈ ααα 20S/ C ₂₈ ααα 20R	C ₃₀ βα/ C ₃₀ αβ	C ₃₁ αβS/ C ₃₁ αβR	C ₃₁ βα/ C ₃₁ ββ
2655	Interbedded Evaporites	0.74	High	1.37	0.43	0.02	1.19	0.64
2709		0.82	High	1.39	0.50	0.07	1.15	0.39
3402	Argillaceous Diatomites	0.26	Low	0.01	0.04	1.16	0.07	0.16
3474		0.29	Low	0.03	0.08	1.40	0.03	0.10
3675	Pre-Evaporites	1.66	Moderate	0.06	0.28	0.32	0.79	0.16
3810		0.72	Moderate	1.14	0.43	0.22	0.73	0.02

Table 2. Indices and distribution of steranes and hopanes measured by selective reaction monitoring (SRM) of the aliphatic hydrocarbons, Levant Basin MSC lipid extract. Depositional units as in Table 1. Selected samples and thermal maturity-dependent ratios from SRM analysis include C₂₇ steranes (Ensminger et al., 1978; Peters et al., 2005, 1980), and C₃₀ and C₃₁ hopanes (Peters and Moldowan, 1993; Rullkötter and Marzi, 1988). Note the higher maturity values in the Interbedded Evaporites relative to the over- and underlying intervals.